ABSTRACT

Title of Dissertation: EXPERIMENTS WITH FREQUENCY CONVERTED PHOTONS FROM A TRAPPED ATOMIC ION

John Hannegan
Doctor of Philosophy, 2022

Dissertation Directed by: Professor Qudsia Quraishi
Army Research Laboratory and Department of Physics

Trapped atomic ions excel as local quantum information processing nodes, given their long qubit coherence times combined with high fidelity single-qubit and multi-qubit gate operations. Trapped ion systems also readily emit photons as flying qubits, making efforts towards construction of large-scale and long-distance trapped-ion-based quantum networks very appealing. Two-node trapped-ion quantum networks have demonstrated a desirable combination of high-rate and high-fidelity remote entanglement generation, but these networks have been limited to only a few meters in length. This limitation is primarily due to large fiber-optic propagation losses experienced by the ultraviolet and visible photons typically emitted by trapped ions. These wavelengths are also incompatible with existing telecommunications technology and infrastructure, as well as being incompatible with many other emerging quantum technologies designed for useful tasks such as single photon storage, measurement, and routing, limiting the scalability of ion-based networks.

In this thesis, I discuss a series of experiments where we introduce quantum frequency conversion to convert single photons at 493 nm, produced by and entangled with a single trapped $^{138}Ba^{+}$ ion, to near infrared wavelengths for reduced network transmission losses and improved quantum networking capabilities. This work is the first-ever to frequency convert Ba^{+} photons, being one of three nearly concurrent demonstrations of frequency converted photons from any trapped ion. After discussing our experimental techniques and laboratory setup, I first showcase our quantum frequency converters that convert ion-produced single photons to both 780 nm and 1534 nm for improved quantum networking range, whilst preserving the photons' quantum properties. Following this, I present two hybrid quantum networking experiments where we interact converted ion-photons near 780 nm with neutral ^{87}Rb systems. In the initial experiment, we observe, for the first time, interactions between converted ion-photons and neutral Rb vapor via slow light. The following experiment is a multi-laboratory project where we observe Hong-Ou-Mandel interference between converted ion-photons and photons produced by an ensemble of neutral Rb atoms, where notably these sources are located in different buildings and are connected and synchronized via optical fiber. Finally, I describe an experiment in which we verify entanglement between a $^{138}Ba^{+}$ ion and converted photons near 780 nm. These results are critical steps towards producing remote entanglement between trapped ion and neutral atom quantum networking nodes. Motivated by these experimental results, I conclude by presenting a theoretical hybrid-networking architecture where neutral-atomic based nondestructive single photon measurement and storage can be integrated into a long-distance trapped-ion based quantum network to potentially improve remote entanglement rates.

Experiments with Frequency Converted Photons from a Trapped Atomic Ion

by

John Michael Hannegan II

Dissertation submitted to the Faculty of the Graduate School of the
University of Maryland, College Park in partial fulfillment
of the requirements for the degree of
Doctor of Philosophy
2022

Advisory Committee:
Dr. Norbert Linke, Chair
Dr. Qudsia Quraishi, Co-Chair/Advisor
Dr. Edo Waks, Dean's Representative
Dr. Thomas Murphy
Dr. James Siverns

For Gloria.

Acknowledgments

Throughout my time at UMD, I've been fortunate to meet and work with a variety of individuals who have, in one way or another, helped me get through graduate school and present this thesis. First, I'd like to thank my advisor, Qudsia Quraishi, who provided me the opportunity to work on this research in her lab. In her group, I have always felt that my thoughts and opinions on how to move the experiment forward were valued, even at the very start, and I appreciate the freedom she has allowed me to put my own stamp on our lab. I also appreciate her enthusiasm to include me in discussions and meetings with collaborators, even in instances when a graduate student maybe wouldn't normally be included.

The next member of our research group I must thank is James Siverns. Having the same post-doc/research scientist working with you in the lab from start to finish is a luxury most other graduate students are not afforded, certainly not with one who has built a lab from scratch twice! We certainly would have gotten nearly as much of the work presented in this thesis done without him. As with Qudisa, James afforded me a lot of freedom in the lab, and taught me about optics, atomic physics, and critically, when things are good enough to run (and why you shouldn't always try and mess with something if its already working!). I also now know a ton of British phrases and sayings I wouldn't know otherwise. The last lab members I'd like to thank are the various undergraduate students who have had short stints in the lab over the years, including Julian Hammett, Mattie Anastopulos, and Jake Cassell.

There are many people outside of our research group without who I'm also extremely grateful to have worked and have discussions with. To start with, much of the work in this thesis is the result of collaborative efforts with other research groups. Sandy Craddock, Dalia Ornelas, and AJ Hatchel all deserve praise for working with myself and James to get the ion-Rydberg networking experiment up, running, and working. I can't think of a better group of people to have conversations with at 1 AM whilst waiting for coincidence data to slowly accumulate. When it came to discussing/analyzing the data and presenting the results, I also learned a lot from their advisors Steve Rolston and Trey Porto, and from our local quantum optics aficionado, Elizabeth Goldschmidt. Our other major collaboration has been with Edo Waks and graduate student Uday Saha. Its been nice to have another graduate student regularly in the lab to talk to and relate with, and I've learned a lot about integrated photonic devices in our bi-weekly meetings. I look forward to seeing a trapped ion quantum network set up between our labs, and I'm excited to see what types of photonic devices you are able to integrate into it.

I would also like to mention the members, past and present, of UMD's trapped ion community that I have had the pleasure of having interactions with including Clayton Crocker, Ksenia Sosnova, Wen Lin Tan, Allison Carter, Patrick Becker, Kate Collins, Kevin Landsman, Patrick Becker, Antonis Kyprianidis, Daiwei Zhu, Drew Risinger, Michael Kwan, Mika Chmielewski, Nhung Nguyen, Connor Graham, Andreq Laugharn, Denton Wu, Michael Straus Marty Lichtman, Jiehang Zhang, Alaina Green, Henry Luo, Marko Cetina, Crystal Noel, Kristi Beck, Kai Hudek, Jason Amini, Joe Britton, Norbert Linke, Chris Monroe, and others. The regular super-group meetings we have had are always helpful, informative and open, and have really helped me feel a sense of community, even during the COVID lock-downs of 2020. I should also thank Chris for providing us with the blade electrodes that are used for our ion trap.

Early on in graduate school, I was part of an impromptu study group including Kyle Sendgikoski, Tsz Chun Tsui, and Kaustubh Wagh. In addition to studying, we ended up getting lunch on a regular basis, and finding fun things to do on and around campus when we needed a break from work and research. Recently, Kyle suggested we all meet up to write our theses together, which has been a big help as well. I'm glad to have had their friendship and support, especially at the start of graduate school.

I wouldn't have even made it anywhere near a graduate school if it wasn't for the support of my family throughout the years. My mom and dad always pushed me to do my best when I was young and always believed in me. There are also my siblings: Steve, who got me hooked on learning at a young age and has always been a source of life advice, Ryan, who I'm glad to have been able to go to a ton of Nationals games with throughout the past 6 years, especially during that 2019 World Series run, and Megan, who has always been down to go on hikes and even lent her older brother her car for a year.

Most importantly, I must thank my wife, Gloria. She has done more than she knows to keep me sane throughout graduate school: always reminding me to take time to relax, being patient with me after a stressful day in the lab, and making sure I was well fed on the days I got home late. This thesis would not exist without her love, support, and encouragement over these past 6 years.

Table of Contents

List of Tables

List of Figures

List of Abbreviations

AHWP	Achromatic Half Waveplate
AL	Aspheric Lens
AOM	Acousto-Optic Modulator
APD	Avalanche Photodiode
AR	Anti-Reflection (Optical Coating)
BS	Beamsplitter
BSA	Bell State Analyzer
DDS	Direct Digital Synthesizer
DFG	Difference Frequency Generation
DM	Dichroic Mirror
ECDL	External Cavity Diode Laser
EIT	Electromagnetically Induced Transparency
FPGA	Field-Programmable Gate Array
HWP	Half Waveplate
NA	Numerical Aperture
PBS	Polarizing Beamsplitter
PMF	Polarization-Maintaining Fiber
PPLN	Periodically-Poled Lithium Niobate
QFC	Quantum Frequency Conversion
QWP	Quarter Waveplate
REIT	Rydberg Electromagnetically Induced Transparency
RF	Radio-Frequency
SHG	Second Harmonic Generation
SMF	Single Mode Fiber

SNR	Signal to Noise Ratio
SPAD	Single-Photon Avalanche Photodetector
TEC	Thermo Electric Cooler
TTL	Transistor-Transistor Logic
UV	Ultraviolet

Chapter 1: Introduction

The development of classical digital computing combined with long-distance fiber-optic-based digital communications beginning in the middle of the previous century have fundamentally changed and undoubtedly improved the way we process, store, and transfer classical information. These improvements have so widely impacted our society that historians now refer to our current era as the *Information Age* [1]. With the hope that improvements in the way we process and *transmit* quantum information can have a similar positive impact (at least to some extent), the field of quantum information science has experienced rapid growth in the past few decades. Much of the current research and development in this field is focused on trying to enable:

- Large-scale quantum computers and simulators to solve problems in optimization, chemistry, and cryptography that take too long for classical computers to feasibly solve [2–7].
- Quantum sensors for the improved sensitivity of clocks, navigation, and the improved measurement of other physical phenomena [8–10].
- The secure transfer and processing of information via quantum cryptography [11, 12].

Only time will tell how successful we are at developing these technologies - will the Information Age will be followed by the *Quantum Information Age*?

In this thesis I present a set of experiments in which we perform quantum frequency

conversion on single photons from a trapped ion, for the purpose of improving trapped ion quantum communication networks. To motivate this work, this chapter provides a brief introduction to quantum networks, trapped ions in quantum information, and how quantum frequency conversion techniques can be used to improved trapped ion quantum networks. Following this, I also provide a brief description and outline of this thesis.

1.1 Quantum Networking

Critical to the long-term success of quantum computing, quantum sensing, and quantum cryptography is the development of scalable quantum networks. Quantum networks are used to send quantum information in the form of qubits from one location to another to entangle multiple remote quantum devices or processors for enhanced quantum operations [13–15]. Entangling multiple quantum computing processing units, for instance, allows for a distributed quantum computing architecture, where the total number of error-corrected computational qubits is increased far past the limits of a single processing unit [3, 16]. Entanglement between N quantum sensors has been shown to, in many cases, improve the precision scaling of measurements from the standard quantum limit of $1/\sqrt{N}$ for classically-connected quantum sensors to $1/N$ for the entangled sensors [10, 17, 18]. One of the most notable applications of such a sensor network could be the construction of a global network of atomic clocks [10]. Finally, quantum networks can enable the secure transfer of sensitive information via quantum cryptography techniques such as quantum key distribution [19], as well as ”blind quantum computing”, where a remote user can execute operations on a quantum computer while keeping their inputs and results hidden from others [20, 21].

1.1.1 Basic Quantum Network Components

The key basic components required for scalable quantum networks, as well as some basic network architectures using these components are shown in Fig. 1.1. Ideally, a network contains, at the minimum, the following components [15]:

1. **Quantum communication channels** connecting network components through which the "flying" qubits (typically photons) carrying the quantum information used to generate remote entanglement can be transmitted. The combination of channel and flying qubit should be chosen to allow for ease of connectivity whilst minimizing qubit transmission losses.

2. **Classical communication channels** connecting network components used to transmit classical information needed for many quantum communications protocols as well as to provide timing and frequency synchronization signals.

3. **End nodes** for processing quantum information and performing the target quantum task (sensing, computation). Ideally end nodes consist of multiple qubits on which the user can perform high-fidelity quantum operations and quantum state readout and communication qubits for remote entanglement generation.

4. **Repeater nodes** used to combat channel loss and assist in entanglement generation over long distances. Successive repeaters are entangled over shorter distances, creating a long chain of entangled pairs (Fig. 1.1 b). Entanglement swapping protocols [13, 16, 22, 23] can then be used to create entanglement between the end nodes.

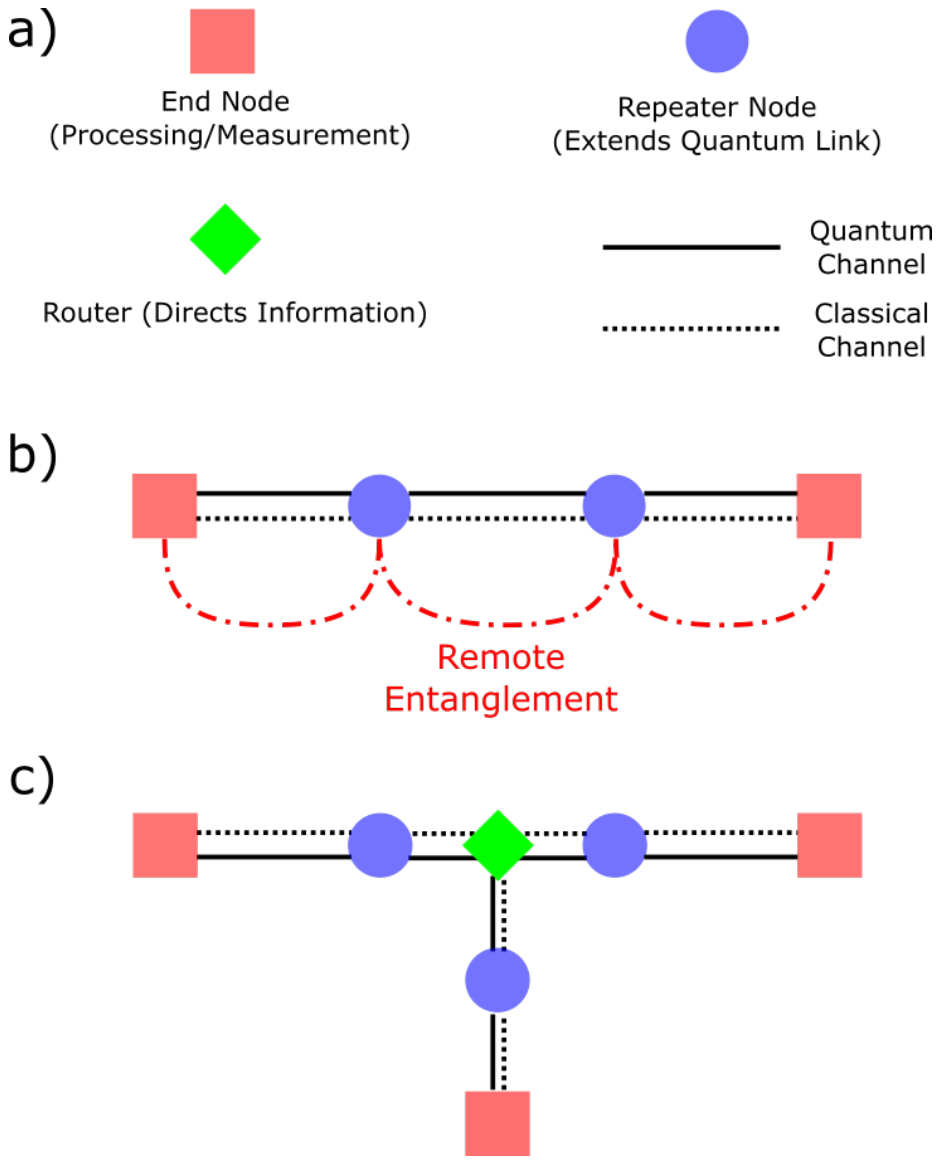

Figure 1.1: **Basic Quantum Network Components** a) Quantum networks consist of entangled end nodes for enhanced processing and measurement, as well as repeater nodes used to extend quantum communication/entanglement range. Other tools such as routers are useful for expansion to multiple end nodes. All nodes are connected by both quantum and classical communication channels b) Successive quantum repeaters create a "chain" of entanglement connecting end nodes. Entanglement swapping can then be used to directly entangle end nodes. c) Single photon routing in a multi-node network allows for the selective entanglement of multiple nodes.

This list is by no means exhaustive, but covers the core parts of a (long-distance) quantum network. Other components, such as nodes for routing and switching (Fig. 1.1 c) [15,24], as well as techniques such as time and frequency multiplexing [25] and entanglement distillation [26] will likely also be required in a large scale, multi-end-node quantum network.

1.1.2 The need for heterogeneity

Many different platforms are being explored for use in quantum networks, such as trapped ions [27–34], neutral atoms [35–40], nitrogen vacancy centers [41–44], and quantum dots [45–48], to name a few. With different strengths and weaknesses, it is highly unlikely that any one of these platforms is ideal to use for all of the network components discussed above. Therefore the ideal quantum network will likely be constructed using different types of quantum systems for each type of networking node [15, 49–51]. In fact, the networking nodes themselves may consist of heterogeneous components, optimized for different tasks such as communication, flying qubit storage, and processing. Finally, what makes an ideal networking node may depend on the task being performed by the quantum network (such as computing vs sensing vs quantum key distribution). It is therefore critical to design quantum nodes and networks with the ability to interface with other types of quantum systems and technologies.

1.2 Trapped Ions as Quantum Networking Nodes

The focus of this thesis is based around the use of trapped atomic ions as the end nodes (Fig. 1.1) of a quantum network. Trapped ions are a well developed and leading technology for both quantum computation [52–55] and simulation [56–59]. Trapped ion systems also excel as

quantum sensors, such as for timekeeping [60, 61] and magnetometry [62]. With the relatively straightforward methods [28, 63–68] in which one can generate photons (serving as the flying qubits discussed in Sec. 1.1.1) entangled with the internal qubit states of an ion, the construction of a large-scale trapped-ion-based network a very appealing idea.

1.2.1 Ions as Qubits and Processors

Modern trapped ion systems provide qubits meeting most of the requirements for universal quantum computation and communication [69][1]. Trapped ion qubits demonstrate long coherence and trapping lifetimes, with a recent experiment [70] demonstrating coherence times of over one hour. These systems additionally demonstrate a universal gate set with high fidelity single qubit gates [71], and high fidelity multi-qubit entangling gate operations [72–74]. Somewhat unique to trapped ion systems is the "all-to-all" connectivity of these entangling gates, where any two qubits in an ion trap can be selectively entangled, reducing the total number of gates required in many protocols [75].

The greatest difficulty when working with trapped ions is the issue of scalability. It is generally agreed that trapped ion systems will be limited at best to around 50-100 qubits in a single trapping region [76]. One key approach to deal with this is the so-called QCCD ion trap architecture [55, 76], where ions can be shuttled between multiple independent trapping regions consisting of smaller chains. Entanglement operations can be performed on these smaller chains, which can then be broken up and shuttled to other trapping regions to distribute entanglement. Recently, a basic, proof-of-principle QCCD-based ion trap quantum computer has been demonstrated [55],

[1] Some may argue that all requirements have been met - but I would argue true scalability has not yet been achieved, particularly when considering long distance communication or large scale quantum computers.

albeit with only six qubits. Another key strategy to scaling up trapped ion qubit numbers is through the use of photonic interconnects [16]. This involves connecting and entangling multiple remote trapped ion processors, via photonic-based quantum networks as described above, and serves as one of the key motivations for this thesis.

1.2.2 Ions in Quantum Networks

Basic short-range two-node trapped ion quantum networks have been demonstrated [16,30, 68], with the most recent [30] achieving remote entanglement rates above 180 Hz with a remote entanglement fiedelity of 0.94. To my knowledge, this represents the highest entanglement rates of any network achieving remote entanglement fidelities above 0.9. These basic network demonstrations, however, have all been limited in entanglement generation rate due to low photon collection efficiencies. A large amount of research is currently focused on increasing the photon collection efficiency of trapped ion systems. Approaches include using in-vacuo optics for high-numerical-aperture photon collection [65], novel trap designs [77–79], and coupling ions to optical cavities for directional and near deterministic photon collection [32, 80].

In addition to low photon collection efficiencies, the native photon emission frequencies of trapped ions have served as a key barrier to scalable and long-range ion-based networks. Trapped ions typically emit photons in the blue and ultraviolet (UV), wavelengths at which light experiences heavy attenuation when transmitted through optical fiber. This attenuation leads to an exponential decrease in remote entanglement rates as the network length increases. This fact alone has played a major role in limiting previous network demonstrations to a few meters in node separation. Furthermore, these colors are not conducive to the construction of

heterogeneous quantum networks. Many of the technologies currently being developed as useful quantum networking tools, such as on-chip integrated photonics for photon routing (Fig. 1.1 c) and multiplexing [25], are designed for use at infrared telecommunications wavelengths rather than in the blue and UV [24, 29, 81].

1.3 Quantum Frequency Conversion for Improved Trapped Ion Quantum Networks

To deal with the problems caused by the native photon emission wavelength of trapped ion systems, this thesis is largely focused on the integration of quantum frequency conversion (QFC) into a trapped ion network. In QFC, a photon at one frequency is converted to another frequency whilst preserving its quantum properties and, if performed carefully, QFC also preserves entanglement the photon may have with another qubit. This process is typically performed through the three-wave mixing process of difference frequency generation (DFG) in a non-linear ($\chi^{(2)}$) material, as will be discussed later in this thesis. Fundamentally, QFC allows the user complete control[2] of the final wavelength of the photon after conversion, making it an attractive choice to improve photon fiber transmission and to enable coupling to other types of systems and devices in a hybrid quantum networking architecture. Therefore, QFC may be necessary to connect trapped ion quantum nodes to the heterogenous quantum networks discussed in Sec. 1.1.2.

1.3.1 Faster Networking Rates and Reduced Infrastructure

Even without high-efficiency conversion, QFC can drastically improve a potential long-distance trapped ion based quantum network by reducing photon loss during fiber transmission. These reduced losses both increase the remote entanglement rates between distant nodes for a

[2] As we will see, there are material property and noise considerations one must take into account in a real system.

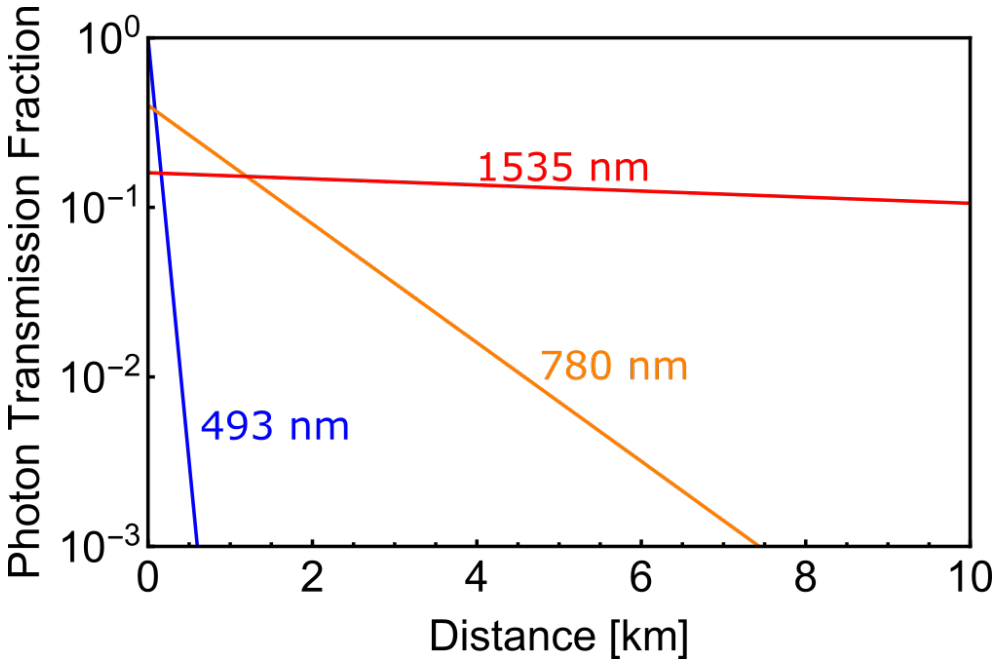

Figure 1.2: **Fiber Transmission Before and After Quantum Frequency Conversion.** Two stages of conversion are assumed, each having 40% conversion efficiency. The first stage takes 493-nm photons to 780 nm and the second stage takes 780-nm photons to 1535 nm.

given separation and reduce the amount of total infrastructure needed in the form of quantum repeaters (Fig. 1.1). As an example of how QFC can greatly reduce loss, Fig. 1.2 shows the transmission probability through optical fiber for photons produced by a Ba^+ ion, before and after conversion, at distances up to 10 km. We assume up to two-stages of QFC, where the first stage of QFC takes 493-nm photons emitted by Ba^+ to 780 nm and the second stage takes the resulting 780-nm photons to 1535 nm. Assuming a conversion efficiency of 40%[3] for each stage and typical fiber transmission losses[4], a single stage of conversion to 780 nm outperforms the 493-nm network after only ≈ 90 m. The two-stage-QFC (total conversion efficiency 16%) 1535-nm network outperforms the 780 nm network after ≈ 1.2 km, at which point the 493 nm photon transmission is down to less than a part in a million[5].

[3] Around the maximum of what is achieved in the work presented in this thesis.
[4] Using values given for fibers available from Thorlabs.
[5] The entanglement rate between two Ba^+ ions would be reduced by a factor of 10^{12} at this point.

1.3.2 Hybrid Quantum Networking: Trapped Ions and Neutral Atoms

Due to the control it gives over the final wavelength of the converted photon, QFC also provides a convenient pathway to interact the photons produced by a trapped ion with different quantum systems and networking components operating at completely different colors. Of particular interest to this thesis is using QFC to integrate neutral-atom-based quantum technologies into a trapped ion network. Neutral atomic systems are well suited to act as quantum repeaters [35, 82] and can be used for tasks not typically achievable with ions such as single photon storage [39, 83–85], nondestructive single photon measurements [40, 86, 87], and as a mediator for photonic gates [88]. Additionally, neutral-atom systems themselves are excellent candidates for quantum computing [89] and simulation [90, 91], making them attractive networking end nodes in their own right. It may be the case that these different quantum networking and computing platforms exist in parallel, making the direct entanglement of a trapped ion node with a neutral atomic node even more advantageous.

1.4 Thesis Outline

This thesis presents a series of experiments performed using frequency converted photons from an elementary trapped Ba^+ ion quantum networking node. These experiments demonstrate the feasibility of using quantum frequency conversion to improve long distance trapped-ion-based networks and explore interactions between trapped-ion photons and neutral atomic systems to enable hybrid/heterogeneous quantum networks. Additionally, this thesis contains a theoretical investigation into how the integration of neutral-atom-based nondestructive photon measurement and storage into a trapped ion network can potentially increase remote entanglement generation

rates. Having hopefully motivated these topics in this chapter, the remainder of this thesis is organized (roughly chronologically) as follows:

Chapter 2: The Barium Ion as a Quantum Networking Node serves as an introduction and motivation to using barium ions as nodes in a basic quantum network. It includes background on the techniques we use to trap ions, initialize ions into certain states, and to produce ion-photon entanglement. Finally, it describes how two-photon interference can be used to generate remote entanglement between Ba^+ and another (potentially different) quantum networking node.

Chapter 3: General Laboratory Setup provides details on the experimental realization of our trapped ion quantum node. It includes descriptions of the vacuum, laser, and control systems used, as well as the apparatuses and techniques used for light delivery and photon collection.

Chapter 4: Quantum Frequency Conversion Setups provides some theoretical background on how we perform quantum frequency conversion using periodically-poled lithium niobate waveguide devices and describes (in an admittedly overly detailed manner) the physical implementation of the various frequency conversion setups used throughout this thesis, providing details on their conversion efficiencies and noise as well as procedures for alignment.

Chapter 5: Quantum Frequency Conversion of Single Photons From a Trapped Ion describes experiments performed to verify and analyze the conversion of single photons from a trapped ion to 780 nm for hybrid networking applications, and to 1534 nm for use in long distance quantum networks. Some theoretical background on these measurements is also provided. The majority of this chapter is adapted from the published works [29, 92], with the 1534 nm work performed in collaboration with the group of Edo Waks. The 780-nm work in particular, was among the first

demonstrations [33, 34, 92] of the frequency conversion of photons from a trapped ion.

Chapter 6: Trapped Ion Slow Light describes a proof-of-principle experiment in which 780 nm frequency converted photons from a trapped ion are slowed, in a tunable manner, via transmission through a neutral atomic vapor. This represents the first demonstration of an interaction of single photons originating from a trapped ion with a neutral atomic system and provides a future pathway for the storage of single photons via neutral atomic systems in a trapped-ion-based quantum network. It is adapted from [93].

Chapter 7: Two Photon Interference Between Photons From a Trapped Ion and Neutral Atomic System describes a collaborative effort with the group of Steve Rolston and Trey Porto in which we demonstrate two-photon interference between photons from a trapped ion and neutral atomic ensemble located in different buildings, to demonstrate the feasibility of a remote hybrid quantum network entangling fundamentally different quantum systems. It is adapted from [50], and many of the details on the neutral atom portion of this experiment, as well as data processing and analysis can also be found in the theses of Alexander Craddock [94] and Dalia Ornelas-Huerta [95].

Chapter 8: Quadrupole Transition in Ba^+ discusses the implementation of qubit state detection via optical shelving of the 1762 nm quadrupole transition in Ba^+, and describes various measurements performed using this transition to determine the efficiency of this shelving as well as some of the techniques described in Chapter 2.

Chapter 9: Ground State Zeeman Qubit in $^{138}Ba^+$ discusses the apparatus and techniques we use to address and characterize the Zeeman qubit in $^{138}Ba^+$.

Chapter 10: Ion-Photon Entanglement at 780 nm combines the techniques and setups described in Chapters 2, 3, 4, 8, and 9 to demonstrate entanglement between our trapped ion quantum node and a photon before and after frequency conversion to 780 nm.

Chapter 11: Using Nondestructive Photon Measurement and Storage to Improve Ion Network Entanglement Rates provides a theoretical demonstration of how the integration of (potentially neutral-atom based) nondestructive measurement and storage techniques into a hybrid trapped ion-based quantum networking architecture can potentially lead to greatly improved ion-ion entanglement rates. This is adapted from [51].

Chapter 12: Outlook provides a brief summary of the results of this thesis and discusses some of the potential next steps (from my point of view) our experiment can take.

Chapter 2: The Barium Ion as a Quantum Networking Node

2.1 Introduction

In this chapter, I discuss how we can use Ba^+ as a quantum networking node. First, I provide some background on how we can confine ions such that they may be manipulated by lasers for coherent operations. Following this, I provide some motivation as to why we use Ba^+ in particular and then discuss some of the key techniques we use to cool, control, and prepare the qubit states of a single $^{138}Ba^+$ ion. Critically, I also show how we can extract single photons entangled with the ion's ground state Zeeman qubit for use in a quantum network.

The techniques discussed in this chapter are used, with some variations, in every experiment presented in this thesis. The experimental setups used to realize these operations are discussed in the next chapter. A large part of my work in the lab involved the development of both state detection of and manipulations on the Zeeman qubit in $^{138}Ba^+$. These techniques are discussed in Chapters 8 and 9, respectively and are critical for the ion-photon entanglement experiment demonstrated in Chapter 10.

To conclude the chapter, I will discuss how we can actually use the ion and its photons in a quantum network. I will show how the photons entangled with the ion can be used to entangle the ion with another quantum node via two-photon interference. This final discussion will be extended to include cases where the ion and the other node in question do not necessarily produce

identical photons, as would be the case in a hybrid quantum network involving Ba^+ and Rb. This discussion is useful for understanding the two-photon interference experiment between photons produced by Ba^+ and Rb in Chapter 7.

2.2 Ion Trapping Basics

Confining a charged particle in space is most easily achieved through the use of electric fields. It was shown by Earnshaw however [96], that static fields in a charge-free region alone cannot be used to confine a charged particle, as the electric potential resulting from such fields has no maxima or minima - only saddle points. Fields oscillating in time, however, can be used to confine a charged particle by essentially rotating these saddle points before the charge can completely escape via the "down-curve" of the saddle potential [97, 98][1].

A common setup to confine ions is known as a linear radio-frequency (RF) Paul trap [28, 99–101]. It consists of at least 4 electrodes, in practice usually rods or thin blades, with a pair of RF electrodes separated diagonally around the trap center and another pair of static and grounded electrodes, also separated diagonally around the trap center. Additional static electrodes are typically used as "end-caps" to provide an electric field along the axis of the trap (typically defined as z-direction) at the center of these two electrode pairs.

The exact electric potential produced by such an ion trap depends on the specific geometry of these electrodes (Our trap geometry will be briefly discussed in the next chapter). One can approximate the electric potential produced by the electrodes near the midpoint of the trap axis as [97],

[1] There are a number of very good videos online demonstrating this using a physical ball and saddle.

$$V(x,y,z,t) = \frac{\kappa V_0}{2}\left(1 + \frac{x^2 - y^2}{r^2}\right)\cos\Omega t + \frac{\rho U_0}{z_0^2}\left(z^2 - \frac{x^2+y^2}{2}\right), \tag{2.1}$$

where V_0 and Ω are the applied RF voltage amplitude and frequency respectively, U_0 is the static potential applied to the end-cap electrodes, r is the minimum distance between the trap axis and the nearest electrode, and z_0 is the axial separation between the trap center and the end-cap electrodes. The terms κ and ρ are geometric factors for the specific trap geometry [65, 97].

The first term of Eqn. 2.1 represents the radial confinement provided by the applied RF field, whereas the second term represents the axial confinement provided by the static end-cap electrodes. The electric field acting on the particle can be found via the gradient of this potential, leading to the equations of motion for the particle. This process is well studied and covered in various texts [28, 97, 99, 101], so I will not cover it here. The first order solutions for the motion of the ion in the trap are given in each direction, $i = x, y, z$, by

$$r_i(t) = A_i \cos\omega_i t\,[1 + \cos\Omega t]\,, \tag{2.2}$$

where A_i depends on the initial conditions of the ion and

$$\omega_i \approx \frac{1}{2}\Omega\sqrt{a_i + \frac{1}{2}q_i^2} \tag{2.3}$$

is known as the secular frequency of the ion trap along the direction i with

$$
\begin{aligned}
a_x &= a_y = -\frac{4e\rho U_0}{mz_0^2\Omega^2}, \\
q_x &= -q_y = \frac{2e\kappa U_0}{mr^2\Omega^2}, \\
a_z &= -2a_x, \\
q_z &= 0.
\end{aligned}
\tag{2.4}
$$

From Eqn. 2.2, we see that although the ion is confined to a small space, it constantly exhibits oscillatory motion at both the applied RF frequency, Ω, as well as at each of the secular frequencies ω_i. These oscillations are known as the (intrinsic[2]) micromotion and the secular motions of the ion respectively.

Averaging over the micromotion frequency components, the secular motion can be treated as an oscillator in a static potential [99]. This allows us to treat the secular motion as a quantum harmonic oscillator, with motional Fock states $|n_i\rangle$ spaced by energy $\hbar\omega_i$. Futhermore, the laser interactions used to manipulate the internal states of the ion can also drive transitions between these motional energy states [67, 100, 102]. This motional coupling between the laser is particularly strong when the laser is detuned from its target transition by $\pm\omega_i$. For narrow enough transitions[3], one can resolve these motional sidebands when performing spectroscopic measurements on the ion. In Chapter 8, we leverage these sidebands to determine the axial-motional temperature of the ion and observe the effects this motion has on our optical shelving efficiency.

[2]It should be noted that when the potentials provided by the RF and the static electrodes are not both at a minimum at the same point, we can instead get residual excess micromotion. This can be corrected for by use of additional, "compensation" electrodes.

[3]Where the linewidth of the transition is significantly less than ω_i.

2.3 $^{138}Ba^{+}$

The energy level structure of $^{138}Ba^{+}$, our ion of choice, is shown in Fig. 2.1. Our lab chooses to work with barium ions for a few key reasons:

- All of the dominate dipole transitions commonly used when working with Ba^{+} can be addressed with visible lasers, allowing us to avoid using the UV lasers commonly needed for other species of ions such as Yb^{+} (369 nm [16]) and Ca^{+} (397 nm [34]).

- Our ion trap has the ability to co-trap Yb^{+}, a commonly used ion in quantum computing [3, 16, 27, 64, 65, 75, 103, 104]. We can potentially co-trap Yb^{+} and Ba^{+}, using the former as a local processor while the latter acts as a quantum networking qubit.

- Although we use $^{138}Ba^{+}$, many of the techniques developed in this thesis apply to $^{133}Ba^{+}$, a potential candidate for use in quantum computers [103], as well as the other isotopes of Ba^{+}.

- Critically, as we will see in Chapter 4, the 493 nm photons we produce with Ba^{+} are at long enough of a wavelength allow us to reach telecommunications wavelengths in two stages of frequency conversion while avoiding some of the main sources of noise produced by the conversion itself. The conversion scheme we use also allows for low-noise conversion to 780 nm for hybrid networking experiments with neutral Rb systems.

In this section, I will discuss how we leverage the strong dipole transitions at 493 nm and 650 nm to cool the ion, optically pump the ion into certain states, and to produce photons at 493 nm that are entangled with the ion's ground state Zeeman qubit (denoted by $|0\rangle$ and $|1\rangle$ in

Fig. 2.1). These operations are critical to all of the work discussed in this thesis. Information on the physical setups used to implement these operations will be discussed in the next chapter. Qubit state detection, leveraging the quadrupole transition at 1762 nm, will be discussed in detail in Chapter 8 and direct radio-frequency operations on the qubit will be discussed in Chapter 9.

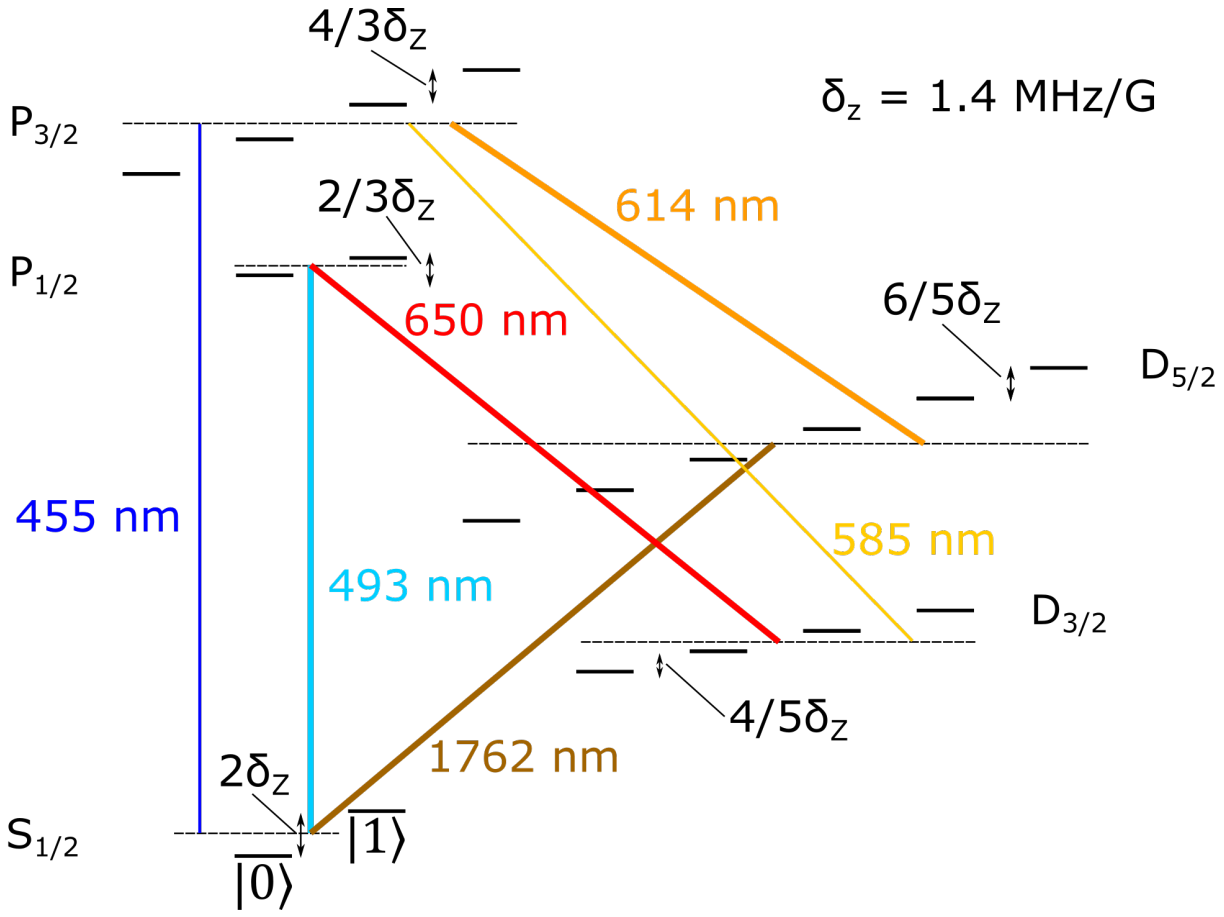

Figure 2.1: **Barium 138 Ion Energy Levels.** Zeeman splittings are included.

2.3.1 Ionization of Neutral Barium

To produce Ba^+, we directly ionize neutral barium in the ion trap. Our lab's source of neutral barium, discussed in Chapter 3, produces a beam of hot neutral atoms which, having no net charge, pass through our ion trap unaffected. If a single atom is ionized while in the trapping

region and does not have enough kinetic energy to escape, it will be confined within the ion trap.

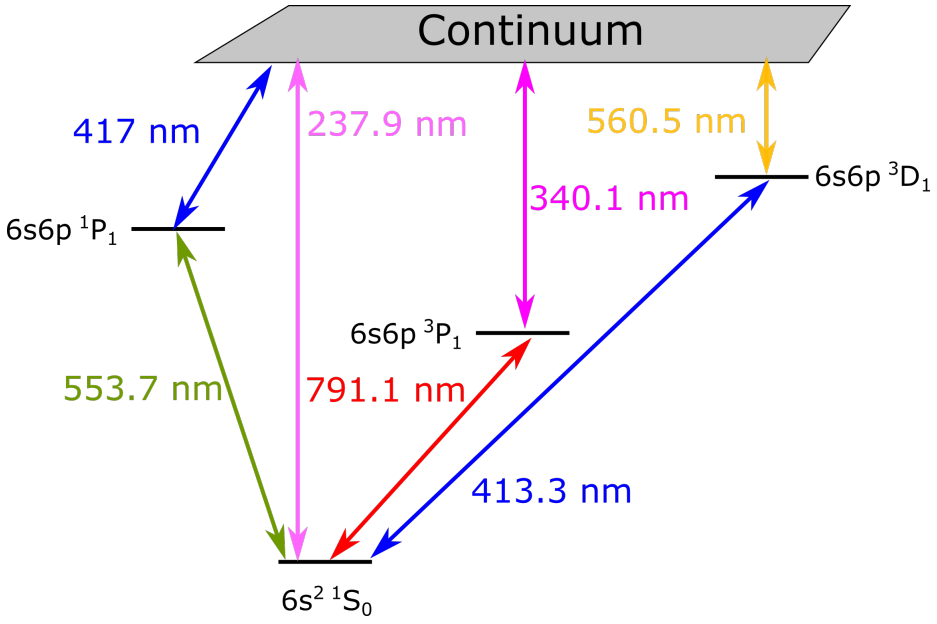

Figure 2.2: **Neutral barium energy levels relevant for common ionization schemes.**

To highlight some of the popular Ba^+ ionization schemes, a partial energy level diagram of neutral barium is shown in Fig. 2.2. Although one can directly ionize the atom with light at or below ≈ 237.9 nm, it is typically preferable to avoid working with expensive UV lasers and hitting one's ion trap with light in the deep ultraviolet [4]. One popular scheme involves driving a transition from $6s^2\ ^1S_0 \rightarrow 6s6p\ ^3D_1$ at 413 nm, at which point any light with a wavelength below ≈ 560 nm will ionize the atom. This second step of ionization is therefore performed with the same laser (or with the 493 nm Doppler cooling light), making this technique rather practical and cost efficient. Another possible scheme is to drive the strong $6s^2\ ^1S_0 \rightarrow 6s6p\ ^1P_1$ transition at 553 nm, followed up with a second step of ionization using light with a wavelength < 417 nm. This scheme has been shown to provide an increase in ionization efficiency of more than two orders of magnitude [105], but requires use of either a dye laser or frequency doubling of

[4] Additionally, this method is not particularly isotope selective.

laser light at ≈ 1107 nm, along with a second laser when compared to the first scheme, making it much less cost efficient and much more difficult to implement than other schemes.

In our lab, we use a scheme based on driving the $6s^2\ ^1S_0 \rightarrow 6s6p\ ^3P_1$ transition. This transition is driven by 791 nm light, at which point any light below ≈ 340 nm[5] can be used to ionize the atom. Although this method requires an extra light source compared to the 413 nm method, this light can be sourced from a cheap LED [106] rather than a laser. Our ionization light sources at 791 nm and ≈ 300 nm are discussed in Chapter 3.

2.3.2 Doppler Cooling

We perform Doppler cooling of the ion via the closed Λ system formed by the 493-nm $S_{1/2} \leftrightarrow P_{1/2}$ and 650-nm $P_{1/2} \leftrightarrow D_{3/2}$ transitions. For this purpose, we illuminate the ion with all polarizations of 650 nm light, and π-polarized 493 nm light. The relatively large branching ratio ($\approx 27\%$) of the $P_{1/2} \leftrightarrow D_{3/2}$ transition requires that care be taken when setting the relative detunings of the 493 nm and 650 nm beams to avoid Raman resonances [107]. Raman resonance is achieved through equal relative detunings of both colors from their respective transitions and leads to so-called "dark states" where ion florescence, and therefore cooling rate, is reduced. Therefore we require that the main 493 nm cooling beam be tuned red of resonance to provide cooling, with the 650 nm beam tuned blue of resonance to avoid these dark states[6].

Previous theoretical investigations into the optimal laser parameters for cooling Ba^+ [107] suggest that the optimal detuning for the 493 nm beam given our applied magnetic field (≈ 5.23 G) is ≈ 15 MHz, or a detuning of about one linewidth [7]. Optimization of our cooling parameters

[5] This is still rather deep in the UV, but not *as UV* as 240 nm and this step does not require a UV *laser*.

[6] It turns out that tuning the 650 nm blue of resonance also serves to maximize ion florescence.

[7] Interestingly, this work also suggests a minimal dependence on the 650 nm frequency (as long as one avoids

via temperature measurements on the $S_{1/2} \leftrightarrow D_{5/2}$ quadrupole transition suggest that this is roughly the case. These measurements are discussed in more detail in Chapter 8.

2.3.3 Ground State Qubit Initialization

We prepare the ion into one of the ground Zeeman states via optical pumping with 493-nm light. With the frequency splitting of these qubit states comparable the transition linewidth, laser frequency-based pumping [108] is not possible. We instead rely on the polarization-based optical pumping scheme shown in Fig. 2.3, where we drive 493-nm $\sigma^-(\sigma^+)$ transitions to prepare the ion into $|0\rangle(|1\rangle)$. To prevent optical pumping into the $D_{3/2}$ manifold, we illuminate the ion with all polarizations of 650 nm during this process.

The efficiency of this optical pumping is limited by the polarization purity of the 493 nm σ-light. For a relatively pure polarization of the 493-nm light, the intensity at the ion should be kept below saturation. At intensities above saturation, the scattering rate of impure polarization components will increase relative to the target, reducing the overall fidelity of the process [63]. In Chapter 8, I present measurements of our typical qubit state preparation efficiency.

2.3.4 Production of Photons Entangled with $^{138}Ba^+$

2.3.4.1 Photon Production Procedure

We produce single photons from $^{138}Ba^+$ through the process shown in Fig. 2.4. We optically pump the ion into the $m_J = 3/2$ edge state of the $D_{3/2}$ manifold using simultaneous pulses of π-polarized 493-nm light and π- and σ^+-polarized 650-nm light, as shown in Fig. 2.4 a. The

dark resonances), which is consistent with our own observations.

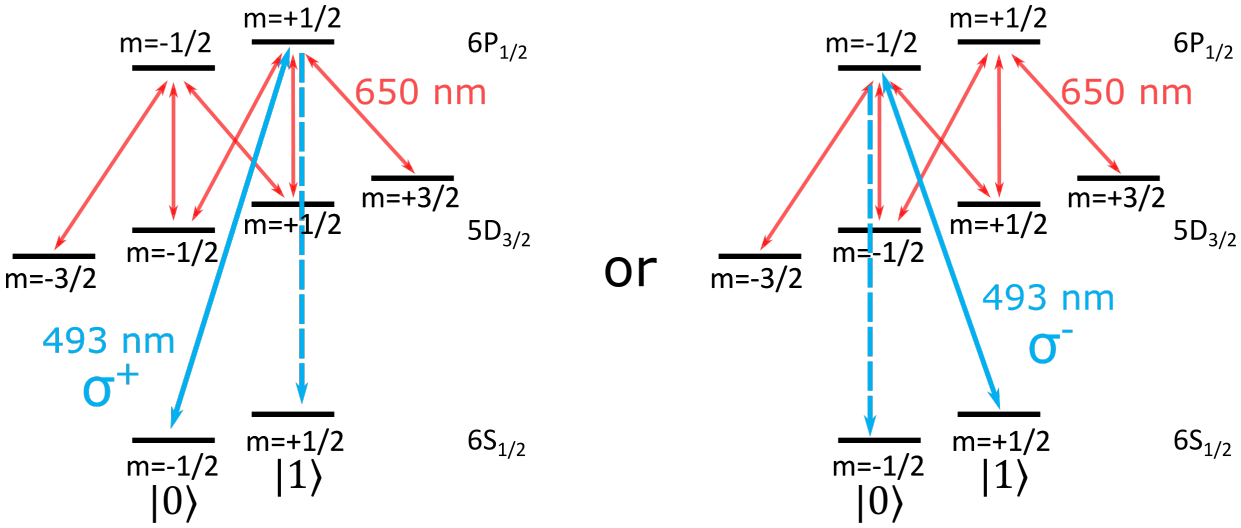

Figure 2.3: **S-State Optical Pumping.** Circularly-polarized $\sigma^+(\sigma^-)$ light is used to prepare the ion into the $m = +1/2(m = -1/2)$ state of the $S_{1/2}$ manifold. All polarizations of 650-nm light are used.

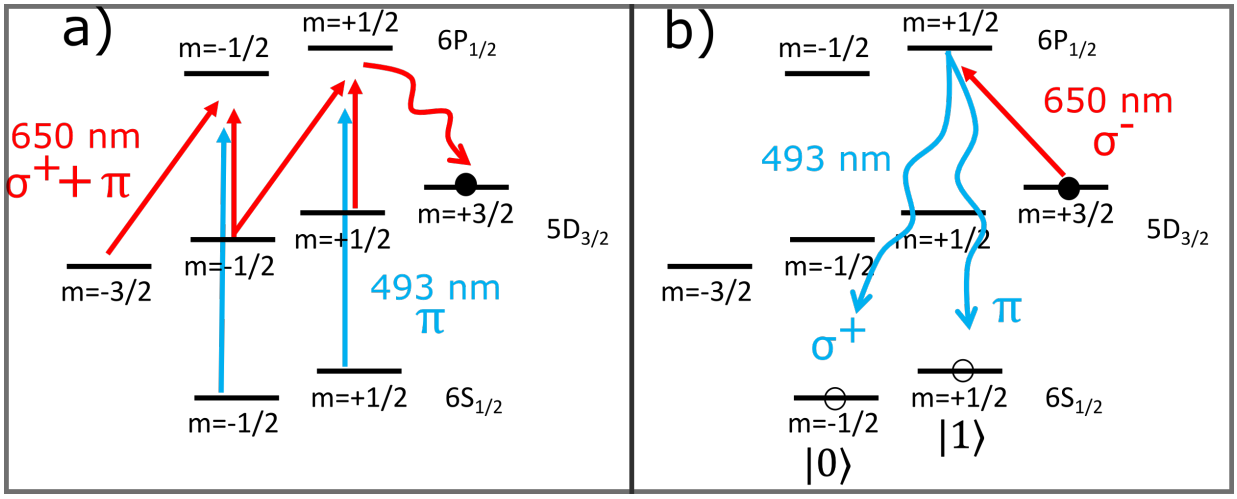

Figure 2.4: **Photon Production Scheme.** a) State preparation into the $m = +3/2$ stretch state of the $D_{3/2}$ manifold. b) Photon extraction via a 650-nm σ^- excitation pulse.

ion is then excited with a short pulse of σ^--polarized 650-nm light to excite it to the $m_J = 1/2$ state of the $P_{1/2}$ manifold, from which a 493-nm photon can spontaneously emit from the ion (Fig. 2.4 b).

With this scheme, only one 493-nm photon can be emitted, no matter the length or intensity of the final 650-nm pulse. Additionally the probability of the ion emitting a 493-nm photon can be made to be $> 94\%$ with a long enough pulse [28]. Finally, the 650-nm excitation pulse is easily separable from the 493-nm photon signal via optical filtering. This is in contrast to so-called "weak" excitation schemes [68, 109], where in the case of Ba^+, a low intensity 493-nm pulse is used to excite the ion on the $S_{1/2} \leftrightarrow P_{1/2}$ transition. In this method increasing the single photon production probability (by increasing the pulse intensity) risks re-excitation and production of a second photon at 493 nm, destroying any entanglement between the ion and the photon. Furthermore, laser scatter at 493 nm cannot be separated from the photon signal via optical filtering, reducing signal-to-noise ratios. It is possible to avoid these issues via "strong" excitation with a pulsed laser, but this would require pulse lengths on the 10s of picoseconds up to a nanosecond, at a color where high power pulses at these pulse lengths are not easily available [65].

2.3.4.2 Ion-Photon Entanglement

As shown in Fig. 2.4, the final qubit state of the ion after emission of a 493-nm photon is tied to the polarization of that photon. This emission is not equally probable for each polarization, with the emission probabilities being governed by the Clebsh-Gordan coefficients shown in Fig. 2.5 a. Thus, photon emission results in the ion-photon entangled state given by

$$|\Psi_{IP}\rangle = \sqrt{\frac{2}{3}}\,|0\rangle\,|\sigma^{+}\rangle + \sqrt{\frac{1}{3}}\,|1\rangle\,|\pi\rangle\,. \tag{2.5}$$

This state, although entangled, is not a maximally entangled Bell state [110]. If photons are collected perpendicular to the quantization axis, however, the imbalance between each polarization is perfectly canceled out by the different spatial intensity patterns of the π- and σ-polarized light [28, 31]. Along this collection axis, these polarizations also project to be orthogonal, and we arrive at a maximally entangled Bell state,

$$|\Psi_{IP}\rangle = \sqrt{\frac{1}{2}}\,|0\rangle\,|V\rangle + \sqrt{\frac{1}{2}}\,|1\rangle\,|H\rangle\,, \tag{2.6}$$

where $|H\rangle$ and $|V\rangle$ represent horizontally and vertically polarized photons in the laboratory frame. Therefore, we collect our photons perpendicular to the quantization axis. Our photon collection setups are discussed in Chapter 3.

2.3.4.3 Infidelity from Multiple Excitations

The excitation of the ion to the $P_{1/2}$ manifold shown in Fig. 2.4 b, can instead result in the emission of a photon at 650 nm with the ion decaying back to the $D_{3/2}$ manifold. This occurs with a relatively high probability given by the branching ratio of $\approx 27\%$ from the $P_{1/2}$ manifold back to the $D_{3/2}$ manifold, as shown in Fig. 2.5 b. Should this occur while the 650 nm σ^{-} excitation light is still incident on the ion, the ion may be re-excited back to the $P_{1/2}$ manifold, from which it may again spontaneously decay and emit a 493-nm or 650-nm photon. In fact, this process can occur multiple times throughout the duration of the 650-nm pulse, albeit with a decreasing probability for higher and higher order re-excitations.

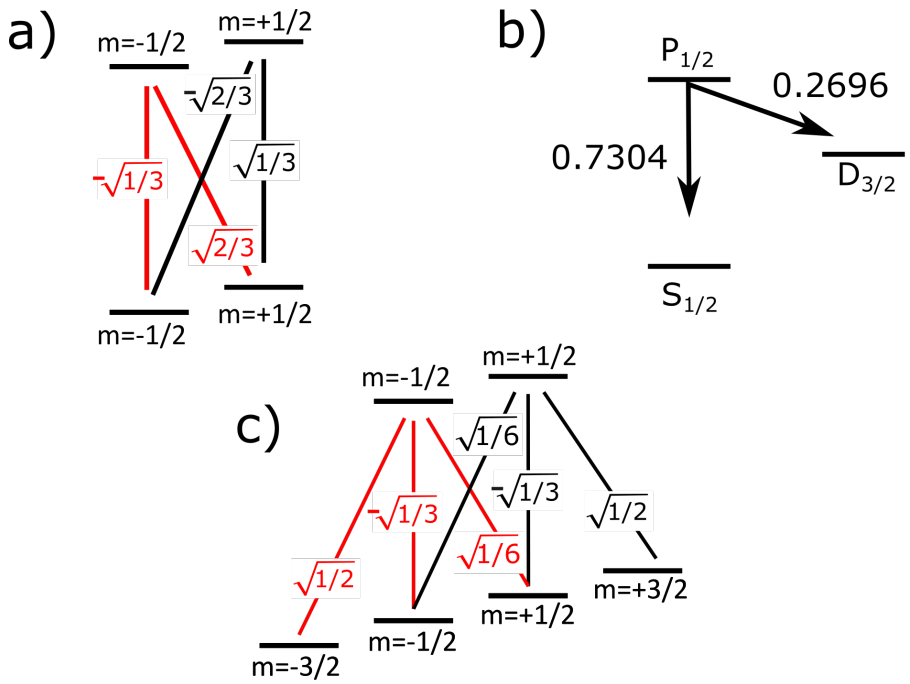

Figure 2.5: **Barium Ion Clebsch-Gordon Coefficients and Branching Ratios.** a) Clebsch-Gordan coefficients for decay at 493 nm from the $6P_{1/2}$ manifold to the $6S_{1/2}$ ground state manifold. b) Branching ratios for decay from the $6P_{1/2}$ manifold. c) Clebsch-Gordan coefficients for decay at 650 nm from the $6P_{1/2}$ manifold to $5D_{3/2}$.

To some extent, these re-excitations are advantageous, as they provide repeated opportunities to produce a 493-nm photon given a 650-nm photon emission event. Consider, however, spontaneous emission to the $m = +1/2$ state of the $D_{3/2}$ manifold. This occurs $1/3$ of the time a 650-nm photon is emitted from the $m = +1/2$ state in the $P_{1/2}$ manifold (Fig. 2.5 c). From this state, the σ^- excitation beam then re-excites the ion to the $m = -1/2$ state in the $P_{1/2}$ manifold. Spontaneous emission of a 493-nm photon at this point results in an ion-photon entangled state,

$$|\Phi_{IP}\rangle = \sqrt{\frac{1}{2}}\,|0\rangle\,|H\rangle + \sqrt{\frac{1}{2}}\,|1\rangle\,|V\rangle\,. \tag{2.7}$$

With the opposite entanglement between the photon polarization and ion qubit states, this state has zero fidelity when compared to Eqn. 2.6.

In principle, this source of infidelity can be almost completely avoided by use of a pulsed laser at 650 nm, such that the ion is no longer illuminated before photon emission becomes probable. Such a laser is typically expensive, and the pulse lengths and energies required are not easily available from a commercial source[8]. Thankfully, the possible decay paths and branching ratios shown in Fig. 2.5 limit the total infidelity from these multiple excitations to only $\approx 9\%$ even when using the worst case scenario of an infinitely long 650 nm σ^- pulse. Our colleagues in the group of Chris Monroe have also shown [64] that an acousto-optic modulator (AOM) generated π-pulse with a temporal length on the order of the excited state lifetime ($\approx$ 10 ns) leads to less than 0.4% infidelity.

Another option to avoid the majority of the infidelity caused by these multiple excitations is through filtering out photons in time. As can be verified through use of the optical Bloch

[8] Via discussions James Siverns and myself have had with multiple laser companies.

equations for Ba^+ [65,104], the incorrectly-polarized photons leading to the ion-photon entangled state given by Eqn. 2.7 are much more likely to be emitted towards the end of the detected photon arrival profile. The beginning of this photon arrival profile, in contrast, consists almost entirely of photons corresponding to the correct ion-photon entangled state. Thus by only accepting photons in a temporal window towards the beginning of the photon arrival profile, infidelities from multiple excitations can be reduced, albeit at the expense of (usable) photon production rate. The length of this window depends on the particular parameters of the 650-nm excitation pulse, such as pulse power and shape. This method is not as robust as simply shortening the excitation pulse, but is useful when the pulse length cannot be easily shortened due to experimental constraints (such as AOM rise-time or laser power). Given our typical excitation pulse length on the order of 200 ns, this is the method we use for the ion-photon entanglement measurements discussed in Chapter 10.

2.4 Entanglement Swapping via Two Photon Interference

Entanglement between an ion (or other matter-based qubit) and a photon, such as the scheme discussed in Sec. 2.3.4, allows for the quantum information of the ion to be distributed to a remote location. To entangle two distant ions, each entangled with their own photon, a commonly used protocol [16,30] is through interference of the two photons on a beamsplitter via the Hong-Ou-Mandel effect [111,112]. This technique *heralds* ion-ion entanglement, given the detection of both photons after this interference. Though this makes this protocol by definition probabilistic, it critically makes the generated ion-ion entangled state much more robust[9] to infidelities based on photon loss when compared to single-photon entanglement schemes [113]. This and similar

[9] If our detectors didn't have noise, this method would be completely immune to photon loss.

protocols are typically referred to as *entanglement swapping*, as the entanglement between each matter qubit and its photon is swapped to entanglement between each ion, through a projective measurement on the photon states.

In this section I will discuss the basics of the Hong-Ou-Mandel effect, followed by a discussion of a typical entanglement swapping setup and entanglement rates. Finally, as a primer to the work demonstrated in Chapter 7, I will show how both of these are effected in the case where the input photons are not identical. I will use notation similar to our work in [50], from which some of this discussion is adapted.

2.4.1 Two Photon Interference: The Hong-Ou-Mandel Effect

Consider a 50:50 beamsplitter. We denote photons incident on the beamsplitter by the raising operators $\hat{a}^\dagger$ and $\hat{b}^\dagger$, with each operator corresponding to one of the two beamsplitter input ports. The action of the beamsplitter on the input photons can be described by the unitary relation

$$\begin{pmatrix} \hat{a}^\dagger \\ \\ \hat{b}^\dagger \end{pmatrix} \rightarrow \frac{1}{\sqrt{2}} \begin{pmatrix} 1 & i \\ \\ i & 1 \end{pmatrix} \begin{pmatrix} \hat{x}^\dagger \\ \\ \hat{y}^\dagger \end{pmatrix}, \tag{2.8}$$

where $\hat{x}^\dagger$ and $\hat{y}^\dagger$ represent the raising operators for photons at each of the exit ports. This equation is purposefully inverted to give the inputs in terms of the outputs as this is useful for the following discussion.

From here on we will denote photon states as fock states with $|n_a, n_b\rangle_{in}$ representing the photon numbers at each of the input ports. We denote $|x_a x_b, y_a y_b\rangle_{out}$ to represent the photon number states at each of the outputs x and y, keeping track of which photon port each output photon originated from, as this will be useful later when considering cases where the input

photons are not identical. We use a similar notation for the output operators, i.e. $\hat{a}^\dagger \rightarrow \frac{1}{\sqrt{2}}\left(\hat{x}_a^\dagger + i\hat{y}_a^\dagger\right)$. We see, for example, that with only a single photon incident at port a, we have the expected operation of the beamsplitter,

$$|1_a, 0_b\rangle_{in} = \hat{a}^\dagger |0_a, 0_b\rangle_{in} \rightarrow \frac{1}{\sqrt{2}}\left(\hat{x_a}^\dagger + i\hat{y_a}^\dagger\right)|0,0\rangle_{out} = \frac{1}{\sqrt{2}}\left(|1_a, 0\rangle_{out} + i\,|0, 1_a\rangle_{out}\right), \quad (2.9)$$

where we have an equal probability of detecting the photon at each of the output ports, with a relative phase shift between transmission and reflection.

If we instead have two photons, one incident on each port of the beamsplitter, one finds

$$\begin{aligned} |1_a, 1_b\rangle_{in} = \hat{a}^\dagger\hat{b}^\dagger |0_a, 0_b\rangle_{in} &\rightarrow \frac{1}{2}\left(\hat{x_a}^\dagger + i\hat{y_a}^\dagger\right)\left(i\hat{x_b}^\dagger + \hat{y_b}^\dagger\right)|0,0\rangle_{out} \\ &\rightarrow \frac{1}{2}\left(i\hat{x_a}^\dagger\hat{x_b}^\dagger + \hat{x_a}^\dagger\hat{y_b}^\dagger - \hat{x_b}^\dagger\hat{y_a}^\dagger + i\hat{y_a}^\dagger\hat{y_b}^\dagger\right)|0,0\rangle_{out}. \end{aligned} \quad (2.10)$$

If the photons are completely distinguishable, this results in an equal chance for each photon to independently exit each port of the beamsplitter, with both photons exiting the same port of the beamsplitter 50% of the time. If the photons are *indistinguishable* however, we can write $\hat{x_a}^\dagger = \hat{x_b}^\dagger = \hat{x}^\dagger$ and $\hat{y_a}^\dagger = \hat{y_b}^\dagger = \hat{y}^\dagger$ and Eqn. 2.10 becomes

$$|1_a, 1_b\rangle_{in} = \hat{a}^\dagger\hat{b}^\dagger |0_a, 0_b\rangle_{in} \rightarrow \left(\hat{x}^\dagger + i\hat{y}^\dagger\right)\left(i\hat{x}^\dagger + \hat{y}^\dagger\right)|0,0\rangle_{out} = \frac{i}{\sqrt{2}}\left(|2,0\rangle_{out} + |0,2\rangle_{out}\right) \quad (2.11)$$

where both photons exit the *same* port of the beamsplitter, with a 50% chance of exiting either

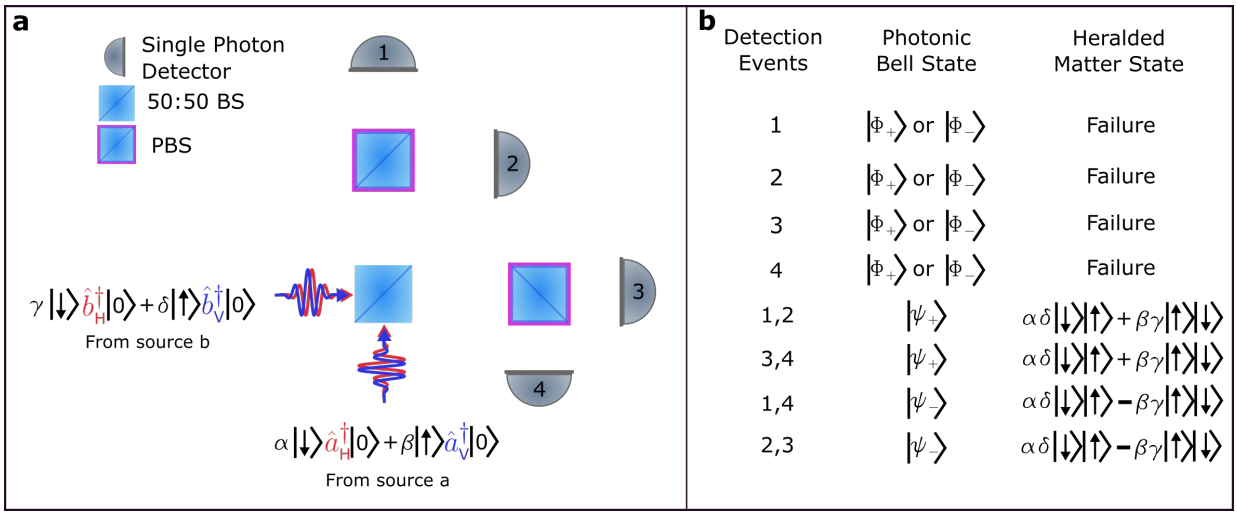

Figure 2.6: **Setup to herald entanglement between distance matter qubits.** **a**, incoming photons have their polarizations entangled with their corresponding matter qubit's internal states. A 50:50 beamsplitter (BS) is used to interfere the two photons, allowing for the heralding of entanglement between the matter qubits after detection using polarizing beamsplitters (PBSs) and single-photon detectors. **b**, different combinations of detector clicks correspond to the detection of certain photonic bell states. Depending on which set of detectors click (labeled in **a**), different entangled states between the matter qubits can be heralded. In the case of any individual detector clicking, the Φ_+ and Φ_- photonic bell states cannot be distinguished from one another, resulting in a failed attempt to entangle the matter qubits. All other combinations of detector clicks not shown should not be possible in the case of perfect two-photon interference, and are ignored in the case of imperfect interference.

port together. This is the Hong-Ou-Mandel effect: The interference of the identical photon wavefunctions on a 50:50 beamsplitter results in both photons always exiting the same port of the beamsplitter. In the following section we will extend this effect to the case where the photons are entangled with their matter qubit source.

2.4.2 Entanglement Swapping

Consider the common entanglement generation scheme shown in Fig. 2.6 and described in [114]. The setup consists of a 50:50 beamsplitter (BS), followed by two polarizing beamsplitters (PBS) and four single-photon detectors. This is known as a Bell State Analyzer (BSA) [110].

For the purposes of general analysis, we will assume that each matter qubit produces single photons with the polarization degree of freedom of each photon entangled with the internal qubit states of its source system. For clarity, we also switch from our Fock-state representation to a polarization-vector state representation for the photons states (with $|0\rangle$ still representing the absence of a photon). Additionally, we will assume the detectors used have negligible dark count rates. With the photons from each source arriving at the beamsplitter simultaneously, we write the total state of the system as:

$$\begin{aligned} |\Psi_1\rangle_{\text{in}} &= (\alpha\,|\downarrow\rangle\,|H\rangle_{\text{in}} + \beta\,|\uparrow\rangle\,|V\rangle_{\text{in}}) \otimes (\gamma\,|\downarrow\rangle\,|H\rangle_{\text{in}} + \delta\,|\uparrow\rangle\,|V\rangle_{\text{in}}) \\ &= \alpha\gamma\,|\downarrow\downarrow\rangle\,|H,H\rangle_{\text{in}} + \beta\delta\,|\uparrow\uparrow\rangle\,|V,V\rangle_{\text{in}} + \alpha\delta\,|\downarrow\uparrow\rangle\,|H,V\rangle_{\text{in}} + \beta\gamma\,|\uparrow\downarrow\rangle\,|V,H\rangle_{\text{in}}\,, \end{aligned} \tag{2.12}$$

where we have made the assumption that horizontal (vertical) photon states, denoted by $|H\rangle$ ($|V\rangle$), are entangled with the $|\downarrow\rangle(|\uparrow\rangle)$ internal states of their corresponding atomic systems. Here α, β, γ and δ are the quantum mechanical probability amplitudes of their respective states. It is informative to rewrite $|\Psi_1\rangle_{\text{in}}$ in the photonic Bell basis [115]:

$$\begin{aligned} |\Psi_1\rangle_{\text{in}} &= \alpha\gamma\,|\downarrow\downarrow\rangle\,(|\Phi_+\rangle_{\text{in}} + |\Phi_-\rangle_{\text{in}}) + \beta\delta\,|\uparrow\uparrow\rangle\,(|\Phi_+\rangle_{\text{in}} - |\Phi_-\rangle_{\text{in}}) \\ &\quad + \alpha\delta\,|\uparrow\downarrow\rangle\,(|\psi_+\rangle_{\text{in}} + |\psi_-\rangle_{\text{in}}) + \beta\gamma\,|\downarrow\uparrow\rangle\,(|\psi_+\rangle_{\text{in}} - |\psi_-\rangle_{\text{in}}) \\ &= (\alpha\gamma\,|\downarrow\downarrow\rangle + \beta\delta\,|\uparrow\uparrow\rangle)\,|\Phi_+\rangle_{\text{in}} + (\alpha\gamma\,|\downarrow\downarrow\rangle - \beta\delta\,|\uparrow\uparrow\rangle)\,|\Phi_-\rangle_{\text{in}} \\ &\quad + (\alpha\delta\,|\downarrow\uparrow\rangle + \beta\gamma\,|\uparrow\downarrow\rangle)\,|\psi_+\rangle_{\text{in}} + (\alpha\delta\,|\downarrow\uparrow\rangle - \beta\gamma\,|\uparrow\downarrow\rangle)\,|\psi_-\rangle_{\text{in}}\,, \end{aligned} \tag{2.13}$$

where

$$|\Phi_{\pm}\rangle = \frac{1}{\sqrt{2}}(|H,H\rangle \pm |V,V\rangle)$$
$$|\psi_{\pm}\rangle = \frac{1}{\sqrt{2}}(|H,V\rangle \pm |V,H\rangle). \tag{2.14}$$

In the following, we use similar notation to Sec. 2.4.1 for the definitions of $\hat{a}^{\dagger}$,$\hat{b}^{\dagger}$,$\hat{x}^{\dagger}$,$\hat{y}^{\dagger}$, with additional subscripts of H and V denoting horizontally and vertically polarized photons, respectively. Computing the action of the beamsplitter on the $|\Phi_{\pm}\rangle$ photonic Bell states, and assuming that photons of the same polarization are identical, one can show [115]:

$$\begin{aligned}
|\Phi_{\pm}\rangle_{\text{in}} &= \frac{1}{\sqrt{2}}(|H,H\rangle_{\text{in}} \pm |V,V\rangle_{\text{in}}) = \frac{1}{\sqrt{2}}(\hat{a}_H^{\dagger}\hat{b}_H^{\dagger} \pm \hat{a}_V^{\dagger}\hat{b}_V^{\dagger})\,|0,0\rangle_{\text{in}} \\
&\rightarrow \frac{1}{2\sqrt{2}}[(\hat{x}_H^{\dagger} + i\hat{y}_H^{\dagger})(i\hat{x}_H^{\dagger} + \hat{y}_H^{\dagger}) \pm (\hat{x}_V^{\dagger} + i\hat{y}_V^{\dagger})(i\hat{x}_V^{\dagger} + \hat{y}_V^{\dagger})]\,|0,0\rangle_{\text{out}} \\
&\rightarrow \frac{i}{2}\left[|HH,0\rangle_{\text{out}} + |0,HH\rangle_{\text{out}} \pm (|VV,0\rangle_{\text{out}} + |0,VV\rangle_{\text{out}})\right],
\end{aligned} \tag{2.15}$$

where notation such as $|ij,0\rangle$ corresponds two photons with polarization i and j exiting the same port of the 50:50 beamsplitter. In a similar fashion:

$$|\psi_{+}\rangle_{\text{in}} \rightarrow \frac{i}{\sqrt{2}}(|HV,0\rangle_{\text{out}} + |0,HV\rangle_{\text{out}}), \tag{2.16}$$

$$|\psi_{-}\rangle_{\text{in}} \rightarrow \frac{1}{\sqrt{2}}(|H,V\rangle_{\text{out}} - |V,H\rangle_{\text{out}}). \tag{2.17}$$

From equation (2.15) we see that the action of the beamsplitter on the $|\Phi_{+}\rangle_{\text{in}}$ and $|\Phi_{-}\rangle_{\text{in}}$ photonic Bell states results in photons with the same polarization exiting out of the same ports of the 50:50 BS. Therefore, measurement using the setup shown in Fig. 2.6 cannot distinguish

$|\Phi_+\rangle_{\text{in}}$ from $|\Phi_-\rangle_{\text{in}}$. The $|\psi_+\rangle_{\text{in}}$ input state results in two oppositely polarized photons exiting the same port of the 50:50 BS, and the $|\psi_-\rangle_{\text{in}}$ input state results in two oppositely polarized photons exiting opposite ports of the 50:50 BS.

The measurement shown in Fig. 2.6 can distinguish between $|\psi_+\rangle_{\text{in}}$ and $|\psi_-\rangle_{\text{in}}$. This partial measurement of the photonic Bell state of the photons can therefore be used to herald an entangled state between the matter qubits, determined by examination of Eqn. 2.13. The possible photon measurement outcomes using this scheme are summarized in Fig. 2.6 b, as well as the heralded entangled state between the matter qubits. Critically, in cases where one of the photons is lost, resulting in only a single detector click, this scheme is designed to give a null result, making it robust to photon loss. Finally, for $\alpha = \beta = \delta = \gamma = 1/\sqrt{2}$, such as would be the case for two Ba^+ ions producing photons as in Sec. 2.3.4, a maximally entangled matter-qubit Bell state is heralded.

2.4.3 Remote Entanglement Generation Rate

For the entanglement swapping scheme discussed in Sec. 2.4.2, a successful entanglement herald requires two simultaneous detection events. If a photon from either source is lost at any point in the network, entanglement must be reattempted with new photons. The remote entanglement generation rate is given by

$$R_{ent} = \frac{1}{2} p_a p_b R_{rep} \tag{2.18}$$

where $p_a(p_b)$ is the probability a photon produced by source a(b) is detected at the Bell state analyzer of Sec. 2.4.2 and R_{rep} is the repetition rate that photons can be requested from both

sources such that the photons arrive at the beamsplitter simultaneously. The factor of 1/2 comes from the fact that we can only measure two out of the four possible photonic Bell states with this setup. For identical sources, we see that the entanglement rate depends the square of the collection and transmission probabilities of the photons, making photon loss have a large impact on entanglement rates. In Chapter 11, we will explore potential network architectures that leverage nondestructive single photon measurement and storage to deal with this problem of loss and improve this entanglement rates.

2.4.4 Dealing with Degrees of Distinguishability

In real world quantum networks, there is always some amount of distinguishability between photons produced by different sources. Distinguishability between the input photons can refer to properties such as photon polarization, frequency, or spatial-temporal mode and can depend on the basis of measurement [50, 116]. Furthermore, this distinguishability is not binary - one can characterize the degree to which two photons are identical via two-photon correlation measurements, as is discussed in Chapter 7.

As in [50, 94], one can characterize the mode overlap of the photons by a real number c, with $0 \leq c \leq 1$. We can then redefine our output raising and lowering operators as

$$
\begin{aligned}
\hat{x_a}^\dagger &\rightarrow \hat{x}^\dagger \\
\hat{y_a}^\dagger &\rightarrow \hat{y}^\dagger \\
\hat{x_b}^\dagger &\rightarrow \sqrt{c}\,\hat{x}^\dagger + \sqrt{1-c}\,\hat{x}_n^\dagger \\
\hat{y_b}^\dagger &\rightarrow \sqrt{c}\,\hat{y}^\dagger + \sqrt{1-c}\,\hat{y}_n^\dagger,
\end{aligned}
\tag{2.19}
$$

where $\hat{x}_n^\dagger$ and $\hat{y}_n^\dagger$ encompass all photon modes orthogonal to $\hat{x}^\dagger$ and $\hat{y}^\dagger$[10]. Using this notation, Eqn. 2.10 becomes

$$
\begin{aligned}
|1_\mathrm{a}, 1_\mathrm{b}\rangle \rightarrow |\psi_{out}\rangle = \frac{i}{2}\Big(&\sqrt{2c}\,|2,0\rangle_{out} + \sqrt{1-c}\,|1\ 1_n, 0\rangle_{out} + \sqrt{2c}\,|0,2\rangle_{out} + \sqrt{1-c}\,|0,1\ 1_n\rangle_{out}\Big) \\
&+ \frac{\sqrt{1-c}}{2}\left(|1,1_n\rangle_{out} - |1_n,1\rangle_{out}\right),
\end{aligned}
\tag{2.20}
$$

where we see that setting $c = 1$ recovers Eqn. 2.11. Whereas with identical photons, we are guaranteed to observe both photons exiting the same port of the beamsplitter, in general this is observed with a probability given by

$$
P_{same} = |\langle 2,0|\psi_{\text{out}}\rangle|^2 + |\langle 0,2|\psi_{\text{out}}\rangle|^2 + |\langle 1\ 1_n, 0|\psi_{\text{out}}\rangle|^2 + |\langle 0,1\ 1_n|\psi_{\text{out}}\rangle|^2 = \frac{2(c+1)}{4}. \tag{2.21}
$$

This equation gives the correct results for distinguishable ($c = 0$) and indistinguishable ($c = 1$) photons as discussed above. Similarly, the probability of the photons exiting separate ports is

[10]Mathematically, $\langle 0|\,\hat{x}^\dagger\hat{x}_n^\dagger\,|0\rangle$=0

given by

$$P_{separate} = 1 - P_{same} = \frac{1-c}{2}. \tag{2.22}$$

Thus, by measuring the probability the two photons exit separate ports, one can directly determine c, the degree of indistinguishably between the input photons. We use this fact to demonstrate indistinguishability between frequency converted photons from our ion and photons produced by an ensemble of Rb atoms in Chapter 7.

Now lets further extend our discussion to see how this overlap parameter c impacts the fidelity of the final matter qubit entangled state when performing the entanglement swapping discussed in Sec. 2.4.2. We can rewrite the input state, Eqn. 2.12 as:

$$\begin{aligned} |\Psi\rangle_{\text{in}} &= \left[\alpha\,|{\downarrow}\rangle\,(\sqrt{c}\,|H\rangle_{\text{in}} + \sqrt{1-c}\,|H_n\rangle_{\text{in}}) + \beta\,|{\uparrow}\rangle\,(\sqrt{c}\,|V\rangle_{\text{in}} + \sqrt{1-c}\,|V_n\rangle_{\text{in}}\right] \otimes \left[\gamma\,|{\downarrow}\rangle\,|H\rangle_{\text{in}} + \delta\,|{\uparrow}\rangle\,|V\rangle_{\text{in}}\right] \\ &= \sqrt{c}\,|\Psi_1\rangle_{\text{in}} + \sqrt{1-c}\,|\Psi_2\rangle_{\text{in}}\,, \end{aligned} \tag{2.23}$$

where $|H_n\rangle$ and $|V_n\rangle$ represent polarized photons that are nonidentical to $|H\rangle$ and $|V\rangle$ in their spectral, spatial, or temporal profiles and $|\Psi_2\rangle_{\text{in}} = \alpha\gamma\,|{\downarrow\downarrow}\rangle\,|H_n, H\rangle_{\text{in}} + \beta\delta\,|{\uparrow\uparrow}\rangle\,|V_n, V\rangle_{\text{in}} + \alpha\delta\,|{\downarrow\uparrow}\rangle\,|H_n, V\rangle_{\text{in}} + \beta\gamma\,|{\uparrow\downarrow}\rangle\,|V_n, H\rangle_{\text{in}}$. The action of the beamsplitter on the first term has already been examined in Sec. 2.4.2. The action of the beamsplitter on the second term can be shown to give:

$$
\begin{aligned}
|\Psi_2\rangle_{\text{in}} \rightarrow \alpha\gamma\,|{\downarrow\downarrow}\rangle\,(i\,|HH_n,0\rangle_{\text{out}} + i\,|0,HH_n\rangle_{\text{out}} - |H,H_n\rangle_{\text{out}} + |H_n,H\rangle_{\text{out}}) \\
+ \beta\delta\,|{\uparrow\uparrow}\rangle\,(i\,|VV_n,00\rangle_{\text{out}} + i\,|0,VV_n\rangle_{\text{out}} - |V,V_n\rangle_{\text{out}} + |V_n,V\rangle_{\text{out}}) \\
+ \beta\gamma\,|{\uparrow\downarrow}\rangle\,(i\,|HV_n,0\rangle_{\text{out}} + i\,|0,HV_n\rangle_{\text{out}} + |V_n,H\rangle_{\text{out}} - |H,V_n\rangle_{\text{out}}) \\
+ \alpha\delta\,|{\downarrow\uparrow}\rangle\,(i\,|H_nV,0\rangle_{\text{out}} + i\,|0,H_nV\rangle_{\text{out}} - |V,H_n\rangle_{\text{out}} + |H_n,V\rangle_{\text{out}}).
\end{aligned}
\tag{2.24}
$$

Now we can investigate how the total output state is affected by the measurement of a coincidence between the detectors shown in Fig. 2.6. As an example, we use the measurement of the $|\psi_-\rangle_{\text{in}}$ photonic Bell state, which corresponds to the measurement of a horizontal and vertical photon out of opposite ports of the 50:50 beamsplitter. In this case of perfect interference this will herald the $|\psi_-\rangle_m = (|{\uparrow\downarrow}\rangle - |{\downarrow\uparrow}\rangle)/\sqrt{2}$ matter Bell state. This is represented by the measurement operator:

$$
\begin{aligned}
M_{\mathcal{C}} = &|H,V\rangle\langle H,V| + |V,H\rangle\langle V,H| + |H_n,V\rangle\langle H_n,V| + |V,H_n\rangle\langle V,H_n| \\
&+ |V_n,H\rangle\langle V_n,H| + |H,V_n\rangle\langle H,V_n| + |H_n,V_n\rangle\langle H_n,V_n| + |V_n,H_n\rangle\langle V_n,H_n|\,.
\end{aligned}
\tag{2.25}
$$

In the case of perfect interference, any terms containing H_n or V_n are unnecessary. We calculate the density matrix describing the state of the two matter qubits after such a measurement:

$$\rho_m = Tr_{\text{photons}}[M_C \left|\Psi\right\rangle_{\text{out}} \left\langle\Psi\right|_{\text{out}}]$$
$$= N \left(c \begin{bmatrix} 0 & 0 & 0 & 0 \\ 0 & |\alpha|^2|\delta|^2 & -\alpha\beta^*\gamma^*\delta & 0 \\ 0 & \alpha^*\beta\gamma\delta^* & |\beta|^2|\gamma|^2 & 0 \\ 0 & 0 & 0 & 0 \end{bmatrix} + (1-c) \begin{bmatrix} 0 & 0 & 0 & 0 \\ 0 & |\alpha|^2|\delta|^2 & 0 & 0 \\ 0 & 0 & |\beta|^2|\gamma|^2 & 0 \\ 0 & 0 & 0 & 0 \end{bmatrix} \right), \tag{2.26}$$

where N is a normalization factor given by:

$$N = \frac{1}{|\alpha|^2|\delta|^2 + |\beta|^2|\gamma|^2}, \tag{2.27}$$

and where $\left|\Psi\right\rangle_{\text{out}}$ represents the state $\left|\Psi\right\rangle_{\text{in}}$ after exiting the beamsplitter. If we set $\alpha = \delta = \beta = \gamma = 1/\sqrt{2}$ in $\left|\Psi\right\rangle_{\text{in}}$, our measurement will herald the matter state $\left|\psi_-\right\rangle_m$ with a fidelity:

$$F = \left\langle\psi_-\right|_m \rho_m \left|\psi_-\right\rangle_m = \frac{1+c}{2}. \tag{2.28}$$

A similar analysis gives the same result for the heralding of the $\left|\psi_+\right\rangle_m$ Bell state[11].

From this analysis, we see that if there is some degree of distinguishability between the input photons, i.e. if $c < 1$, this will result in a loss of fidelity for the heralded remote entanglement between the distant matter qubits. In Chapter 7, we measure interference between photons emitted by a trapped Ba^+ ion (via. the method described in Sec. 2.3.4) and photons produced by an ensemble of Rb atoms. Coming from two heterogeneous quantum sources, there is some

[11] Additionally, this analysis is valid for other types of qubits, such as time-binned or frequency qubits, as long as the PBSs used here are replaced with the relevant measurements for the other types of qubits (for instance dichroic mirrors could be used for frequency qubits).

distinguishability between these photons. For these sources[12], the parameter c is equivalent to the visibility of this interference, such that we can directly predict what the fidelity of entanglement between these matter qubits should we attempt to entangle them in the future.

[12] Pure single-photon sources.

Chapter 3: General Laboratory Setup

3.1 Introduction

A trapped ion quantum node requires a relatively complex setup of vacuum components, multiple lasers and optics, as well as synchronized timing and frequency control electronics. In this chapter, I will describe our experimental setup for trapping, controlling, and collecting light from our trapped ions. I played a direct role in the design or construction (or some combination thereof) of many of these experimental components. Other parts of the experimental setup (the vacuum system in particular) were designed and constructed by James Siverns[1], which I will still describe here, given that this is the first thesis out of our research group. The frequency conversion setup(s), also critical to the work discussed in this thesis, are described in Chapter 4.

No experimental setup is perfect - there is always some degree of difficult/annoying optical alignment and things that we would change in hindsight. With this in mind, I will also try and leave comments and experimental details (in this chapter, and this thesis as a whole) that will hopefully be useful to future graduate students working in our lab and elsewhere. In particular, I will include our alignment procedures for certain optical systems in the lab as well as try to highlight things that could be improved with our setup.

[1] Post-Doc turned Assistant Research Scientist

3.2 Vacuum System and Ion Trap

Although we can confine ions using a combination of static and oscillating electric fields, collisions with other particles can easily knock ions out of the trap or cause unwanted reordering of the ions (when working with a chain). Therefore, trapped ion experiments require we put our ion trap in an ultra-high-vacuum (UHV) environment such that the probability of such collisions are extremely low. The vacuum system used to enable UHV must be designed in such a way to not greatly inhibit other aspects of the experiment such as optical access for lasers and light collection from the ion. In this section I will describe our vacuum chamber and ion trapping apparatus, designed almost entirely by James Siverns. I joined the lab just as construction was almost complete and was able to assist in the final construction[2] and baking of this system.

3.2.1 Chamber Design

The full vacuum apparatus is shown, with highlights on critical components, in Fig. 3.1. The ion trap (Sec. 3.2.2) is housed in a 4.5" "spherical octagon"[3], consisting of eight 1.33" conflat (CF) ports/flanges. Optical laser access is provided via windows mounted to six of these ports, four of which are anti-reflection (AR) coated from 355 nm to 935 nm. Another 1.33" CF port (top of the octagon) is used for the electrical feedthroughs for the radio-frequency (RF) voltage applied to the ion trap. The final of these ports (bottom of the octagon) is connected to the remainder of the vacuum system via 5-way cross[4], as well as serving as a channel for the electrical feedthroughs for the static (DC) trap electrodes and atomic ovens (Sec. 3.2.3). Two larger 4.5" CF

[2] My job in particular was the construction, testing, loading, and installation of the atomic ovens described below.
[3] Kimball Physics MCF450-SphOct-E2A8
[4] Kurt J Lesker C5-0133

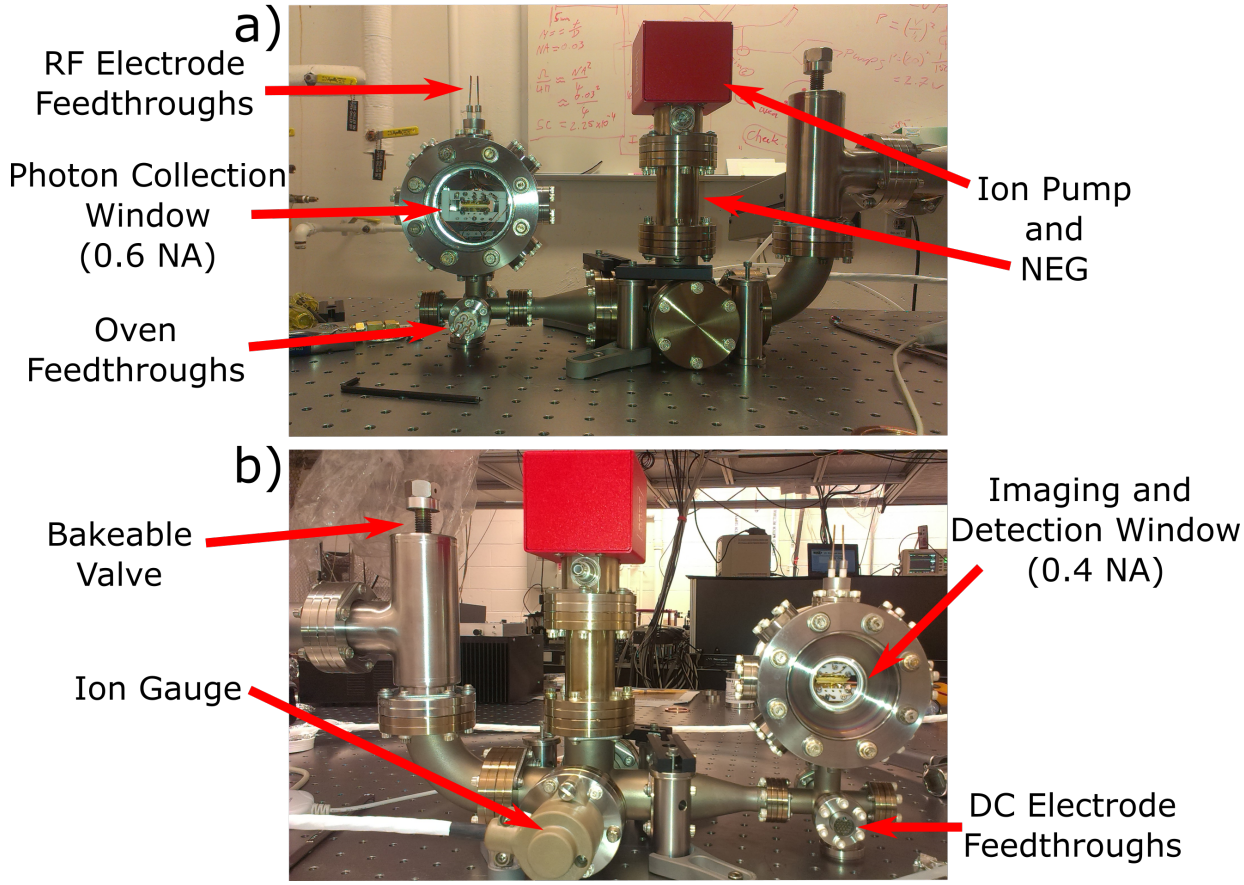

Figure 3.1: **Vacuum System.** a) Vacuum system viewed facing the 60 mm photon collection window. b) Vacuum system viewed facing the 30 mm imaging and detection window. Labeled components are discussed in the text.

ports, located on opposite sides of the spherical octagon, are used to mount large custom recessed windows[5] for high-numerical aperature (NA) optical access. One of these (Fig. 3.1 a) is used for photon collection (Sec. 3.4.3), allowing for a 0.6 NA lens to be used for photon collection when combined with the trap design. The opposite window (Fig. 3.1 b) is used for ion imaging and florescence detection (Sec. 3.4.2) with a 0.4 NA lens.

The remainder of the vacuum apparatus connected to the spherical octagon via a 5-way cross consists of components used to create, maintain, and monitor the UHV environment within the chamber. A UHV gate valve[6] (Fig. 3.1), when opened, allows for vacuum to be pulled using a turbo pump[7] before closing the valve. An ion-pump and non-evaporable getter[8] (NEG) are used to continually pump the chamber during operation to maintain UHV pressures. Finally, an ion gauge[9] can be used to monitor the vacuum pressure, though we turned this off years ago as we were not having vacuum issues and these gauges can sometimes slightly raise vacuum pressure when turned on.

3.2.2 Ion Trap Design

For the ion trap itself, we use a linear blade trap [28, 117] consisting of two blades for application of RF voltages and two blades for static (DC) voltage application, shown in Fig. 3.2 a. These blades[10] are made out of gold coated alumina and are mounted to the vacuum chamber using a custom-built Macor holder (Fig. 3.2 b). The main advantage of this blade trap design is the optical access provided by the blades. The blades taper down to a point (50 μm width) and

[5] UK Atomic Energy Authority
[6] Kurt J. Lesker VZCR40R
[7] Pfeiffer HiCube 30
[8] NEXTorr D 100-5
[9] Agilent Varian UHV-24p 9715015
[10] Kindly given to our lab by Chris Monroe.

are placed at angles to allow room for up to 0.86 NA of photon collection[11] (in the x-direction of Fig. 3.2 a) via recessed windows located near the trap (Fig. 3.2 c).

Each blade is split into five segments (Fig. 3.2 b) to allow for individual voltages to be applied to each segment for control of the trapping potential along the trap axis. The nominal spacing between each segment is 50 μm, with the middle three segments being 250 μm wide at their tips (nearest to the ion). In the case of the RF blades, these segments are electrically shorted to one another such that one RF voltage is applied to the blade as a whole. With a spacing of $\approx$ 300 μm between the tips of the top RF and top DC blades and a spacing of $\approx$ 500 μm between the top RF and bottom DC blades (Fig. 3.2 a), we expect a deep trapping potential (≈ 0.4 eV) when applying $\approx$ 625 V at 38.4 MHz to the RF electrodes and $\approx$ 5 V to segments 2 and 4 (Fig. 3.2 b) on each DC electrode[12].

Static voltages are applied to the DC blades via feedthroughs after filtering via a three-stage low-pass RC filter with each stage having a cuttoff frequency < 10 Hz. To provide the high RF voltages needed for trapping, we use a bi-filer resonator [118], operating at 38.4 MHz with a Q of 50, attached to the top of chamber. This resonator, built by James Siverns, filters and steps up the voltage of the RF, with the bi-filer design allowing us to apply a static compensation voltage to one of the RF blades in addition to the RF. This removes the need for additional static electrodes for excess micromotion compensation [119]. Using this setup, we have performed basic micromotion compensation by adjusting the static fields applied to the DC and RF blades whilst correlating the ion fluorescence to the phase of the RF as in [119]. Note that with the beam geometry discussed in Sec. 3.4.1, we cannot compensate for micromotion present in the direction

[11] When not considering the remainder of the vacuum chamber.

[12] These values are just as an example, but are approximately what we apply before any micromotion compensation.

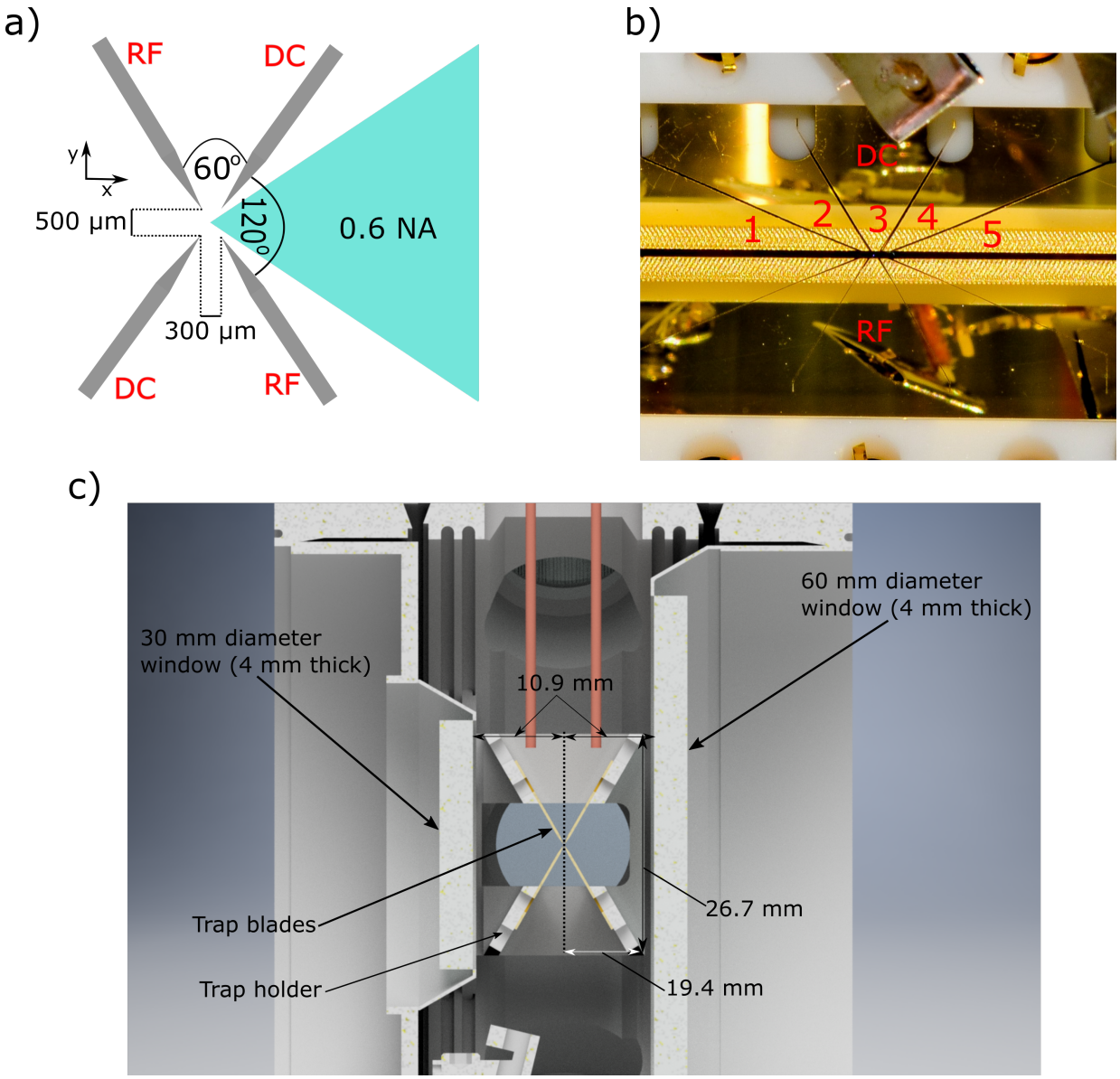

Figure 3.2: **Trapping Electrodes.** a) Basic layout of the trap blade electrodes to allow >0.6 NA of light collection when combined with the vacuum system photon collection window. b) A zoom in on the trap blades, as viewed from the photon collection window. The five DC-electrode segments are visible and numbered. c) Mounting of the ion trap within the vacuum system.

of our imaging system (Sec. 3.4.2) using this technique. In this direction, we adjust our voltages to minimize the de-focus of our ion as viewed by our imaging system when decreasing the RF amplitude. This compensation has been sufficient for the work presented in this thesis.

3.2.3 Atomic Ovens

Loading ions into the trap requires a source of neutral atoms which can then be ionized with lasers directly in the trapping region. To provide these neutral atoms we use home-built atomic ovens, as shown in Fig. 3.3 a. The basic oven design consists of a stainless steel tube[13] open on one end and welded shut on the other end. This tube is loaded with the neutral atom source of choice. Welded to the closed end of the tube is a bare copper wire leading to one of the oven feedthroughs shown in Fig. 3.1 a. These ovens are mounted to the interior of the vacuum chamber via "groove grabbers"[14] designed to hold the open end of these stainless steel tubes just below, and pointing at, the trapping region (Fig. 3.3 b). The oven mounts are designed to electrically ground the ovens at the point of contact. The application of a positive voltage at the oven feedthrough causes a large current to flow through the wire and stainless steel tube, heating the tube to high temperatures and vaporizing some of the neutral atoms within. This hot neutral atomic vapor exits the open end of the stainless steel tube, providing a flux of neutral atoms in the trapping region to be ionized and trapped.

Multiple variations of this oven design were simulated[15], built[16], and tested in a separate vacuum chamber before the final design was used. This was done for both neutral barium and

[13] Small Parts Inc. HTX-19X-12. Inner Diameter 0.035", Outer Diameter 0.042"

[14] Kimball Physics MCF450-GrvGrb-C01

[15] Using a MatLab simulation program provided by Jason Amini in Chris Monroe's group at UMD. These simulations would provide the temperature of all oven components for a given current.

[16] Using a micro TIG welder provided by Chris Monroe's group.

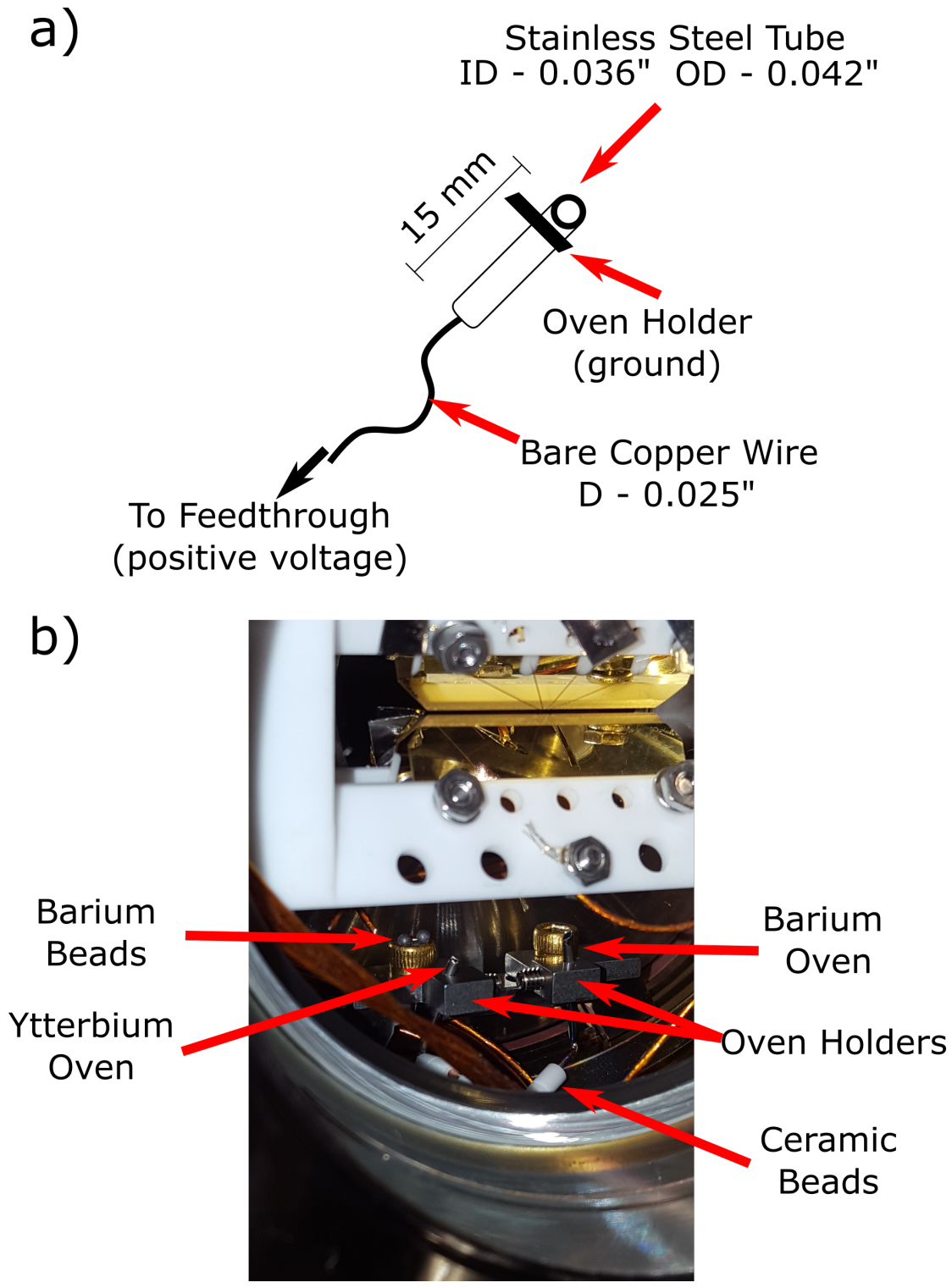

Figure 3.3: **Atomic Ovens.** a) Basic design of the atomic ovens. b) The atomic ovens as mounted with holders within the vacuum system. Ceramic beads are used to electrically isolate the oven's copper wires from the vacuum chamber serving as ground. Extra barium beads are placed to allow the user to identify which oven is which.

ytterbium[17] ovens. Testing consisted of measuring the minimum current needed to view neutral fluorescence on a camera pointed at these test ovens when illuminating the neutral flux with 791 nm or 399 nm light for barium and ytterbium respectively. Changes between the different oven designs included different thicknesses of copper wire and different lengths of the stainless steel tubes used. Additionally, oven designs which included a tungsten coil filament welded between the copper wire and steel tube were found to greatly reduce the amount of current[18] needed to view neutral florescence. This tungsten was very brittle however, and easily snapped when attempting to load it into our vacuum chamber. Thus, we settled on the final oven design shown in Fig. 3.3 a. Using this design, we are able to consistently trap Ba^+ running 6.5 A of current through the oven for around 30 seconds.

One concern with this oven design was the bare copper wire used within the vacuum chamber, which could easily short to the vacuum walls. Kapton coated copper wires were originally to be used to provide insulation and prevent shorting, but this coating was found by James Siverns to be able to vaporize if too high of a current was run through the wire. Thankfully we found that we could use a train of hollow ceramic beads[19] placed around the wire to serve as a semi-flexible insulation and prevent electrical shorting. These are visible in Fig. 3.3 b.

Care must be taken when loading barium into the atomic ovens for a few reasons. First, barium is highly reactive, and will oxidize when left out in air. This can produce an oxidation layer which requires much higher oven temperatures to break through before a strong neutral atomic flux can be achieved. Additionally, barium is a commonly used getter material, meaning that it will readily absorb contaminants within the vacuum chamber or oven tube. Any contaminants

[17] We have the capability to co-trap Yb^+ and Ba^+, but do not currently have any optics set up for Yb^+.
[18] These ovens required only about half the amount of current to view neutral florescence.
[19] McMaster-Carr 87085K61. Inner Diameter 0.040", Outer Diameter: 0.090".

within the oven may be shot directly at the ion trap when the oven is turned on. These contaminants may also react with barium to form molecules which will not be ionized[20].

Considering the potential issues discussed above, we adopted the following procedure to install our ovens and load barium into them:

1. Clean the empty ovens in an ultrasonic bath of isopropanol.

2. After all vacuum parts have been cleaned and have gone through their initial pre-bake, install the ovens into the chamber, without loading the barium.

3. Pull vacuum on the chamber using a turbo pump.

4. Run the oven at a high current (7A) for an extended period of time (40 min) to allow them to "self-bake" and eject contaminants.

5. Using a glove bag filled with argon around the entire chamber, vent the vacuum system to argon.

6. Open the barium container in the argon environment and load the oven with 2-3 barium beads[21] (shown in Fig. 3.2.3 b) using tweezers.

7. Close and pull vacuum on the chamber and proceed with standard vacuum baking to remove remaining contaminants from the system.

With this procedure we were able to trap ions using our oven. We did not have the issue other groups working with barium have typically had [64], where the ovens must be run at a

[20] We had observed with our test ovens that sometimes they would just stop working although they were getting hot leading us to wonder about this.

[21] In the case of Yb, these were more of "flakes".

relatively high current (as high as 15 A) in order to break an oxide layer blocking atomic flux. When running the ovens for the first time, we did, however, observe large increases in vacuum pressure, likely due to contaminants captured by the barium. To deal with this, we ran the ovens at a set current until the pressure began to decrease and reached a lower equilibrium before again stepping up the oven current. This was repeated until we reached our expected oven current[22] near 6.5 A[23], at which point we are able to trap ions.

3.2.4 Magnetic Field

The work presented in this thesis uses two different methods for magnetic field generation at the point of the ion. Originally, we produced our magnetic field using two coils of wire placed on opposite ends of the spherical octagon in a Helmholtz-like[24] configuration. These coils were built with 200 turns of Kapton wire with a coil radius of approximately 1.25". Each coil was centered around one of the windows of the spherical octagon (top-right and bottom-left windows/viewports in Fig. 3.1 a), roughly 2.5" from the center of the ion trap. These coils were found to produce a field of $\approx$ 5 G at the location of the ion with $\approx$ 6 A of current resulting from an applied voltage of $\approx$ 13 V. Two additional adjustment coils (smaller coils - only 100 turns each) were also used to compensate for stray fields at the location of the ion as well as any misalignment of these main field coils, one placed near the imaging window, and another placed around a window port orthogonal to the main coils. This coil configuration was used for the work presented in Chapters 5-7.

When beginning to work with the Zeeman qubit in $^{138}Ba^{+}$, we became concerned that our

[22] Provided by a BK Precision 1688B Voltage/Current Driver.

[23] 6 A is the operation current for the Yb oven.

[24] These technically are not Helmholtz coils as the separation between the two is not equal to half the radius, but this has a negligible effect on uniformity near the ion.

magnetic field coil design would lead to a relatively large amount of magnetic field noise at the ion resulting from our current supplies. Though stabilization techniques exist for these types of coil designs [120], we opted to instead switch out our coils for permanent magnets. We use two neodymium ring magnets[25], mounted in 1" optics holders and again centered around the spherical octagon windows, to produce a measured magnetic field of 5.23 G at the location of the ion. In this configuration we do not use our adjustment coils[26], but this does not seem to greatly affect[27] our laser operations or optical pumping. These permanent magnets are used for the work presented in Chapters 8-10.

3.3 Laser Systems and Frequency Control

3.3.1 Laser Frequency Monitoring

With the large range of laser wavelengths used in our lab (493 nm - 1762 nm), we use a variety of tools to monitor our laser frequencies. For visible and NIR wavelengths, we monitor our lasers' center frequencies and verify single mode operation using a HighFinesse WSU-2 wavelength meter (wavemeter), operating at wavelengths from 360 nm - 1100 nm with an absolute accuracy of 2 MHz and precision of 100 kHz. This wavemeter is customized with two fiber-optic switch inputs, allowing for up to 10 laser frequencies to be read out in quick succession ($\approx$ 1 ms per laser). For Ba^+, we use this wavemeter to monitor and provide frequency drift locks for our lasers at 493 nm, 650 nm, 791 nm, and 614 nm.

To measure the remaining infrared (IR) wavelengths used in the lab, we use a Bristol

[25] McMaster-Carr 3360K77.
[26] We did try for a time, but found that this seemed to greatly increase the magnetic field noise on the ion.
[27] At least not at a level we care about for the work presented in this thesis.

Model 621 NIR laser wavelength meter. This wavemeter officially operates from 520-1700 nm, but we are able to provide enough power ($\approx$ 1 mW) at 1762 nm for it to provide a frequency reading here as well[28]. Unfortunately, this wavemeter only has a precision of $\approx$ 20 MHz, reads in frequencies much too slowly to be usable for frequency feedback, and does not have an optical switch to allow for monitoring of multiple laser frequencies. Additionally, it only provides a wavelength/frequency value and gives no information on the quality of the laser frequency mode. For this reason, it is only used as a rough monitor of our IR wavelengths at 1762 nm, 1228 nm, 1343 nm and 1590 nm[29]. When frequency mode monitoring or laser locking is required, we use optical cavities with the Bristol wavemeter serving to help us get our frequencies close to their target (See Secs. 3.3.4 and 3.3.5).

3.3.2 Diode Laser Systems for Doppler Cooling, Optical Pumping, and Photon Production

The 493-nm and 650-nm light used for Doppler cooling, optical pumping, and photon production are provided by Toptica DL pro ECDLs. We use the HighFinesse wavemeter described in Sec. 3.3.1 to read in these laser frequencies and to provide feedback to the laser frequencies. This drift-lock allows us to stabilize the frequency of these lasers to $\approx$ 2 MHz, without any additional linewidth narrowing[30].

Light from each of these lasers is sent to different parts of the lab via the optical setups shown in Fig. 3.4 and Fig. 3.5 for the 493-nm and 650-nm lasers respectively. In both setups,

[28] When we inquired with Bristol about if this would work, they were not sure, but asked us to test it for them.
[29] These final two frequencies are used in the frequency conversion discussed in the next chapter.
[30] The free-running fast linewidth of these lasers is specified to be on the order of $\approx 100 - 200$ kHz

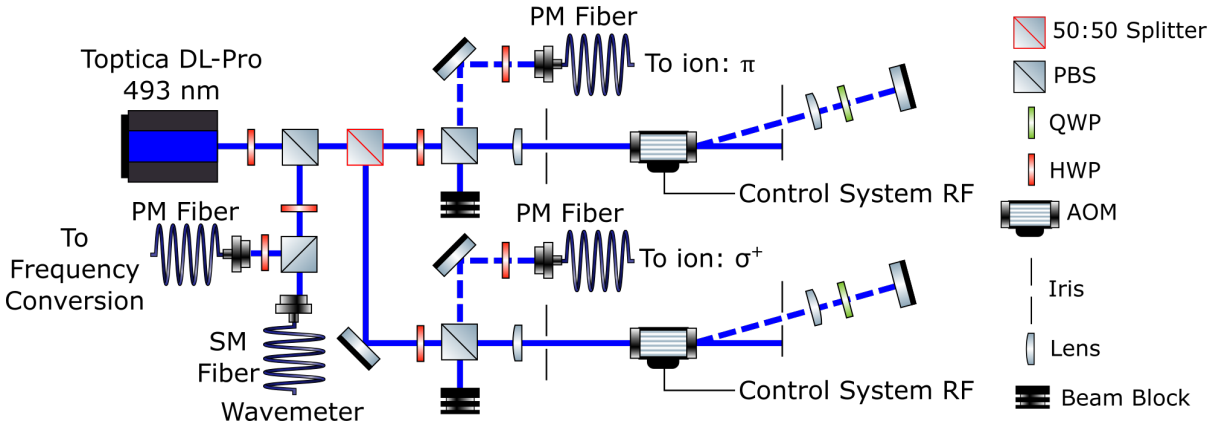

Figure 3.4: **493 nm Laser Setup.** Two double pass acousto-optic modulator (AOM) setups provide switching and frequency control of light sent to the ion for driving both π- and σ transitions. Additional light is sent to the wavemeter for frequency locking and to other parts of the lab for testing of quantum frequency conversion setups.

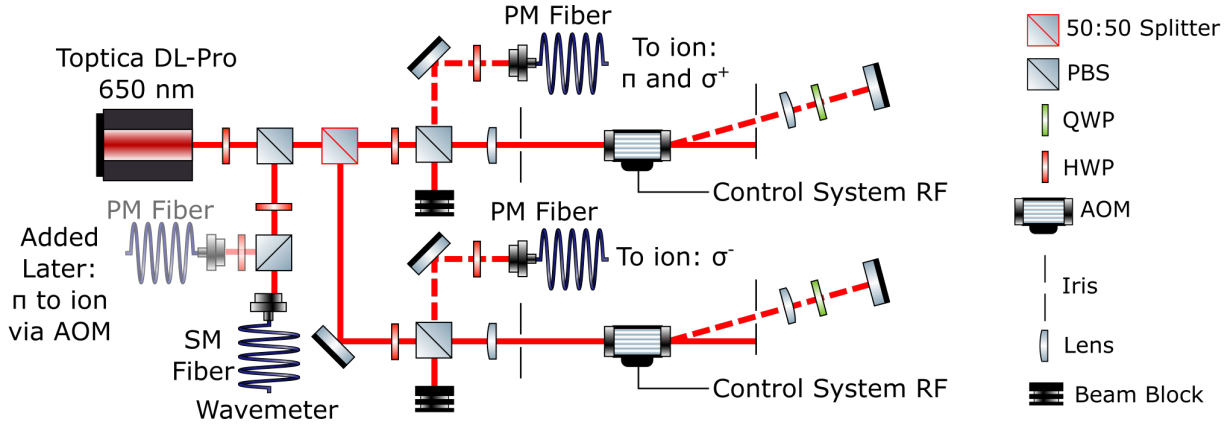

Figure 3.5: **650-nm Laser Setup.** Two double pass acousto-optic modulator (AOM) setups provide switching and frequency control of light sent to the ion. π- and σ^+ transitions are tied together via one AOM, with σ^- transitions driven by light originating from the remaining AOM. As with the 493-nm setup, additional light was used for wavemeter-based locking. Later on, an additional fiber leading to a third double-pass AOM setup was added for independent driving of π-transitions.

light is sent to the ion trap setup via multiple acousto-optic modulators (AOM). Each AOM[31] is mounted on a 5 axis-stage[32] and setup in a double-pass configuration [121]. In this configuration, the application of an RF signal[33] originating from our control system (Sec. 3.5) to the AOM deflects the light and shifts its frequency an amount equal to the frequency of the applied RF. The deflected light is represented by the dashed paths in Figs. 3.4 and 3.5. After a second pass through the AOM, the now twice-frequency-shifted light is fiber coupled and sent to the ion. This enables fast switching of both the amplitude and frequency of the light sent to the ion via the amplitude and frequency of the applied RF, with the double-pass configuration allowing for larger frequency shifts to be used while maintaining efficient fiber coupling when compared with a single-pass setup.

For the 493-nm setup (Fig. 3.4), we use two of these aforementioned AOM setups, with one setup providing light to drive π-transitions and the other setup providing the light used to drive σ^+-transitions[34]. In addition to these AOMs, we also fiber couple light to send to the HighFinesse wavemeter for laser frequency locking and to send to the quantum frequency conversion setups described in Chapter 4. Power is diverted to each of these components through use of half-wave plates (HWPs) and polarizing beamsplitter cubes (PBSs).

The 650-nm setup (Fig. 3.5) is very similar to that at 493 nm. In this case however, one AOM provides light to drive σ^--transitions, while the other AOM provides light to drive both σ^+- and π-transitions[35]. Thus, for the majority of the work presented in this thesis σ^+- and π-transitions are driven simultaneously. For the work presented in Chapter 10, we added an

[31] IntraAction ATM-80A1.
[32] Thorlabs PY005
[33] $\approx$ 80 MHz
[34] In the work presented here, we never have a simultaneous need to drive both 493 nm σ-transitions.
[35] The polarization control is discussed in Sec. 3.4.1

additional fiber coupling to this setup (labeled as "added later" in Fig. 3.5). This fiber leads to a third double-pass AOM setup allowing us to separately control π-light sent to the ion.

3.3.3 Light for Ionization

We ionize neutral barium using the scheme discussed in Section 2.3.1. Light at 791 nm is provided by a MogLabs ECDL[36]. This laser is drift locked via the HighFinesse wavemeter, and sent to the ion via optical fiber. A simple iris is used to block the light when not in use.

To complete the ionization process, light is required with a wavelength less than ≈ 340 nm. To this end, we use a ThorLabs fiber-coupled LED[37] centered around 300 nm, which provides up to $\approx 320\mu$W of power out of a multimode fiber. The output fiber is setup in a cage mounted lens system next to the ion trap vacuum system to directly deliver light to the trapping region[38].

3.3.4 1762 nm Laser and Locking to Address Quadrupole Transitions

For the work presented in Chapters 8-10, we use light from a 1762-nm Toptica ECDL to address the $S_{1/2} \leftrightarrow D_{5/2}$ quadrupole transition in Ba^+. This transition is extremely narrow (≈ 3 mHz), requiring frequency narrowing of the laser[39] to a narrow linewidth optical cavity.

To both lock the laser frequency and send 1762-nm light to the ion, we built the setup outlined in Fig. 3.6. Coarse changes to the laser frequency are monitored via fiber-coupled light sent to the Bristol wavemeter discussed in Sec. 3.3.1. A 40 MHz AOM[40] is used to to provide fine-step frequency control of the 1762 nm light seen by the ion and to rapidly switch this light on

[36] MogLabs ECD004/r3
[37] ThorLabs M300F2
[38] The light is not particularly well focused here, but the intensity seems sufficient for a reasonable rate of ionization
[39] The free running fast linewidth is ≈ 100 kHz.
[40] IntraAction ACM-402AA10

and off at the ion. The 0th diffraction order (non-frequency-shifted) AOM output is picked off, fiber coupled, and sent to a monitor scanning cavity[41] to ensure single-frequency mode operation of the 1762-nm ECDL[42].

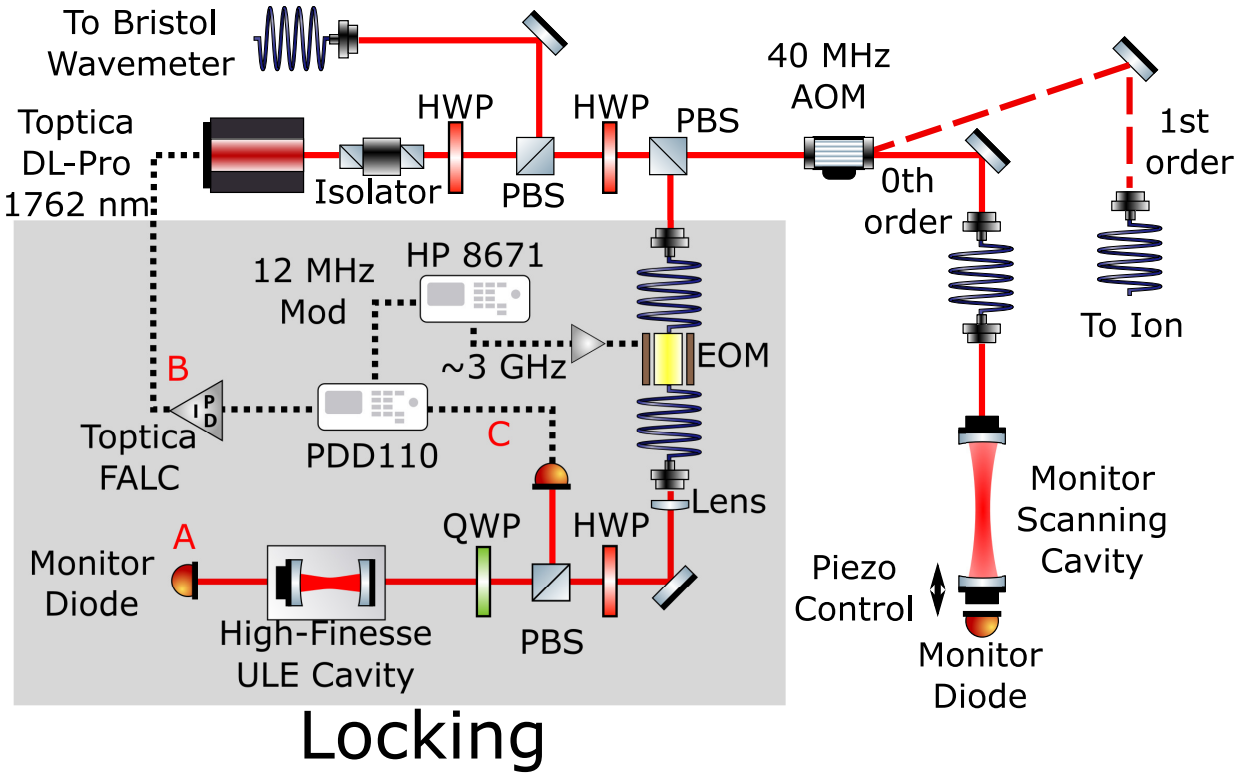

Figure 3.6: **1762 nm Laser Setup and Locking.** Light is sent to the ion via the 1st order output of a single-pass acousto-optic modulator (AOM) driven at 40 MHz. Coarse frequency monitoring of the laser is performed via fiber coupled light sent to the Bristol wavemeter. Single mode operation of the laser is monitored via un-shifted 0th order AOM output light sent to a scanning monitor cavity via optical fiber. Laser locking and linewidth narrowing is performed via the Pound-Drever-Hall locking setup denoted by the shaded region and discussed in the text.

The laser is locked to a high finesse optical cavity[43] via the Pound-Drever-Hall technique [122, 123]. The gray box in Fig. 3.6 highlights the important components for implementing this lock. The 1762 nm light from the laser is modulated via a fiber-coupled electro-optic-modulator[44]

[41] ThorLabs SA200-12B, 7.5 MHz linewidth

[42] Initial attempts to lock the laser without this monitor cavity were inconsistent, due to the laser going slightly multimode over time.

[43] Stable Laser Systems 6010-4, Finesse 10000-30000

[44] Thorlabs LN53S. Designed for use at 1550 nm, but we have enough modulation depth at 1762 nm to produce frequency sidebands for locking.

(EOM). The modulated light at the output of the EOM is then focused[45] and sent to the optical cavity. The reflected signal is then measured on a photodiode[46] and demodulated using Toptica's PDD 110 Pound-Drever-Hall detector (including both a modulation source and demodulator), included with the 1762 nm ECDL. This produces an error signal which is then sent to a fast analog laser servo (Toptica FALC) that feeds back to both the piezoelectric actuator controlling the ECDL grating angle and to the laser diode current for both low and high frequency feedback.

Due to the fact that the free spectral range (FSR) of the cavity ($\approx$1.5 GHz) is much larger than tuning range ($\approx$ 10 MHz) of our 40 MHz AOM, we would likely be unable to address the ion if the laser were locked directly to cavity resonance. Therefore, we use a variation of the PDH locking technique known as electronic-sideband (ESB) locking [124]. Using a HP 8671 frequency synthesizer, we drive our EOM with a tunable $\approx$ 3 GHz signal that is itself modulated by a 12 MHz signal originating from the PDD 110's modulation source. This produces a frequency spectrum as shown in Fig. 3.7 a, where the carrier (black) has been modulated to produce first order sidebands (blue) at $\approx \pm 3$ GHz, each having their own $\pm$ 12 MHz sidebands (red). The error signal used to lock the laser is then based on interference of the positive frequency-shifted 3 GHz sideband with its own 12 MHz sidebands (demodulation, this error signal is also at 12 MHz). This allows the laser to be locked with a known and tunable (over the entire cavity FSR) offset relative to cavity resonance.

The classic demodulated PDH error signal produced when scanning the laser frequency is shown by the yellow oscilloscope trace in Fig. 3.7 b. The blue trace in Fig. 3.7 b represents the light transmitted through the cavity as measured on the monitor diode at the output of the

[45] To properly couple to the fundamental mode of the high finesse cavity - we estimate at least 25% coupling to this mode.

[46] ThorLabs PDA10D2

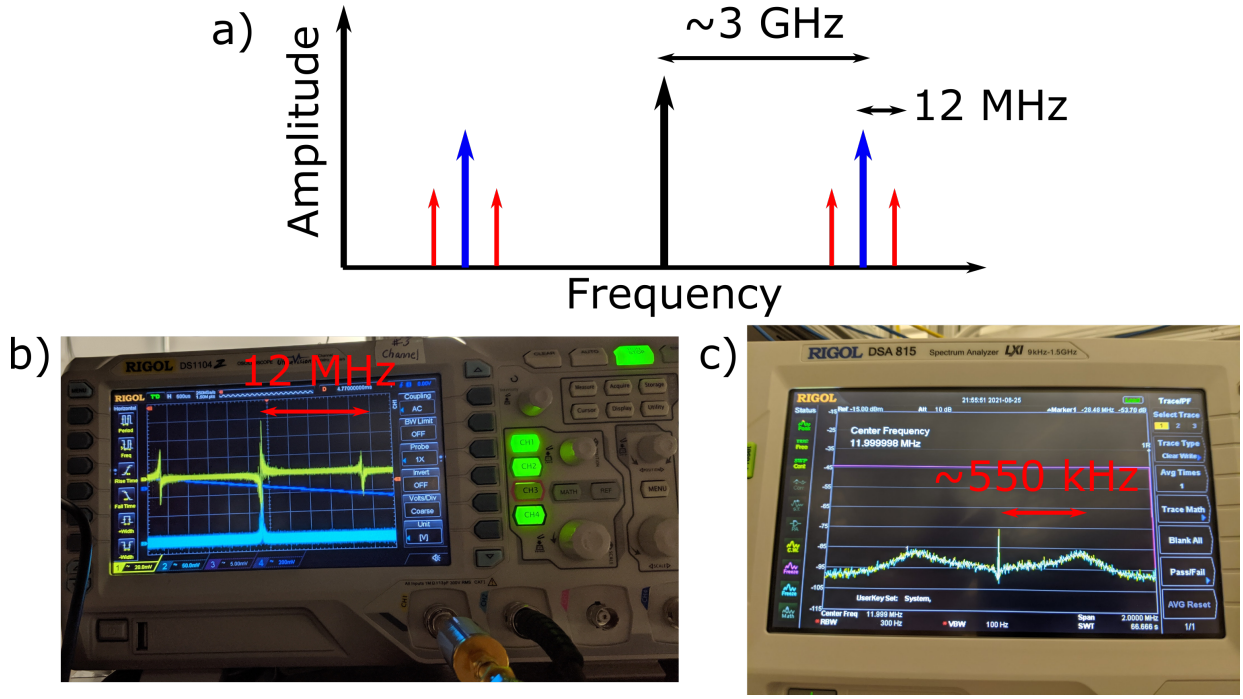

Figure 3.7: **Pound-Drever-Hall (PDH) Locking Frequencies.** a) The frequency spectrum of the 1762 nm light sent to the PDH locking cavity, as a result of frequency modulation of the 3 GHz electro-optic modulator signal, itself modulated at 12 MHz. b) The blue trace represents the cavity transmission measured at point A in Fig. 3.6. Transmission is not visible for the 12 MHz sidebands. The yellow trace represents PDH error signal resulting from scanning the laser frequency, measured at point B in Fig. 3.6. c) In-loop error signal, measured before demodulation (point C in Fig. 3.6).

high-finesse cavity in Fig. 3.6. To optimize the lock, we monitor the in-loop error signal (before demodulation) on a spectrum analzyer and adjust the loop filter settings on the Toptica FALC to maximize the lock bandwidth[47]. During the optimization, the average transmission of the cavity was used to verify that the laser was not driven into oscillations by the feedback[48]. The optimized in-loop error signal before demodulation, as viewed on our spectrum analyzer[49], is shown in Fig. 3.7 c, with servo bumps near $\approx$ 550 kHz.

The laser linewidth resulting from this lock is much narrower than we can directly measure in the lab. We haveperformed self-heterodyne measurements [125] of the laser light using a 6 km fiber delay, bounding the laser linewidth to be well under 16 kHz. Although we cannot directly measure the linewidth of the laser, independent measurements using the 1762 nm quadrupole transition suggest the linewidth to be on the order of a few hundred Hz.

3.3.5 Homebuilt 614-nm Laser System

Driving the $P_{3/2} \leftrightarrow D_{5/2}$ dipole transitions in Ba^+ requires light at 614 nm. This transition is critical for returning the ion to the ground state after optical shelving (Chapter 8). Unfortunately, there are no commercially available laser diodes operating at this color, preventing the use of standard ECDLs. Given the high cost of frequency-doubled laser systems (combined with this light not needing to have a particularly narrow linewidth for our de-shelving purposes), we opted to build our own laser at 1228 nm, which can then be frequency doubled to 614 nm using commercially available second harmonic generation (SHG) devices.

The 1228 nm laser we use (which I built) is shown in Fig. 3.8. It is a Littrow ECDL based on

[47] One of our collaborators, Sandy Craddock [94] gave me some very helpful tips for doing this.
[48] Oscillations would cause a large decrease in the average power transmitted through the cavity.
[49] Rigol DSA815

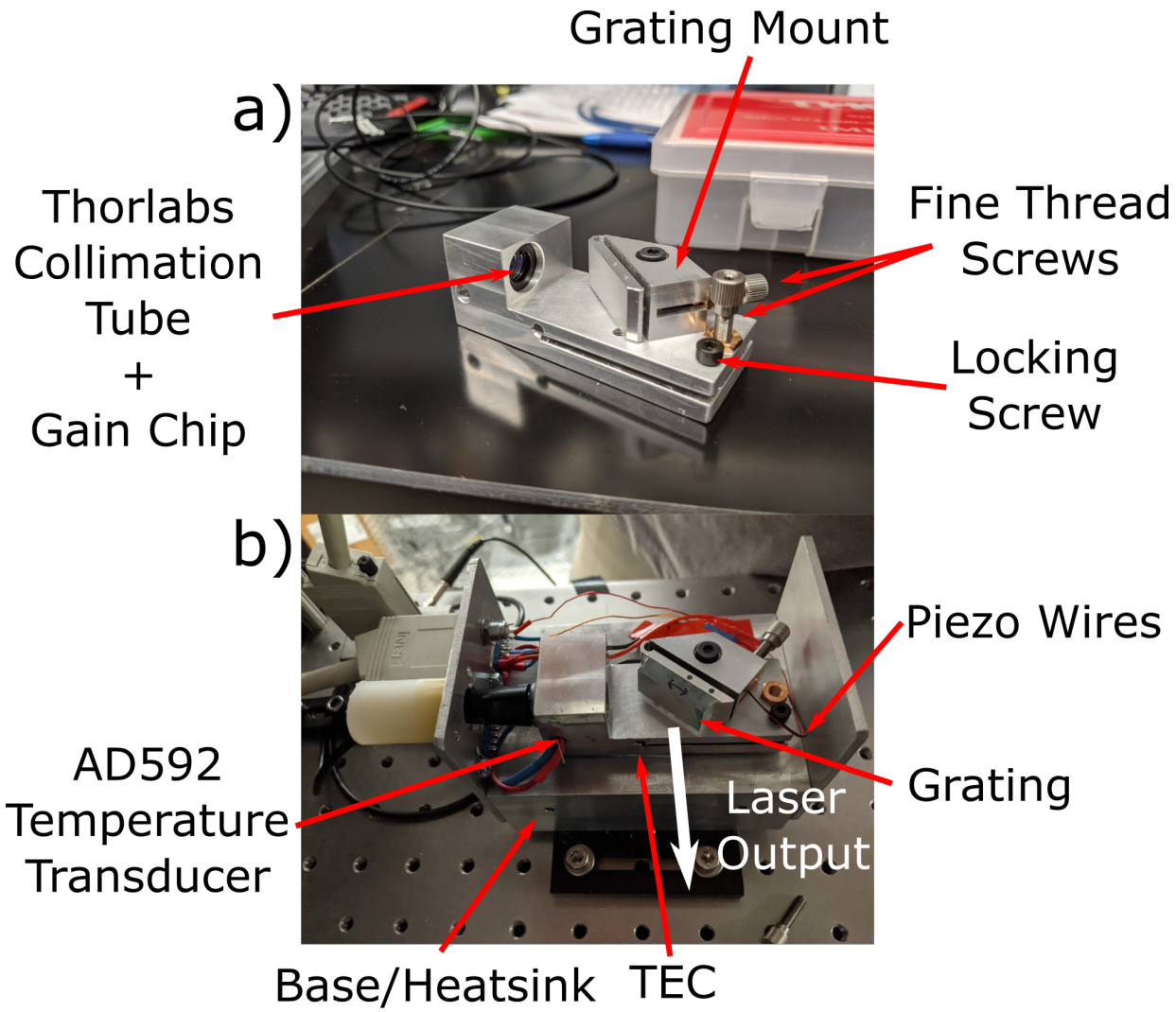

Figure 3.8: **Home-built 1228 nm External Cavity Diode Laser.** a) The main laser body consists of an L-shaped aluminum block. A slit machined out of one end of the block allows for vertical adjustment of the grating mount relative to the laser gain chip located in the collimation tube. b) The full laser, where the main laser L-block is mounted on top of a large base with a thermoelectric cooler (TEC) used between the two for temperature control. The first order diffraction from the grating provides feedback to the gain chip. Labeled parts are discussed in the text.

designs from both the University of Sussex [126] and the National University of Singapore [127], consisting of an L-shaped block of aluminum with multiple holes drilled into it for mounting various laser components. Rather than a laser diode for a gain medium, the laser uses a gain chip[50]. The gain chip is mounted in a laser diode collimation tube[51], which is itself mounted in a large hole drilled into the vertical wall of the L-shaped block (Fig. 3.8 a). This collimation tube comes with pre-wired sockets to provide an electrical connection between a current controller[52] and the gain chip. An aspheric lens[53] is also mounted in this collimation tube and is adjusted to roughly collimate the output from the gainchip. To properly orient the polarization of the output light, the collimation tube may be rotated freely within its mounting hole until locked in position by multiple set screws.

The gain chip does not have a lasing cavity and will not self-lase, relying entirely on the external cavity provided by the optical grating[54] mounted towards the opposite end of the L-piece for optical feedback (Fig. 3.8 b). A slit machined out of the middle of the L-piece allows for this feedback to be adjusted in the vertical direction through use of a fine thread screw[55]. This adjustment may be locked in place using the locking screw in Fig. 3.8 b. A second fine thread screw in the grating mount allows for coarse frequency and horizontal feedback adjustment via the angle of the grating. A piezo actuator[56] mounted between this fine thread screw and the grating allows for fine adjustment of the laser frequency via a high voltage driver[57].

A thermoelectric cooler (TEC) placed between the L-shaped block and a large aluminum

[50]Innolume GC-1220-110-TO-200-B
[51]Thorlabs LT230P
[52]Thorlabs LDC210C.
[53]Thorlabs C230TMD-C.
[54]Newport 33066FL01-220H.
[55]Owis FGS 7-7.5.
[56]Piezomechanik PSt150/4/5 bS.
[57]Thorlabs MDT694B.

base/heatsink allows for temperature control of the entire ECDL. To try and help temperature conduction to/from the gain chip, we place thermal paste between the collimation tube and the L-shaped block. The temperature is measured just under the gain chip collimation tube using a temperature transducer[58] and this signal is fed back to the TEC via a temperature controller[59].

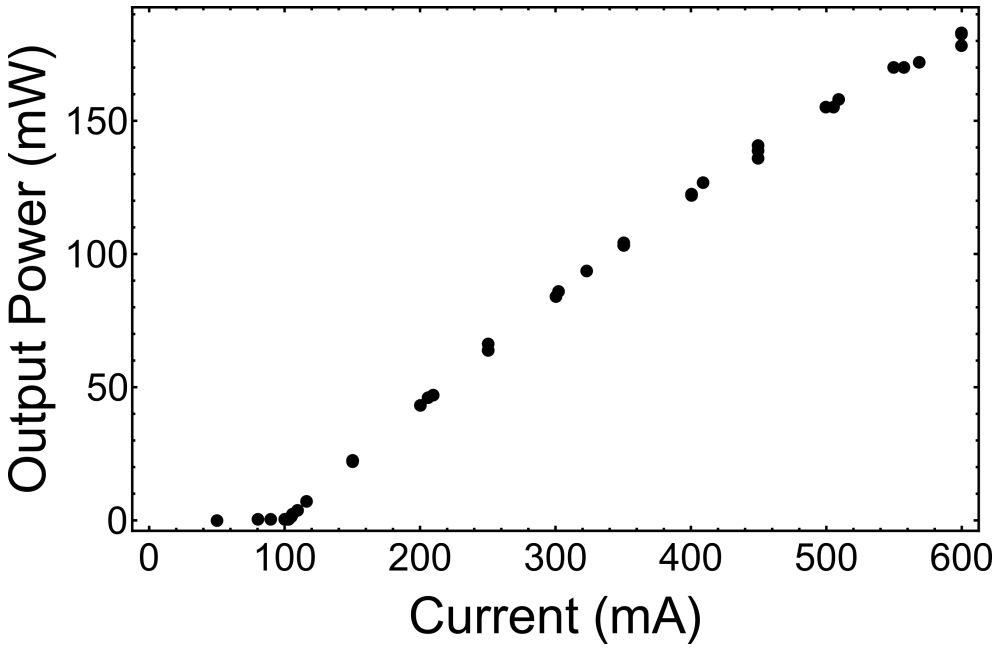

Figure 3.9: **P-I Curve for 1228-nm Laser.** Typical output power of the 1228 nm laser as a function of gain chip drive current. The lasing threshold is approximately 100 mA.

The output power of the 1228-nm laser as a function of the current run through the gain chip is shown in Fig. 3.9. This is measured after aligning the laser feedback to optimize single-mode operation[60] rather than maximizing output power[61]. We achieve output powers of > 180 mW at a current of ≈ 600 mA with relatively stable single-mode operation. Throughout the day, the laser current and grating angle (via the piezo-actuator) must be adjusted to maintain single

[58] Analog Devices AD592
[59] Thorlabs TED200C
[60] This is checked at 614 nm using the HighFinesse Wavemeter
[61] We believe that we actually have too much feedback in this case, and have to purposefully misalign the feedback to achieve single mode operation. Use of a lower efficiency grating (such as Thorlabs GR25-1210) could potentially fix this.

mode operation much more often than our commercially acquired laser systems (every few hours vs every few weeks). We believe this is due to a slow temperature stabilization of the laser gain chip, due to a combination of poor thermal contact between the gain chip and the collimation tube, with the large heat load produced by the relatively large currents (max 1 A) that need to be run through the chip[62].

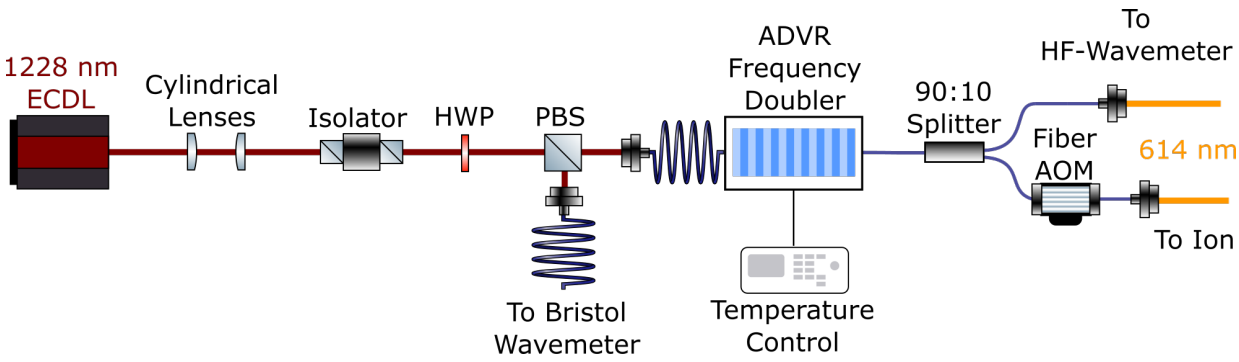

Figure 3.10: **1228-nm/614-nm Laser Setup.** Light from the home-built 1228 nm ECDL is shaped via cylindrical lenses before being fiber coupled and frequency doubled to 614 nm. A 90:10 fiber splitter is used to send the majority of the 614-nm light to a fiber-based AOM connected to the ion trap setup, with the remaining light being sent to the HighFinesse wavemeter for mode monitoring and frequency locking. A small portion of 1228-nm light is sent to the Bristol wavemeter for coarse frequency measurements before frequency doubling.

To produce and control 614-nm light using our 1228-nm laser, we use the optical setup shown in Fig. 3.10. To improve fiber coupling, a pair of cylindrical lenses are used to re-shape the highly elliptical output[63] of the laser, resulting in fiber coupling efficiencies of around $\approx 55\%$. A small amount of light is picked off and sent to the Bristol Wavemeter (Sec. 3.3.1) to set the laser near our target frequency. Light from the 1228-nm laser is coupled into fiber and sent to a fiber-coupled frequency doubler[64], which operates with a conversion efficiency of $\approx 150\%$/W before fiber losses. A temperature controller[65] connected to the frequency doubler is adjusted to

[62] The use of brass rather than aluminum for the laser block could help with this.
[63] Before shaping, Gaussian fits to the beam diameter suggest a roughly 4.9 mm x 0.9 mm beam.
[64] ADVR Fiber coupled SHG
[65] Thorlabs TTC001

maximize the output 614-nm light. The resulting fiber-coupled 614-nm light is split via a fiber splitter that sends $\approx 10\%$ of the light to the HighFinesse wavemeter for frequency and mode monitoring as well as for laser frequency feedback. The majority of the light is sent to a fiber coupled AOM[66], operating at a fixed frequency of 200 MHz, that serves as a fast optical switch for light sent to the ion. This AOM is switched on and off via TTL pulses sent by our control system. With this setup, we are able to send ≈ 1 mW of fiber-coupled 614-nm light to the ion setup.

3.4 Light Delivery, Florescence Detection and Single Photon Collection

3.4.1 Laser Light Delivery

As briefly mentioned in Sec. 3.2.1, laser access to the ion trap is provided via windows at each of the six 1.33" CF ports shown in Fig. 3.1. Figure 3.11 shows how we use this optical access to deliver light of various polarizations to the ion. Through one of the four available AR coated windows (shaded pink in Fig. 3.11), we send linearly polarized light at both 650 nm and 493 nm to the ion and at an angle 45° relative to the trap axis and 90° to the applied magnetic field (Sec. 3.2.4). The polarization of this light can be set to be parallel to the applied magnetic field in order to drive π-transitions[67]. Similarly, we send circularly polarized light at 493 nm and 650 nm along the applied magnetic field in order to drive σ-transitions. We also send the 791 nm light required for ionization along this path. We send both the 1762 nm and 614 nm light needed for addressing the quadrupole transition in Ba^+ (Chapter 8) along the trap axis and 45° to the applied magnetic field through an uncoated window. Finally, though not shown in Fig. 3.11, we

[66] AA Opto-Electronic MT200-R18-Fio-SM-J1-A-VSF.

[67] In some cases, we purposefully set this polarization to drive both σ and π transitions.

send the UV light near 300 nm needed for the second step of ionization through the remaining uncoated window, counter-propagating to the 1762-nm and 614-nm beams.

The current[68] optical setup used to combine and deliver the π-beams to the ion is shown in Fig. 3.12. A fiber-based wavelength division multiplexer[69] (WDM) is used to combine the 493-nm and 650-nm beams, delivered from the double pass AOMs discussed in Sec. 3.3.2, into a single fiber. We use a reflective collimator based on an off-axis parabolic mirror[70] to help ensure that both beams are collimated exiting this fiber[71]. With both beams collimated, an achromatic doublet lens[72], adjustable via a 3-axis translation stage, is used to ensure both beams are focused at the position of the ion, producing an estimated focal spot sizes of $\approx$45 um and $\approx$65 um for the 493-nm and 650-nm beams respectively. The polarization of these beams is filtered through use of a polarizing beam splitter, with the quarter and half waveplates just before this splitter used to maximize transmission of both beams. The position of the final half waveplate[73] is optimized for the 650-nm beam, as the polarization of this 493-nm beam is not critical to either of the optical pumping schemes discussed in Sec. 2.3.4. Optimization is performed by minimizing ion florescence using this waveplate when only the π-beams are present.

The setup used for σ-beam delivery is shown in Fig. 3.13. Similarly to the π-beams, we use WDMs to combine the 493-nm and 650-nm σ^+-beams[74] and to combine the 650-nm σ^--beam with the 791-nm ionization beam[75]. Again, reflective collimators and an achromatic

[68] We have had a few different iterations of this and other light delivery setups, but for brevity, I will only discuss our final versions.

[69] Thorlabs RB61F1.

[70] Thorlabs RC04APC-P01

[71] Originally, we tried using a standard aspheric lens here, but it resulted in significantly different focal spots at the ion due to the slightly different divergences of the "collimated" beams.

[72] Thorlabs AC254-250-A.

[73] Tower Optical Z-17.5-A-.250-B-650

[74] Thorlabs RC04APC-P01

[75] Thorlabs NR74A1

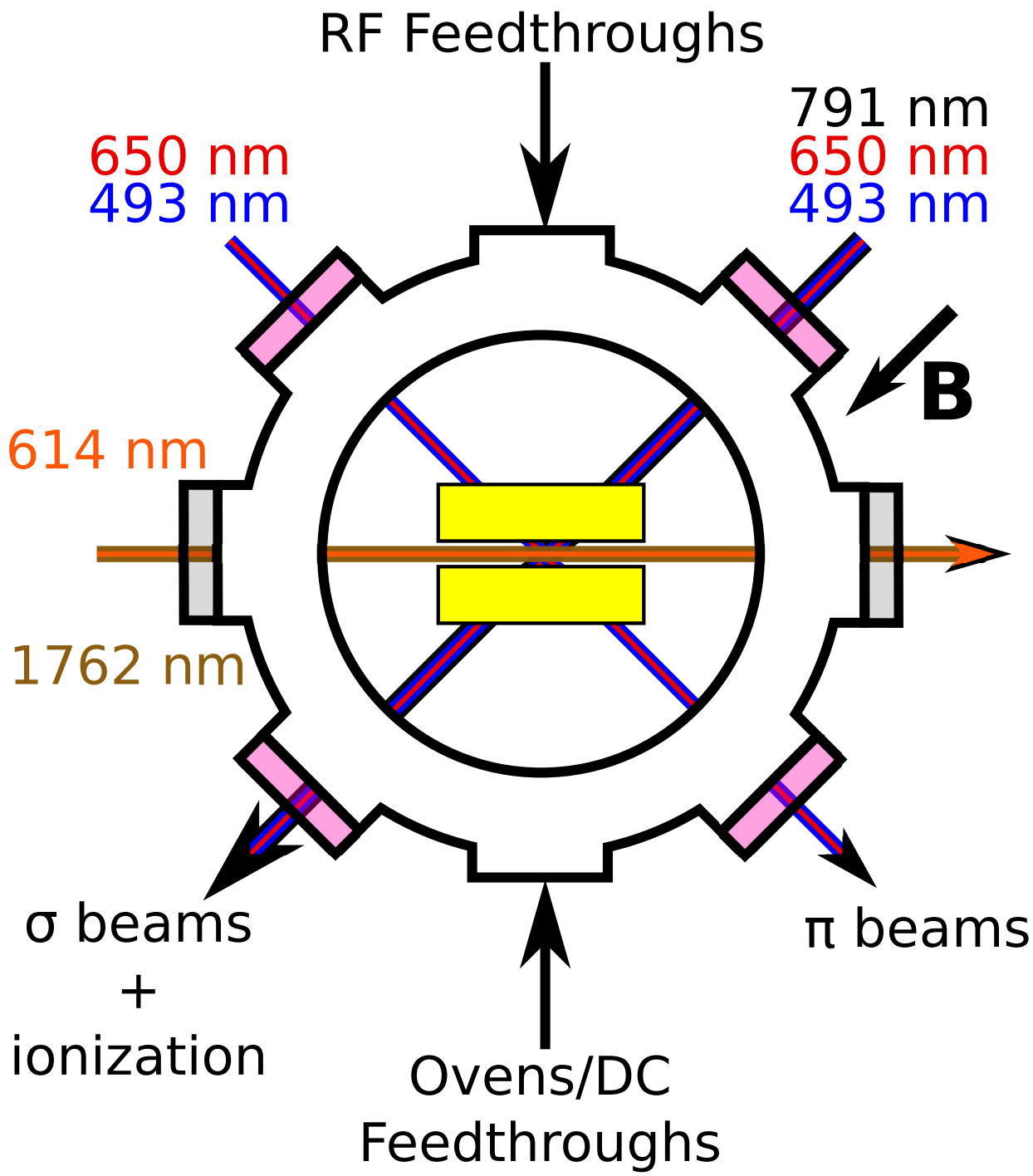

Figure 3.11: **Beam Orientations Through Vacuum System.** The applied magnetic field is at 45° relative to the trap axis. Light for driving π-transitions (σ-transitions) at 493 nm and 650 nm is sent through coated windows perpendicular (parallel) to the applied magnetic field and at 45° to the trap axis. The 1762-nm light used to drive quadrupole transitions, as well as 614-nm re-pump light, is sent down the axis of the trap through uncoated windows. For ionization, light at 791 nm is sent along the σ-beam path, and ≈ 300 nm light (not shown) is sent counter propagating to the 1762 nm beam.

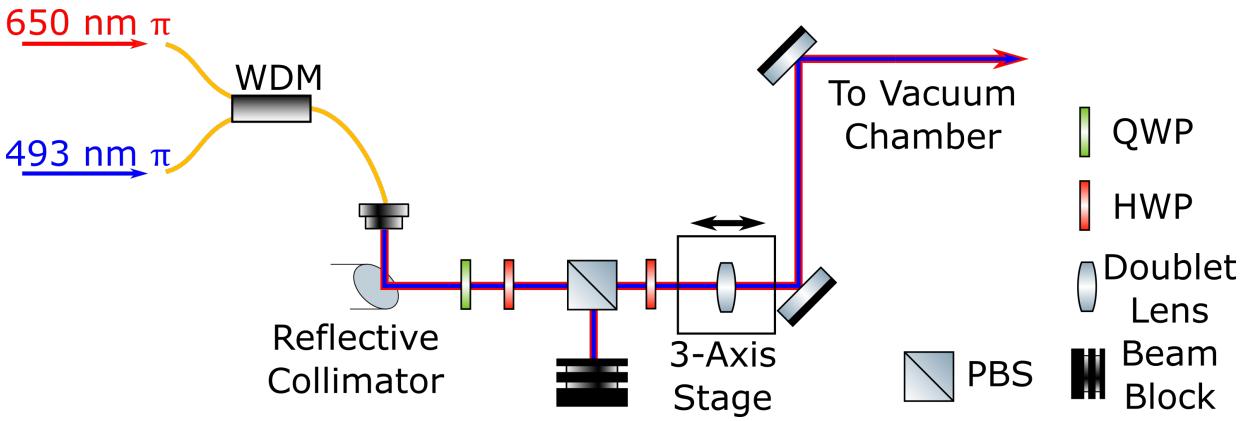

Figure 3.12: **Pi Beam Delivery Optics.** A fiber-based wavelength-division multiplexer (WDM) is used to combine light at both 493 nm and 650 nm into a single optical fiber. A reflective collimator and achromatic doublet allow both beams to focus at roughly the same spot in the vacuum chamber. A polarizing beamsplitter (PBS) is used for polarization filtering, with a 650 nm half waveplate located after this PBS used to set the polarization of the light sent to the ion.

doublet[76] mounted on a 3-axis translation stage are used to help focus all beams on the ion, and a polarizing beam splitter common to all beam paths is used for polarization filtering. Estimated $1/e^2$ Gaussian beam diameters at the focus are ≈35 um and ≈50 um for the 493 nm and 650 nm beams respectively. This setup also includes a permanent ring magnet in an 1-inch lens tube mounted directly to the final cage-mirror mount just before the vacuum chamber window. A second ring magnet is independently mounted on the opposite side of the vacuum chamber.

In contrast the π-beam setup, the polarizations of both the 493-nm beam and both 650-nm beams affect both D-state and S-state optical pumping efficiencies (Sections 8.5 and 2.3.4). Because of this, we use both an achromatic quarter waveplate[77] and an achromatic half waveplate[78] to set the polarizations of the beams before they are sent to the ion. As the name suggests, these waveplates have a much smaller variance in retardance at different wavelengths, such that this retardance is roughly the same at both 493 nm and 650 nm. We do find, however, that the

[76] Thorlabs AC254-200-A
[77] Thorlabs AQWP05M-580
[78] Thorlabs AHWP05M-600

optimal waveplate positions for each beam do vary[79] slightly. Typically, we choose to optimize the achromatic waveplate positions for the 650-nm σ^+-beam, as our Optical Bloch simulations suggest this will have the largest effect on ion-photon entanglement fidelity. Optimization is performed through an iterative processes of adjusting the achromatic waveplates such that the ion florescence is minimized when only the 650-nm σ^+-beam[80] is present as well as when this beam and both π-beams are present.

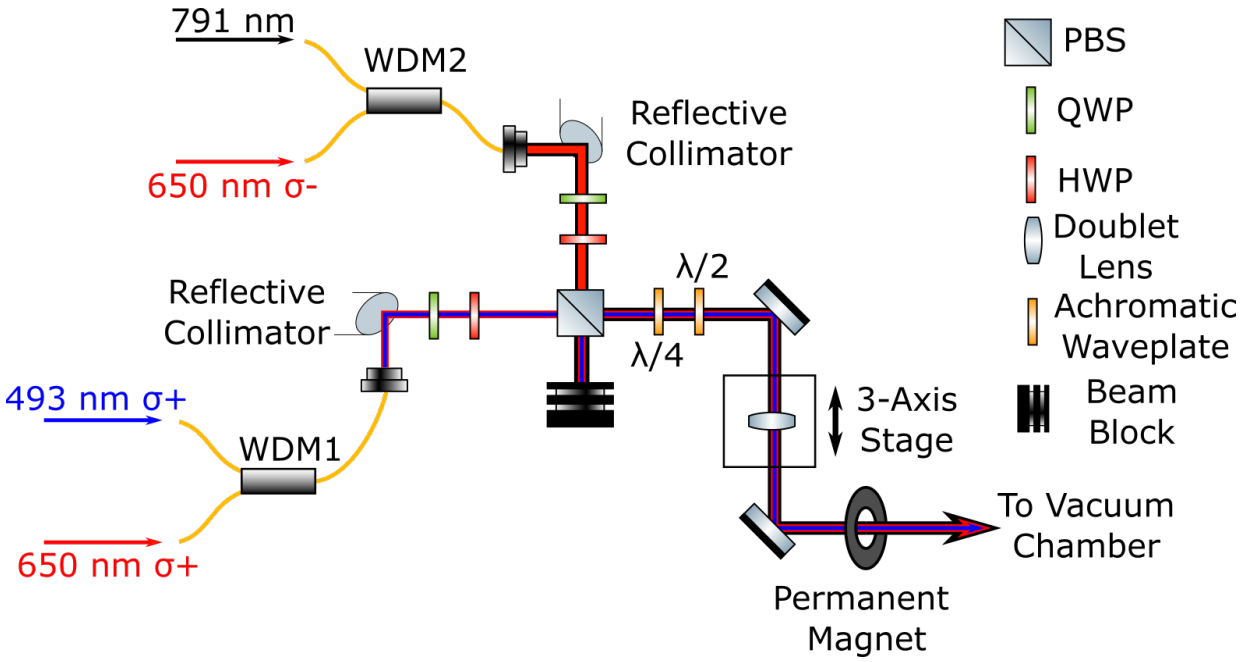

Figure 3.13: **Sigma Beam Delivery.** Two fiber-based wavelength-division multiplexers are used with one combining 493 nm and 650 nm σ^+ light and the other combining 650 nm σ^- and 791 nm ioniziation light. Polarization filtering of all beams is achieved with a polarizing beamsplitter (PBS). Achromatic half and quarter waveplates are used to simultaneously control the polarization of light sent to the ion. As with the π-beam setup, reflective collimators and an achromatic doublet lens are used to focus all beams to roughly the same spot in the vacuum chamber. For magnetic field generation, one of the permanent magnets used is directly mounted to this setup.

The beam path for the 1762 nm and 614 nm beams is much simpler than those shown in

[79] On the order of $\approx 1-2$ degrees between the two 650-nm σ-beams and $\approx 2-3$ degrees between the 493-nm and 650-nm σ^+-beams for the quarter waveplate.

[80] We do check that the ion is relatively dim for the other σ-beam as well to ensure that we have not driven the ion into some other type of dark state.

Figs. 3.12-3.13. The beams are independently collimated from separate fibers and combined on a dichroic mirror[81] before being aligned to the ion trap via walking mirrors and a lens mounted on a 3-axis stage. The lens is coated for 1762 nm, with about $\approx 50\%$ loss at 614 nm. With plenty of power available at 614 nm, this is not a large concern. The estimated focal spot size of the 1762 nm beam is $\approx 120\ \mu$m[82]. As the beams are traveling down the axis of the ion trap with the least amount of optical access, we expect that they are clipping the trap blades, reducing their intensity at the ion by an unknown amount.

3.4.2 Ion Imaging and Flourescence Detection

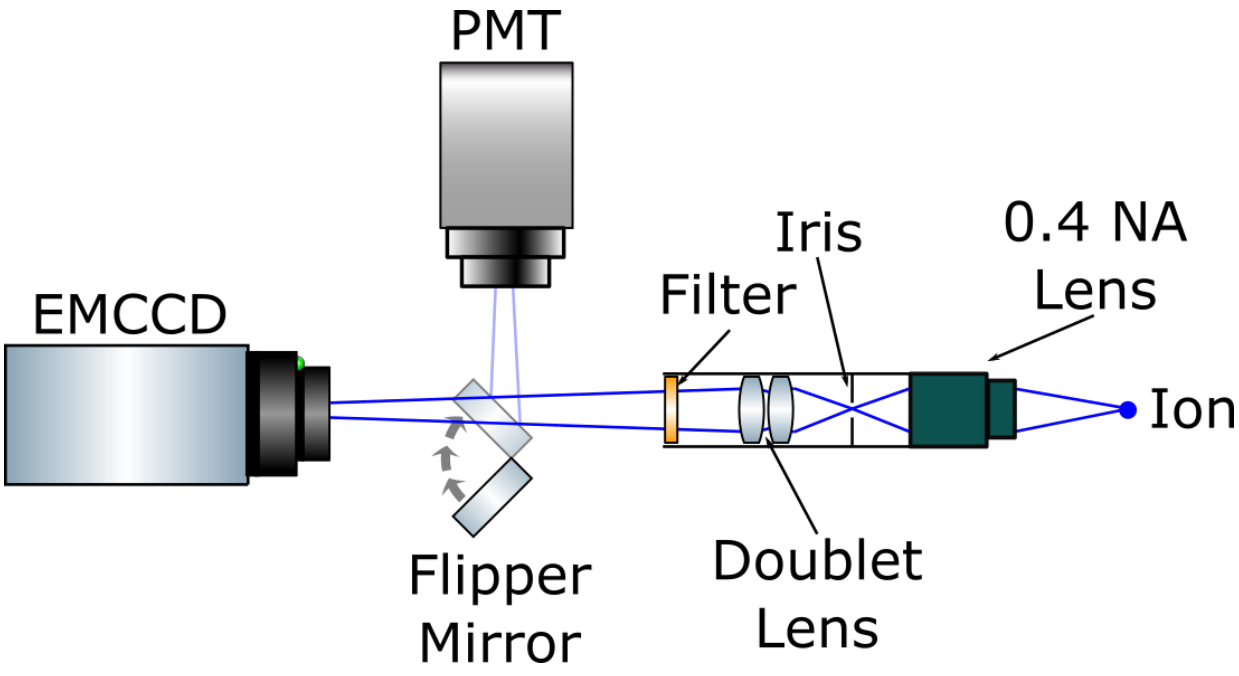

Figure 3.14: **Imaging and Florescence Detection.** A 0.4 NA multi-element objective, doublet lens, iris and optical filter are mounted in a 1" lens tube to collect and focus light collected from the ion. The focused light is sent to an EMCCD camera or to a photomultiplier tube (PMT) via a TTL-controlled flipper mirror. The lens tube is mounted on a three-axis stage to facilitate alignment to the ion.

[81] Thorlabs E02. Technically, this is a mirror for visible light but transmits 1762 nm, thereby acting as a dichroic.
[82] We have not calculated this value at 614 nm, as the beam is likely focused nowhere near the ion.

We perform both ion imaging and florescence measurements by collecting ion light from the imaging and detection window shown in Fig. 3.1. Light from the ion is collected and refocused onto our imaging EMCCD camera[83] using a multi-element 0.4 NA objective lens[84] combined with a doublet lens, all mounted in a single 1" lens tube, as shown in Fig. 3.14. The doublet lens is chosen to give the system a total magnification of ≈ 125 at the camera. This lens tube is mounted on a three-axis stage[85] with digital micrometers[86] to allow for easy alignment of the entire lens tube system to the ion. An iris is used to help remove noise produced via laser scatter, along with a 493 nm bandpass filter [87] to remove any florescence or laser scatter at 650 nm and/or 614 nm. A TTL-controlled flipper mirror optionally directs the light to a photo-multiplier tube[88] (PMT), capable of single photon detection, for ion florescence measurements. An additional iris is sometimes used just before the flipper mirror to reduce laser scatter measured by the PMT. The entire setup is kept in a nearly light-tight box to prevent room light from damaging the EMCCD and PMT and to reduce the background counts as measured on the PMT.

3.4.3 High NA Single Photon Collection

We collect and fiber couple single photons emitted by the ion out of the large 0.6 NA photon collection window shown in Fig. 3.1. Here I will discuss the two fiber coupling setups we have used, with a focus on the current, 0.6 NA collection and fiber coupling setup.

[83] Andor iXon Ultra 897.
[84] Special Optics. Designed by Jiehang Zhang in Christopher Monroe's group.
[85] Newport 406A
[86] Mitutoyo 350-352-30
[87] Semrock FF01-488/10-25
[88] Hamamatsu H11870-01

3.4.3.1 Single Photon Collection Using a 0.6 NA Lens

The setup for mounting and aligning our custom[89] 0.6 NA objective lens[90] is shown in Fig. 3.15. A tip-tilt stage[91] is mounted to a 3-axis stage[92] via a custom-machined L-shaped adapter plate[93] to allow for 5-axis adjustment of the lens position. A v-groove mount[94] is used to mount the (featureless) objective to the tip-tilt stage. This mounting setup is visible in Fig. 3.15 a, before installation of the 0.6 NA objective.

The objective is designed to couple light collected from the ion directly into an optical fiber. Therefore the remainder of the optical setup consists of an AR-coated optical fiber[95] independently mounted on a mirror mount serving as a tip-tilt stage[96] mounted on a 3-axis translation stage[97]. This fiber mount is visible in Fig. 3.15 c. This mirror mount accepts optical cage rods, which are used to easily swap the fiber out with a cage-mounted lens and CCD camera[98] for temporary free-space imaging of the ion during alignment.

Alignment of the 0.6 NA objective-fiber system to the ion is a difficult and tedious process. The alignment procedure we use is based on a combination of discussions with Clayton Crocker [64] as well as information learned from theses produced by the ion trap group at Oxford [63]. After coarsely aligning the objective by placing it approximately a working distance (≈ 16.8 mm) away from the ion centered on the photon collection window, we align the objective and fiber via

[89] Designed for operation at 493 nm, 370 nm, and 650 nm.
[90] Photon Gear 15920-S
[91] Newport PY004
[92] Thorlabs XR25P-K2
[93] Designed by James Siverns.
[94] Newport VB-2
[95] Thorlabs 405AR
[96] Thorlabs KS1T
[97] Thorlabs MBT616D
[98] FLIR BFS-U3-16S2M-CS

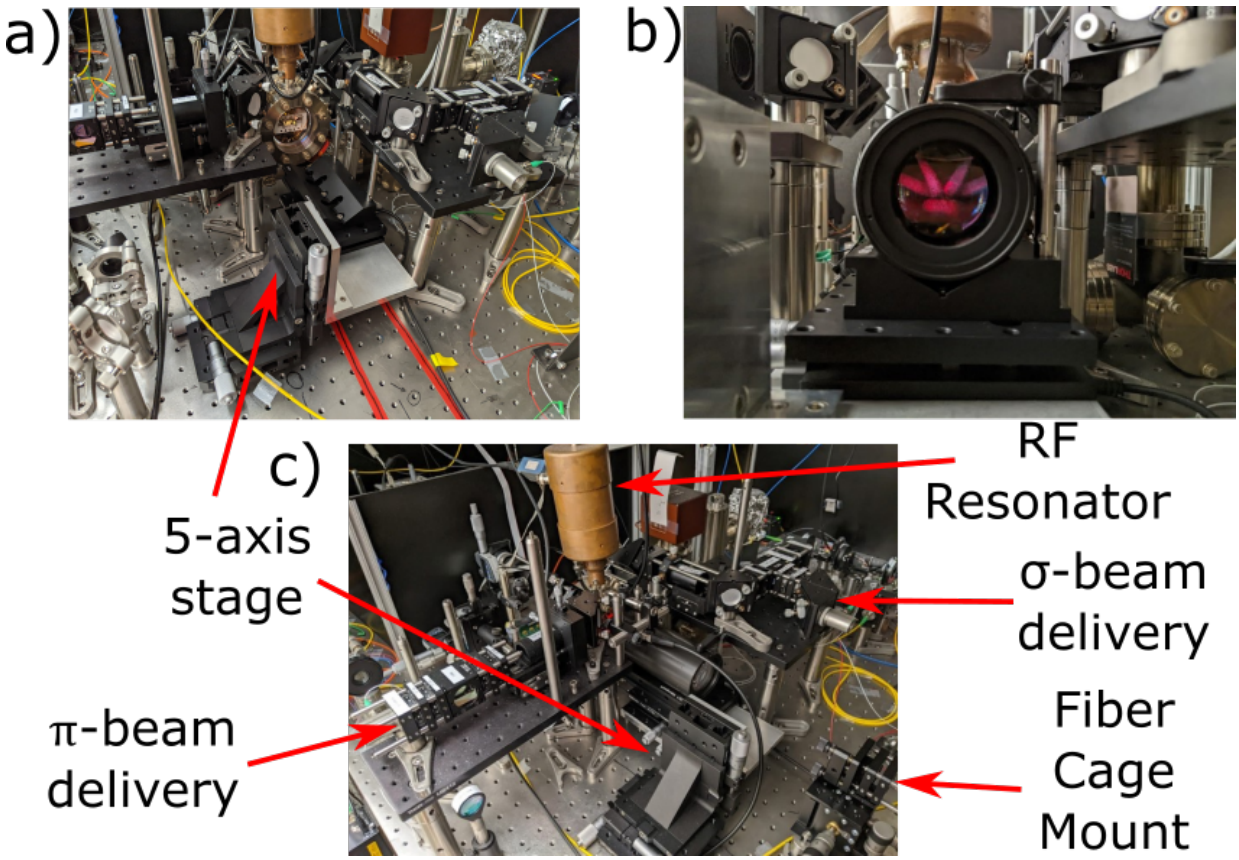

Figure 3.15: **Setup for the 0.6 NA Objective.** a) Picture of the mount and stages used for the 0.6 NA objective. Mounting consists of a V-groove mounted on a tip-tilt stage which is itself mounted to a 3-axis stage via a custom L-bracket. b) Photo of the 0.6 NA lens as mounted on the V-groove in front of the ion trap. Laser light scattered by the trap blades is visible. c) The full optical setup for fiber coupling using the 0.6 NA objective. The tip-tilt and 3-axis mounts used to move the optical fiber are visible in the bottom right of the picture. Also visible are the RF resonator (Sec. 3.2.2) and the π- and σ- beam delivery optical setups of Figs. 3.12 and 3.13.

the procedure outlined in Fig. 3.16. First, the fiber is placed roughly in its correct position behind the objective ($\approx$ 260 mm), and heavily attenuated 493-nm light is run backwards through the fiber and the objective (Fig. 3.16 a). With a good enough initial alignment (or with enough 493-nm light), the fiber image is visible on our ion imaging system EMCCD (discussed in Sec. 3.4.2), usually as a very out-of-focus diffraction pattern. The objective and fiber are then adjusted to produce a fiber image on the EMCCD with a similar size and shape to that of the ion image.

The second step of alignment (Fig. 3.16 b) is focused on viewing and removing optical aberrations due to remaining misalignment of the objective lens. The fiber is swapped out for a cage-mounted lens and CCD camera, as briefly mentioned above, and the lens position is adjusted to produce a magnified image of the ion on the CCD[99]. Checking the image both in and out of focus in a manner similar to [63], the objective lens and fiber mount are then adjusted to remove aberrations in the CCD image. At this point, the alignments we perform in this step are done to eliminate easily visible aberrations as viewed on the CCD, and we do not perform fits or numerical analysis of the ion image to determine the remaining optical aberrations. Such image analysis techniques are discussed in [63, 65], and may be implemented by our lab in the future to improve fiber mode matching further.

In the final step of alignment, the lens and camera are replaced with the original optical fiber. Light is run backwards through the fiber and the fiber image and ion image are overlapped on the EMCCD via alignment of the optical fiber 3-axis stage. The optical fiber is then connected to a single photon detecting avalanche photodiode[100] (APD) as in Fig. 3.16. The ion is Doppler cooled, and the 3-axis fiber stage as well as the focus of the objective[101] are adjusted to optimize

[99] Here, the lens is designed to collimate the light from the objective, verified by physically sliding the CCD camera on the cage mounts and making sure the image size doesn't significantly change.

[100] Perkin Elmer SPCM-AQR-15.

[101] We do not risk further alignment of the objective after compensating for abberations in the previous step.

the amount of ion florescence detected on the APD. At this point, we can produce single photons from the ion as discussed in Sec. 2.3.4 and determine the per-shot photon collection efficiency.

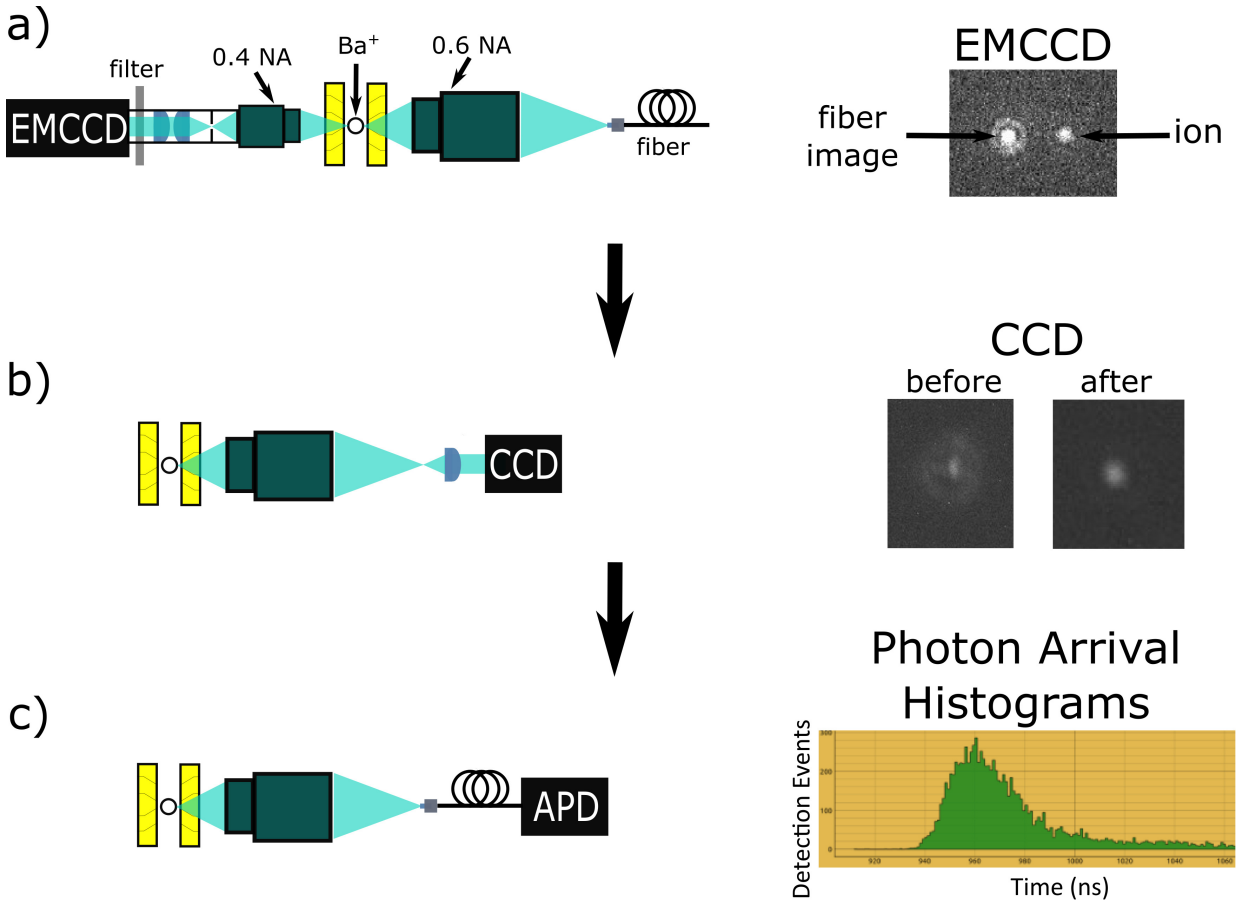

Figure 3.16: **Alignment and Fiber Coupling Procedure for the 0.6 NA Objective.** a) Light is run backwards through the fiber and objective and the resulting fiber image is viewed on the imaging EMCCD. The objective and fiber are adjusted to match the fiber and ion images by eye. b) The fiber is replaced by a lens and CCD camera to directly image the ion through the 0.6 NA objective and adjustments are made to remove easily visible optical aberrations. c) The fiber is replaced and connected to a single photon detecting avalanche photodiode (APD) and the fiber is aligned to the ion to peak up the collected florescence signal before measuring the arrival probability of photon via on-demand photon production measurments.

Using this alignment method, we have measured per-shot single photon detection efficiencies of up to 8.2×10^{-3}, corresponding to $\approx 2.1\%$ total photon collection into fiber when accounting for the specified detection efficiency (40%) of the APD. This is significantly lower than our expected max collection efficiency of $\approx 4\%$, taking into account the mode mismatch between

the light emitted by the ion and a fiber mode (0.8 overlap [30]), the branching ratio of the ion (0.75), optical transmission (0.95) and mode mismatch due to the design of the 0.6 NA lens (0.7 overlap). This is likely due to remaining optical aberrations which could possibly be removed through numerical analysis of the ion image [63, 65] as briefly mentioned above.

An issue with this current setup is the need for a graduate student to physically align the fiber to the ion, given observed drifts in the ion-fiber coupling throughout the day, and on longer timescales. Because of this drift, and the need to maintain other laboratory components rather than constantly align the fiber, we typically run at lower photon collection efficiencies ($5 - 7 \times 10^{-3}$ per-shot) when running experiments. This can in theory be improved through installation of piezo-drivers for the 3-axis fiber stage and on the focus of the 0.6 NA lens, as is done in [63], combined with automated experimental feedback to the fiber and lens positions based on ion florescence detection.

3.4.3.2 Single Photon Collection Using a 0.4 NA Lens

Before installation of the 0.6 NA objective lens discussed above, we instead used a 0.4 NA objective (the same type discussed in Sec. 3.4.2) for fiber coupling. This objective was not designed for efficient fiber coupling, but we intended to temporarily use it for the initial experiments performed prior to the installation of the 0.6 NA lens. As shown in Fig. 3.17 a, this objective was mounted in a lens tube containing an iris, doublet lens[102], optical filter[103] and triplet collimator[104]. Light collected by the 0.4 NA objective was focused and re-collimated using the adjustable doublet lens, before being fiber coupled via the triplet fiber collimator. The entire lens

[102] Focal length $\approx$ 43 mm
[103] Semrock FF01-488/10-25
[104] MicroLasers FC5-VIS1- APC

tube was mounted on a tip-tilt stage [105], itself mounted on a 3-axis translation stage[106].

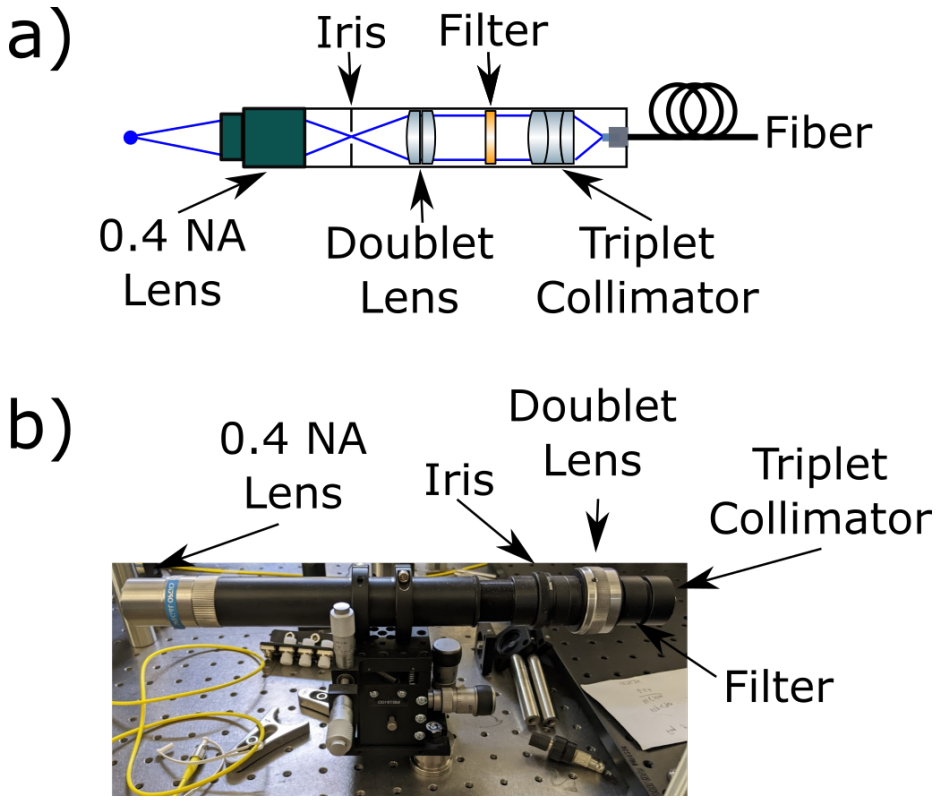

Figure 3.17: **Setup for fiber coupling photons using the 0.4 NA Objective.** The 0.4 NA objective and fiber coupling optics are mounted in a 1" lens tube. A doublet lens collimates light collected and focused by the objective. A triplet fiber collimator is then used to focus the light into a single mode fiber. An iris and optical filter are used to reduce the amount of background light coupled into the optical fiber. The entire setup is mounted on a tip-tilt stage itself mounted on a three-axis translation stage.

Alignment of the objective and fiber to the ion was performed in a similar manner to the 0.6 NA lens (Fig. 3.16), except that a CCD camera was not used to attempt to remove optical aberrations. Instead aberrations as viewed on the EMCCD when running light backwards through the fiber were removed (not attempting to decouple from possible aberrations present in the imaging system itself) before peaking up ion florescence on an APD. With this setup we were able to produce photons on-demand with a detection efficiency of $\approx 1.2 \times 10^{-3}$. Though far from

[105]Thorlabs APY002
[106]Thorlabs MBT610D

an optimal setup and not intended to be permanent, this setup, being easier to align and more inherently stable than the 0.6 NA objective alignment, was used for the majority of the works presented in this thesis. It was replaced by the 0.6 NA objective for the entanglement experiment discussed in Chapter 10.

3.5 Experimental Control and Data Collection

We use various control and data collection equipment and software to perform the experiments presented in this thesis. I summarize some of the key components in this section.

3.5.1 Control Systems

Critical to any atomic physics experiment is a control system to provide fast TTL pulses for triggering and switching on other experimental components as well as to provide fine frequency control for devices such as AOMs (see Sec. 3.3) and antennas to directly address qubit states (Chapter 9). In some cases[107], the control system must also perform logic and live decision branching based on measurements made during the experiment. Finally, all of this control must be performed with sufficient time and frequency synchronization in order to obtain the correct experimental results.

Our lab uses FPGA-based control systems, where an FPGA is programmed to control components such as direct digital synthesizers (DDSs) as well as digital (TTL) and analog voltage inputs and outputs and in some cases also perform data collection tasks such as time-tagging. Our current FPGA control system is based on ARTIQ[108]. Our ARTIQ control system consists of

[107] Particularly for the ion-photon entanglement experiment discussed in this thesis.
[108] M-labs. https://m-labs.hk/experiment-control/artiq/.

a set of rack-mounted and connected devices based on the Sinara hardware family[109]. A master FPGA is used to control multiple connected DDS boards, providing us RF signals from up to 8 programmable DDSs[110] on a shared clock, as well as up to 24 programmable TTL input/output channels. More channels can be relatively easily be added later as they become necessary[111]. This control system enables experimental timing down to the nanosecond level and is somewhat user friendly, being programmable via a python-like coding language.

For applications where complex experimental logic is not required, but we have a need for fast and repetitive laser pulse sequences, we sometimes use a SpinCore PulseBlasterUSB TTL pulse generator. It provides up to 24 TTL output channels which can all be programmed to output pulse sequences with 10 ns resolution. It is easily programmable and can be triggered by an external TTL pulse, otherwise holding in a set user state (We usually set it to cool the ion, for instance.). It does not provide any ability to perform live digital-logic-based control however, and because of this we have begun to completely replace it with ARTIQ-based solutions.

3.5.2 RF and AOM Switching

The most common action performed by the control systems discussed above is to quickly switch on and off laser pulses via switching of the RF to the lasers' respective AOMs. Though this can in theory be done using the FPGA control system's internal DDS RF switches, we (and just about everyone we've talked to) find it faster (in terms of latency) to instead leave the RF output of each of our DDSs constantly on, with each connected to its own external TTL-enabled

[109] https://m-labs.hk/experiment-control/sinara-core/

[110] Analog Devices: AD9910

[111] We are nearly using all of these channels as of the ion-photon entanglement experiment discussed later in this thesis.

RF switch[112]. The RF control is then limited by the speed and accuracy of the TTL pulses sent by the control system, which can be sent with nanosecond-level precision, combined with the RF switch turn on speed (≈ 5 ns).

3.5.3 Time Tagging

For all of the single photon experiments discussed in this thesis, precise and accurate timing of photon arrival times is critical. This is performed either through "start-stop" measurements, where the time between photon detection events on two different detectors is recorded, or through "time-tagging" of photon detection events, where timestamps corresponding to the arrival of incoming TTL pulses from our single photon detectors are recorded for each channel independently and then processed through software written in-house. For either method we typically require nanosecond (sub-nanosecond in some cases) precision.

For many of our experiments, we use a PicoHarp 300 single photon counting system for processing photon arrival events. This system has two input channels is able to perform both start-stop and time-tagging measurements with as low as 4 ps resolution. The start-stop type measurements are recorded and processed via software provided with the PicoHarp, whereas we processes time-tagging data using our own python-based software[113].

When performing an experiment which needs to use the photon arrival data live for logic purposes, we use our ARTIQ control system to perform photon time tagging. Using ARTIQ, we can time tag the arrival time of photons with a precision of 1 ns, and use these time tags to control the frequency output and timing of other experimental components in a phase coherent

[112] Reverse engineered Minicircuits ZASWA-2-50-DR+.
[113] https://github.com/ionquantumnetworks

manner. This is particularly important for the ion-photon entanglement experiment presented in Chapter 10.

Chapter 4: Quantum Frequency Conversion Setups

4.1 Introduction

Together with the ion-trap and laser systems described in Chapter 3, the quantum frequency conversion setups developed in our lab are a key component in every experiment discussed in this thesis. This chapter focuses on the design and implementation of these setups, and on using such setups to perform and characterize the frequency conversion of single photons collected from a trapped Ba^+ ion.

I begin with an overview on the theory enabling quantum frequency conversion, focusing in particular on difference frequency generation (DFG). This discussion is classical in nature, but is also extended to a quantum mechanical picture, which is the more accurate description when working with single photons. Additionally, I briefly discuss the potential sources of noise (many of which themselves are a result of nonlinear optical processes) that can be problematic when dealing with single photon levels of light.

Following this theory discussion, I then describe the frequency conversion schemes and setups we use to convert our single photons to both neutral-atom-compatible wavelengths in the near infrared and to telecommunication wavelengths. Here, I go through the many iterations of our conversion setups, discussing our design decisions, the improvements made between each iteration, and what improvements can still be made. For each type of setup, typical conversion

efficiencies and noise levels are also discussed. For the current entanglement preserving setup being used by our lab for the ion-photon entanglement experiment discussed in Chapter 10, I also spend some time discussing the procedure developed for alignment.

4.2 Frequency Conversion: Basic Theory

4.2.1 Classical Picture

Here, I derive a basic form for the classical coupled wave equations in a nonlinear medium. This will then lead us to the equation our lab uses to fit for the single photon conversion efficiency of our QFC devices as a function of of input pump laser power. This closely follows other common derivations such as in [128, 129].

We begin with Maxwell's equations

$$\nabla \times \mathbf{E}(\mathbf{r}, t) = -\frac{\delta \mathbf{B}(\mathbf{r}, \mathbf{t})}{\delta t} = -\mu_0 \frac{\delta \mathbf{H}(\mathbf{r}, \mathbf{t})}{\delta t}, \tag{4.1}$$

$$\nabla \times \mathbf{H}(\mathbf{r}, \mathbf{t}) = \mathbf{J}(\mathbf{r}, \mathbf{t}) + \frac{\delta \mathbf{D}(\mathbf{r}, \mathbf{t})}{\delta t} = \frac{\delta \mathbf{D}(\mathbf{r}, \mathbf{t})}{\delta t}, \tag{4.2}$$

$$\nabla \cdot \mathbf{D}(\mathbf{r}, \mathbf{t}) = \rho, \tag{4.3}$$

$$\nabla \cdot \mathbf{B}(\mathbf{r}, \mathbf{t}) = 0, \tag{4.4}$$

where the electric and magnetic fields are given by $\mathbf{E}(\mathbf{r}, t)$ and $\mathbf{H}(\mathbf{r}, t)$, the electric displacement and magnetic flux density are given by $\mathbf{D}(\mathbf{r}, t)$ and $\mathbf{B}(\mathbf{r}, t)$, and the free charge density and free current are given by ρ and $\mathbf{J}(\mathbf{r}, t)$. We will assume we are working with a source free region,

which gives $\rho = 0$, $\mathbf{J}(\mathbf{r}, t) = 0$ and,

$$\mathbf{B} = \mu_0 \mathbf{H}, \tag{4.5}$$

(i.e. there is no magnetization of the material) resulting in the final equality in Eqs. 4.1 and 4.2.

The displacement vector can be written in terms of the electric field as well as an induced polarization, $\mathbf{P}(\mathbf{r}, t)$, the latter of which is itself dependent on electric field. Critically, in a nonlinear material, this dependence has a component, $\mathbf{P}^{\text{NL}}(\mathbf{r}, t)$, that is nonlinear in the electric field present such that,

$$\mathbf{P}(\mathbf{r}, t) = \mathbf{P}^{\text{L}}(\mathbf{r}, t) + \mathbf{P}^{\text{NL}}(\mathbf{r}, t), \tag{4.6}$$

and we can write

$$\mathbf{D}(\mathbf{r}, t) = \epsilon_0 \boldsymbol{\epsilon} \mathbf{E}(\mathbf{r}, t) + \mathbf{P}^{\text{NL}}(\mathbf{r}, t), \tag{4.7}$$

where we've made the substitution $\boldsymbol{\epsilon} \equiv 1 + \boldsymbol{\chi}^{(1)}$, where $\boldsymbol{\chi}^{(1)}$ is the linear susceptibility[1]. This nonlinear dependence of the polarization to the electric field is what allows for the nonlinear mixing between waves at different frequencies in the medium.

To obtain a wave equation for the fields in our nonlinear medium, we take the curl of Eq. 4.1, and substitute in Eqs. 4.2 and 4.7 to obtain[2]

$$\nabla^2 \mathbf{E}(\mathbf{r}, t) - \frac{\boldsymbol{\epsilon}}{c^2} \frac{\delta^2 \mathbf{E}(\mathbf{r}, t)}{\delta t^2} = \frac{1}{\epsilon_0 c^2} \frac{\delta^2 \mathbf{P}^{\text{NL}}(\mathbf{r}, t)}{\delta t^2}, \tag{4.8}$$

which is an inhomogenous wave equation for $\mathbf{E}(\mathbf{r}, t)$, with $\mathbf{P}^{\text{NL}}(\mathbf{r}, t)$ serving as a driving term.

[1] In an isotropic medium or in one dimension, $\boldsymbol{\epsilon}$ is a scalar, and known as the relative permittivity.
[2] Assuming $\nabla(\nabla \cdot \mathbf{E}) = 0$

This is known as the nonlinear wave equation in nonlinear optics [129]. Writing each field as sums of fields of varying amplitudes and frequencies, we can obtain a similar equation for each frequency component:

$$\nabla^2 \mathbf{E}_n(\mathbf{r},t) - \frac{\boldsymbol{\epsilon}}{c^2}\frac{\delta^2 \mathbf{E}_n(\mathbf{r},t)}{\delta t^2} = \frac{1}{\epsilon_0 c^2}\frac{\delta^2 \mathbf{P}_n^{\mathrm{NL}}(\mathbf{r},t)}{\delta t^2}, \tag{4.9}$$

where

$$\mathbf{E}_n(\mathbf{r},t) = \sum_n \mathbf{E}_n(\mathbf{r}) e^{-i\omega_n t} + c.c., \tag{4.10}$$

and

$$\mathbf{P}_n^{\mathrm{NL}}(\mathbf{r},t) = \sum_n \mathbf{P}_n^{\mathrm{NL}}(\mathbf{r}) e^{-i\omega_n t} + c.c.. \tag{4.11}$$

Here we've made an implicit distinction between the electric field amplitude $\mathbf{E}_n(\mathbf{r})$ and the total time dependent electric field, $\mathbf{E}_n(\mathbf{r},t)$, with a similar distinction being made for the induced polarization.

From this point forward we will consider our fields to be plane waves propagating through a nonlinear medium in the z-direction, as shown in Fig. 4.1 a. This is still a reasonable assumption

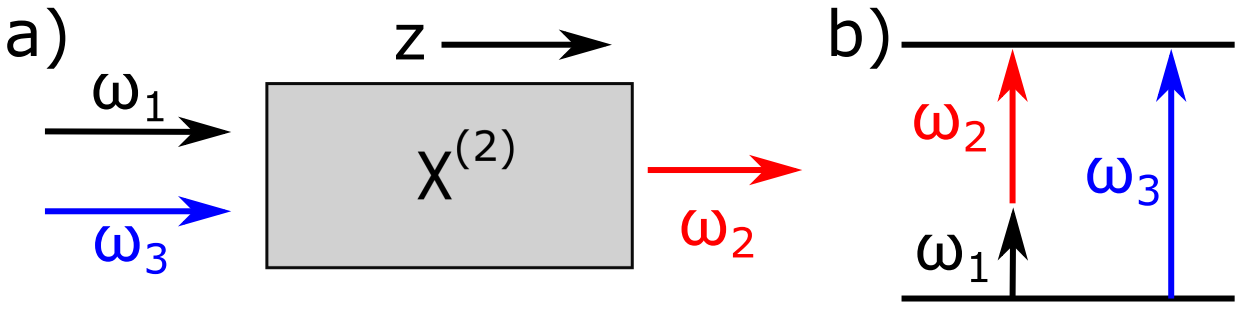

Figure 4.1: **Schematic for difference frequency generation.** a) Input waves at ω_1 and ω_3 are coupled into and travel in the z-direction of a nonlinear $\chi^{(2)}$ material, creating a wave at frequency ω_2. b) The required energy conservation relation for the process discussed in the text. Here, $\omega_3 = \omega_2 + \omega_1$

for our real world frequency conversion devices, which use waveguides to guide the input fields along one direction of the crystal. Therefore we write

$$E_i(z,t) = A_i(z)e^{i(k_i z - \omega_i t)} + c.c., \tag{4.12}$$

where $A_i(z)$ is a slowly varying envelope and $k_i = n_i\omega_i/c$, with $n_i = \sqrt{\epsilon(\omega_i)}$ being the refractive index of the material at frequency ω_i. Our focus here will be on the nonlinear process used in our lab, difference frequency generation (DFG) via the mixing of three waves at frequencies ω_1, ω_2, and $\omega_3 = \omega_1 + \omega_2$. In this case we write the scalar magnitudes of the nonlinear polarizations as

$$P_1^{\text{NL}}(z) = 2\epsilon_0 d_{eff}^* E_2^*(z)E_3(z), \tag{4.13}$$

$$P_2^{\text{NL}}(z) = 2\epsilon_0 d_{eff}^* E_1^*(z)E_3(z), \tag{4.14}$$

$$P_3^{\text{NL}}(z) = 2\epsilon_0 d_{eff} E_1(z)E_2(z), \tag{4.15}$$

where d_{eff} is the effective nonlinear coefficient, assumed to be real, and is defined as half of the second order nonlinear susceptibility, $\chi^{(2)}$. This coefficient is dependent on a combination of physical factors, including the nonlinear medium, waveguide structure, and polarization of the input light relative to the crystal structure of the medium.

Combining Eqs. 4.9-4.15, and assuming the amplitudes A_i are slowly varying [129], we can obtain coupled equations for the electric field amplitudes, $A_i(z)$, at each position z in the material

$$\frac{dA_1}{dz} = \frac{i\omega_1^2 d_{eff}}{c^2} A_2^* A_3 e^{-i\Delta kz}, \tag{4.16}$$

$$\frac{dA_2}{dz} = \frac{i\omega_2^2 d_{eff}}{c^2} A_1^* A_3 e^{-i\Delta kz}, \tag{4.17}$$

$$\frac{dA_3}{dz} = \frac{i\omega_3^2 d_{eff}}{c^2} A_1 A_2 e^{i\Delta kz}, \tag{4.18}$$

where $\Delta k = k_1 + k_2 - k_3$ is known as the phase mismatch. In this thesis we are typically more interested in photon flux rather than the intensity of the converted field so it is useful to make the substitution

$$u_i(z) \equiv \left(\frac{n_i \epsilon_0 c}{2\hbar\omega_i}\right)^{1/2} A_i, \tag{4.19}$$

such that $|u_i|^2 = I_i(z)/\hbar\omega_i$ is the photon flux at frequency ω_i. One can solve the coupled equations, Eqs. 4.16-4.18, after making this substitution. Assuming a strong, undepleted, pump field at frequency ω_1 (i.e. $|u_1(z)|^2 = |u_1(0)|$) and no initial field at frequency ω_2 (i.e. $|u_2(0)|^2 = 0$), the photon fluxes relative to the initial photon flux at frequency ω_3, $|u_3(0)|^2$, are given by

$$\frac{|u_2(z)|^2}{|u_3(0)|^2} = \frac{|\gamma|^2}{\Delta k^2/4 + |\gamma|^2} \sin\left(\sqrt{\Delta k^2/4 + |\gamma|^2}\, z\right)^2 \equiv \eta, \tag{4.20}$$

$$\frac{|u_3(z)|^2}{|u_3(0)|^2} = \cos\left(\sqrt{\Delta k^2/4 + |\gamma|^2}\, z\right)^2 + \frac{\Delta k^2}{\Delta k^2 + 4|\gamma|^2} \sin\left(\sqrt{\Delta k^2/4 + |\gamma|^2}\, z\right)^2, \tag{4.21}$$

where

$$|\gamma|^2 = \frac{2|d_{eff}|^2\omega_2\omega_3}{n_1 n_2 n_3 \epsilon_0 c^3} I \tag{4.22}$$

with I being the intensity of the pump field at frequency ω_1. Here Eqn. 4.20 is the photon frequency conversion efficiency, denoted by η.

From these equations we see that photon flux at ω_3 is depleted as photons are converted to frequency ω_2, until $\sqrt{\Delta k^2/4 + |\gamma|^2}\, z = \pi/2$, after which back-conversion to frequency ω_3 occurs[3]. We also see that the single photon frequency conversion efficiency, η (Eqn. 4.20), is limited by the degree of phase matching in the system, given by Δk. Thankfully, the companies and collaborators we work with to obtain our frequency conversion devices use techniques such as quasi-phase-matching [128–131] to ensure that, with temperature control of our nonlinear medium[4], we can approximate $\Delta k \approx 0$[5] such that Eqn. 4.20 becomes

$$\eta = \sin\left(\frac{\pi}{2}\sqrt{\frac{I}{I_{max}}}\right)^2, \tag{4.23}$$

where we've assumed a constant length of the nonlinear material and made the substitution

$$I_{max} = \frac{\pi^2}{4z^2}\frac{n_1 n_2 n_3 \epsilon_0 c^3}{2|d_{eff}|^2\omega_2\omega_3}, \tag{4.24}$$

with I representing the input pump intensity.

In the lab, we typically work with pump powers rather than intensities and our interacting fields are represented by waveguide modes rather than true plane waves. This allows for the same form of Eqn. 4.23, except that I_{max} includes additional terms to account for the spatial overlap of

[3]This is through the inverse process of difference frequency generation, known as sum frequency generation.
[4]This allows us to have some control over n_i, leading to a change in k_i
[5]This also causes an effective change in the nonlinear coefficient but we can just roll that change into d_{eff}.

the modes, ω_i (see [128] for details). For this reason, when determining the conversion efficiency of real devices, we use

$$\eta = \eta_{max} \sin\left(\frac{\pi}{2}\sqrt{\frac{P}{P_{max}}}\right)^2, \tag{4.25}$$

where η_{max} is the total measured conversion efficiency of the device, including inefficiencies due to mode mismatch, and P and P_{max} represent powers rather than intensities. This allows us to simply fit our conversion results to Eqn. 4.25 using both η_{max} and P_{max} as free fitting parameters.

4.2.2 Quantum Frequency Conversion

The above derivation is purely classical, but it turns out the resulting form of Eqn. 4.23 holds when a quantum mechanical treatment is given. The full quantum mechanical derivation is cumbersome and beyond the scope of this thesis, but I will now try and give the reader a flavor of how the frequency conversion process works quantum mechanically. Much of what is presented in the remainder of this section closely follows [132].

One can write the effective Hamiltonian for three wave mixing in a lossless nonlinear medium as [128, 132]

$$H = i\hbar\chi\left(\hat{a}_1\hat{a}_2\hat{a}_3^\dagger - c.c.\right), \tag{4.26}$$

where $\hat{a}_i$ is the annihilation ladder operator for photons at frequency ω_i and where χ is a nonlinear coupling proportional to the classical $\chi^{(2)}$. The $\hat{a}_i$ serve similar roles to the A_i or u_i used in the classical discussion above. Again we will treat ω_1 as our pump field, with $\omega_3 = \omega_1 + \omega_2$ and consider light traveling down the z-axis of our nonlinear medium. We will also assume perfect

phase-matching.

Applying the non-depleted pump approximation in this case is equivalent to setting $\hat{a}_1 = \langle \hat{a}_1 \rangle$ such that the Hamiltonian becomes

$$H = i\hbar\chi \langle \hat{a}_1 \rangle \left(\hat{a}_2 \hat{a}_3^\dagger - c.c. \right) = i\hbar\Gamma \left(\hat{a}_2 \hat{a}_3^\dagger - c.c. \right), \tag{4.27}$$

where we've substituted $\Gamma = \chi \langle \hat{a}_1 \rangle$. Working in the Heisenberg picture, and using the standard ladder commutation relation $\left[\hat{a}_j, \hat{a}_j^\dagger \right] = \delta_{jk}$, one arrives at a set of coupled first order differential equations for the operators $\hat{a}_2$ and $\hat{a}_3$

$$\frac{d\hat{a}_2}{dz} = -\Gamma \hat{a}_3, \tag{4.28}$$

$$\frac{d\hat{a}_3}{dz} = \Gamma \hat{a}_2, \tag{4.29}$$

which have a general solution

$$\hat{a}_2(z) = \hat{a}_2(0)\cos(\Gamma z) - \hat{a}_3(0)\sin(\Gamma z), \tag{4.30}$$

$$\hat{a}_3(z) = \hat{a}_3(0)\cos(\Gamma z) + \hat{a}_2(0)\sin(\Gamma z). \tag{4.31}$$

It is at this point we can calculate the conversion efficiency of the medium of length z, for a given input pump intensity. Assuming an input state consisting of n photons of frequency ω_3 and no photons at frequency ω_2, our input state at z=0 is given by $\psi = |n_2 = 0\rangle_2 |n_3 = n\rangle_3$. The conversion efficiency, η, at position z is then given by the ratio of the number of photons at

frequency ω_2 to the original number of photons at frequency ω_3. One finds, using Eqns. 4.30 and 4.31,

$$\eta = \frac{\langle\psi|\hat{a}_2^\dagger(z)\hat{a}_2(z)|\psi\rangle}{\langle\psi|\hat{a}_3^\dagger(0)\hat{a}_3(0)|\psi\rangle} = \sin\left(\Gamma z\right)^2 = \sin\left(\chi\left\langle\hat{a}_1\right\rangle z\right)^2. \tag{4.32}$$

This result has the same form as 4.23, and the same dependence on both z and pump intensity, with $\langle\hat{a}_1\rangle \propto \sqrt{I_i}$.

Lastly, as first shown by [132], the quantum properties of the photon(s) are preserved before and after conversion. The quantum properties of the two frequency modes can be determined by some functions $\hat{f}_2(\hat{a}_2)$ and $\hat{f}_3(\hat{a}_3)$ with initial expectation values

$$\left\langle\hat{f}_2\right\rangle_{z=0} = \langle n_2|\hat{f}_2(\hat{a}_2(0))|n_2\rangle\,, \tag{4.33}$$

$$\left\langle\hat{f}_3\right\rangle_{z=0} = \langle n_3|\hat{f}_3(\hat{a}_3(0))|n_3\rangle\,, \tag{4.34}$$

and final expectation values after complete conversion of

$$\left\langle\hat{f}_2\right\rangle_{z=\pi/2\Gamma} = \langle n_2|\hat{f}_2(\hat{a}_2(\pi/2\Gamma))|n_2\rangle = \langle n_2|\hat{f}_2(-\hat{a}_3(0)))|n_2\rangle\,, \tag{4.35}$$

$$\left\langle\hat{f}_3\right\rangle_{z=\pi/2\Gamma} = \langle n_3|\hat{f}_3(\hat{a}_3(\pi/2\Gamma))|n_3\rangle = \langle n_2|\hat{f}_3(\hat{a}_2(0)))|n_2\rangle\,. \tag{4.36}$$

This means that at z=0, the quantum properties of the modes at ω_2 and ω_3 are determined by their respective initial input photon states, $|n_2\rangle$ and $|n_3\rangle$. After conversion, however this is switched,

and the quantum properties of the modes at ω_2 and ω_3 are determined by $|n_3\rangle$ and $|n_2\rangle$, meaning that the quantum properties of the modes (aside from their frequency) have swapped. We test this experimentally for the case of single-photon quantum statistics in Chapter 5. This result is also critical to preserving ion-photon entanglement before and after frequency conversion, which we show experimentally in Chapter 10.

4.2.3 Noise Processes

As we are primarily interested in the conversion of single photons, we must be wary of any potential noise photons produced in the quantum frequency conversion process. Aside from filtering out the high intensity pump itself, the dominant noise processes we are concerned with are shown in Fig. 4.2. These processes have been studied in detail elsewhere [128, 133, 134], but I will give a basic explanation here and describe what implications this has on choosing what pump frequencies we will work with.

The first process, spontaneous parametric down conversion (SPDC), is depicted in Fig. 4.2 a. This is a process in which a pump photon at frequency ω_p, through interaction with a nonlinear $\chi^{(2)}$ material, splits into two photons at frequencies ω_1 and ω_2, with $\omega_p = \omega_1 + \omega_2$ by energy conservation. As with any $\chi^{(2)}$ effect, this process does require some degree of phasematching. This phasematching, although weak, has been shown [128] to occur in many QFC devices partially due to errors in the processes used to achieve the quasi-phase-matching needed for efficient QFC. These effects lead to a "pedestal" of noise photons at frequencies lower than that of the pump laser. Due to the relatively high pump powers, ≈ 100 mW or $\approx 6 \times 10^{18}$ photons/s, needed to achieve complete conversion in our devices, this is a significant noise source even if

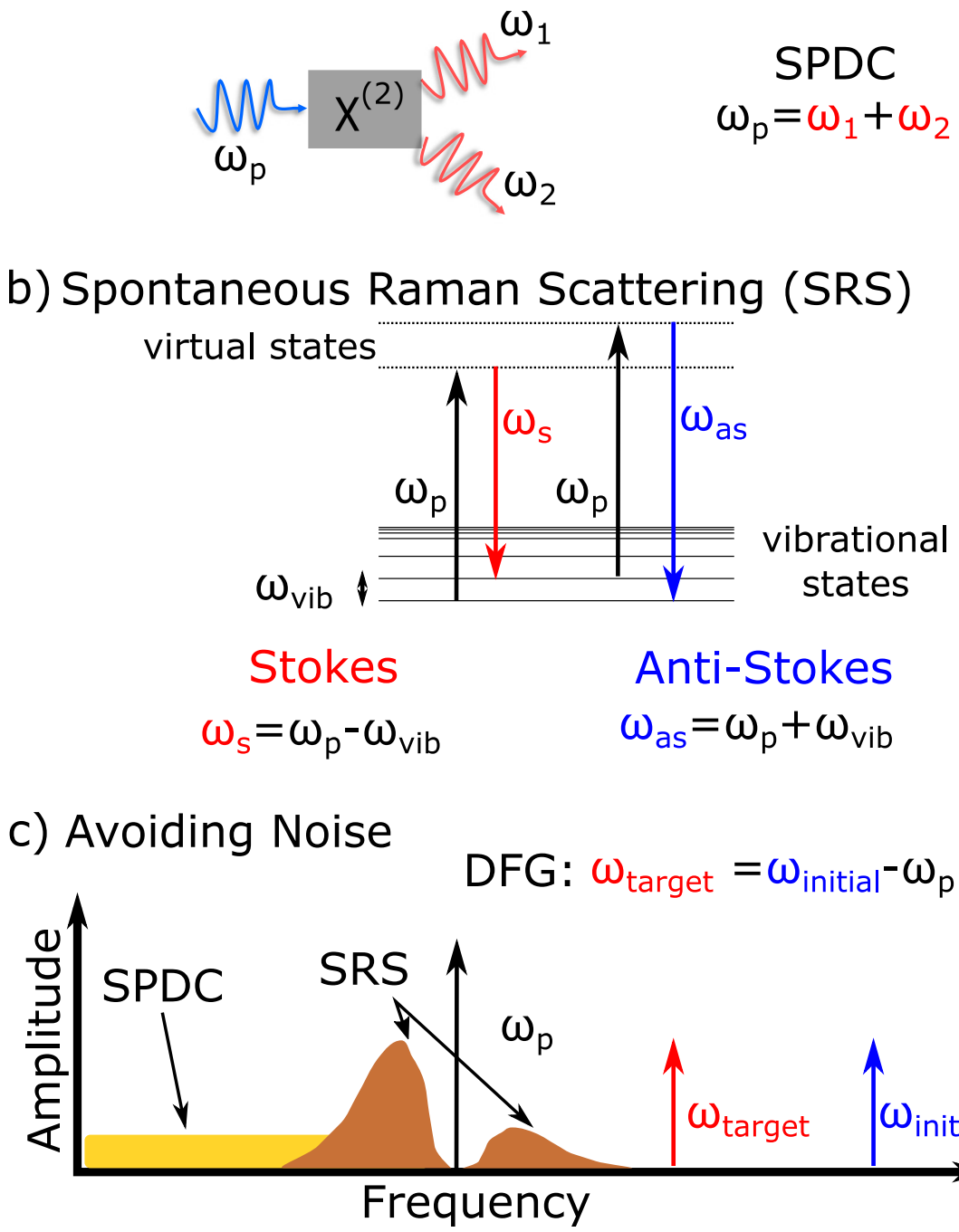

Figure 4.2: **Important Noise Processes in Quantum Frequency Conversion Devices.** a) In spontaneous down conversion (SPDC) a pump photon in a $\chi^{(2)}$ medium splits into two lower frequency photons governed by energy conservation. b) Spontaneous Raman scattering (SRS), where a pump photon is scattered and gains or loses energy via destruction or creation of a phonon of frequency ω_{vib} in the material. c) The ideal arrangement of frequencies chosen to avoid noise in a difference frequency generation (DFG) process, adapted from [128].

one were to consider extremely low SPDC conversion efficiency. Therefore, when choosing a QFC scheme, one should aim to make the pump the lowest frequency (longest wavelength) used in the process, such that SPDC noise can be avoided.

The second process shown in Fig. 4.2 b, is spontaneous Raman scattering (SRS). In SRS, photons from the pump laser can inelastically scatter in the nonlinear material, either losing energy (decreasing frequency) and exciting a phonon in the material, or the photon can gain energy (increase frequency) through the destruction of a phonon. These processes are referred to as Stokes and anti-Stokes Raman scattering, respectively. This process, particularly the magnitude of scattered signal, has been closely studied for our nonlinear medium of choice, lithium niobate (LiNbO3) [128, 135, 136]. The main effect is that two noise peaks are produced near to and centered around the pump frequency, with the lower frequency noise (Stokes) being larger in magnitude[6]. Far away from the pump frequency these noise peaks are greatly reduced. Therefore it is beneficial to choose a pump frequency such that the converted photon is distant from the pump in frequency.

In summary, to avoid noise in the difference frequency generation based QFC discussed in this thesis, one should choose a pump frequency (assuming that the initial photon frequency is fixed by our ion photon source) such that the following two conditions are met (Fig. 4.2 c):

1. The pump wavelength is the longest wavelength (lowest frequency) field involved in the process.

2. The converted photon wavelength is sufficiently far from the pump wavelength.

[6]In theory, one can reduce the anti-Stokes noise to near-zero by lowering the temperature of the crystal, thereby reducing the phonons present in the material. This would require phase-matching for the QFC process to also occur at this temperature.

With the first condition meant to avoid noise photons produced via spontaneous parametric down conversion and the second condition meant to avoid noise from Raman scattering and from the pump laser itself[7]. The latter condition is one we push the limit of when it comes to conversion to the telecommunications C-band discussed in Chapter 5.

4.3 Difference Frequency Generation Schemes and Setups

To take the 493-nm photons produced by Ba^+ to telecommunication wavelengths, whilst avoiding excessive noise photons produced via spontaneous parametric downconversion, requires at least two frequency conversion stages to ensure that the pump light is the longest wavelength light in both DFG processes (Sec. 4.2.3) [8]. Choosing Ba^+ as our qubit however, allows us to avoid a requirement for even more frequency conversion steps, as would be required for ions which emit UV photons, such Yb^+, which emits at 369-nm. Thus, with an eye on eventually taking 493-nm photons to one of the telecommunication bands, our lab has considered the frequency conversion scheme shown in Fig. 4.3. This consists of two separate stages of DFG: the first converting 493-nm photons to 780-nm photons via a 1343-nm pump and the second taking the resulting 780-nm photons to 1534 nm (telecommunications C-band) by using a pump laser at 1590 nm. The nonlinear medium allowing for DFG in each stage is a waveguide written into a periodically-poled lithium niobate (PPLN) crystal.

A key benefit of this particular scheme is that, with careful control of the pump laser wavelength, the first stage allows us to produce photons resonant with neutral Rubidium atoms. Additionally, fiber transmission losses of 780-nm light are greatly reduced when compared to

[7] This includes noise at the intended pump frequency ω_p as well as common noise sources near ω_p resulting from amplification, and from amplified spontaneous emission (ASE) in the pump laser frequency spectrum.

[8] One stage to 1550 nm for instance, would require 724-nm light.

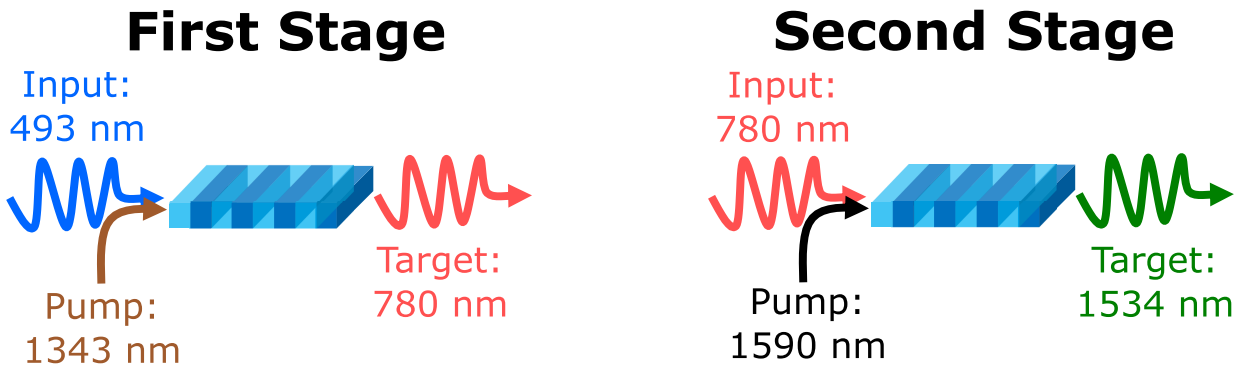

Figure 4.3: **Frequency Conversion Scheme Used in our Lab**. In the first stage of frequency conversion, a 493-nm photon from the ion is converted to 780 nm using a high intensity pump at 1343 nm. In the second stage of frequency conversion this 780-nm photon is converted to 1534 nm through use of a 1590-nm pump.

493-nm light[9], making this first stage potentially useful for quantum networking experiments on the scale of a few kilometers, even without going to telecommunication wavelengths. This first stage alone has been the main focus of our lab during my tenure and allowed us to perform the numerous "hybrid quantum networking" experiments that I will discuss in later chapters, and notably, allowed us to do some preliminary networking experiments between labs located in separate buildings on the University of Maryland campus [50].

What has not worked as well however, in terms of noise, is the second stage of conversion. Though it avoids SPDC-based noise, noise photons produced via anti-Stokes Raman Scattering (Sec. 4.2.3), as well as photons present in the 1589-nm pump laser beam itself at the 1534-nm conversion target (likely from amplified spontaneous emmission (ASE)), overwhelm our single-photon signal originating from the ion[10]. Even with this noise, we decided that this stage was still worth building for extremely low networking losses[11], and we have successfully demonstrated two-stage single photon conversion to 1534 nm using this scheme, as will be

[9] Roughly 3 dB/km at 780 nm vs 50 dB/km at 493 nm.
[10] There is however a pathway to improving this with improved photon collection.
[11] Roughly 0.25 dB/km.

discussed in section 5.3. We have also been able to use this stage to demonstrate the first switching of single photons from a trapped ion in a photonic integrated circuit, a useful quantum networking tool, in an experiment led by collaborator Uday Saha [24].

The following subsections will provide detail on our implementation of these conversion stages, which have been improved over 3 iterations. I will discuss these different iterations in the chronological order they were constructed. This will provide both insight into the evolution of our design decisions as well as serving as a reference for the conversion schemes used in the work highlighted in later chapters. I will only discuss the the 493 nm $\rightarrow$ 780 nm conversion, as the setups are extremely similar for the second stage. The conversion efficiency and noise of the second stage (780 nm $\rightarrow$ 1534 nm) will be discussed later in Sec. 5.3.

4.3.1 Fiber Pig-tailed PPLNs

The first iteration of our DFG setups were centered around the idea of directly bonding a fiber to the PPLN waveguide. This would, in theory, allow for enhanced modularity of the QFC setup by being able to potentially plug the output converted photons directly into your quantum network, or into another stage of conversion. Such modularity becomes critical in a complicated laboratory experiment, where one would like to be able to test different experimental components independently and in parallel.

4.3.1.1 Device and Optical Setup

Normally, alignment of the multiple disparate colored inputs into this waveguide can be a rather difficult task, as the PPLN waveguide chips used typically have 10s of waveguides (each

with dimensions on the order of 10 μm) written into them. On top of this, these waveguides are typically highly multimode at 493 nm and 780 nm, making alignment to the fundamental waveguide mode (critical for efficient conversion) even more difficult. The fiber pig-tail therefore also allows easier alignment into the waveguide by simply running light backwards through the fiber and overlapping the input beams with it.

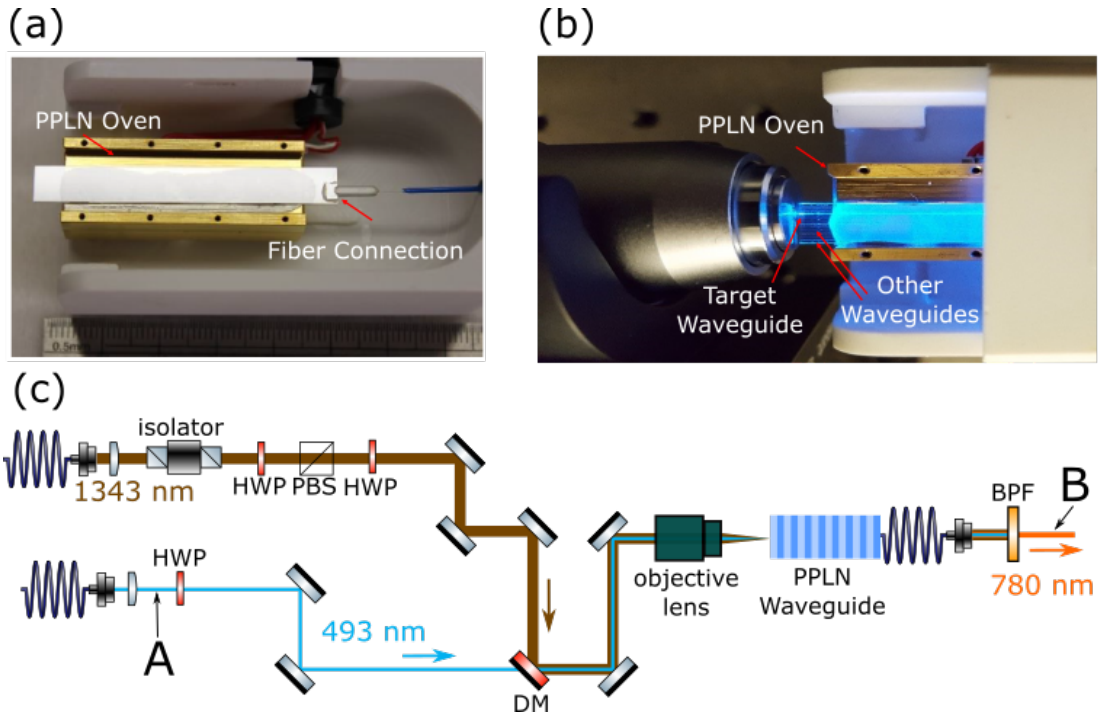

Figure 4.4: **DFG Setup with Fiber-Pigtailed PPLN** a) The periodically poled lithium niobate chip is glued to a resistive oven. A fiber is glued to the output of one of the waveguides written into the crystal. b) Zoom in on the input of the crystal, showing 493-nm light coupled into one of the waveguides. c) Optical setup used to couple light into the waveguide. Abbreviations: PBS - polarizing beamsplitter, DM - dichroic mirror, BPF - band pass filter, HWP - half waveplate.

The typical fiber pig-tailed PPLN setup used by our lab is shown in Fig. 4.4. Fig. 4.4 a shows a picture of a PPLN waveguide chip, with its attached fiber pig-tail, designed by SRICO[12], a company which we worked with and had design these chips as part of a US Army SBIR research grant[13]. The chip is flat-faced, and in the case of these particular devices, was not anti-reflection

[12]Part number: Srico 2000-1004
[13]US Army SBIR 14-021

coated, allowing for etalon effects[14] as well as additional input coupling losses ($\approx$ 14% at 493 nm). Waveguides are written into the crystal via reverse-proton exchange [128, 137] and are therefore buried below the crystal surface. The fiber pigtail is attached to the optimal waveguide on the device (out of many, see Fig. 4.4 b), as determined by internal testing at SRICO. The chip is glued to a resistive oven[15], allowing for heating of the chip to optimal phase-matching temperatures (typically in the range of 40-70 °C).

The optical setup used for achieving DFG with these fiber pig-tailed PPLN devices is shown in Fig. 4.4 c. Light at both 493 nm and 1343 nm, delivered from their respective fibers, is combined on a dichroic mirror[16]. Each beam path consists of its own walking mirrors and waveplates to allow for independent optical and polarization alignment of each color. An optical isolator[17] is included in the 1343-nm beam path to protect the 1343-nm laser and amplifier from high-powered back reflections off of the face of the PPLN crystal.

The combined light is focused and coupled into the waveguide by a 20x objective lens[18]. This objective is coated for visible light to optimize 493-nm light coupling, with the 1343-nm light experiencing around $\approx$ 30% loss. This trade-off is acceptable as we have plenty of power available at 1343-nm via our fiber amplifier, but cannot amplify the single 493-nm photons[19] that are sent into the setup.

Though the output fiber[20] is single mode at 780 nm, a significant amount of pump light will couple into and exit out of the $\approx$ 1m long fiber, as well as unconverted 493-nm light (this

[14] We observe $\approx$ 15% fluctuations in coupling efficiency as the pump frequency is scanned, for instance.
[15] Covesion PV50
[16] Thorlabs DMSP650
[17] Thorlabs IO-4-1310-VLP
[18] Edmund Optics 33-438
[19] See the no-cloning theorem [138].
[20] Nufern PM780-HP

fiber is multimode at 493-nm). Optical interference filters are used to remove as much of this remaining light as possible, and to remove noise photons produced by the high intensity pump. These filters consist of two low-pass filters with a 1326-nm cuttoff[21] for pump removal[22], and a 10 nm bandpass[23] (later upgraded to a 3 nm bandpass[24]) filter centered at 780-nm for the removal of noise photons and any remaining 493-nm light. Converted 780-nm light (along with some noise photons produced) is re-coupled into an optical fiber after this filtering.

4.3.1.2 Alignment and Temperature Tuning of Fiber Pig-Tailed PPLN Devices

Initial alignment of these devices consisted of connecting a fiber alignment pen ($\approx$ 635 nm) to the output 780-nm fiber glued to the PPLN chip. With this light running backwards, both the 493-nm and 1343-nm beams are overlapped by eye on viewing cards. This is enough to see small amounts of coupled light exit the output 780-nm fiber. The coupling of 493-nm light is then peaked via the use of the walking mirrors combined with translation of the PPLN[25] along the axis of the objective lens, as well as translation of the aspheric lens used to collimate the 493-nm light out of its fiber[26]. The polarization of the light is also adjusted for maximum coupling, as these waveguides only propagate vertically polarized light. The 1343-nm pump light is aligned in a similar fashion, but without translating the PPLN to preserve the 493-nm signal light coupling[27].

In addition to optical alignment, the PPLN crystal must be tuned in temperature to achieve the proper phasematching condition (Sec. 4.2) required for efficient conversion. This is achieved

[21] Semrock FF01-1326/SP

[22] Technically, we do not use enough filtering to completely remove all of the 1343-nm pump light. This is okay as our Si-based detectors are extremely insensitive to light at this wavelength.

[23] Thorlabs FBH05780-10

[24] Semrock LL01-780

[25] Mounted on a 5-axis stage, though we typically only adjust the focus in this configuration.

[26] Optimal coupling is not necessarily achieved with collimated light - this will be a problem later!

[27] Again, we have plenty of pump power available, and can eat a relatively large loss.

by first tuning the crystal temperature to its estimated phasematching temperature[28], and tuning the frequency of our pump laser to peak the measured DFG signal. This usually gives a small signal which can then be increased by tuning the temperature of the device. An iterative process of walking the pump laser towards the desired frequency with temperature adjustments to peak up the measured conversion efficiency can then be performed in cases where a specific frequency for the converted 780-nm photons is desired[29].

4.3.1.3 DFG and Noise Data

We measure the "end-to-end" conversion efficiency of the device, defined as the ratio of 780-nm power measured at point B in Fig. 4.4 c to the 493-nm input power measured at Point A in Fig. 4.4 c, multiplied by the ratio of photon energies at these colors. Though we typically collect this data with low levels of laser light, these results are also valid at the single photon level [132].

A handful of these pig-tail PPLN devices have been used by our lab over the past few years [50, 92, 93], with varying conversion efficiencies. The end-to-end single photon conversion efficiency from 493 nm to 780 nm as a function of the pump power measured out of the PPLN fiber is shown in Fig. 4.5 (black circle data points) for our highest performing pig-tailed device [92]. With this device, we were able to achieve an end-to-end conversion efficiency of $\approx 19\%$, with around 220 mW of pump light measured at the output (just before the 780-nm filtering). Higher levels of pump light result in a reduction in conversion efficiency (Eqn. 4.23), suggesting back conversion to 493 nm.

[28] This is typically given to us by the manufacturer.

[29] We have also done this by altering the frequency of the 493-nm light, but it is easier for us to keep the 493-nm laser locked to the ion-photon frequency.

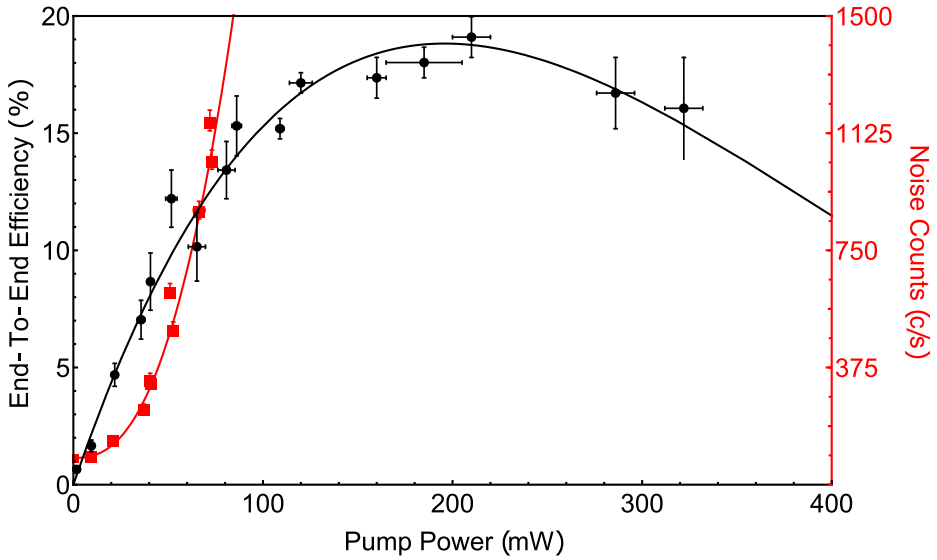

Figure 4.5: DFG Conversion Efficiency and Noise Data. The end-to-end conversion efficiency of the DFG from 493 nm to 780 nm (black circles and left-hand axis) and noise produced in the bandwidth allowed by our filtering (red squares and right-hand axis) as a function of pump power measured out of attached output fiber. The error bars on the pump power are from fluctuations of the measured power and the error bars on the efficiency are primarily from DFG signal power fluctuations.

This conversion efficiency is thought to be limited by the mode overlap of the 493-nm and 1343-nm light. The 493-nm mode can not be measured directly out of the PPLN waveguide, due to the presence of the 780-nm fiber, which itself is multimode at 493 nm. Therefore, with this setup, it is impossible to verify that the 493-nm light is coupled into the fundamental mode of the waveguide, which is required for maximum conversion and coupling of the 780-nm light into the output fiber.

As previously mentioned, our conversion schemes are chosen to try and limit the amount of noise photons produced by the high power pump. Nevertheless, we are able to measure a non-negligible level of noise with these devices. The noise measurement is made by first re-coupling the converted 780-nm light into a fiber after noise filtering. Turning off the input 493-nm light and connecting this fiber to our single photon detecting avalanche photodiodes[30], we measure

[30]PerkinElmer SPCM-AQR-15

noise photons, represented by the red data points in Fig. 4.5. This noise may be from a variety of sources, including remaining leakage light at 1343 nm or at 675 nm produced though second harmonic generation of the pump. Noise within the filter bandwidth can be produced through anti-stokes Raman scattering (Sec.4.2.3) or through a two step process where SPDC near ≈ 1860 nm is produced by the pump, and then is up-converted to 780 nm via sum frequency generation with the pump. Other measurements made with varying filtering bandwidths suggest that this noise is proportional to the filtering bandwidth used[31] around the photon frequency. Therefore, for the experiments shown in Chapters 6 and 7, a Bragg grating (bandwidth 0.15 nm) is used to reduce the noise measured out of these devices by a factor of ≈ 60 relative to the data shown here.

4.3.1.4 Conclusions

In summary, the fiber pig-tailed PPLN devices used in many of the experiments that will be discussed in this thesis (Chapter 5 [92], Chapter 6 [93], Chapter 7 [50]) offer quick alignment, relatively high conversion efficiencies, and at least some degree of modularity. The attached fiber however, turns out to be a detriment when it comes to alignment into the proper waveguide mode and may itself contribute up to 50% loss[32] at its interface with the PPLN crystal. These fibers also serve as likely failure points for the devices. For example, the epoxy attaching the fiber to the crystal has a temperature limit near 100°C, which has led to permanent disconnection of the fiber when temperature tuning past devices. Additionally, any dust near the fiber tip can lead to burning of the fiber due to the high power pump present, which can be a problem

[31] The filtering bandwidth here is 10 nm.

[32] This is a typical value given by multiple PPLN wavguide companies when asked about expected fiber pig-tail losses. This is also consistent with the DFG efficiencies we have observed using non-fiber-pig-tailed devices.

when regularly swapping out fiber connections when performing measurements, serving to partly counter the ease-of-modularity motivation for these devices[33]. Finally and most importantly, these devices can only be used for one polarization of input 493-nm light and therefore do not easily allow for entanglement-preserving frequency conversion for the polarization-based ion-photon entanglement used in our lab, as will be discussed in Section 4.3.3. The combination of these factors led us to remove the fiber pig-tail from the setups described in Sections 4.3.2 and 4.3.3.

4.3.2 Free-Space PPLNs

The second iteration of our frequency conversion setups removed many of the problems inherent in the fiber pig-tailed PPLNs discussed in Sec. 4.3.1 and allows some other advantages. The large loss ($\approx 50\%$) at the fiber-PPLN interface is removed, and the pump, unconverted light, and converted signal can be separated by free space optics, allowing for easier noise filtering and simultaneous power measurements. Additionally, we are able to more easily couple to the fundamental mode of the waveguide as the ouput mode can be directly viewed at the output of the PPLN crystal.

4.3.2.1 Optical Setup

The optical setup for this second design is shown in Fig. 4.6 a. The PPLN waveguide crystal (PPLN-WG) used was again developed in collaboration with SRICO[34] and is mounted on a resistive oven as before. The input optics are very similar to the design for the fiber pig-

[33] We typically combat this by using an extra dedicated patch cable connected to the PPLN fiber, so that if a fiber is burned we can replace it.

[34] Part Number: SR050117.4.C4

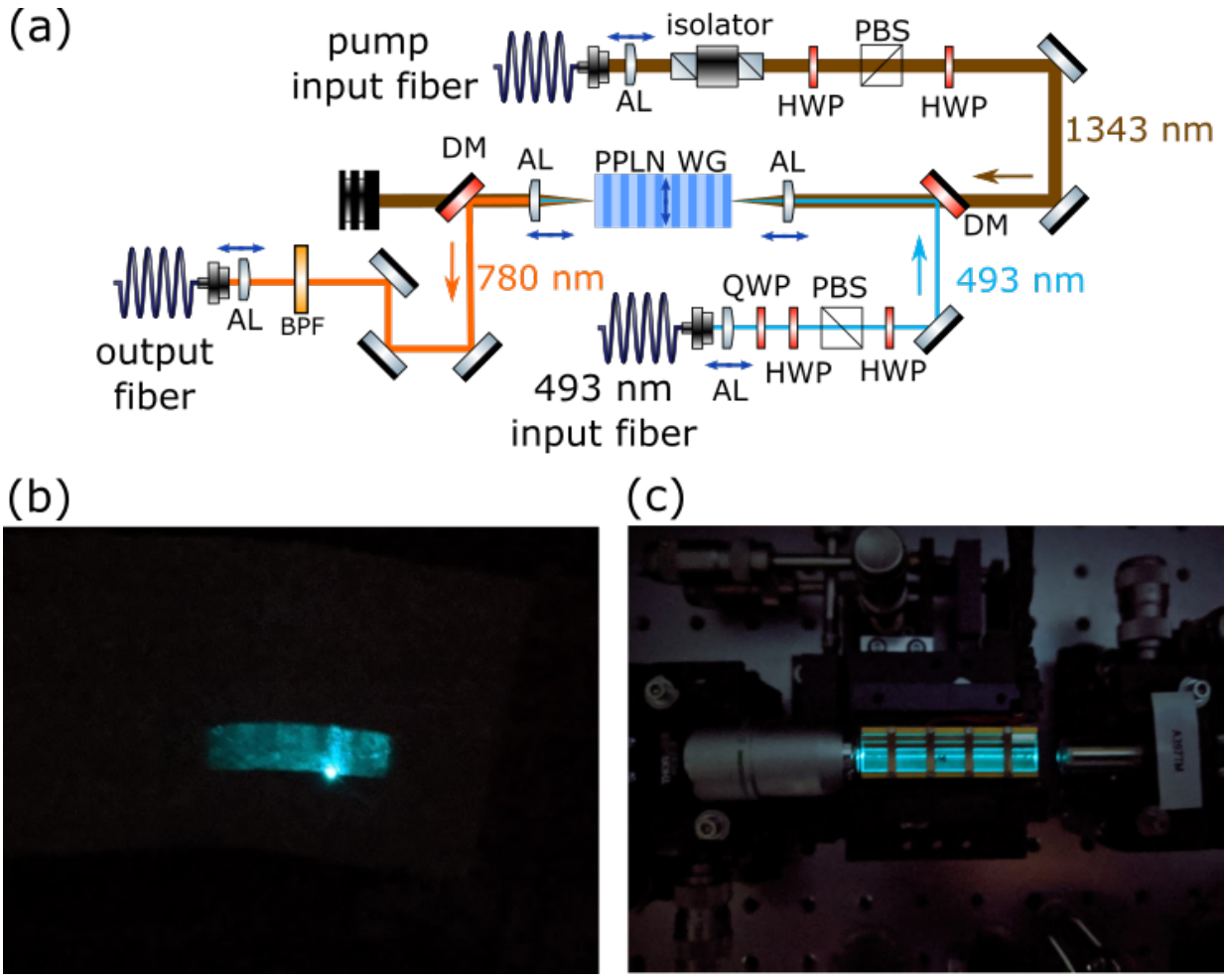

Figure 4.6: **Free-space PPLN Setup.** a) Optical setup for coupling light into and collecting light from the free-space PPLN waveguide (PPLN WG). b) Output mode of a waveguide as viewed on an index card during initial alignment. c) Lens setup for initial alignment. For final alignment the objective on the left is replaced with an aspheric lens. Abbreviations: PBS - polarizing beamsplitter, DM - dichroic mirror, BPF - band pass filter, HWP - half waveplate, QWP - quarter waveplate, AL - aspheric lens.

tailed PPLN crystal discussed in Sec. 4.3.1 and shown in Fig. 4.4, with the main differences being additional polarization filtering in the 493-nm beam path and the use of a stage-mounted and uncoated aspheric lens (AL) for input coupling rather than an objective lens. With no fiber attached to the output facet of the crystal, another aspheric lens is used for output coupling[35]. A dichroic mirror[36] (DM) on the output allows for easy separation of the 1343-nm pump light from the 493/780-nm light exiting the waveguide. This allows for the user to easily simultaneously monitor the coupled pump power and DFG signal. A set of walking mirrors allows for output 780-nm light to be coupled into fiber after free space filtering with a bandpass filter.

4.3.2.2 Optical Alignment

Optical alignment is much more difficult in this setup when compared to the setup in Sec 4.3.1, as there is no fiber to easily run light backwards through as a spatial alignment guide. We begin by aligning 493-nm light through the input aspheric lens and, by use of a multi-axis stage[37], moving the PPLN crystal face into the resulting focal spot. During this process, an objective lens is placed roughly one focal distance away from the output of the output facet of the crystal (Fig. 4.6 c.), followed by an index card used for viewing the output 493-nm mode (or scatter) by eye. Aligning to a waveguide, unfortunately, involves the art of learning what different shapes of the output scatter correspond to in terms of beam placement, and the ability to discern scatter from an actual waveguide mode. We place the PPLN crystal roughly at the focal point of the aspheric lens, and purposefully lower the crystal below the 493-nm beam. The crystal is then raised into the beam just until the the rectangular shaped scatter shown in

[35] To begin with, an objective lens was used here for imaging of the waveguide during initial alignment.
[36] Thorlabs DMLP950
[37] Thorlabs MBT402

Fig. 4.6 b is visible due to weak guiding by the bulk crystal. As the waveguides for this device are written just below the surface, this gives one the best chance of stumbling onto the waveguide with horizontal translation of the PPLN in the focal plane. If things are done just right, a bright spot corresponding to a waveguide can be located (Fig. 4.6 b). This spot is then isolated with an iris and the signal peaked up by translation of the PPLN 5-axis stage, use of walking mirrors at the input, and iterative adjustments of the 493-nm collimation out of the fiber and the distance of the PPLN-WG from the input aspheric lens. As the coupling improves, the rectangular scatter is greatly reduced, and the spot corresponding to the waveguide becomes much brighter.

With initial alignment to a waveguide, it then becomes a matter of coupling into the correct mode of the waveguide. This is also a bit of an art, and essentially involves adjustments of input mirrors and PPLN WG position to try and make what looks to be a gaussian-like spot[38] by eye on a white card[39]. This spot is then irised off and the signal peaked up. Following this, one attempts to couple this output mode into a single mode fiber[40] temporarily put into the setup, as this should serve as a good Gaussian mode filter to verify the proper mode has been coupled into. Using this method, we estimate that we are able to couple $\approx 50\%$ of our input 493-nm light into the fundamental mode of the waveguide, when accounting for optical losses at each aspheric lens and at each face of the PPLN.

Following alignment of the 493-nm beam, the 1343-nm pump is aligned to the PPLN only through use of its walking mirrors and the aspheric lens for fiber output collimation, using the 493-nm input light as a guide. As with the fiber pig-tailed PPLN, this does not produce the

[38] We expect the mode to be near-gaussian (though somewhat elliptical) via simulations provided by SRICO.

[39] You may be wondering why a beam profiler isn't used here. This is essentially due to the fact that a very small amount of light (<250 nW) is used at 493-nm to not cause photorefractive damage to the PPLN crystal, too small to reliably view on the beam profilers we currently have available. Thankfully, the human eye is extremely sensitive to light at 493 nm.

[40] Thorlabs SM405 Fiber

optimal conditions for coupling of the pump, but with access to a few Watts of pump power, this is sufficient for peak conversion.

To couple the converted 780-nm output light to a fiber involves first running this fiber backwards using laser light at 780 nm and, using the 493-nm light pass through the PPLN-WG as guide light, aligning this laser light to maximize coupling to the PPLN-WG. This alignment is optimized in a similar way to the 493 nm input coupling, through walking of mirrors and iteratively adjusting the aspheric lens on the output of the PPLN-WG and at the input of the 780-nm fiber. After a DFG signal is found and maximized via temperature tuning of the crystal[41], the fiber coupling is again adjusted to maximize coupling for the converted mode.

4.3.2.3 DFG Conversion Efficiency

The best fiber-to-fiber single photon conversion efficiency measured with this iteration of setups, and after testing multiple waveguides, is shown in Fig. 4.7. This data is measured with $\approx$ 200nW of input 493-nm laser light. A fit using Eqn. 4.25 suggests a peak conversion efficiency of $\approx 37\%$, though the peak measured efficiency is $\approx 40\%$ with $\approx$170 mW of pump power coupled into the waveguide.

At the peak conversion efficiency we measure around 200 noise photons per second (≈ 400 cps when correcting for detector efficency), over an order of magnitude decrease from the fiber pig-tailed PPLNs. Though we are not sure of the exact cause of this, we believe it to be related to the lack of fiber attached to the PPLN crystal, which itself can serve as a nonlinear medium through which noise photons can be produced. It is also possible that our detectors are able to pick up more 1343-nm photons than anticipated, and the free space separation of the beams and

[41] Measured first in free space which usually results in a decent fiber-coupled signal.

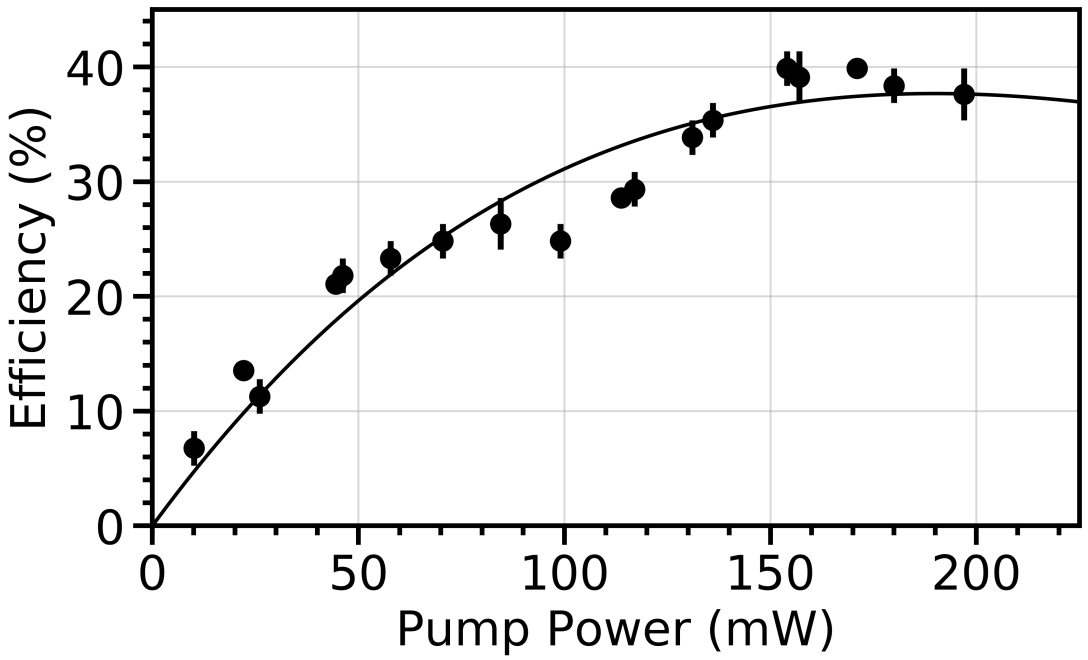

Figure 4.7: **DFG Conversion Efficiency with the free space PPLN**. Fiber-coupled DFG conversion efficiency as a function of estimated pump power coupled into the wave guide. The solid line represents a fit to Eqn. 4.25 with a fitted peak conversion efficiency of $\approx 37\%$.

fiber coupling helps to mitigate pump light reaching the detectors when compared to the fiber pig-tailed devices.

The large dip in conversion efficiency near 100-140 mW, when compared to the theory fit, is believed to be due to pump-induced phase-matching shifts [139]. These shifts appear to be time dependent, with the initial conversion efficiency at these pump powers being much closer to that of the fit initially, before decreasing to the values represented by the data in Fig. 4.7. Some of the conversion efficiency can be recovered by temperature tuning, but what we really care about is the conversion efficiency at the peak, which is what the crystal temperature is optimized for. This could be investigated more closely, but this effect is not visible in the latest iteration of our setups, using Zn-doped PPLN crystals (See Sec. 4.3.3, Fig. 4.10).

4.3.2.4 Conclusions

Overall, the removal of the fiber pig-tail enabled us to more carefully couple into the PPLN waveguide and achieve even higher conversion efficiencies and lower noise. This type of setup however, is still not useful for the preservation of polarization-based entanglement, for reasons that will be explained in the following section. Nevertheless, this type of setup was used for the single polarization frequency conversion to both 780-nm and to the telecommunications C-band, as will be discussed in Sec. 5.3, and was used for a single-photon on-chip switching experiment [24] demonstrated in collaboration with the labs of Edo Waks (UMD) and Dirk Englund (MIT).

4.3.3 Entanglement Preserving PPLN

In order for our QFC setups to be useful in a real trapped-ion quantum network, the conversion must not destroy the entanglement between the ion and photon. In the polarization-based entanglement scheme used in our laboratory (Sec. 2.3.4), this amounts to the QFC needing to be polarization independent. Difference frequency generation in PPLN however is polarization-dependent, with the largest nonlinear coefficient[42] corresponding to, in the case of our lab, vertically polarized light in the lab frame. Therefore, a more complicated optical setup is required for entanglement preservation than has been discussed so far.

[42] d_{33} [129]

4.3.3.1 Optical Setup

The final optical setup for the polarization preserving frequency converter is shown in Fig. 4.8. This conversion setup is designed around the idea of coupling each polarization of the input 493-nm light into opposite sides of the ZnO:PPLN waveguide. A rotation on one of these polarizations just before waveguide coupling allows for both to be efficiently converted to 780 nm. This setup is also inherently phase-stable, as both polarizations of 493/780 nm light take the same overall optical path length and should not cause any phase-related issues with ion-photon entanglement [43].

Rather than the standard lithium niobate crystals used in our previous setups, we use a ZnO-doped periodically poled lithium niobate (ZnO:PPLN) waveguide crystal[44] for better resistance to photo-refractive damage that can be induced by the 493-nm test light. This allows us to use much higher powers for alignment and testing, and makes comparing the input and output modes of coupled light on a beam profiler possible. This crystal is also anti-reflection coated ($< 0.5\%$ at all colors), leading to better input and output coupling efficiencies and greatly reduced etalon effects. The ZnO:PPLN crystal is mounted on a 5-axis stage[45] placed between two silver-coated parabolic mirrors[46] for input and output coupling, each on their own 6-axis stages[47]. Temperature control of the crystal is achieved with a TEC[48] and controller[49] as opposed to the resistive heaters used in previous setups.

[43] Unless a mirror is moving particularly far and fast in the 5 nanoseconds or so it should take a photon to travel through the setup!
[44] NTT Electronics WD-1344-000-A-C-C-TEC, device courtesy of the group of Edo Waks
[45] Newport 562F-XYZ and 562F-TILT
[46] Thorlabs MPD00M9-P01
[47] Combination of ThorLabs LX30, PY005, and RSP05
[48] FerroTec 9501/023/040B
[49] Thorlabs TED200C

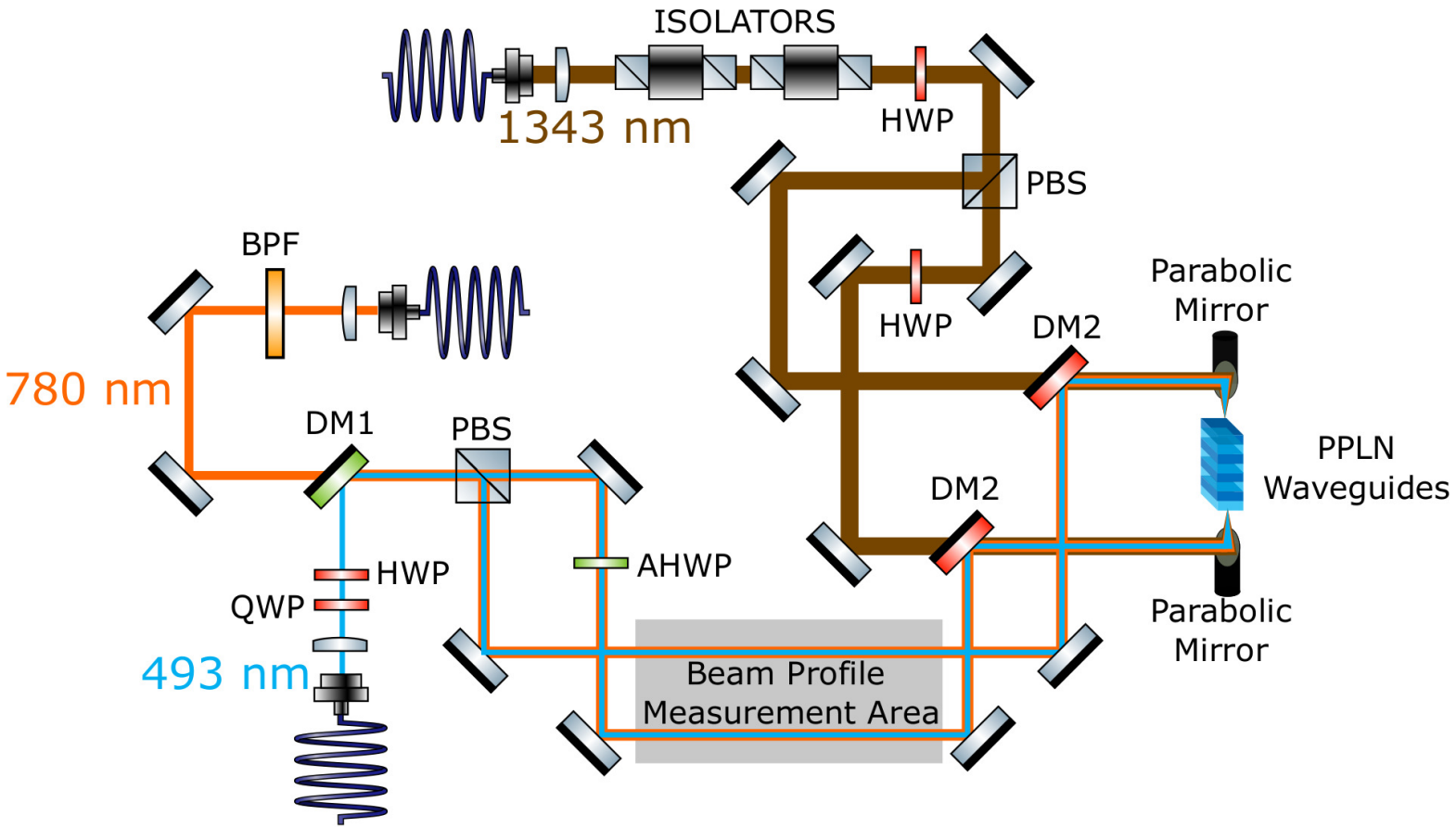

Figure 4.8: **Two-Way QFC Implementation.** Parabolic mirrors are used both to couple light into the waveguide as well as collimate light out of the waveguide for all three colors. The beam profile measurement area allows for characterization of the 493-nm and 780-nm modes before and after coupling into the waveguide. The setup is further described in the text. Abbreviations: PBS - polarizing beamsplitter, DM - dichroic mirror, BPF - band pass filter, HWP - half waveplate, QWP - quarter waveplate, AHWP - achromatic half waveplate.

Signal light at 493 nm is split off by polarization at a polarizing beamsplitter (PBS) dual-coated for 493 nm and 780 nm[50], and sent via walking mirrors to dichroic mirrors[51] (DM2) for combination with the pump light just before the parabolic mirrors. The converted 780-nm light takes the same beam paths, but in the opposite direction, before being separated from the 493-nm path by a dichroic mirror[52] (DM1) after both polarizations are recombined on the dual-coated PBS. One of these beam paths includes an achromatic half waveplate[53] (AHWP) to rotate P-polarized 493-nm light to S-polarization for conversion, and to rotate the output 780-nm light from S- to P-polarization such that it transmits through the PBS.

The pump light at 1343-nm takes an independent path up until the dichroic mirrors (DM2) combining it with the 493-nm light. It is split into two paths by polarization on a PBS, again with a half waveplate in one path for polarization rotation to enable conversion. A half waveplate before this PBS allows for control of the relative power between the two paths, helping the user control the conversion efficiency for each polarization independently. Additional isolators are used to protect the pump laser and amplifier from light traveling backwards after successfully being coupled into the waveguide.

The use of parabolic mirrors is critical for this setup. The aspheric lenses used in Sec. 4.3.2 were found to impart too large of chromatic focal length shifts such that the simultaneous coupling and collimation of the 493-nm and 780-nm input and output beams was not possible. The off-axis parabolic mirrors used here however, have a focal length that is in principle wavelength independent, operating off of reflection rather than refraction. Additionally, to operate properly, all beams are required to be collimated, making the setup largely optical path length independent.

[50] Lambda Research Optics BPB-10SF2-450-800
[51] Thorlabs DMLP950
[52] Thorlabs DMLP650
[53] Thorlabs AHWP05M-580

This means that optimal focusing and coupling of the input 493-nm light in one direction into the waveguide will simultaneously be optimal for collimation of the 780-nm light exiting the waveguide on either side of the crystal (and for the pump light as well). The downside however, is that off-axis parabolic mirrors are difficult to align when compared to simple lenses, with misalignments from the optical axis of the mirror easily causing large optical aberrations, reducing coupling efficiency.

4.3.3.2 Alignment

Careful alignment of the PPLN crystal relative to the parabolic mirrors in the setup is critical to efficient operation of the converter. We achieve this through the multi-step alignment procedure outlined in Fig. 4.9 a-d. First, before the PPLN stage is placed in the setup, we mount an optical fiber[54] on a 5-axis stage, roughly positioned where the PPLN crystal will be mounted. After adjusting the fiber such that it is roughly parallel to the table and at the estimated height of the PPLN waveguide when mounted, we place one of the parabolic mirrors a focal distance away. We carefully align this parabolic mirror to the optical axis of the fiber output through the use of a shearing interferometer [140–142] setup, consisting of a shear plate, and magnified viewing screen[55], as shown in Fig. 4.9 a. We use these to iteratively check the collimation of the 493-nm light from the fiber in both the vertical and horizontal directions while making adjustments to the 6-axis stage the parabolic mirror is mounted on. Fig 4.9 e shows how the interference fringes look on the shearing interferometer when collimation is achieved in one direction (horizontal), with the interference fringes parallel to a guide line (itself parallel to the table) on the viewing

[54] SM405
[55] Thorlabs SI050 and SIVS

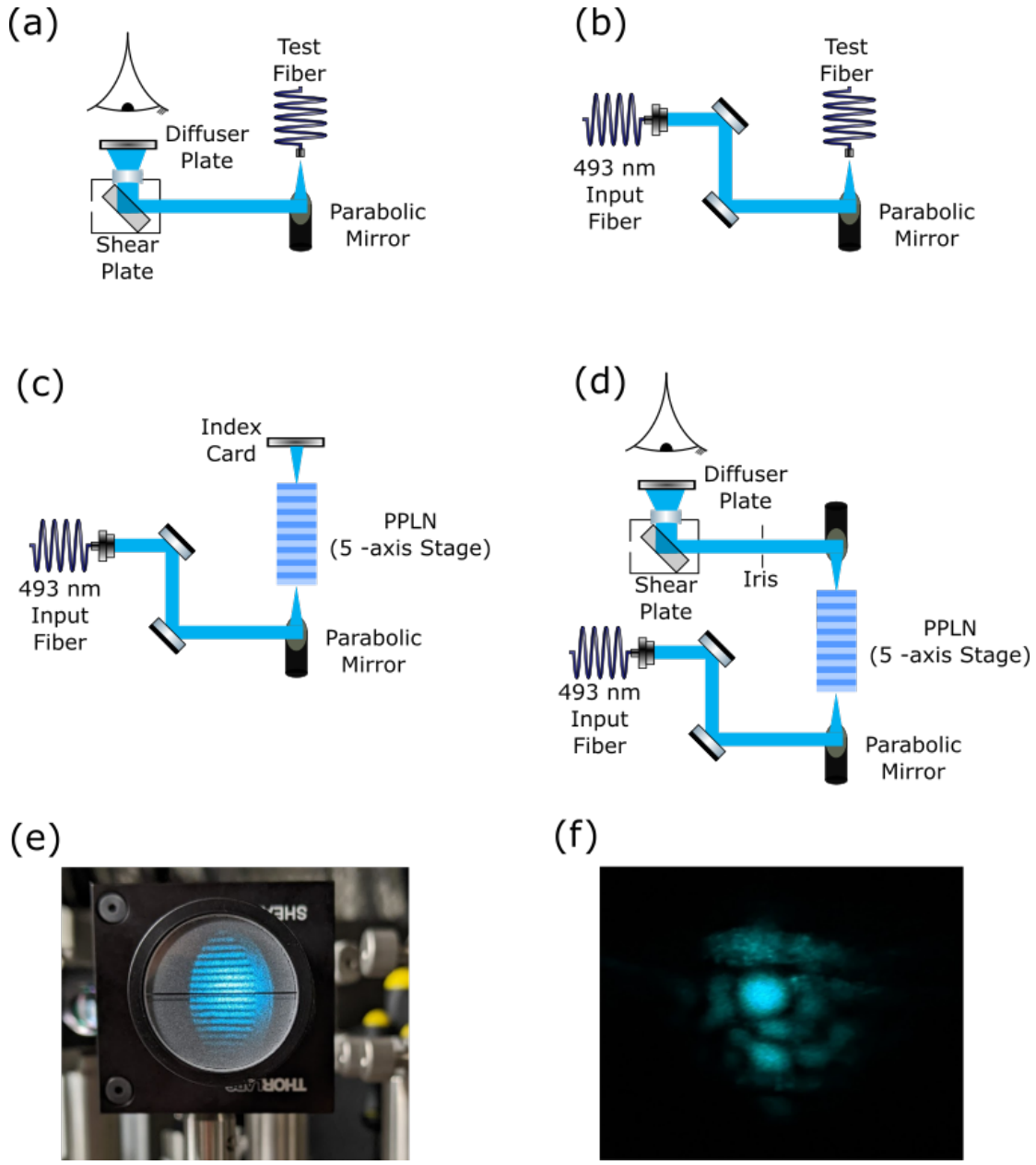

Figure 4.9: **Two-Way QFC Initial Alignment** a) A test fiber is placed roughly in the intended position of the PPLN crystal. The parabolic mirror is aligned to this fiber through use of a shearing interferometer to collimate the light in both the horizontal and vertical directions, as well as to remove aberrations. b) The output from the test fiber-parabolic mirror system is coupled into the 493-nm input fiber for the DFG setup. c) The test fiber is replaced with the PPLN waveguide and initial coupling is achieved by moving the PPLN stage and viewing the output on an index card. d) The second parabolic mirror is aligned to the PPLN waveguide through use of a shearing interferometer setup in a manner similar to a). e) Picture showing the interference pattern produced by the shearing interferometer when light is roughly collimated in one direction. f) Waveguide mode at 493 nm as viewed on an index card after initial alignment.

screen.

After alignment of the parabolic mirror to this test fiber, we set up one of the optical paths for the 493-nm light (shown only as walking mirrors here for simplicity) and use walking mirrors to align the collimated light from the parabolic mirror into the input 493-nm fiber that will deliver ion light to the PPLN (Fig. 4.8), without any adjustment of the parabolic mirror or temporary test fiber. This process, depicted in Fig. 4.9 b, ensures that the 493-nm input light is aligned to the optical axis of the parabolic mirror, minimizing abberations at the focus.

Following this alignment, we replace the test fiber with the PPLN, mounted on its five-axis stage, and run 493-nm light forwards through the input 493-nm fiber. We then align the PPLN to the 493-nm light focused by the parabolic mirror by adjustment of its stage, without touching any other optics, as in Fig. 4.9 c. We then view the output 493-nm mode on a white index card during alignment[56]. Once a waveguide is found, we use a power meter and iris to maximize coupling into the waveguide. This results in an output mode that looks similar to that shown in Fig. 4.9 f.

With initial alignment to the waveguide, the second parabolic mirror is placed into the setup and roughly aligned by eye. We iris off the fundamental waveguide mode[57], and again use a shearing interferometer to collimate this output mode, as shown in Fig. 4.9 d. After this parabolic mirror is, to the best of our ability[58], aligned to the output facet, the pump laser optical beam paths are put in place and each path is roughly aligned to the waveguide in either direction via overlap with the 493-nm beam, before a power meter is used to peak up these couplings. After finding and peaking a DFG signal, we add in the additional beam path necessary for 780-nm fiber coupling. Future (small) adjustments are made as needed for all colors (without complete

[56]The same initial alignment tactic discussed in Sec.4.3.2 is used here, but without an output objective.
[57]Or what we think is the fundamental mode.
[58]The mode here isn't perfectly Gaussian, leading to some apparent aberrations when using the shear plate.

realignment from scratch) only using mirrors, as the PPLN waveguide and parabolic mirrors are assumed to be co-axial after this alignment procedure.

The increased power handling provided by the Zn doping of the PPLN waveguides used in this setup also enabled us to more carefully mode match to the waveguide modes at both 493 nm and 780 nm[59]. Being able to couple more light enabled measurements of the beam profile of the output waveguide modes[60], in the shaded area designated in Fig. 4.8. This allowed us to better determine the collimated size of (what is thought to be) the fundamental 493-nm waveguide mode after initial alignment and to change out the fiber collimation aspheric lens used at the input[61]. This led to an estimated increase in coupling of the 493-nm light into the fundamental mode from $\approx 40\%$ to $\approx 60\%$ for this device, with a proportional increase in DFG conversion efficiency. The collimated mode of the converted DFG was also viewed in this method, with the aspheric lens used to couple into the output 780-nm fiber based on this measurement (estimated $\approx 65\%$ coupling efficiency).

4.3.3.3 Conversion Efficiency and Noise Measurements

The fiber-to-fiber single photon conversion efficiencies of this device are shown in Fig. 4.10 for both P- and S-polarized input light at 493 nm. Peak conversion efficiencies of 37.9(9)% and 34.5(4)% are measured for each polarization respectively. The displayed fits suggest slightly lower peak efficiencies of 36.6(3)% and 34.2(3)% instead. Smaller deviations from the measured data and the fits are observed when compared to the setup discussed in Sec. 4.3.2. This is believed to be an additional benefit of the increased power handling of the waveguides, which should also

[59] Again, we did not bother at the pump wavelength, as we have plenty of power.

[60] We've never been able to get a solid waveguide mode profile from any of the PPLN companies we have worked with - this device is no exception.

[61] Careful use of irises prevented the need for complete realignment of 493-nm light the parabolic mirrors.

reduce any effect of pump-induced index change.

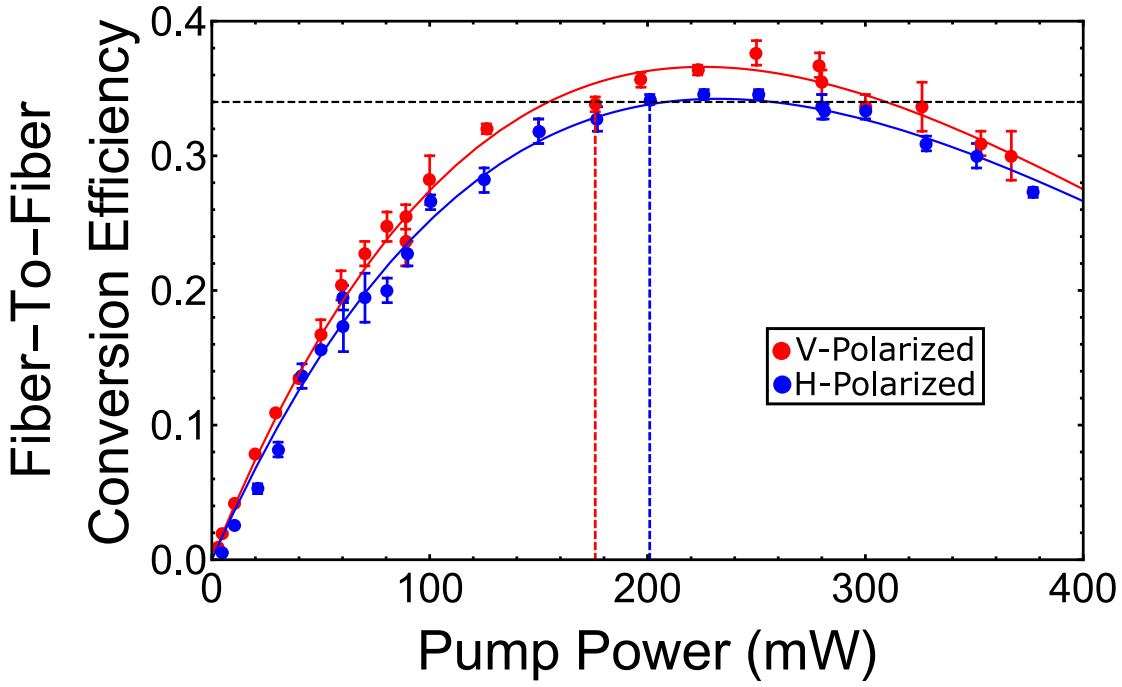

Figure 4.10: **Two-Way QFC Conversion Efficiency**. Single photon frequency conversion efficiency for the two-way converter for each polarization of 493-nm light sent into the setup, as a function of the pump power coupled into the waveguide. The displayed fits to Eqn. 4.25 correspond to peak conversion efficiencies of 36.6(3)% and 34.2(3)%. The horizontal dotted line represents the conversion setting allowing each polarization to have the same conversion efficiency, and the colored vertical lines correspond to the measured pump powers required to hit this efficiency.

The difference in conversion efficiency in each direction is due to alignment disparities[62] between the maximum 493-nm waveguide coupling for one polarization/propagation direction when compared to the best 780-nm fiber coupling for the other polarization/propagation direction. Small iterative adjustments are made for each direction to find a reasonable compromise for conversion efficiencies[63]. In addition to simple misalignment, the peak conversion efficiencies are limited by a combination of optical losses ($\approx 20\%$[64]), and remaining mode mismatch between

[62] In theory, we would expect these to be nonexistent - but it is likely an issue of slightly different parabolic mirror alignments to the waveguide itself.

[63] When focused only on single-polarization operation, we have seen upwards of 40% single photon conversion efficiency into fiber.

[64] $\approx 5\%$ loss at the dual-coated PBS (once for 493 nm and once for 780 nm), and at each parabolic mirror.

the Gaussian fiber modes and the (slightly) elliptical waveguide modes.

Having control of the relative pump powers sent in each direction of the setup, we are able to select pump powers allowing for the same conversion efficiency of each polarization for arbitrary 493-nm light sent into the setup. This will help preserve the fidelity of the input ion-photon entangled state measured in Chapter 10. The red and blue dashed lines in Fig. 4.10 designate the pump powers needed to allow for equal conversion of both polarizations. These pump powers are chosen to give the maximum conversion efficiency of the polarization with the lowest peak efficiency, in this case the S-polarized light.

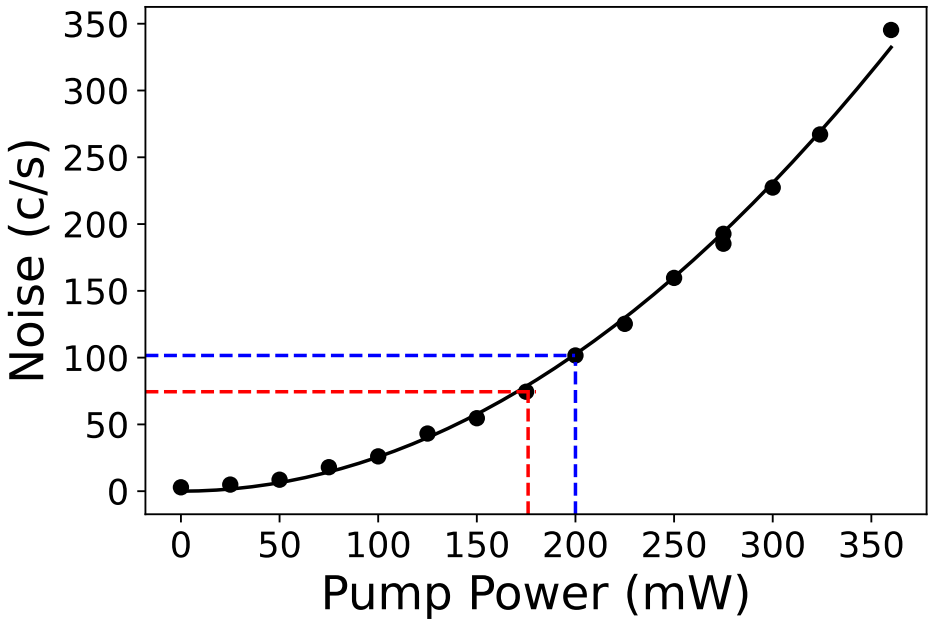

Figure 4.11: **Two-Way QFC Noise Measurement**. The data shown is background subtracted to only include noise resulting from the QFC setup. A quadratic fit is applied to the data. The red and blue dashed lines correspond to the noise expected when converting each polarization shown in Fig. 4.10.

With no 493-nm light present, we can also measure the noise photons produced by the setup as a function of pump power, in a manner similar to Sec.4.3.1. This is shown in Fig. 4.11, using a frequency filtering bandwidth of 3 nm, polarization filtering and running the converter

in the S-polarized direction (similar noise levels are found running in the P-polarized direction). Background counts ($\approx$ 170 counts/sec) due to detector dark noise as well as room lights are subtracted from this data. We see that we can expect around $\approx$ 100 counts/sec noise at peak conversion when running in single-polarization conversion mode. When converting both polarizations simultaneously, we see a factor of $\approx$ 2 increase in noise with pump running in both directions. The quadratic dependence in pump power (fit line in Fig. 4.11) leads us to believe that this noise is due to either leakage of second harmonic-generated light near 671 nm or 780 nm light produced via sum frequency generation between the 1343 nm pump light and SPDC produced by the pump near 1860 nm [143][65], but this has not been investigated further at this point.

In conclusion, the switch to parabolic mirrors for input and output coupling allowed for high conversion efficiencies for both input polarizations and is critical to the entanglement experiment demonstrated in Chapter 10. Additionally, the relatively low noise count rates can likely be improved through tighter bandwidth filtering using devices such as fiber Bragg gratings as is used in some of our single-polarization conversion work [29, 93]. This will be attempted in the future, after improvements to our detector background counts, which are at a comparable level. Given our current photon collection efficiencies, the photon conversion efficiency combined with noise counts leads to a $\approx$ 6% reduction to the ion-photon entanglement fidelity discussed in Chapter 10.

[65] For low conversion efficiencies, both SPDC and SFG are linear in pump power, making the combined effect quadratic.

Chapter 5: Quantum Frequency Conversion of Single Photons from a Trapped Ion

In this chapter, I present measurements we have made to characterize the ion as a single photon source and to verify the preservation of the quantum properties of the emitted photons after frequency conversion. First, in Sec 5.1, I provide some theoretical background on normalized second order intensity correlation functions, $g^{(2)}(\tau)$, which we use to characterize our photons. In Sec. 5.2, I present and discuss experiments where we measure $g^{(2)}(\tau)$ using 493-nm photons emitted from the ion converted first to 780 nm using one stage of frequency conversion. This result has served as the backbone for all of the other experiments demonstrated in this thesis and has provided our lab a unique niche in interacting our photons with neutral-atomic-based quantum systems. Finally, in Sec. 5.3, I present work performed in collaboration with Edo Waks and graduate student Uday Saha that demonstrates the conversion of 493 nm photons from our ions to 1534 nm, enabling long-distance[1] trapped-ion quantum networking by using two concatenated frequency conversion stages. To my knowledge, this is the only such work sending trapped ion photons through two successive stages of conversion in order to reach telecommunication wavelengths. These final two sections correspond to two of our lab's publications, [92] and [29] respectively, which have been slightly adapted for use in this thesis.

[1] This has also enabled coupling of our photons into photonic integrated circuits [24].

5.1 The Second Order Correlation Function

The (non-normalized) second order intensity correlation function is typically defined formally as [144, 145]

$$G^{(2)}(t,\tau) = \left\langle E^{\dagger}(t)E^{\dagger}(t+\tau)E(t+\tau)E(t)\right\rangle, \tag{5.1}$$

where $E(t)$[2] represents the positive frequency part of the electric field mode at time t and τ represents a time delay relative to t. If we assume that the field is statistically stationary[3], we can drop the t dependence and write $G^{(2)}(\tau) = G^{(2)}(t,\tau)$. We can normalize this function using the intensity of each field, $I(t) = E^{\dagger}(t)E(t)$, to arrive at

$$g^{(2)}(\tau) = \frac{\left\langle E^{\dagger}(t)E^{\dagger}(t+\tau)E(t+\tau)E(t)\right\rangle}{\left\langle E^{\dagger}(t)E(t)\right\rangle \left\langle E^{\dagger}(t+\tau)E(t+\tau)\right\rangle}, \tag{5.2}$$

which is known as the normalized second order intensity correlation function.

Quantum mechanically, we can write $g^{(2)}(\tau)$ in terms of the ladder operators of the quantized electromagnetic field $\hat{a} \propto e^{i\omega t}E(t)$ as

$$g^{(2)}(\tau) = \frac{\left\langle \hat{a}^{\dagger}(t)\hat{a}^{\dagger}(t+\tau)\hat{a}(t+\tau)\hat{a}(t)\right\rangle}{\left\langle \hat{a}^{\dagger}(t)\hat{a}(t)\right\rangle \left\langle \hat{a}^{\dagger}(t+\tau)\hat{a}(t+\tau)\right\rangle} = \frac{\left\langle \hat{a}^{\dagger}(t)\hat{a}^{\dagger}(t+\tau)\hat{a}(t+\tau)\hat{a}(t)\right\rangle}{\left\langle \hat{n}(t)\right\rangle \left\langle \hat{n}(t+\tau)\right\rangle}, \tag{5.3}$$

where $\hat{n} = \hat{a}^{\dagger}\hat{a}$ is the number operator.

It is at this point we can begin to see the usefulness of $g^{(2)}(\tau)$. Consider $\tau = 0$. We then

[2] Technically, $E(t)$ can be defined to have positional dependence as well, where we'd have $G^{(2)}(t_1, t_2, r_1, r_2)$, but for this discussion we are only interested in a single position ($r_1 = r_2$).

[3] Meaning that the processes producing the electric/light field are constant or "stationary" in time.

have

$$g^{(2)}(0) = \frac{\langle \hat{n}(t)(\hat{n}(t)-1)\rangle}{\langle \hat{n}(t)\rangle^2}. \tag{5.4}$$

If our quantum state can be described by a Fock state $\psi = |n\rangle$, one finds

$$g^{(2)}(0) = 1 - \frac{1}{n},\ n \geq 1. \tag{5.5}$$

Therefore we see that if we have an input Fock state, measurement of $g^{(2)}(0)$ tells us that state, making it a useful parameter when working with certain types of quantum photonic states. In particular, for a single photon state ($\psi = |1\rangle$), $g^{(2)}(0) = 0$. This is the value of $g^{(2)}(0)$ we expect to be able to attain with our trapped ion system, before and after frequency conversion of the photon. For a true single-photon emitter, such as a trapped ion, we also have [144]

$$g^{(2)}(0) \leq g^{(2)}(\tau), \tag{5.6}$$

which is an indication of photon anti-bunching, or in other words, this means that photons are more likely to be spaced far apart rather than close together, especially for small τ.

Furthermore, for a more general quantum state $\psi = \sum_n c_n |n\rangle$ it can be shown [145]

$$1 - \frac{1}{\langle n\rangle} \leq g^{(2)}(0) \leq 1. \tag{5.7}$$

This should be compared to the classical case where,

$$g^{(2)}(0) = \frac{\langle I^2(0)\rangle}{\langle I(0)\rangle^2} \geq 1, \tag{5.8}$$

where the inequality is due to the definition and positivity of the classical variance $\mathrm{Var}(A) = \langle A^2\rangle + \langle A\rangle^2 \geq 0$ [94,95]. Therefore, one can see that a measurement of $g^{(2)} < 1$ is a tell-tale sign of non-classical light - the light must have some quantum component to it. Thus, $g^{(2)}(0) = 1$ is known as the classical limit for the second order intensity correlation function.

From the discussion above, it is clear that a measurement of $g^{(2)}(\tau)$, especially near $\tau \approx 0$ is extremely useful for determining if a light source is truly a quantum single photon source. Such a measurement essentially amounts to determining the probability of a photon detection event at time $t + \tau$, given that a photon was originally detected at time t. Measuring successive single photon events with such small delay times, however, is generally not possible with the bandwidth/deadtime of current single photon detectors[4]. The detectors[5] in our lab for instance, exhibit dead times on the order of ≈ 50 ns after detection of a photon during which a second photon, if present, cannot be detected. This would prevent measurement of $g^2(\tau)$ for $\tau < 50$ ns. Given that our ion has the ability to emit a single photon every ≈ 10 ns or so, this would prevent us from measuring it as a single photon source.

This problem can be circumvented through use of an extra detector and a beamsplitter, in what is known as a Hanbury-Brown-Twiss interferometer [146] as shown in Fig. 5.1. This allows for the measurement of two successively emitted photons, one on each detector, for delay times down to $\tau \approx 0$, limited now by the timing resolution of the detectors (and of the electronics used to time tag the detector signal), which are typically well below 100 ps. Typically, photons are

[4] In theory, you could use a photon-number-resolving detector, but such technology is still in its infancy and is generally not commercially available.

[5] Perkin Elmer SPCM-AQR

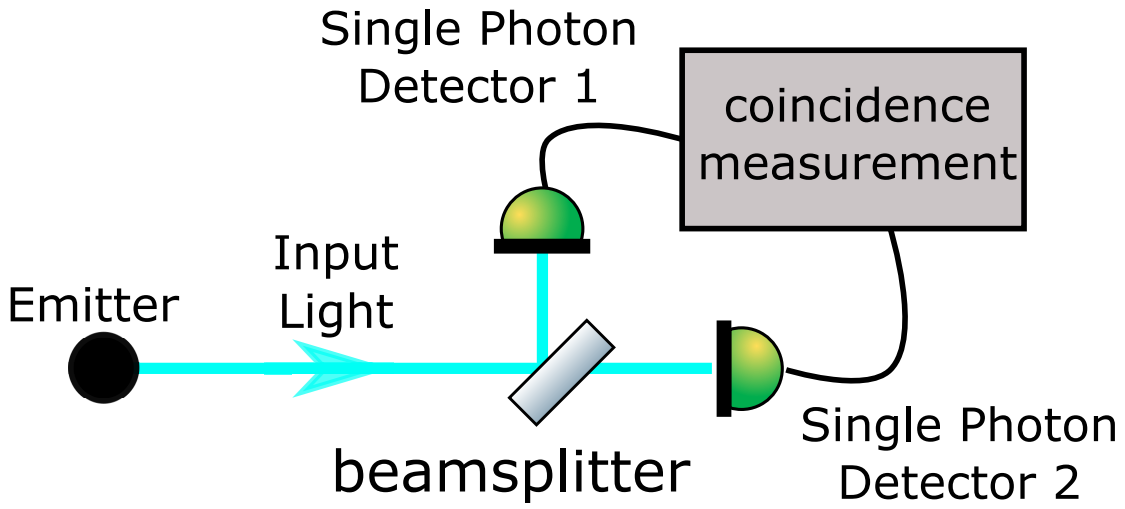

Figure 5.1: **Hanbury-Brown-Twiss Interferometer**. Input light from a photon emitter is split at a beamsplitter and sent to one of two detectors. Photon detection events at each detector are used to measure if two photons were coincident at the beamsplitter at the same time.

time tagged, and coincidences are measured either live or in post processing to determine $g^{(2)}$, as will be discussed in the next sections.

5.2 Single Photons from a Trapped Ion Converted to Neutral Atom (Rb) Wavelengths

In this section, I describe our lab's first results [92] showing the conversion of 493 nm photons, emitted from a single barium ion, to a 780 nm wavelength tuned to the D_2 transition in neutral ^{87}Rb. We verify this via measurements of $g^{(2)}(\tau)$ (Sec. 5.1) before and after this frequency conversion. Conversion to this wavelength is critical for enabling hybrid quantum networking components consisting of both trapped ions and neutral atoms, and as discussed in Sec. 4.3, greatly increases the range of a Ba^+-based network through reduced fiber losses.

When performed, this work was among the first to demonstrate the frequency conversion of single photons from a trapped ion, with other groups have converting photons from Ca^+ to 1530 nm preserving their quantum statistics [33] and, separately, to 1310 nm with ion-photon

entanglement demonstrated [34]. This first experimental result from our group paved the way for the hybrid-species quantum networking experiments discussed in Chapters 6 and 7, with the same basic setup being used in both experiments. Therefore, although we have since greatly improved our 780-nm QFC setups since this demonstration, I've chosen to keep it in this thesis.

5.2.1 Experimental Setup

As shown in Fig. 5.2 a and discussed in Chapters 2 and 3, we trap and cool a single single $^{138}Ba^{+}$ ion and collect light from both collection windows using two 0.4 NA lenses. The single photons used in this experiment are produced by continuously Doppler cooling the ion. Collection lens A sends light directly to the photomultiplier tube (PMT) located in our imagaing setup. Photons collected via lens B are coupled into a single mode fiber (SMF) (coupling efficiency of $\sim$17%) and sent either directly to an avalanche photon-detector (APD) [6] or sent to the frequency conversion setup (Fig. 5.2(b)) where they are converted to 780 nm and sent to the APD. With the Doppler beam frequencies stabilized to $\sim$2 MHz, we observe a maximize fluorescence rate from the ion of $\sim$20,800 c/s on the PMT, and the measured 493 nm photon count rate on the APD is $\sim$26,600 c/s.

To convert photons to 780 nm, we use the fiber pig-tailed frequency conversion setup described in Sec. 4.3.1 and shown in Fig. 5.2 b. To facilitate hybrid interactions, it is important that the PPLN DFG output be tuned to resonance with the ^{87}Rb D_2 transition at 384.228 THz [147] while at the same time the input frequency needs to be resonant with the barium ion. This double resonance condition gives two constraints which are met by identifying appropriate pump wavelength and PPLN oven temperature operation points. To determine these values, the DFG

[6] Perkin Elmer: SPCM-AQR-15. Quantum efficiencies of $\approx 40\%$ at 493 nm and $\approx 60\%$ at 780 nm.

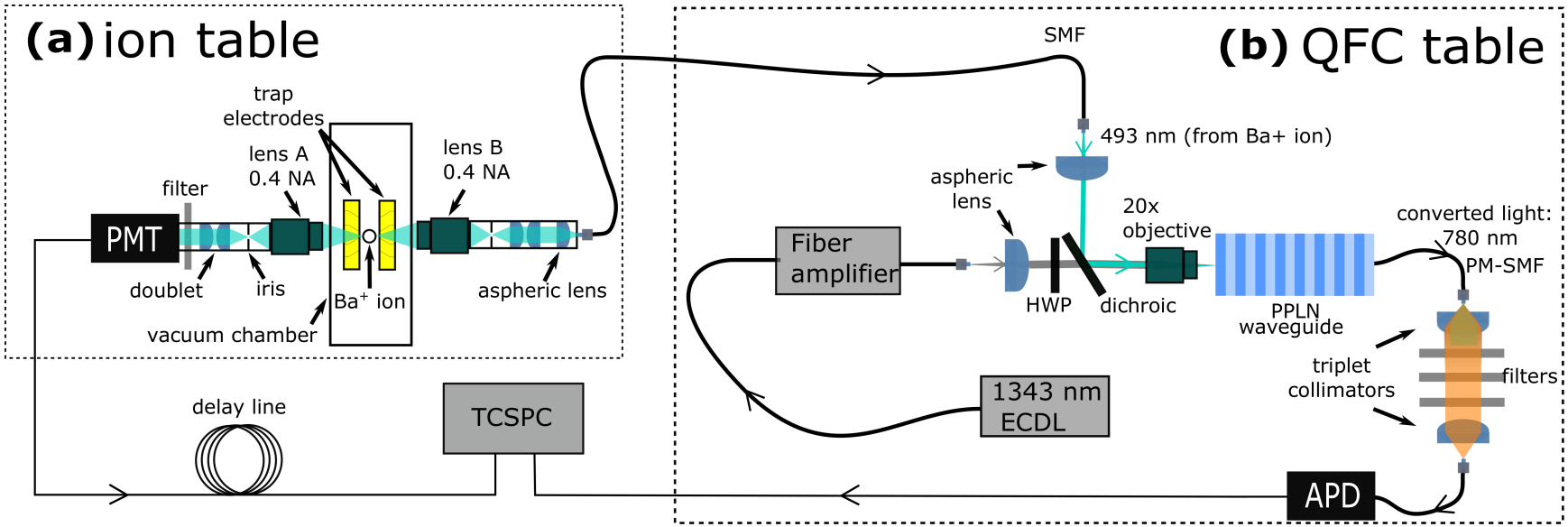

Figure 5.2: **Experimental Setup for 780 nm Single Photon Measurements.**(a) Schematic of the trapped ion setup showing two separate optical collection paths which are situated on opposite sides of an ultra-high vacuum chamber. The vacuum windows are anti-reflection coated and allow optical access for two 0.4 NA objectives, lens A and lens B. The 493 nm photons collected by lens B are collimated and launched into single mode fiber (SMF) of a few meters in length. A photomultiplier tube (PMT) measures photons collected by lens A. (b) Shows the quantum frequency conversion (QFC) setup including a dichroic mirror that combines 493 nm and pump photons. A 20x objective couples the combined light into a periodically poled lithium niobate (PPLN) waveguide with a small length of polarization maintaining single mode fiber (PM-SMF) butt-coupled to its output facet. The light emitted from this fiber is free-space propagated to allow for use of optical filters and then recoupled into a standard SMF, a few meters in length, for detection by an avalanche photodiode (APD). Photon detection events are monitored with a time-correlated two-channel single photon counter (TCSPC).

output was maximized at a pump wavelength near 1336 nm at a PPLN oven temperature of 35.5°C. The DFG's wavelength is then tuned to that of the ^{87}Rb D_2 line by increasing the pump wavelength to a value of 1343.169 nm and tuning the PPLN temperature to 43°C. All of the tuning is carried out with the 493 nm laser light locked to Ba^+ resonance. Fine tuning of the DFG signal frequency is possible by adjusting the pump wavelength as shown in Fig. 5.4.

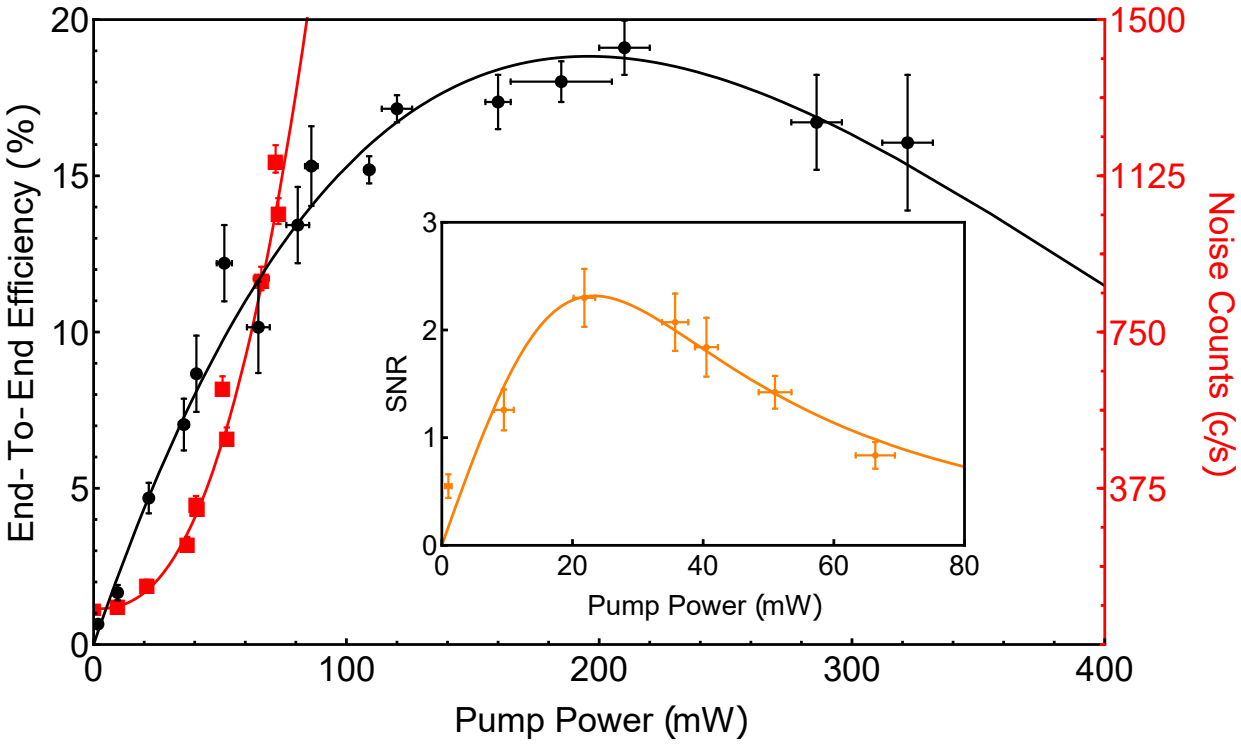

Figure 5.3: **Signal-To-Noise Ratios for 780 nm Single Photon Measurements.** The end-to-end conversion efficiency of the DFG from 493 nm to 780 nm (black circles and left-hand axis) and noise produced in the bandwidth allowed by our filtering (red squares and right-hand axis) as a function of pump power coupled into the waveguide. The inset shows the signal-to-noise ratio of the conversion process for the case where the signal is from the fiber coupled ion-light as described in the main text. The error bars on the pump power are from fluctuations of the measured power and the error bars on the efficiency are primarily from DFG signal power fluctuations.

While operating at the maximum conversion efficiency increases the number of 780 nm photons produced, the larger pump power required results in increased noise photons (Sec. 4.2.3). Therefore, when frequency converting light from the ion, it is critical to chose a pump power that

is close to the maximum signal-to-noise ratio (SNR) of the DFG light. Figure 5.3 shows the noise inside the bandwidth of the filters as a function of pump power coupled into the waveguide as well as the resulting signal-to-noise (SNR) (inset 5.3) for the case of a signal from fiber coupled ion fluorescence.

For single photon measurements we used a pump power which provided close to the optimal SNR (shown in Fig. 5.3 inset) and the pump wavelength and oven temperature shown in Fig. 5.4. With $\sim$40 mW of pump light[7] coupled into the waveguide, we measure a total noise level of $\sim$300 c/s on the APD, which includes an APD detector dark count rate of $\sim$100 c/s. Importantly, there were no detectable levels of 493 nm or 650 nm ion-light making it through the filters, as we observe count rates equal to that of the APD dark counts when only the ion-light is present.

When both 493 nm photons from the ion and the 40 mW pump light are present in the PPLN waveguide, the measured count rate of the the 780 nm DFG light is $\sim$600 c/s, giving a SNR of $\sim$2. A conversion efficiency of $\sim$2.3 $\%$, including all optical and fiber coupling losses, is determined by taking the ratio of the converted photon count rate to the 493 nm photon count rate as measured directly on the APD ($\approx$ 26,100 c/s). Taking into account a factor of two loss in a fiber patch cable between the ion and QFC tables, another factor of two loss for polarization selectivity of the QFC process and other optical loses, this value is consistent with the classically measured value shown in Fig. 5.3[8].

[7] We chose to operate here rather than the peak SNR near 20 mW due to the fact that the DFG efficiency at this point is linear, meaning we could run twice as fast, without *too* much SNR loss.

[8] These losses have since been removed.

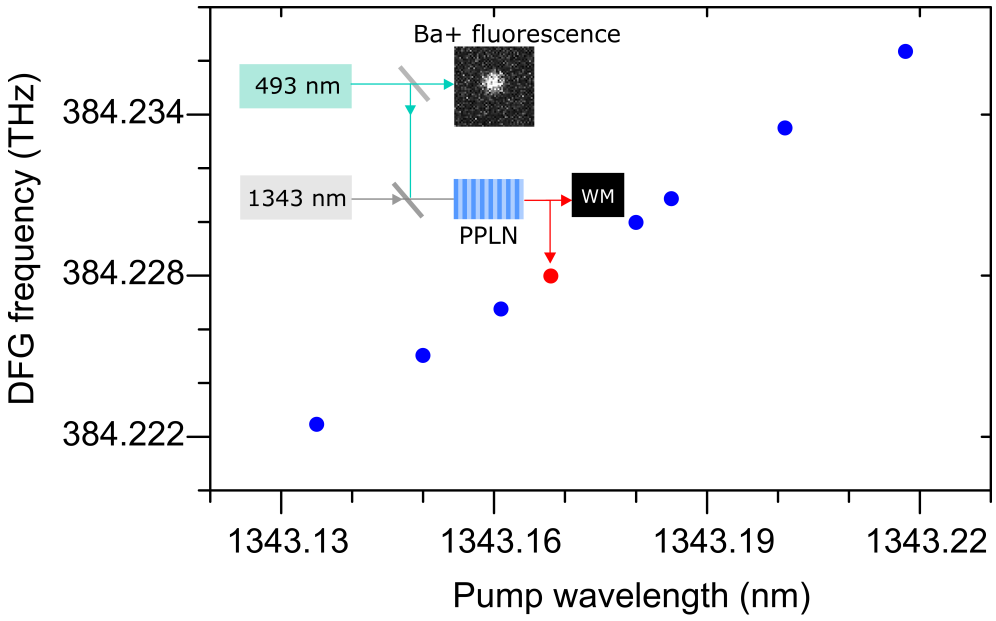

Figure 5.4: **Tuning to Rb Resonance.** Output DFG output frequency is plotted as a function of the pump wavelength near 1343 nm. The inset is a block diagram of the setup showing simultaneous resonant ion fluorescence when the Ba^+ ion Doppler cooling laser ($^2S_{1/2}$ - $^2P_{1/2}$ transition) is locked to 607.425690(2) THz while the DFG PPLN output is at the ^{87}Rb D_2 line frequency of 384.227982(2) THz [147] (red data point) as measured to a 2 MHz accuracy using a wavemeter (WM) (HighFinesse: WSU/2). The PPLN temperature is held at a constant temperature of 43°C during this procedure.

5.2.2 Results

The measurement of the $g^{(2)}(\tau)$ correlation function of single photons produced by the Ba^+ ion was performed using the light collected from the two sides of the ion, as a function of the relative delay, τ, between detection events on either side. In other words, this approach is equivalent to a Hanbury-Brown-Twiss apparatus (Sec. 5.1) where the ion can be treated as the beam splitter. Photons at 493 nm detected by the PMT are correlated to APD-detected photons either directly from the ion, or after after frequency converion to 780 nm.

The output of each detector is sent to a time-correlated two-channel single photon counter (TCSPC) with a resolution of 512 ps[9]. Using the counter's histogram mode, the arrival of a pulse from the PMT triggers a timing circuit which measures the time until a pulse is received from the APD. An electrical delay line was added to the PMT line to allow measurement of negative delay times. The time between pulses on each detector was then binned into 512 ps wide bins. To calculate the $g^{(2)}(\tau)$, the raw coincidence counts were normalized using [148, 149]

$$g^{(2)}(\tau) = \frac{N(\tau)}{N_{PMT} N_{APD} \delta_t T}. \tag{5.9}$$

Here, $N(\tau)$ is the number of coincidence counts in a bin, δ_t is the size of the time bin (512 ps), T is the total integration time, and N_{PMT} and N_{APD} are the total count rates in the PMT and APD channels respectively. The normalized and delay-line compensated $g^{(2)}(\tau)$ measured between non-converted photons (blue) and converted and non-converted photons (red) are shown in Fig. 5.5. The insets show the raw coincidence count data with the electronic delays of 91.65 ns and 53.76 ns present. The periodic oscillation of the counts is due to micromotion of the ion

[9] PicoQuant: PicoHarp 300.

in the trap at a frequency of $\Omega/2\pi$ = 38.4 MHz. The measured $g^{(2)}(0)$ of 493 nm photons directly emitted by the ion and between 493 nm photons and frequency converted 780 nm photons were measured to be 0.167 $\pm$ 0.022 and 0.645 $\pm$ 0.055 respectively.

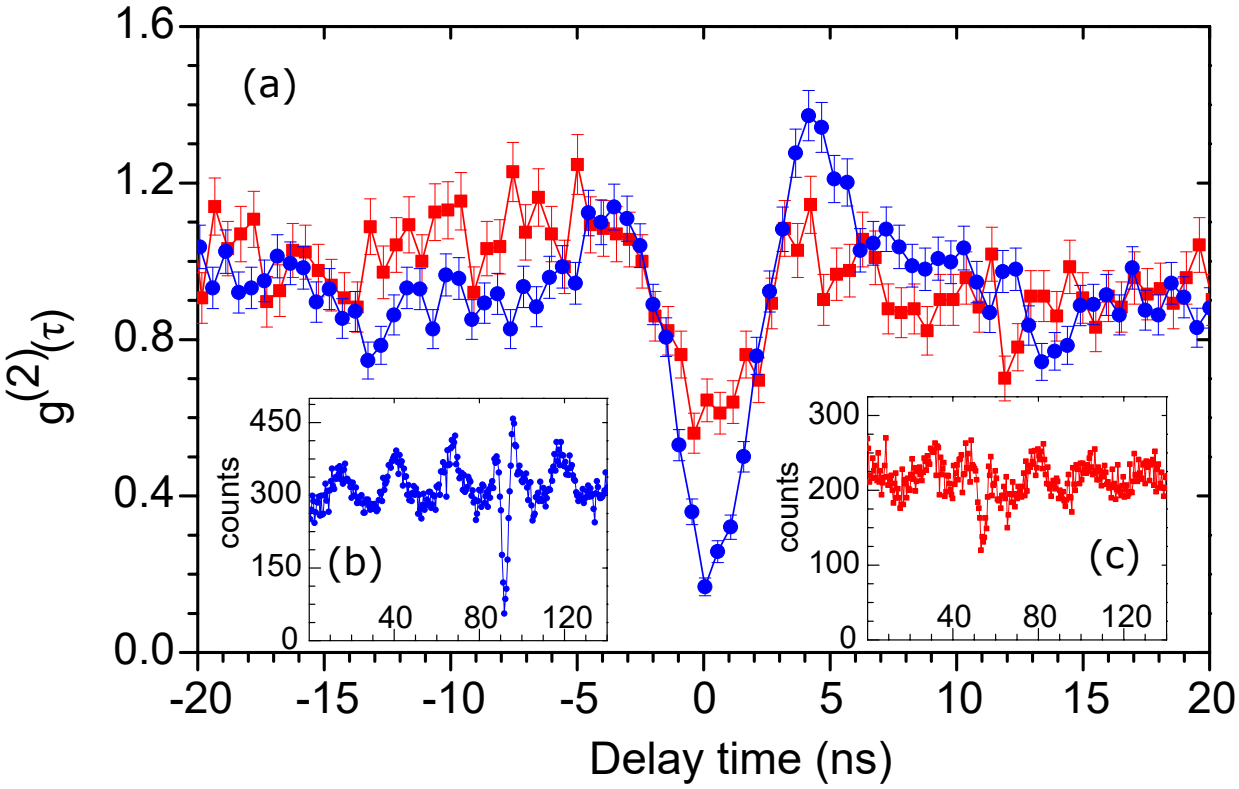

Figure 5.5: **Correlation Measurements.** (a) The $g^{(2)}(\tau)$ correlation function measured between non-frequency converted 493 nm photons (blue) where $g^{(2)}(0) = 0.167 \pm .022$ and between 493 nm and converted 780 nm photons (red) where $g^{(2)}(0) = 0.645 \pm .055$. These measurements agree with expected values given by Eqn. 5.10 given that $\delta_t = 512$ ps. The error bars represent the shot noise from each detector. The insets show the raw, un-normalised, coincidence counts where (b) $N_{APD} = 26,600$ c/s and $N_{PMT} = 19,700$ c/s and $T = 20$ minutes and (c) $N_{APD} = 930$ c/s and $N_{PMT} = 20,500$ c/s and $T = 6.13$ hours.

In a noiseless $g^{(2)}(\tau)$ measurement with infinitely small bin widths, zero coincident counts are expected at $\tau = 0$ from a single photon source, such as an ion. Experimentally however, a finite bin width must be used and noise detector clicks are inevitable. The finite bin width is used to calculate a minimum $g^{(2)}(0)$ of $a = 0.035$, using the methods described in [148]. To take into account the effects of noise and finite bin width, the following is used [150]

$$g^{(2)}_{exp}(t) = 1 + \left(\frac{SNR}{1+SNR}\right)^2 (a-1), \tag{5.10}$$

where SNR is the ratio of the histogram counts per second due to the signal from the ion to the histogram counts per second due to correlations with noise. The latter includes PMT noise-APD noise correlations, PMT signal-APD noise correlations and PMT noise-APD signal correlations.

For the correlation measurement solely between the unconverted 493 nm photons from the ion, the main noise sources were from correlations between the PMT signal and the APD noise and between the PMT noise and APD signal. The histogram count rates from each of these sources was measured to be 276 c/s and 359 c/s respectively. Including a small PMT noise-APD noise contribution (6 c/s) a total noise rate of 641 c/s was measured. Given a total histogram count rate of 10,800 c/s a SNR of ≈15.8 is achieved. The expected $g^{(2)}_{exp}(0)$ is therefore found to be 0.146. This value is in agreement with the measured value of $0.167 \pm .022$.

The measurement between the unconverted 493 nm photons and converted 780 nm photons has noise counts which are dominated by correlations between signal PMT counts and APD noise counts. The measured histogram count rate due to such correlations was found to be 200 c/s and the other noise sources produced a combined 20 c/s. With a total count rate of 615 c/s, this corresponds to a signal to noise ratio of 1.80. The measured value of $g^{(2)}(0)$ was found to be 0.645 ± 0.055 in agreement with the expected value of 0.602, and is also significantly below the classical limit (Sec 5.1), demonstrating the conversion of single photons from 493 nm to a neutral Rb compatible 780 nm.

5.3 Frequency Conversion of Trapped Ion Photons to the Telecommunications C-band

In this section, I demonstrate our lab's work on the QFC of S-P dipole generated 493-nm photons originating from a single trapped $^{138}Ba^{+}$ ion to the telecommunications C-band. To span this large frequency range, we employ two concatenated QFC stages. As discussed in Sec. 4.3, this two-step approach circumvents the noise produced via spontaneous parametric down conversion (SPDC, Sec. 4.2.3) present in any single-stage QFC scheme taking visible light to the C-band [32, 133] and still offers the advantage of having the first-stage conversion resonant with neutral-atom based systems (Sec. 5.2) for integration into a hybrid quantum network [49–51, 93]. We show that each QFC step preserves both the pulse shape and quantum statistics of 493-nm photons produced by the Ba^{+} ion. These results demonstrate the largest QFC shifts achieved using trapped ions, and provide a key step towards long-distance hybrid quantum networks using trapped ion ground-state qubits.

This section has been adapted from our published work [29], performed in collaboration with the research group of Edo Waks. In this experiment, James Siverns and myself ran the trapped ion setup and first stage of frequency conversion. Uday Saha, Jake Cassell and I set up and characterized the second stage of conversion (I would like to highlight here that the heavy filtering required here was set up by Uday). Finally, I set up data collection and performed analysis of the results.

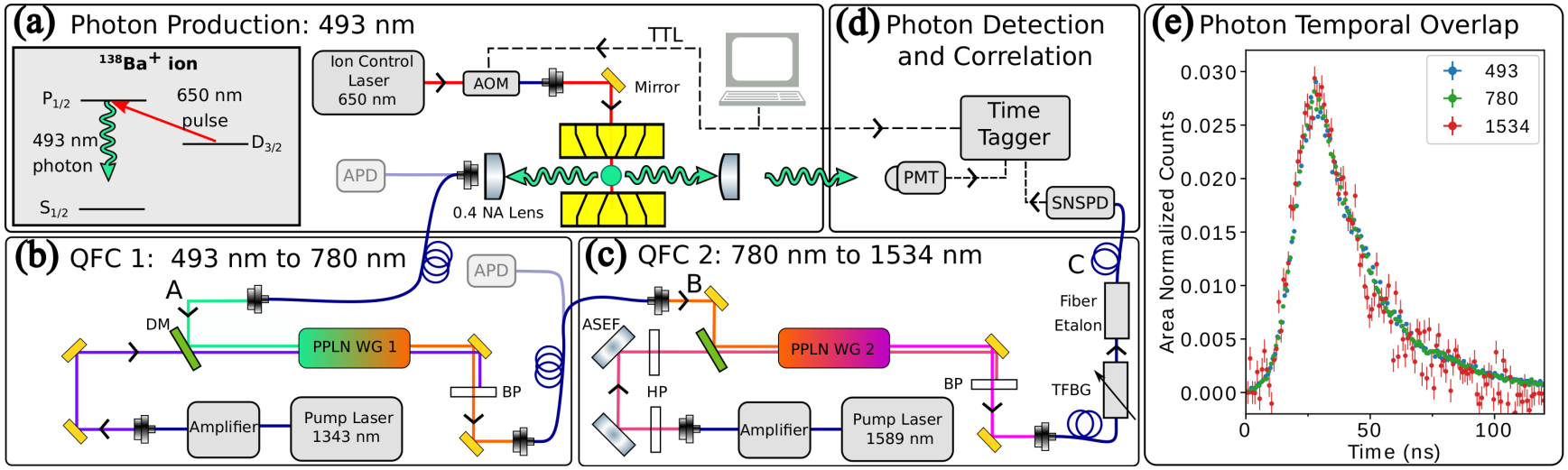

Figure 5.6: **Experimental Setup for Two-Stage Frequency Conversion.**(a) A TTL pulse triggers 650-nm light, exciting a $^{138}Ba^{+}$ ion and allowing for the spontaneous emission of a 493-nm photon. Emitted photons are sent to either a PMT or are fiber coupled and sent to an APD or QFC 1. (b) QFC 1 combines 493-nm single photons with 1343-nm light in PPLN WG 1, producing fiber-coupled 780-nm single photons via DFG. After filtering via a 3 nm band pass filter (BP), these photons are either detected by an APD or sent to QFC 2. (c) QFC 2 combines 780-nm single photons with 1589-nm light in PPLN WG 2, producing fiber-coupled 1534-nm single photons via DFG. A tunable fiber Bragg grating (TFBG) and fiber etalon frequency filter the output of QFC 2, reducing noise. To filter out 1534-nm light present in the pump, we use amplified spontaneous emission filters (ASEF) and 1550 nm high pass filters (HP). (d) Detection events for the PMT and SNSPD and TTL trigger signal are time-tagged for two-photon correlation measurements. (e) Overlap of single photon arrival time histograms at each wavelength.

5.3.1 Experimental Setup

The experimental setup is shown in Fig. 5.6, with photon collection performed as described in Sec. 5.2 and in Sec. 3.4.3. Again, one 0.4 NA lens collects single photons emitted by the ion and sends them to a free-space single photon counting photomultiplier tube (PMT). For this section, I will refer to the photons collected by this lens as PMT-photons. Another 0.4 NA lens couples single photons into a single mode fiber. These 493-nm photons are either sent to a fiber-coupled single-photon counting avalanche photodiode (APD) or to QFC 1 and QFC 2 for down conversion (Figs 5.6 b and c).

We produce single photons from the ion using the three step process of initialization, excitation, and spontaneous emission described in Chapter 2. This is done in contrast to the photon production method using Doppler florescence in Sec. 5.2, to better simulate how we would actually produce photons in a quantum network. After a period of Doppler cooling, the ion is initialized into $\left|5D_{3/2}, m_j = 3/2\right\rangle$ using a 781 ns pulse containing π and σ^- polarized 650-nm light and π polarized 493-nm light. After a 200 ns delay with no light incident on the ion, a 200 ns pulse of σ^+ polarized 650-nm light excites the ion to $\left|6P_{1/2}, m_j = 1/2\right\rangle$, allowing for spontaneous emission of a single 493 nm photon (Fig. 5.6 a).

We convert 493-nm photons emitted by the ion to the C-band using two concatenated QFC setups, illustrated in Figs 5.6 b and c. Each setup is built in the free-space scheme described in Sec. 4.3.2. As discussed in Sec. 4.3, QFC 1 converts 493 nm photons to 780 nm photons using a 1343 nm pump laser and QFC 2 converts 780 nm photons to 1534 nm using a pump at 1589 nm. Using laser light, we measure the efficiency of QFC 1 from the output of the 493-nm input fiber to the output of the 780-nm fiber (A to B in Fig. 5.6) as shown in Fig. 5.7. At the peak

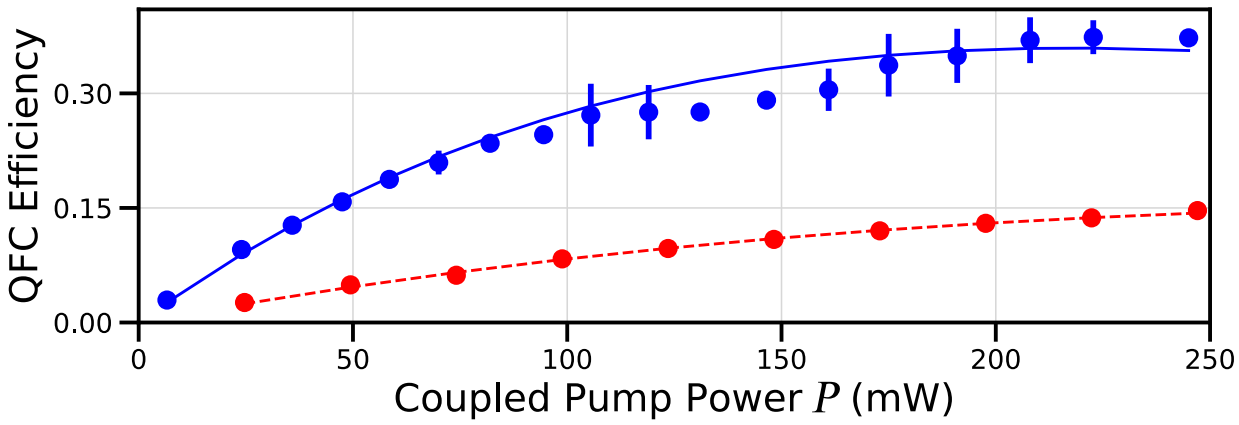

Figure 5.7: **Two-Stage QFC Conversion Efficiencies.**Efficiencies of QFC 1 (blue) and QFC2 (red), measured using low level laser light. Curves represent fits to Eqn. 4.25. Fitted conversion efficiencies are 0.36 and 0.15 for QFC 1 and QFC 2 respectively. Uncertainties represent fluctuations in efficiency observed over measurement.

QFC efficiency of ≈ 0.37, 320 cps noise are detected on our APD after the output 780-nm fiber, including ≈ 100 cps detector dark noise.

In QFC 2 the pump wavelength is very close to the target wavelength of 1534 nm. This stage therefore requires additional noise filtering when compared to QFC 1. In addition to using an amplified spontaneous emission filter[10] before the PPLN to remove any 1534-nm light present in the 1589-nm pump, we use the following components at the output of the converter:

- Free-space interference filters[11] with a 3 nm bandwidth.
- A tunable fiber Bragg grating[12] with a bandwidth of 19 GHz.
- A temperature-stabilized fiber etalon[13] with a bandwidth of 46.1 MHz.

Care must be taken in order to properly transmit photons through this narrow bandwidth filtering. With the 493-nm photon's frequency set by the ion's emission profile, we leave the 1589 nm laser

[10] Coherent NoiseBlock
[11] Semrock NIR01-1535/3
[12] Advanced Photonics International
[13] Micron Optics FF24Z2

free-running[14] and adjust the 1343-nm pump frequency to achieve simultaneous phase matching[15] for both QFC stages and to ensure that the converted 1534-nm light is transmitted through the final filtering stage.

The efficiency of QFC 2 is measured, using laser light, as the ratio of the number of 1534-nm photons after filtering to the number of 780-nm photons at the output of the 780-nm fiber (B to C in Fig. 5.6 c). After QFC 2, photons are detected using a superconducting nanowire single photon detector (SNSPD) ($\approx 78\%$ detection efficiency). At a QFC efficiency of ≈ 0.15, shown in Fig. 5.7, we measure, ≈ 2950 cps noise on average after filtering, with a total filter transmission of $\approx 26\%$ for laser light, corresponding to a transmission of $\approx 19.7\%$ for ion-produced photons (linewidth $\Gamma/2\pi = 14.8$ MHz [151]), reducing the overall QFC efficiency to ≈ 0.03.

Additional non-fundamental losses are present which reduce the probability of photon detection at both 780 nm and 1534 nm. These include drift in the coupling of photons produced by the ion into the collection fiber, reductions in transmission through the second stage filtering due to drift in QFC pump frequencies ($\approx \pm 20$ MHz), and fiber butt-couplings ($\approx 50\%$ transmission) to connect each stage in a modular fashion. Additionally, half of the ion light is of the incorrect polarization to be converted, which can be remedied by re-configuring each QFC stage into a the configuration used in Sec. 4.3.3. With these additional losses included, we measure per-shot detection efficiencies of 1.04×10^{-3} for 493-nm photons (APD efficiency $\approx 43\%$), 1.23×10^{-4} for 780-nm photons over 4 hours of runtime and 6.18×10^{-6} for 1534-nm photons over 37.5 hours of runtime. This gives conversion efficiencies of 19.5% of 493-nm photons to 780 nm and 0.66% for 493-nm photons to the telecom C-band via the two concatenated conversion stages, ignoring

[14] At the time we did not have frequency control over this laser. This has since been remedied.
[15] Beforehand, we set the temperature of the PPLN crystals in both stages such that this would work.

photons lost due to incorrect polarization. Removal of fiber butt coupling losses would take QFC-1 close to the expected 37% photon conversion efficiency. The 1534-nm signal however, only reaches $\approx 45\%$ of its expected value given the known losses in the system. We attribute the remaining loss to factors such as drifts in pump frequency, polarization, and alignment over the experimental run time.

5.3.2 Results

To demonstrate that the QFC preserves the temporal pulse shape of the photons emitted by the ion, we perform time-resolved fluorescence measurements. We compare the temporal pulse shape of the photons at each stage of conversion in Fig. 5.6 e. Each of the photon profiles are area-normalized after background subtraction. The overlap of the photon profiles at each color demonstrates preservation of the photon temporal shape after each stage of QFC.

We characterize the preservation of quantum statistics after the frequency conversion via a measurement of the non-normalized second order intensity correlation function, $G^{(2)}(n)$ of photons emitted by the ion. Here, n represents the number of experimental cycles between photon detection events on separate detectors. As in Sec. 5.2, we measure correlations between PMT photons and fiber-coupled photons, treating the ion itself as a beamsplitter in a Hanbury-Brown-Twiss type setup. Three separate correlation functions are measured: $G^{(2)}_{493}(n)$, between PMT-photons and 493-nm fiber-coupled photons, $G^{(2)}_{780}(n)$, between PMT-photons and 780-nm photons produced by QFC 1, and $G^{(2)}_{1534}(n)$, between PMT-photons and 1534-nm photons produced by QFC 2. For each experiment, we time-tag and record all detector events as well as the trigger pulses tied to each experimental cycle. Additionally, we use both physical and in-software gating

to increase the signal-to-noise ratio of the data used for all correlation calculations.

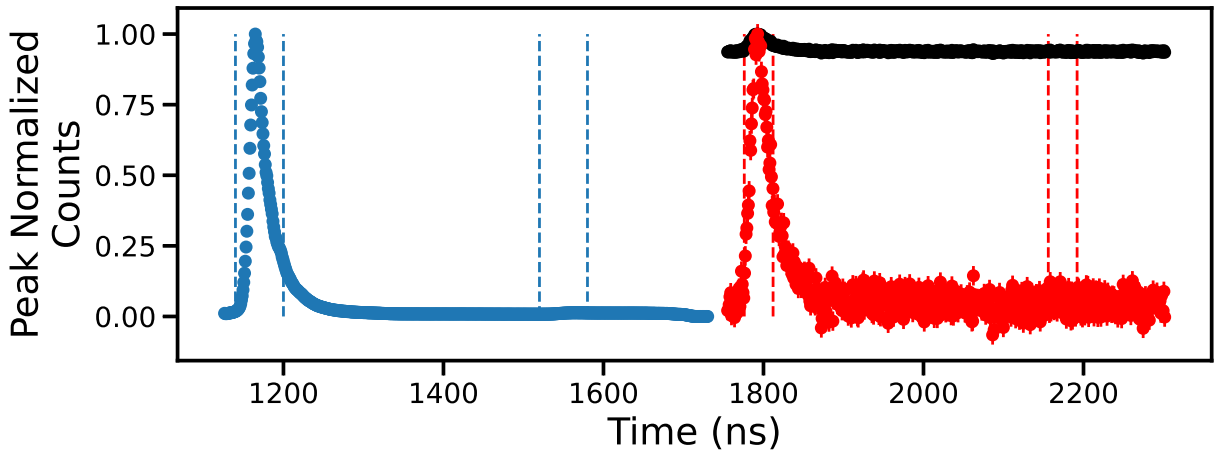

Figure 5.8: **Photon Arrival Histograms at 493 nm and 1534 nm.** Histograms of 493-nm PMT (blue) and 1534-nm (black) photon arrival times following the trigger TTL pulse. Dashed vertical lines indicate gate windows used for correlations (left) and noise measurements (right) for each curve. The red trace shows the background-subtracted 1534-nm data.

Using the collected time-tag data, we produce histograms of ion-produced photon arrival times, relative to the 650-nm excitation pulse. An additional 650-nm pulse is applied 380 ns after the start of the initial excitation pulse to enable measurement of the time-dependent profile of background light present during photon extraction. With these additional pulses and Doppler cooling, the experimental repetition rate is $\approx$ 420 kHz. The result of these measurements are shown in Fig. 5.8 for both 493-nm photons detected on the PMT and for 1534-nm photons detected on the SNDPD during the $G^{(2)}_{1534}(n)$ measurement. In the case of PMT-photons, 650-nm light scatter and detector dark counts dominate the measured background near 1600 ns. This is not the case for the converted 1534-nm photon profile shown in black in Fig. 5.8. Here, the background is attributable to detector dark counts and to Raman noise produced by the pump laser in QFC 2. Due to the low signal-to-noise ratio of the 1534-nm photon signal, we also display a background-subtracted 1534-nm photon profile in red in Fig. 5.8.

The vertical blue and red dashed lines in Fig. 5.8 indicate the software gate windows used to produce the the $G^{(2)}_{1534}(n)$ measurement, with similar gates being used for the 493-nm and 780-nm measurements. We calculate correlations between photons occurring in each signal window, and use the noise windows as a running measure of background in each channel. Gate widths of 60 ns are used for the 493-nm photons detected on both the PMT and APD, as well as for the 780-nm photon data. To increase the signal-to-noise ratio of the 1534-nm photon signal, we use a narrower 36 ns gate. To compensate for drifts in photon arrival time throughout the experiments (due to drifts in AOM turn on time), we reference the gate positions on all channels to the position of the PMT photon arrival time, with this position being updated every hour.

Figure 5.9 shows the results of all correlation measurements. The displayed correlations are calculated as the mean between $G^{(2)}(-n)$ and $G^{(2)}(n)$ for all $n \neq 0$, using the fact that $G^{(2)}(-n) = G^{(2)}(n)$ to reduce statistical fluctuations [50].

Theory lines in each plot of Fig. 5.9 represent the total number of expected correlations in the case of no quantum statistics (blue), as well as the expected noise correlation level (red), for a single photon source with the measured background noise. This noise correlation level includes correlations between the noise in each channel, as well as correlations between signal in one channel with noise in the other. With R photon production attempts over the course of each experiment, we calculate the background noise as

$$G^{(2)}_{theory}(0) = (C_1^S C_2^N + C_1^N C_2^S - C_1^N C_2^N)/R, \tag{5.11}$$

where C_x^S and C_x^N represent the total number of counts measured in the signal and noise windows, respectively, for the xth photon channel. In all cases, the dominant source of noise correlations

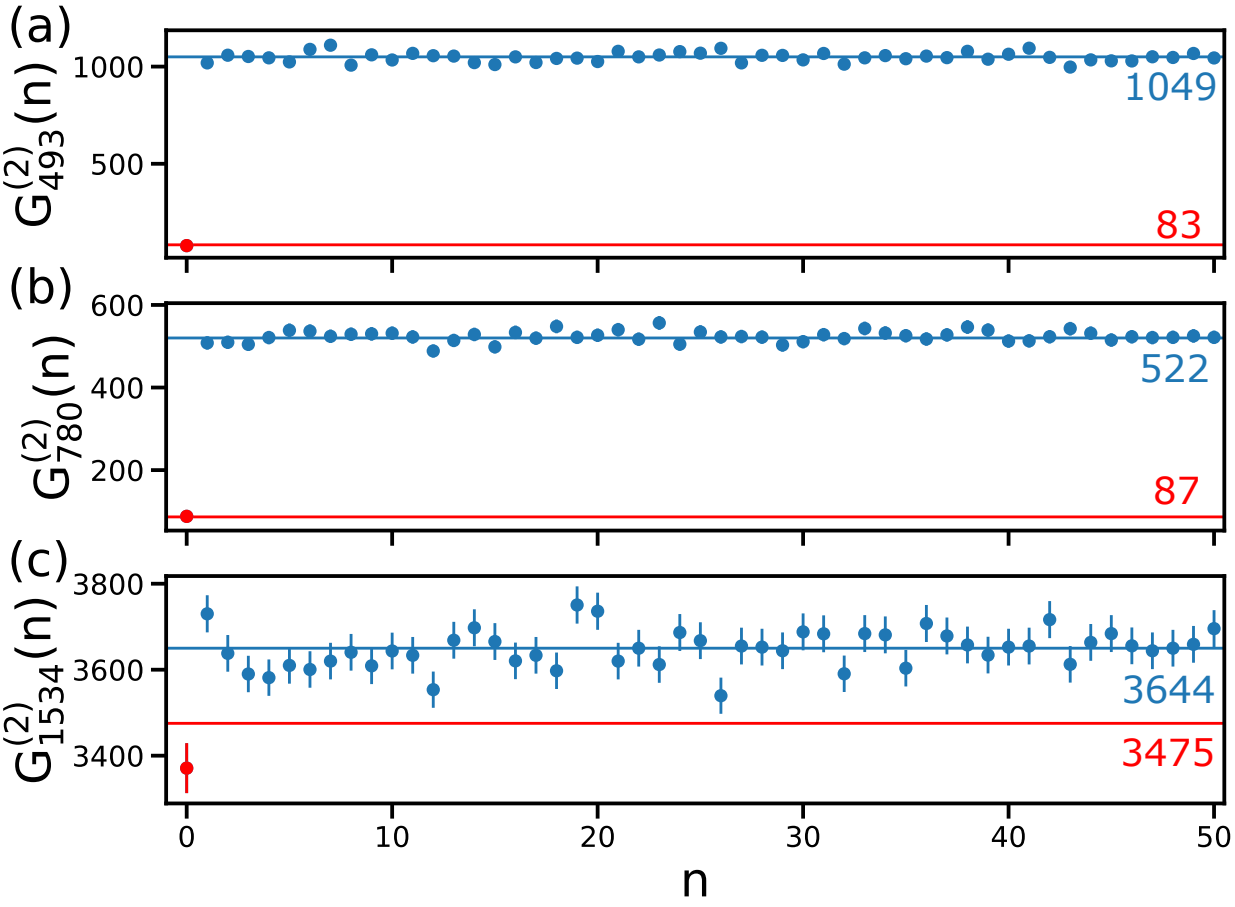

Figure 5.9: **Two-Stage QFC Correlation Measurements.** Correlations between 493-nm PMT photons and: (a) 493-nm photons detected on the APD, (b) 780-nm photons detected on the APD, (c) 1534-nm photons detected on the SNSPD. Lines in each plot represent the expected number of coincidences for $n = 0$ (red) and $n \neq 0$ (blue), calculated using Eqns 5.11 and 5.12. The colored text in each plot gives the values for these lines to the nearest whole number. Error bars are statistical. Run-times: (a) 1 hr, (b) 4 hr, (c) 37.5 hr.

are between PMT signal events and noise events on the APD (493-nm or 780-nm photons) or SNSPD channels (1534-nm photons). In a similar manner, we calculate

$$G^{(2)}_{theory}(n \neq 0) = C_1^S C_2^S / R. \tag{5.12}$$

As seen in Figure 5.9, we find good agreement between the measured and expected values for both $G^{(2)}_{493}(n)$ and $G^{(2)}_{780}(n)$. In addition, due to the relatively high single-photon signal-to-

noise ratio in these experiments (15.7 and 5.6 for the 493-nm and 780-nm photon channels respectively), we observe a large separation between correlations measured with $n = 0$ and correlations measured with $n \neq 0$ at these colors. With these comparisons, we establish the quantum statistics of the 493-nm photons emitted by the ion, and show that such statistics are preserved after conversion of these photons to 780 nm.

Measuring correlations between the 493-nm PMT photons and frequency converted 1534-nm photons, we a observe a large reduction in contrast between $G^{(2)}_{1534}(0)$ and $G^{(2)}_{1534}(n \neq 0)$, due to the low signal-to-noise ratio of 0.04 for the 1534-nm photon channel as measured with the SNSPD. After the experimental runtime of ≈ 37.5 hours[16], we observe a 4.8 σ separation between $G^2_{1534}(0)$ and $< G^2_{1534}(n \neq 0) >$, with $< G^2_{1534}(n \neq 0) >$, in good agreement with the value predicted using Eqn 5.12. We additionally find agreement between the measured value of 3371 ± 58 coincidences for $G^2_{1534}(0)$ and our predicted value of 3475 coincidences, with under 2σ separation between these values. This suggests that the measured value of $G^2_{1534}(0)$ is wholly attributable to noise correlations as calculated by Eqn 5.11.

5.3.3 Potential Improvements

Practical use of this two-stage conversion scheme will require improvements to the signal-to-noise ratio. This can be achieved by either an increase in the single photon signal or by altering the QFC pump wavelengths to reduce the amount of noise. The 493-nm photon probability can be increased using state-of-the-art photon collection [78, 79] or cavity-ion coupling techniques [32, 80], which have shown per-shot photon probabilities of up to 46% into a singe-mode fiber [80],

[16] Due to the low photon probability, we needed to run this long to acquire enough counts to statistically separate $G^{(2)}_{1534}(n \neq 0)$ and $G^{(2)}_{1534}(0)$.

as compared to the $< 1\%$ achieved in this experiment. Additionally, QFC 1 can be improved through the use of anti-reflection coatings on the PPLN and coupling optics, which we estimate to provide a factor of 1.5 improvement over the current setup. Finally, installing dedicated fiber connections between ion collection and the two QFC stages can remove fiber butt couplings that currently halve photon detection probability. These improvements could increase the SNR of the 1534-nm photon channel to > 10 without any reduction in noise.

The noise can be reduced through use of a pump laser at different wavelengths, optimized to minimize anti-Stokes Raman scattering noise [133] at the target signal, while still converting to the telecom S- or C-band. For instance, a pump at ≈ 1640 nm should reduce the noise by a factor of ≈ 10, and convert the photon to ≈ 1515 nm (S-band), with no changes to QFC 1 [133]. To greatly reduce noise, the second stage conversion could instead target the telecom O-band, requiring a pump laser at ≈1930 nm. This should reduce the anti-Stokes Raman scattering noise by well over a factor of 1000. This could serve as a good compromise between fiber transmission distance and noise reduction, while preserving the ability to integrate the system into a hybrid networking architecture.

In conclusion, we have shown the conversion of 493-nm single photons produced by a trapped Ba^+ ion to the telecom C-band. This two-stage conversion provides a pathway for C-band photons directly entangled with trapped ion ground-state qubits and also allows for potential hybrid interactions with neutral Rb-based quantum platforms. This work is an important step in connecting trapped ion quantum systems into existing telecommunications infrastructure for long-range trapped ion based quantum networks.

5.4 Summary

As shown above, through the careful construction of our frequency conversion setups as discussed in Chapter 4, we are able to demonstrate the frequency conversion of single photons from Ba^+ at 493 nm to both 780 nm and to the telecommunications C-band. We are able to do the former with relatively low noise, enabling the experiments discussed in the remainder of this thesis. The latter scheme is currently too noisy for use beyond some proof-of-principle experiments [24] and will likely lead our lab to pursue conversion to the telecommunications O-band instead.

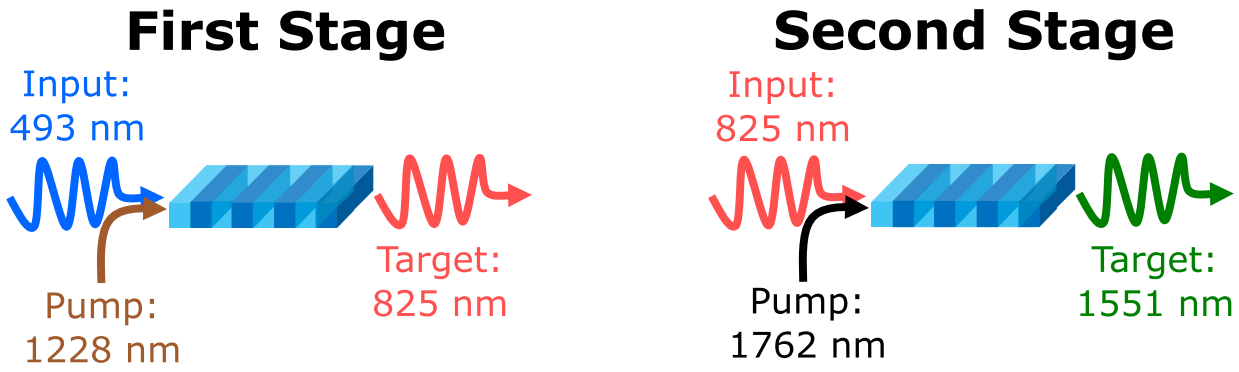

Figure 5.10: **Frequency Conversion Scheme Using Only Barium Lasers**

It is at this point I'd like to mention a scheme I've thought about to potentially allow for low-noise conversion to the telecommunication C-band using no additional lasers than what is already needed to control Ba^+. This scheme is outlined in Fig. 5.10, and consists of a first stage taking 493-nm photons to 825 nm via a pump at 1228 nm followed by a second stage using a pump at 1762 nm for conversion to 1551 nm. With the second stage pump much further from the target than our current scheme, this could drastically reduce the amount of noise photons detected, allowing for less filtering and higher overall efficiencies. The main drawback however,

is that this sacrifices the ability to interact with neutral Rb. This interaction is the focus of the next two chapters.

Chapter 6: Trapped Ion Slow Light

6.1 Introduction

Neutral atom vapors and magneto-optically trapped atoms are commonly used as slow-light media [152–154] either for classical pulses of light or single photons. In this chapter, I present an experiment where we Rb vapor to impose a tunable delay on photons originating from a trapped $^{138}Ba^{+}$ ion. Such tunable delays can be useful for photon synchronization when implementing networking protocols via photonic interference [51, 113]. Furthermore, with a slightly more complicated setup, these results can be extended to enable on-demand photon storage and retrieval via electromagnetically induced transparency (EIT) [39, 84, 85]. This basic presentation showcases how the quantum frequency conversion techniques developed in Chapters 4 and 5 can enable the integration of normally inaccessible quantum technologies into a trapped ion based quantum network for enhanced operation. This chapter is adapted from our published work [93] for use in this thesis.

6.2 Theory

To implement slow light, we require a medium for our photons to travel through with a low group velocity. These conditions can be achieved by tuning photons to a frequency between

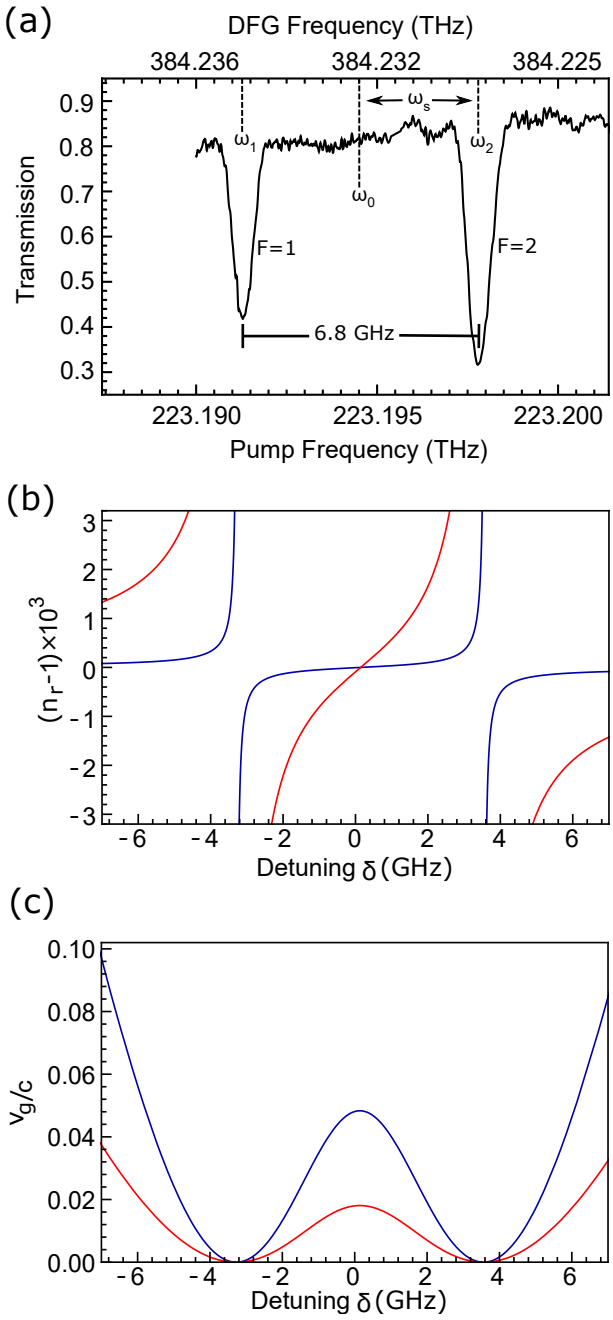

Figure 6.1: **Absorption, refractive index and group velocity within a warm ^{87}Rb vapor.** (a) Absorption profile of the ^{87}Rb D_2 line using 780 nm obtained via quantum frequency conversion (QFC) from 493 nm laser light with the cell at room temperature. The pump laser's mode-hop free tuning range limits the frequency tuning range. The refractive index, (b), and group velocity, (c), in the vicinity of the two absorption peaks as a function of detuning from peak transmission, δ, at 373 K (blue) and 423 K (red).

between two absorption resonances of an atomic medium [154]. These two absorption resonances may be interrogated via electromagnetically induced transparency (EIT) or far-off resonance. Here, we use the two D_2 absorption resonances [152, 153] created by the hyperfine ground state splitting in ^{87}Rb, as shown in Fig. 6.1(a). We operate off-resonance, as this method requires a less complex experimental set-up when compared with EIT-based methods: only single photons at the correct frequency are required to achieve slowing compared to the additional lasers required for EIT.

In this case, the complex index of refraction is given by [153]

$$n(\delta) = 1 - A\left(\frac{g_1}{\delta + \Delta_+ + i\gamma/2} + \frac{g_2}{\delta - \Delta_- + i\gamma/2}\right), \tag{6.1}$$

where g_1 and g_2 are the relative strengths of the two resonances (7/16 and 9/16 respectively for ^{87}Rb), γ is the natural linewidth, δ is the detuning from peak transmission and $\Delta_\pm = \omega_s \pm \Delta$ with $\omega_s = (\omega_2 - \omega_1)/2$ and $\Delta = \omega_s((g_1^{1/3} - g_2^{1/3})/(g_1^{1/3} + g_2^{1/3}))$. The frequencies of the two absorption peaks are given as ω_1 and ω_2. The total strength of the resonance, A, in a vapor cell is a function of the atomic number density, N, and is given by

$$A = \frac{N|\mu|^2}{2\epsilon_0\hbar(g_1 + g_2)} \tag{6.2}$$

where μ is the effective far-detuned dipole moment, ϵ_0 is the vacuum permittivity and $\hbar$ is the reduced Plank constant. Using the real part of equation 6.1, $n_r(\delta)$ (Fig. 6.1(b)), it is possible to derive the group velocity,

$$v_g(\delta) = \left(\frac{\omega_0}{c} \frac{dn_r(\delta)}{d\omega} \right)^{-1}, \tag{6.3}$$

where c is the speed of light in vacuum and ω_0 is defined as the optical frequency at the midpoint between the two absorption resonances to the excited $P_{1/2}$ level. When the photon's optical frequency is tuned to ω_0, there is a maximum in transmission (Fig. 6.1(a)). This frequency will be the target output frequency of our quantum frequency converter. From equation 6.3, in the normal dispersion regime, one can see that a photon with a frequency at the midpoint of two absorption resonances ($\delta = 0$), will have a significantly reduced group velocity as is plotted in Fig. 6.1(c). It is also clear that if N in equation 6.2 is increased, the group velocity will be reduced. Therefore, by changing the atomic number density, N, it is possible to tune the photon delay.

6.3 Experimental Setup

The full experimental setup is shown in Fig. 6.2. Photons emitted by the ion are collected and fiber coupled using the 0.4 NA lens described in Chapter 3. We convert these photons to 780 nm via difference frequency generation in a fiber pig-tailed PPLN QFC device similar to that described in Sec. 4.3.1. After conversion and additional filtering of noise photons, the converted photons are sent to a neutral Rb vapor cell for slow light measurements.

6.3.1 Single Photon Production Sequence

To produce single 493 nm photons, the pulse sequence[1] shown in Fig. 6.3 is used. This is similar to the entangled-photon extraction scheme described in Chapter 2, except that for this

[1] Using the PulseBlaster described in Chapter 3.

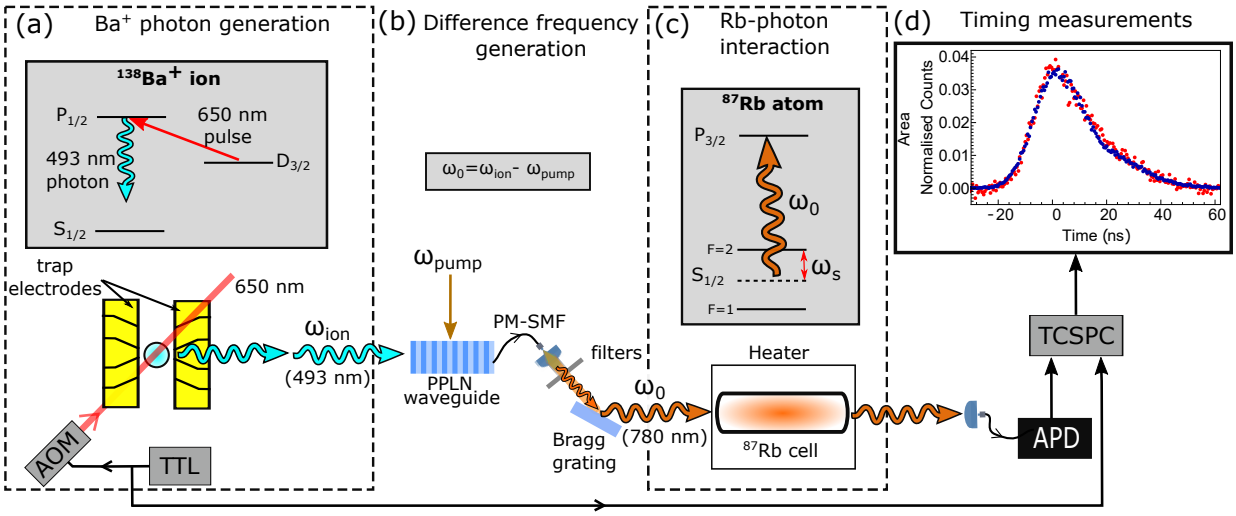

Figure 6.2: **Experimental schematic of photon production from a $^{138}Ba^{+}$ ion, quantum frequency conversion and photonic slowing in a warm neutral ^{87}Rb vapor** (a) The energy levels of $^{138}Ba^{+}$ and schematic showing the ion confined in a segmented blade trap. A TTL pulse activated acousto-optic modulator (AOM) controls 650 nm excitation light. (b) The QFC set-up including a periodically-poled-lithium niobate (PPLN) waveguide. Converted light, ω_0, is at the difference frequency between photons emitted from the ion at ω_{ion} and pump photons at ω_{pump}. The output of the PPLN is fiber coupled to a polarization maintaining single mode fiber (PM-SMF). A series of filters and a Bragg grating filter out pump light and unconverted 493 nm light which reduces the amount of anti-Stokes noise. (c) A ^{87}Rb energy level diagram and a vapor cell housed inside a heater through which converted single photons pass. (d) Photons are detected on an avalanche photo-diode (APD) and a time-correlated single photon counter (TCSPC) collects the arrival time of the photons with respect to the TTL sent to the AOM. As an example, single photon temporal shapes at 493 nm (blue circles) and frequency converted photons after passing through the cell at room temperature (red circles) are shown.

experiment, the optical beams used to perform operations on the ion consist of all polarizations[2]. First, the ion is prepared into the $D_{3/2}$ level using 493 nm light incident on the ion for ≈ 1 μs. The ion is then excited into the $P_{1/2}$ level using 650 nm light pulsed on for ≈ 20 ns, allowing for the emission of a 493 nm photon (Fig. 6.2 a). After a delay of 980 ns, a short 500 ns cycle of Doppler-cooling is performed before the ion is reinitialized in the $D_{3/2}$ level. When running the experiment, this process is repeated 10,000 times before both cooling lasers are turned on to Doppler cool the ion for 1 ms to prevent excessive heating of the ion. Between

[2]At the time of this experiment, we had not yet built the final optical beam delivery setups described in Chapter 3, and therefore did not have clean control over our beam polarizations.

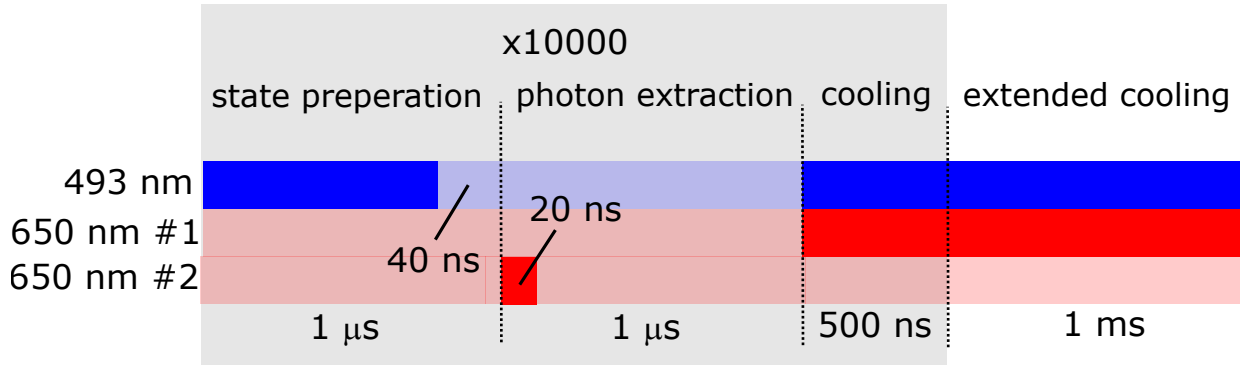

Figure 6.3: **Experimental pulse sequence.** The experimental pulse sequence showing the timing of the laser beams used to state prepare, extract a single photon and Doppler cool the ion. The parts of the sequence contained in the grey shading are repeated 10,000 times before an extended cooling cycle is performed.

the state preparation and extraction pulses, all beams are turned off for 40 ns to prevent accidental detection of 493 nm light originating from the preparation beam rather than the ion.

6.3.2 Additional Filtering of Noise Photons

The frequency converted 780 nm photons are passed through free-space optical interference filters[3] to remove pump light and unconverted 493 nm photons. Additionally, as shown in Fig. 6.2 b, a volume Bragg grating[4] with a spectral bandwidth of 0.15 nm and $\approx 90\%$ transmission efficiency is used to filter remaining noise (Sec. 4.2.3) created by the high intensity pump light. With this filtering approach we achieve the single photon signal-to-noise ratios (SNR) shown in Fig. 6.4, and we operate with around 800 mW total pump power. The inset of Fig. 6.4 shows both the end-to-end efficiency[5] and the noise counts produced as a function of pump power. The maximum achieved SNR and end-to-end efficiency of the conversion were measured to be 9.8 ± 0.6 and $15.5\pm0.7\%$ respectively for this experiment.

[3] Two each of Semrock: LL01-780-25 and FF01-1326/SP-25.

[4] OptiGrate BP-785: Provided by the group of Steve Rolston and Trey Porto.

[5] Defined here as the percentage of 493 nm photons entering the QFC set-up that are converted to 780 nm, including filtering.

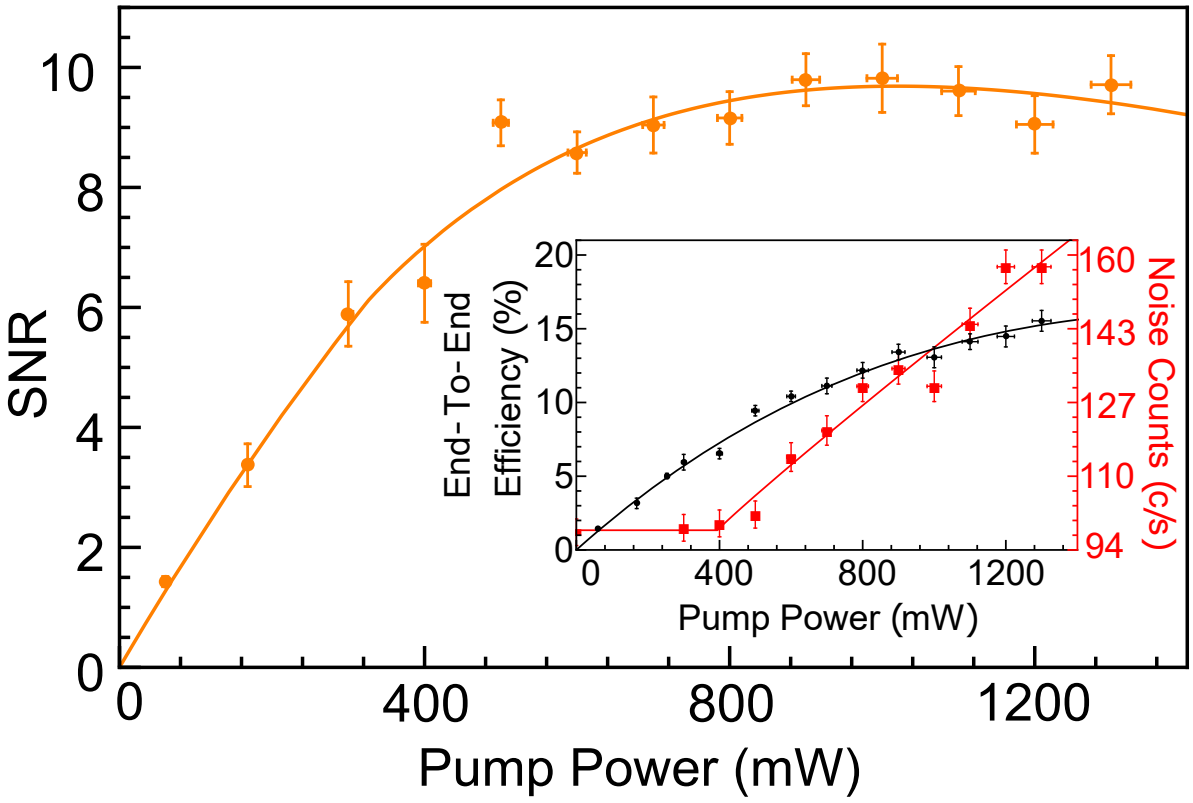

Figure 6.4: **SNR measured after filtering of the frequency converted ion signal.** The orange curve is the SNR given the measured conversion efficiencies and noise at each pump power. **Inset:** Measured conversion efficiency (black) and measured noise counts (red) on the APD as a function of pump power. The black curve is a theoretical fit to Eqn.4.25, and the red curve is an empirical fit to the noise.

6.3.3 Converted Photons Sent Through the Vapor Cell

Once filtered, the converted light is sent through a 75 mm long heated glass cell[6] filled with enriched ^{87}Rb before being fiber coupled and detected on an avalanche photodiode (APD), as shown in Fig. 6.2 c-d. The inside of the vapor cell is coated with aluminum oxide to reduce rubidium diffusion into the glass when the cell is at elevated temperatures. By scanning the QFC pump laser while converting laser light at 493 nm to 780 nm, we are able to obtain the Rb absorption curve shown in Fig. 6.1 a. With appropriate frequency tuning of the pump laser, we

[6]Triad Technology: TT-RB87-25X-75-P-CAL2O3

can produce 780 nm light at a frequency that is between the two optical absorption resonances of the ^{87}Rb D_2 line, ω_0 in Fig. 6.1 a, for implementing slow light.

Photons passed through the rubidium cell at room temperature experience some absorption and scattering, which decreases the SNR of the single photon signal to ≈ 6. We measure the arrival time of 780-nm single photons at the APD with respect to the 650 nm excitation AOM TTL pulse (Fig. 6.2(a)) using a time-correlated single photon counter[7] (TCSPC) with a resolution of 512 ps. Fig. 6.2(d) shows the resulting area-normalized arrival time histograms for photons emitted directly from the Ba^+ ion at 493 nm and for 780 nm photons at ω_0 passed through the ^{87}Rb vapor cell at room temperature. These histograms clearly show the preservation of the photon temporal shape before and after the combination of QFC and traversal through the cell at room temperature.

6.4 Trapped Ion Slow Light

By increasing the temperature of the vapor cell, the density of rubidium atoms, N, may be increased, leading to a larger change of refractive index and a lower group velocity, as described by equation 6.1 and 6.3 and shown in Fig. 6.1 b and c, respectively. The temperature of the Rb cell is measured on a cold finger protruding from the cell, as this cold finger (the coldest part of the cell) controls the density of atoms in the cell. Using heater tape, the cell is heated to temperatures ranging from 296 K (room temperature) to 395 K.

We record photon arrival histograms at various cold-finger temperatures, as shown in Fig. 6.5. Delays in photon arrival time are clearly visible with increasing temperature. The SNR of these histograms monotonically falls with temperature and approaches ≈ 1 at 395 K, due to both an

[7] PicoQuant: PicoHarp 300

increase in absorption[8] as the atomic density of the vapor cell increases, and optical misalignment caused by higher temperatures in our setup. Although there is a lower SNR value for the higher temperature settings, the photon arrival time delays are still clearly visible.

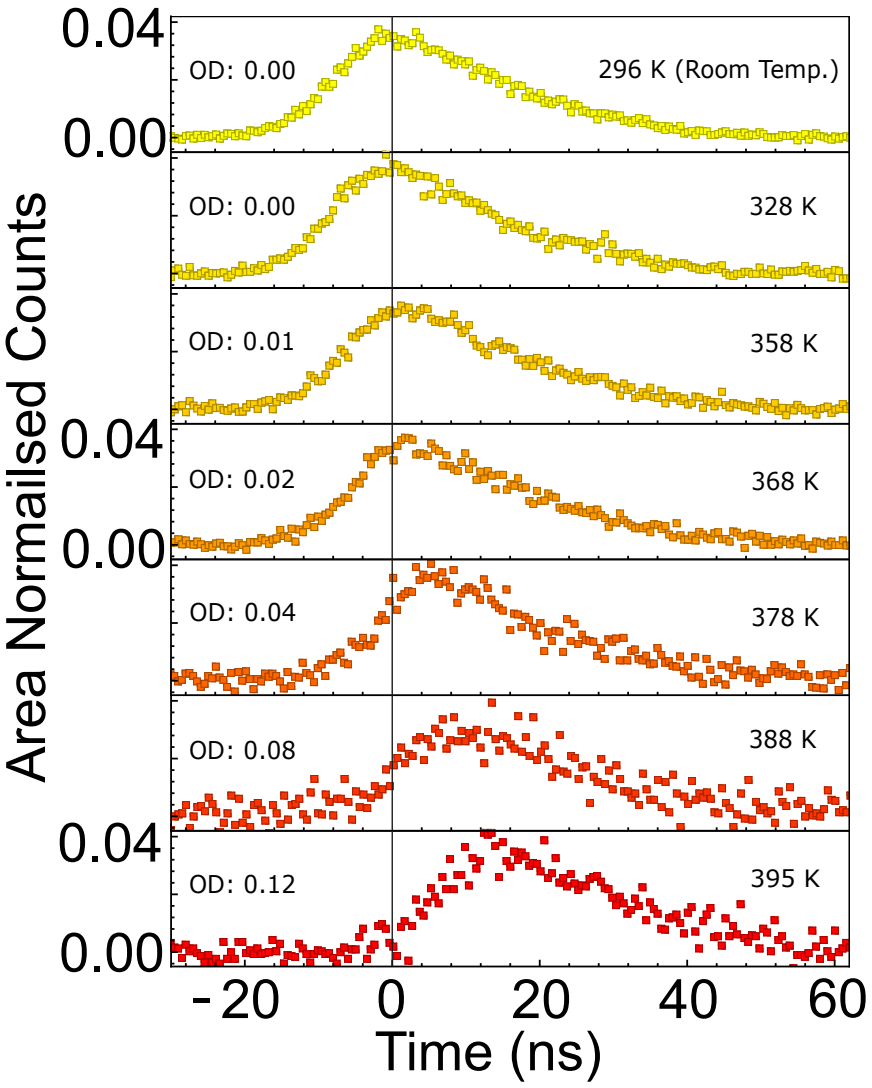

Figure 6.5: **Area normalized temporal photon shapes.** Area normalized temporal shapes of frequency converted photons which have passed through a warm ^{87}Rb vapor cell. The ^{87}Rb vapor cell temperature is set at the values indicated. The optical density (OD) of the warm vapor is stated for each temperature, at a frequency ω_0, and using the same atomic density, N, used to fit the delay curve in Fig. 6.6.

In Fig. 6.6, we plot the photon delay as a function of cell temperature and observe good

[8]The predicted optical density (OD) of the Rb vapor at each temperature is also provided in Fig. 6.5.

agreement with the theory curve derived from equation 6.3, using a scale factor to fit for the atomic number density, N. The measured photon delay is determined by temporally shifting each delayed photon arrival profile to overlap with that at room temperature. We demonstrate temperature-tunable single photon delays of up to 13.5 $\pm$ 0.5 ns at 395K. Although the delay is only $\approx$ 0.5 times the temporal width of the photons produced by the Ba^+ ion in this experiment, additional delays [153, 155] and improved transmission are possible by increasing the non-linear refractive index in the vapor by extending this work using methods such as EIT [156].

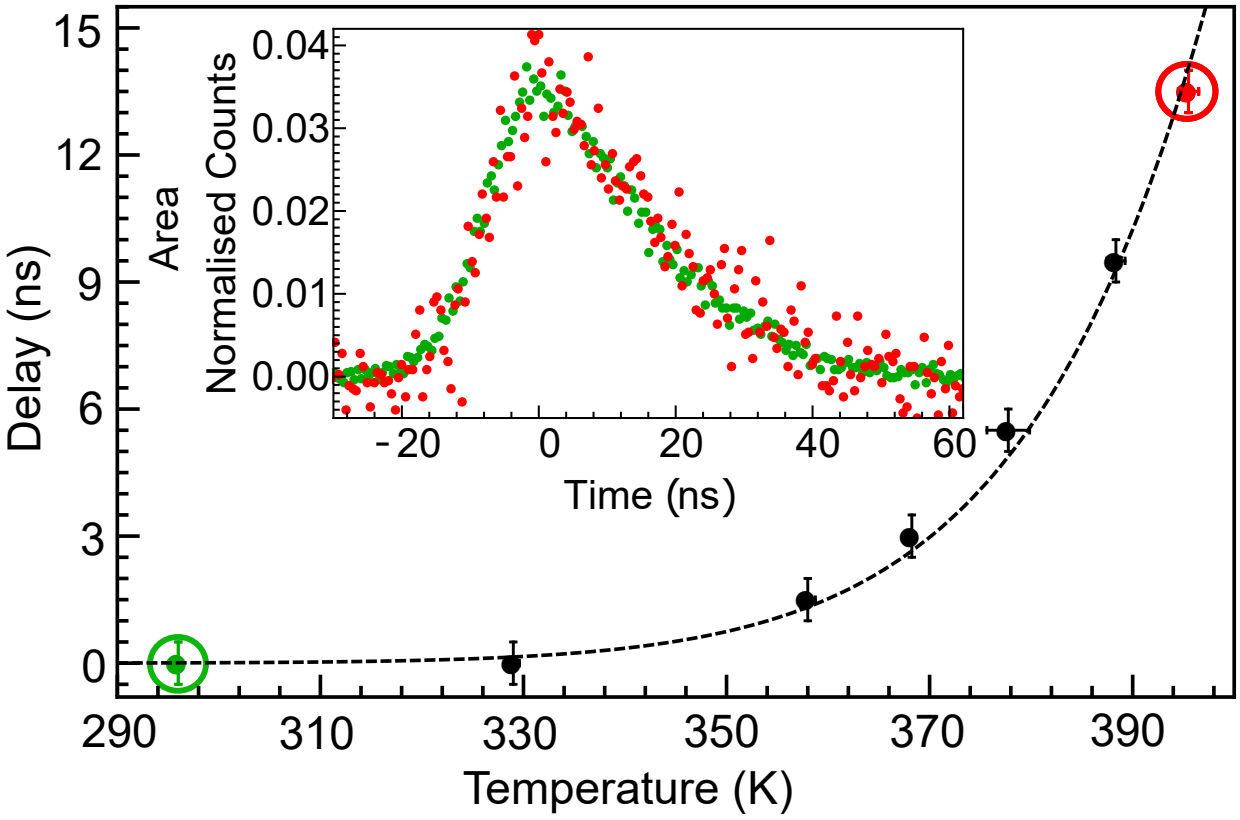

Figure 6.6: **Delay of the frequency converted photons emitted from the trapped Ba^+ ion after passing through a ^{87}Rb vapor cell as a function of the cell's temperature.** The dashed theory curve is a scaled version of equation 6.3 to account for N. The temperature and delay error bars are due to temperature fluctuations over the course of the experiment and the bin width of the histogram photon arrival time data respectively. **Inset:** Overlap of temporal shapes of photons transmitted through a 296 K room temperature cell (green circles) and a 395 K cell (red circles). The relative delay between the two traces has been removed to allow for comparison.

An additional and important factor to consider when slowing photons in this manner is the effect dispersion in the vapor has on the transmitted photon profile. The bandwidth of photons emitted by the Ba^+ ion (with a linewidth $\approx 2\pi \times 15$ MHz) combined with any the drifts in the pump laser frequency (≈ 10 MHz) provide an upper limit on the optical frequency stability of the converted photons. The converted photon's linewidth is still, however, significantly narrower than the splitting between the ^{87}Rb D_2 absorption peaks (≈ 6.8 GHz) such that there is a negligible change in the group velocity (slope of Fig. 6.1 c) between subsequently emitted and slowed photons. This results in negligible fractional broadening of the photon's temporal width, and the pulse retains its initial temporal profile, as shown in Fig. 6.6 (inset). This is in contrast to previous work using quantum dots where the emitted photon linewidths are similar to the splitting of the ^{87}Rb D_2 absorption lines, resulting in large broadening of the delayed photons [157].

6.5 Discussion

In summary, we have demonstrated the first proof-of-principle interaction between photons emitted from a trapped ion with a neutral atom system by slowing frequency converted photons emitted from a trapped ion in a warm rubidium vapor cell. Tunable delays of up to 13.5 $\pm$ 0.5 ns were observed with negligible temporal dispersion of the photons, making this system able to be used as a tunable networking synchronization device in a hybrid quantum network. This work also paves the way for future implementations of on-demand storage and retrieval of photons emitted from trapped ions using a more complicated EIT-based approach. Later, in Chapter 11 [51], we will theoretically explore how such a photon storage device could potentially be used to greatly increase entanglement generation rates in a long-distance trapped ion network.

Chapter 7: Hybrid Two Photon Interference

7.1 Introduction

As discussed in Chapter 1, the complementary strengths and functions of different quantum systems and technologies may give heterogeneous networks an advantage over those consisting of identical nodes. Many remote-entanglement protocols, such as the entanglement-swapping protocol discussed in Chapter 2, rely on the generation and interference of photons produced by nodes within a quantum network. This has largely prevented investigations into photonic-based hybrid entanglement, owing to the large differences in the spectral characteristics of single photons generated by different quantum systems [49, 114, 158]. Although this is not strictly a physical limitation [116, 159], vanishing entanglement generation rates, along with the necessity for detectors with bandwidths orders-of-magnitude greater than currently available has prohibited the linking of heterogeneous systems. Overcoming this spectral disparity will allow for the construction of hybrid networks with practical entanglement rates and expanded capabilities compared to networks based only on homogeneous components [15, 49].

In this chapter, I describe a collaborative effort between our lab and the group of Steve Rolston and Trey Porto in which we achieve high-visibility Hong-Ou-Mandel (HOM) interference [111, 112] between photons generated from a rubidium atomic ensemble and a trapped barium ion after closely matching their center frequencies via difference frequency generation (DFG). The

photons are produced on demand by each source located in separate buildings, in a manner suitable for quantum networking. This demonstration of interference between photons produced by these two systems is a critical step towards the direct entanglement of these two leading quantum information platforms (Chapter 1). From these results we investigate the feasibility of hybrid ion-atomic ensemble remote entanglement generation, demonstrating that a hybrid ion-atomic ensemble quantum network is attainable.

This experiment was performed by James Siverns and I in the trapped ion laboratory, with graduate students Alexander (Sandy) Craddock, Dalia Ornelas, and AJ Hatchel operating the neutral atom Rydberg experiment. When it came to analyzing and interpreting the data, Sandy took the lead on data processing and determining the expected interference signal whereas I led the effort to determine the frequency spectrum of the photon produced by the ion as well as to project entanglement rates and fidelities (see the derivation in Sec. 2.4.4) based on our results. Elizabeth Goldschmidt also provided very useful and important insights on collecting and presenting the interference data. This chapter is adapted our resulting publication [50] for use in this thesis.

7.2 Experimental Layout

The experiment spans two buildings, shown in Fig. 7.1. Building A contains a single trapped $^{138}Ba^{+}$ ion as well as two DFG setups. Building B contains a ^{87}Rb atomic ensemble and a HOM interferometer to measure two-photon interference. A time-tagging device records detection events for two single-photon avalanche photodetectors (SPADs)[1], A and B. Each building contains a Hanbury Brown-Twiss [146] setup (not pictured) for measurement of the second-

[1] Excelitas SPCM-780-13

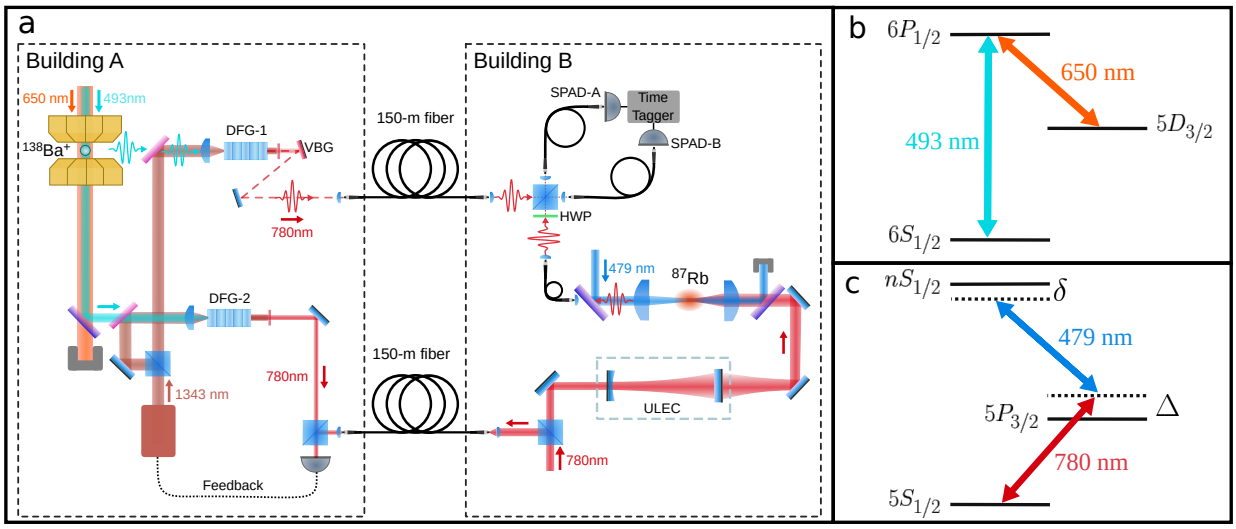

Figure 7.1: **Experimental layout and energy level diagrams for the two sources.** **a**, Building A contains a $^{138}Ba^{+}$ ion which emits photons at 493 nm, and Building B contains a ^{87}Rb atomic ensemble producing 780-nm photons. Ion-emitted photons are converted to 780 nm using DFG-1 and sent to Building B via PMF. DFG-2 produces 780-nm light used to frequency stabilize the output of DFG-1 by optical beatnote locking with reference light sent from Building B. Light from the ion and ensemble source is sent to the HOM interferometer for two-photon interference measurements. A half-wave plate (HWP) in one input path allows for control of the relative polarization of the photons. The photons interfere on a nearly 50:50 beamsplitter before being coupled into two SMF which are connected to SPADs linked to a time-tagging device. Here VBG stands for a volume Bragg grating and ULEC for ultra-low expansion cavity. **b**, Level scheme for $^{138}Ba^{+}$. **c**, Level scheme for ^{87}Rb.

order intensity autocorrelation functions, $g^{(2)}_{\text{ion}}(\tau)$ and $g^{(2)}_{\text{atom}}(\tau)$, of the light from ion and atomic-ensemble sources, respectively (See Sec. 5.1).

7.2.1 Building A: Trapped Ion and Frequency Conversion Setups

The trapped ion setup is as described in Chapter 3. We produce single 493 nm photons from the ion either through Doppler cooling, or through a pulse sequence similar to that described in Chapter 2, as will be described below. Single photon collection and fiber coupling is performed using the 0.4 NA objective described in Sec. 3.4.3. The frequency conversion setup used for single photon conversion, DFG-1, is a fiber pig-tail setup (Sec.4.3.1) with additional filtering

via a volume Bragg grating as described in Chapter 6. After filtering out pump induced noise (Sec. 4.2.3) to a rate negligible compared to the dark count rate of the SPADs, we send the converted photons to the HOM interferometer in Building B via a 150-meter polarization-maintaining fiber (PMF).

To ensure the converted ion-produced photons are at a similar frequency as those produced by the atomic ensemble, we use a second frequency conversion setup[2], DFG-2. Laser light at 493-nm, with a known detuning from the photons emitted by the ion ($\pm$ 10 MHz), is combined with the same pump light used in DFG-1, producing continuous wave light at 780-nm. The output frequencies of DFG-1 and DFG-2 can both be controlled by changing the pump frequency. The 780-nm light from DFG-2 is combined with frequency-locked 780-nm light from building B onto a fast photodetector[3], with which we measure an optical beat note. By using the beat note to produce an error signal that is fed back to the pump laser, we stabilize and set the frequency of the output 780-nm light from both DFG setups. Uncertainties in the center frequency of the converted 780-nm single photons are present ($\pm$10 MHz) in the experiment due to uncertainties in ion spectroscopy, and drifts in the 493-nm and 650-nm laser wavemeter locks.

7.2.2 Building B: Atomic Ensemble

Being operated by our collaborators, detailed information on the entire atomic ensemble setup and photon collection can be found in the theses of Alexander Craddock [94] and Dalia Ornelas-Huerta [95] as well as in [35]. To provide some background, however, I will include the description included our publication.

[2]This setup uses the device discussed in Sec. 5.2, which was put out of commission for single-photon use due to a burned fiber tip.

[3]Electro-Optics Technology ET-2030A

The atomic-ensemble source uses Rydberg blockade [160] to produce single photons from an ensemble of cold ^{87}Rb atoms that are held in an optical dipole trap [161, 162]. The ground, $\left|5\mathrm{S}_{1/2}, F = 2, m_F = 2\right\rangle$, and Rydberg states, $\left|n\mathrm{S}_{1/2}, J = 1/2, m_J = 1/2\right\rangle$ are coupled using a two-photon transition, via an intermediate state, $\left|5\mathrm{P}_{3/2}, F = 3, m_F = 3\right\rangle$, shown in Fig. 7.1c, using 780-nm probe and counter-propagating 479-nm control fields. The probe light that has passed through the cloud is collected and coupled ($\approx 70\%$ efficiency) into a PMF. Operating with Rydberg levels with principal quantum numbers, $n \geq 120$, the blockade radius is significantly larger than the probe beam waist, making the medium effectively one dimensional [162]. The atomic ensemble has a lifetime of $\approx$ 1 s, limited by the background vapor pressure. Thus, to maintain reasonable atom numbers over the course of the measurements, the ensemble must be periodically reloaded.

7.2.3 Interferometer and Single Photon Detection

Light from both sources is transmitted to the interferometer setup via PMF. At the output of each fiber we use a polarizing beamsplitter (PBS) to clean the polarization of the light before it passes to a 50:50 beamsplitter. For the atomic-ensemble source a HWP after the PBS allows us to adjust the relative polarization of the two sources at the 50:50 beamsplitter. We couple the output ports of the 50:50 beamsplitter to a pair of SMFs with similar mode field diameters to the input PMFs, which are connected to the SPADs. Immediately prior to both output SMFs we use a bandpass filter[4] to remove stray light. We use a time-tagger[5] to record timestamps for SPAD detection events, from which we use software to calculate coincidences.

[4] Semrock Brightline 780/12
[5] Roithner-Laser TTM8000

7.3 Interference of Photons Produced Stochastically

First we consider the case where each source continuously produces single photons with stochastic arrival times. In other words, we constantly illuminate our sources and photons are produced as quickly as possible as allowed by the atomic physics of each source, leaving us no control over photon arrival times. This is in contrast to on-demand photon production, where we produce photons such that they arrive within some known emission window, as will be demonstrated later. This stochastic method is not directly useful for quantum networking requiring photons entangled with the nodes themselves, but is an easier first step to take to ensure proper operation of our setup and to check our photon frequencies are close.

7.3.1 Ion-Photon Production

To produce these photons from the ion, we continuously Doppler cool on the $6S_{1/2}$ - $6P_{1/2}$ transition, repumping with 650-nm light, see Fig. 7.1b. The emitted photons have a frequency spectrum centered on the cooling laser frequency, and with a shape determined by the Rabi frequencies and detunings of both the cooling and repumping lasers [163]. We use Rabi frequencies of $\approx 2\pi \times 25$ MHz and $\approx 2\pi \times 11$ MHz for the 493-nm and 650-nm beams respectively. Additionally, the detunings of these beams are $\approx 2\pi \times (-99)$ MHz and $\approx 2\pi \times 29$ MHz respectively. The average count rate of converted photons throughout the experiment, R_{ion}, measured as the sum of counts on SPAD A and B in Building B, is $\approx 400\ \text{s}^{-1}$. Figure 7.2 a shows $g^{(2)}_{\text{ion}}(\tau)$ for the resulting 780-nm photon stream[6]. We measure $g^{(2)}_{\text{ion}}(0) = 0.05(8)$ after background subtraction. Here, the $g^{(2)}_{\text{ion}}$ dip width is set by the effective Rabi frequency ($\approx 2\pi \times 100$ MHz) of

[6]This is measured in Building A just before sending the photons to Building B.

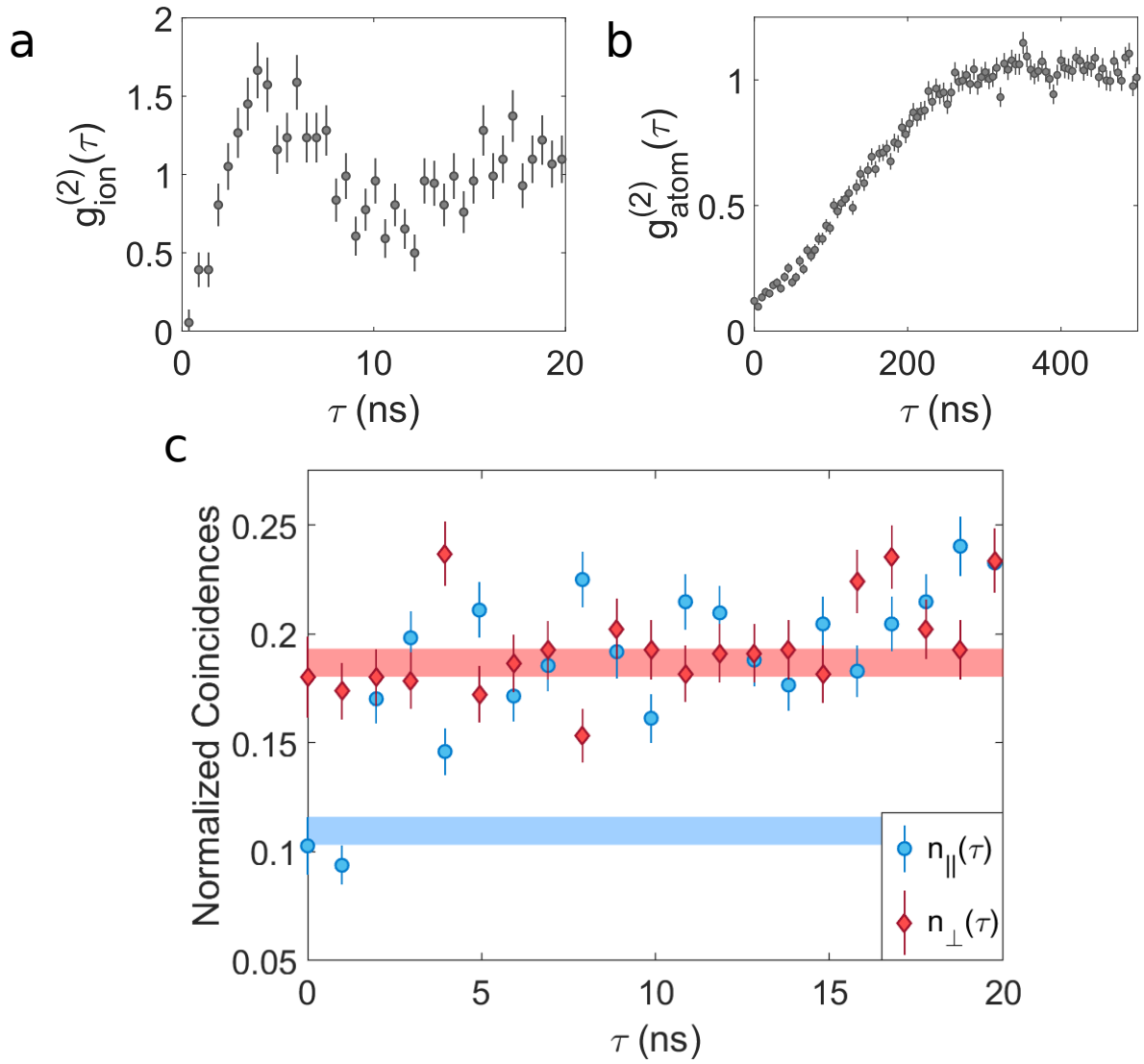

Figure 7.2: **Data for stochastic photon production and interference.** Second-order intensity autocorrelation functions for the **a**, ion source, and **b**, atomic ensemble source. The oscillation exhibited in the ion autocorrelation data is attributed to Rabi flopping of the ion. **c**, Normalized coincidences for the cases where the relative polarization of the two sources at the interferometer are parallel, $n_{\|}(\tau)$, and perpendicular, $n_{\perp}(\tau)$, using 1 ns bins. Lower/blue (upper/red) band corresponds to the expected normalized coincidences when photons from the sources are completely indistinguishable (distinguishable). For the lower/blue band expected coincidences are entirely due to atomic-ensemble source multiphoton events, while for the upper/red band there is an additional contribution from photon distinguishability. Bands indicate the $\pm 1\sigma$ confidence interval in this value due to the uncertainty in $g^{(2)}_{\text{atom}}(0)$. Data shown accumulated in ≈ 30 hours. In all cases the error bars denote statistical uncertainties. All curves shown include background subtraction. Raw two-photon interference data, and calculation of expected coincidence bands can be found in [50, 94].

the driving 493-nm light, which additionally dictates the emitted photon's bandwidth.

7.3.2 Atomic Ensemble Photon Production

To produce a stochastic photon stream from the atomic ensemble source, the probe and control fields are tuned to their respective atomic resonances, $\Delta = \delta = 0$, see Fig. 7.1 c. The strong nonlinearities associated with Rydberg electromagnetically induced transparency (REIT) ensure that only single photons propagate through the medium without large losses [162]. In steady-state operation at a high Rydberg level, $n = 120$, and large optical depth, OD ≈ 30, we observe a background subtracted $g^{(2)}_{\text{atom}}(0) = 0.119(7)$, shown in Fig. 7.2 b. Our collaborators attribute the non-zero value of $g^{(2)}_{\text{atom}}(0)$ to finite probe beam size and input photon flux effects [162, 164]. The width of the $g^{(2)}_{\text{atom}}$ dip is set by the REIT bandwidth [162]. However, the majority of the photons exiting the medium have similar spectral bandwidths to the input probe field [165]. We measure an average photon count rate throughout the experiment, R_{atom}, of $\approx 10^4$ s^{-1}, with an experimental duty cycle of 0.56, where the off time is used for reloading.

7.3.3 Results

The background-subtracted normalized coincidences for the HOM interference are shown in Fig. 7.2 c for the cases where the relative polarization at the interferometer of the photons from the two sources are parallel, $n_{\parallel}(\tau)$, and perpendicular, $n_{\perp}(\tau)$. The subtracted background is predominantly due to SPAD dark counts and ambient photons. We define the visibility of the interference:

$$V = \frac{n_{\perp}(0) - n_{\parallel}(0)}{n_{\perp}(0)} \tag{7.1}$$

and observe $V = 0.43(9)$ using 1-ns bins. For a perfect 50:50 beamsplitter two factors can contribute to a non-unity visibility: multiphoton events from either of the sources, quantified by $g^{(2)}(0)$, and distinguishability. Multiphoton events decrease the visibility by a factor

$$f_{\text{mp}} = \left[1 + \frac{r g^{(2)}_{\text{atom}}(0) + r^{-1} g^{(2)}_{\text{ion}}(0)}{2}\right]^{-1}, \tag{7.2}$$

where $r = R_{\text{atom}}/R_{\text{ion}}$. Equation 7.2 holds for the case where the photon flux is constant over the experiment, which is a valid approximation for this data [50, 94]. Given the independently measured $g^{(2)}(0)$ for the sources and ratio, r, we determine $f_{\text{mp}} = 0.41(1)$. The observed $0.43(9)$ visibility can thus be attributed entirely to multiphoton events, and therefore is consistent with perfect bunching of photons from the two sources. Additionally, we note that $n_{\parallel}(0)$ and $n_{\perp}(0)$ are in agreement with the values expected from the measured $g^{(2)}(0)$'s, shown in Fig. 7.2 c. Due to the disparity in the spectral widths of the photons produced by the sources, the width of the HOM dip, seen in Fig. 7.2 c, is almost entirely determined by the temporally narrower ion-produced photon.

7.4 Interference of Photons Produced On-Demand

To be useful for quantum networking, the photons should arrive on demand in well-defined temporal modes [166]. To this end, we investigate two-photon interference in the case where a single photon from each source arrives at a known time relative to an experimental trigger shared between the two buildings.

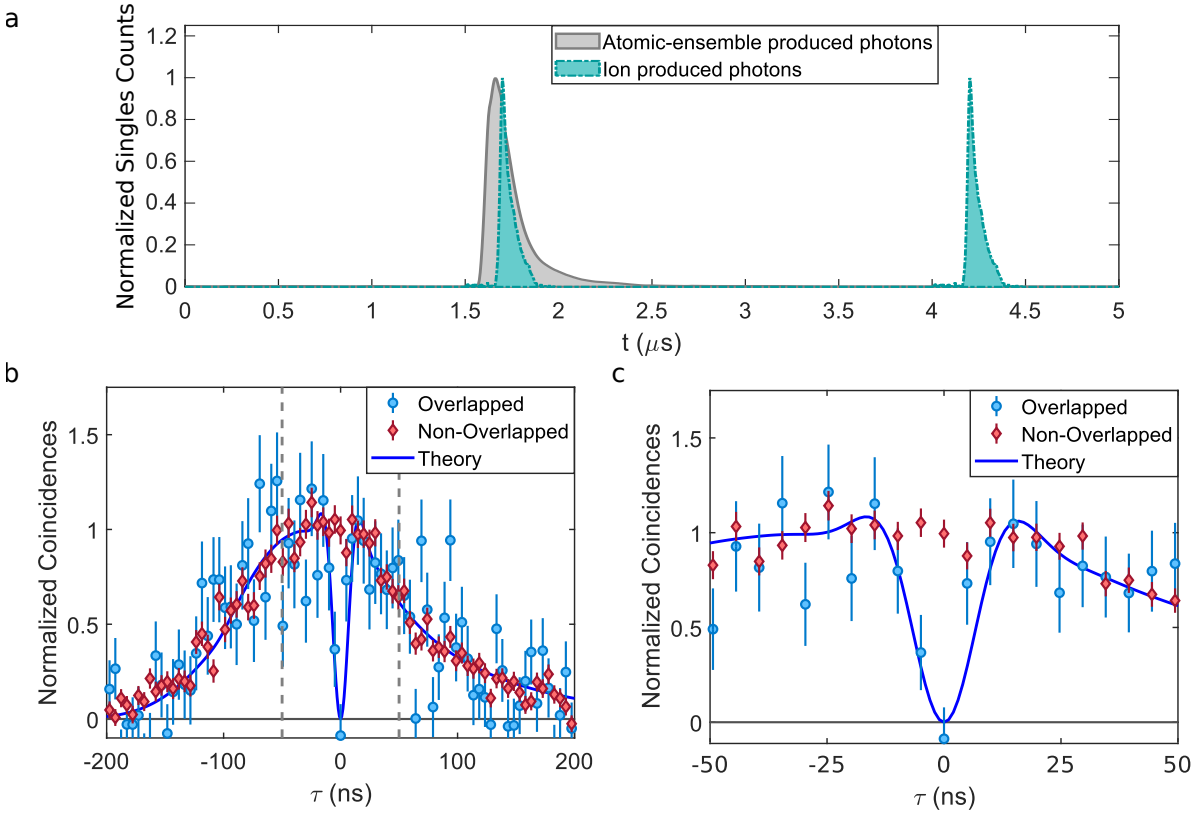

Figure 7.3: **On-demand pulse sequence and interference. a**, Schematic of pulse sequence for one period. The atomic-ensemble produced photon profile, and ion-produced photon profile at $t \approx 4.25\ \mu s$, are measured directly. The ion-produced photon profile at $t \approx 1.75\ \mu s$ is a time shifted copy of that at $t \approx 4.25\ \mu s$ to allow for easy comparison of the photon temporal shapes from the two sources. To lessen the effects of small drifts in the relative arrival time of the photons we offset the ion and atomic-ensemble produced photon average arrival times. **b**, and **c**, Normalized coincidences when the photons from the two sources are temporally overlapped (non-overlapped) shown in blue (red). Both curves represent the data after software gating, background subtraction and using 5 ns bins. Dashed lines in **b** indicate the range shown in **c**. Theory curve obtained taking into account the non-transform limited nature, probabilistic spectrum of the ion-produced photon, and plausible estimates of the relative drift ($2\pi \times 10$ MHz) and offset ($2\pi \times 20$ MHz) between the center frequencies of the photons from the two sources. Data presented accumulated over ≈ 22 hours. In all cases the error bars denote statistical uncertainties. Raw two-photon interference data, and calculation of theory curves can be found in [50, 94].

7.4.1 Production of Ion-Photons On-Demand

We produce single photons from the ion via a modified version of the scheme discussed in Chapter 2[7]. First, the ion is pumped equally into each Zeeman sub-level of the $D_{3/2}$ manifold using only the 493-nm laser for 750 ns. This light is then turned off, and we wait for 60 ns to ensure any laser scatter is not detected during the photon extraction phase. A 200-ns pulse of 650-nm light, separate from that used during Doppler cooling, is then used to excite the ion to the $P_{1/2}$ manifold, from which a 493-nm photon may be emitted immediately, or after decay to and subsequent re-excitation from the $D_{3/2}$ manifold ($\approx 75\%$ branching ratio). This excitation light is linearly polarized and propagates along the quantization axis with a Rabi Frequency of $\approx 2\pi\times$ 30 MHz and detuning of $\approx 2\pi \times 29$ MHz. The 650-nm light is turned off, and after a short period (60 ns) with no light, the ion is Doppler cooled (for a minimum of 500 ns), until a trigger is received from the atomic ensemble lab, and the process is repeated.

We detect a photon at the output of the HOM interferometer with a probability of $\approx 2\times10^{-5}$ per attempt, and measure $g^{(2)}_{\text{ion}}(0) = 0(1)\times10^{-2}$ after background subtraction. Photons are emitted from the ion with a nearly exponential decaying temporal profile (Figure 7.3 a), with a decay constant (≈ 50 ns) set by the effective Rabi frequency of the 650-nm retrieval pulse. Due to the magnetic bias field (≈ 5 G) splitting the Zeeman states in the $6S_{1/2}$ and $5D_{3/2}$ levels, combined with the near-equal population distribution in the $5D_{3/2}$ manifold following pumping, the average photon spectrum consists of several peaks with a center frequency determined by the detuning of the 650-nm laser used to excite the ion from the $5D_{3/2}$-$6P_{1/2}$ transition. This is summarized in Fig. 7.4 and will serve to narrow the resulting interference dip, as will be discussed later.

[7] As with Chapter 6, this modified scheme is a result of not yet having the final beam delivery setup with full polarization control discussed in Chapter 3.

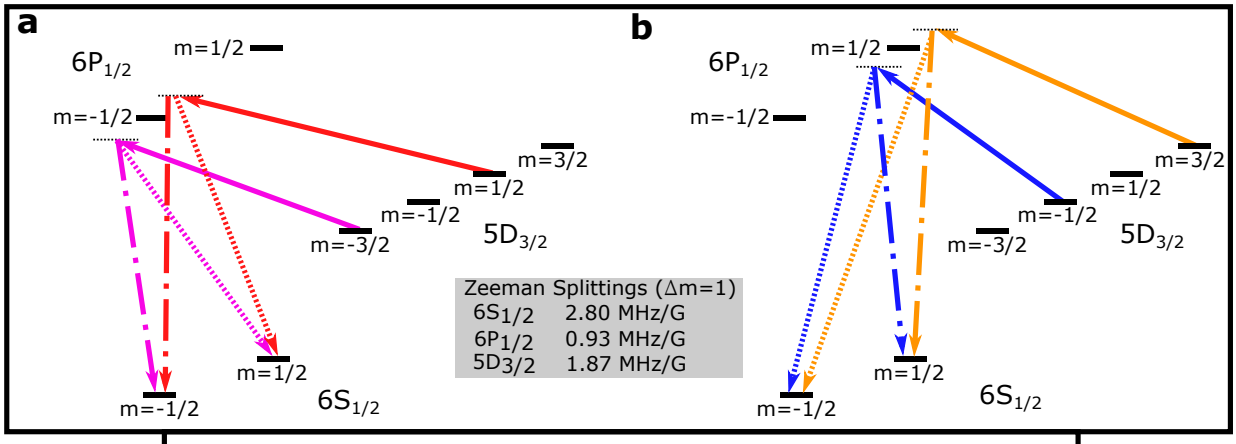

c

Initial $5D_{3/2}$ Sublevel	Final $6S_{1/2}$ Sublevel	Decay Path	Polarization	Detuning From Center (B = 5G)
m=-1/2	m= 1/2		π	-11.67 MHz
m=-3/2	m= -1/2		π	-7 MHz
m= 1/2	m= -1/2		π	11.67 MHz
m= 3/2	m= 1/2		π	7 MHz
m=-1/2	m= -1/2		σ	2.33 MHz
m=-3/2	m= 1/2		σ	-21 MHz
m= 1/2	m= 1/2		σ	-2.33 MHz
m= 3/2	m= -1/2		σ	21 MHz

Figure 7.4: **Barium Photon Frequencies Including Zeeman Splittings.** In our excitation scheme, all possible Zeeman sublevels of $5D_{3/2}$ are equally populated, and only σ excitation transitions are used. **a** Possible excitation and decay paths involving the $\left|6P_{1/2}, m = -1/2\right\rangle$ state of $^{138}Ba^{+}$. **b**, possible excitation and decay paths involving the $\left|6P_{1/2}, m = 1/2\right\rangle$ state of $^{138}Ba^{+}$. **c**, shows the polarization and detuning of the resulting 493-nm photons relative to the center of all possible emission frequencies.

7.4.2 On-Demand Atomic Ensemble Photon Production

For the atomic-ensemble source, our collaborators generate on-demand photons using a write and retrieve protocol, similar to that in [82]. Again, more details can be found in the main publication [50]. A Rydberg collective spin wave excitation is written to the cloud using coherent control and probe pulses, detuned far from intermediate resonance ($\Delta \gg \Gamma$, the linewidth of the intermediate state) and close to two-photon resonance ($\delta = 0$). Rydberg blockade during the write process ensures that a single Rydberg spin wave excitation is stored in the medium. The control field is tuned close to resonance and then turned on, retrieving the spin wave as a single photon with a spatial mode similar to the input probe light. After accounting for background coincidences, we measure $g^{(2)}_{\text{atom}}(0) = 0(1) \times 10^{-4}$, with a per-attempt detection probability $\approx 3 \times 10^{-2}$ at the outputs of the HOM interferometer. The temporal profile of the retrieved photon is determined by the control Rabi frequency ($\approx 2\pi \times 7$ MHz), intermediate state detuning ($\approx 2\pi \times 7$ MHz), and optical depth (≈ 10) of the cloud [167]. Figure 7.3 a shows the temporal profile of the atomic-ensemble produced photon, well approximated by a decaying exponential, with a decay constant ≈ 120 ns.

7.4.3 On-Demand Synchronization

To ensure the photons arrive at the beamsplitter at the correct relative times, we operate in a master-slave configuration with the atomic-ensemble lab, in building B, as the master and the ion lab, in building A, as the slave. The ensemble lab (Building B) generates 1064-nm optical pulses using an AOM with laser light. These pulses are sent over fiber to the ion lab (Building A), where the optical pulses are converted to electronic TTL pulses, using a high bandwidth

photodiode[8], to trigger ion-photon production[9]. Due to drifts in the power of the 1064-nm optical pulse, we observe small drifts ($\leq$ 20 ns over several hours) in the ion-produced photon arrival time relative to that generated by the atomic-ensemble. To ensure the photon profiles overlap, even with these drifts, we offset the average arrival time of the ion produced photon $\approx +40$ ns relative to the atomic-ensemble produced photon. Calculations indicate that with this offset such temporal drifts have negligible effect on the two-photon interference. We observed no measurable drift between the temporally overlapped and non-overlapped photons produced by the ion, with a temporal separation of 2.5 μs.

Along with events on SPAD A and B we additionally record timestamps for an electronic reference, which defines an absolute time reference within the 5-μs pulse cycle, shown in Fig. 7.3 a. This reference was provided by the same electronics that controlled the arrival time of the photons produced by the two systems. Throughout the experiment we observed no drift between the arrival time of the atomic-ensemble produced photon and the electronic reference.

7.4.4 Results

To measure the visibility in a single experimental run, instead of using polarization to make the photons distinguishable, we use a procedure where the ion-produced photons alternately arrive simultaneously on the beamsplitter with the atomic-ensemble produced photons (with identical polarization), interleaved with pulses when their arrival times are not overlapped, depicted in Fig. 7.3 a[10]. We use coincidences across several shifted arrival times to correspond to our

[8] ThorLabs PDA05CF2

[9] In particular, this triggers the PulseBlaster discussed in Chapter 3.

[10] In other words, we purposefully make the photons orthogonal in their spatio-temporal wavefunctions [116] rather than in polarization.

orthogonal mode reference, to reduce statistical noise[11]. Our experimental sequence consists of requesting photons from the atomic ensemble at a rate of 200 kHz, while the ion produces photons at 400 kHz, triggered via the aforementioned 1064-nm synchronization pulse between the buildings. We operate at an experimental duty cycle of 0.6, with the non data-taking time required to reload the atomic ensemble.

To mitigate noise effects, predominantly due to detector dark counts and ambient photons, we software gate SPAD A using a 120-ns time window containing $\approx 80\%$ of the ion-produced photon temporal profile. With this gating, we count the coincidences in detection events between SPAD A and B. Figure 7.3 b and c show the resulting data for 5 ns bins after subtraction of background coincidences and software gating. Using Eqn. 7.1, where $n_{\parallel}$ and $n_{\perp}$ correspond to the temporally overlapped and non-overlapped coincidences respectively, we calculate a visibility of $1.1(2)$, indicating perfect two-photon interference.

The observed width of the interference dip is narrower than expected when only considering the temporal profile of the photons [116]. The causes of this include:

- Decay from the $6P_{1/2}$ manifold to the $5D_{3/2}$ manifold and subsequent re-excitation during the extraction phase destroys the transform limitedness[12] of the ion-produced photons.
- Experimental uncertainties in the detunings of the 493-nm and 650-nm laser frequencies from their corresponding resonance frequencies causes uncertainties in $\Delta\omega$.
- Drift on the ion laser locks produces a corresponding drift in $\Delta\omega$.
- As discussed, the scheme used to pump the ion into the $5D_{3/2}$ manifold, as well as Zeeman

[11] See [50, 94] for more details.
[12] This complicates determining the frequency spectrum of the resulting photon.

splitting, causes the ion to emit photons at multiple frequencies.

However, accounting for the multiple peaks in the ion-produced photon spectra, reasonable laser-frequency drifts and average center-frequency differences of the two photons, we obtain agreement between theory and experiment, seen in Fig. 7.3b and c. Further calculations and details on how these various phenomenon affect the interference dip, can be found in our publication [50] and in the thesis of Sandy Craddock [94], who calculated the theory curve presented in Fig. 7.3 as well as performed the processing of the interference data.

7.5 Projected Hybrid Entanglement Rates and Fidelities

Bin Size	Projected Fidelity	Expected Entanglement Rate With Current Setup (s^{-1})	Projected Entanglement With Experimental Upgrades (s^{-1})
5 ns	1.0 ± 0.1	5.1×10^{-4}	3.1×10^{-2}
10 ns	0.93 ± 0.06	1.2×10^{-3}	7.5×10^{-2}
15 ns	0.72 ± 0.06	1.8×10^{-3}	1.1×10^{-1}

Table 7.1: **Fidelities and entanglement rates for different bin sizes.** The bin size of 5 ns corresponds to that of the results presented in Fig. 7.3 b-c. Additionally, projections are shown for improvements in DFG conversion efficiency, photon collection, and optical losses.

We can use the two-photon interference to project entanglement rates and fidelities in a potential ion-neutral atomic ensemble hybrid quantum network. To calculate prospective entanglement rates, we take the total number of background-subtracted coincidences ($\approx$ 40 for 5-ns bins) at $\tau = 0$ for the non-overlapped on-demand case, divided by the total experimental run time ($\approx$ 22 hours). Using the entanglement swapping scheme described in Sec. 2.4.2 we would reduce our entanglement rates by a factor of two, as only half of the possible Bell states can be heralded. However, in our experiment, only half of the ion-produced photons were used due to polarization filtering. By using all of the photons collected from the ion, this factor of two

can be recovered. With this scheme, the resulting state fidelity, assuming perfect photon-matter entanglement and polarization discrimination, can be related to the visibility of the two-photon interference $F = (1+V)/2$, as is derived in Sec. 2.4.4. For the 5-ns bins in Fig. 7.3 c, we project $F \approx 1$.

Table 7.1 gives fidelities and the expected entanglement rates achievable with our current experimental configuration using various bin sizes for our coincidence measurements. These calculations assume negligible detector dark counts, achievable with commercially-available detectors and through improved shielding of the detectors from ambient photon sources. As can be seen, one must trade off bin size (entanglement rate) for fidelity. This trade off can be reduced through widening of the interference dip by correcting the aforementioned factors leading to narrowing of this dip[13]. The final column of Table 7.1 shows our projections for entanglement rates given improvements in difference frequency generation (DFG) efficiency ($10\% \rightarrow 30\%$ [32, 34]), ion-produced photon collection efficiency (using 0.6 NA lens with 70% fiber coupling [168] as opposed to 0.4 NA lens with 35% coupling efficiency) improvements in single photon detector efficiency ($70\% \rightarrow 90\%$ at 780-nm, achievable with commercially-available superconducting-nanowire single-photon detectors), removal of fiber butt coupling losses (factor of 1.4), and reduction of losses in the optics in the DFG filtering stage (factor of 1.5).

7.6 Summary

In conclusion, we have demonstrated high-visibility quantum interference between photons produced by an ion and atomic-ensemble in both the stochastic and on-demand regime. With the

[13] At the time of writing this thesis $\approx$ 3 years after collecting this data, we have likely solved the majority of these problems.

demonstrated width of the interference dip, we project that entanglement rates of ≈ 2 hour^{-1} are achievable with $F \approx 1$. With 10-ns bins we estimate an entanglement rate of ≈ 4 hour^{-1} with $F \approx 0.9$, still well above the classical limit. Such entanglement rates are comparable with the first experiments using similar schemes with homogeneous matter qubits [66,169]. Furthermore, with practical experimental upgrades, predominantly improving the ion produced photon collection, DFG conversion efficiency and reducing optical losses through various elements, this can be increased to several entanglement events per minute, making further investigations into a hybrid ion-atomic ensemble quantum network practical.

Chapter 8: Quadrupole Tranisition in $^{138}Ba^{+}$

8.1 Overview and Motivation

Lacking the hyperfine structure used for state detection for qubits such as $^{171}Yb^{+}$, deterministic state detection of the ground state Zeeman qubit in $^{138}Ba^{+}$, denoted by $|0\rangle$ and $|1\rangle$ in Fig. 8.1, is not possible using any of the available closed cycling dipole transitions (such as those provided by the Doppler cooling beams at 493 nm and 650 nm). Though it is possible to perform probabilistic state readout using these transitions [64], a deterministic method is preferable as it greatly reduces the number of repetitions required when running experiments [65]. This chapter will focus on work done to address the $S_{1/2} \leftrightarrow D_{5/2}$ quadrupole transitions near 1762 nm in $^{138}Ba^{+}$ in order to perform the deterministic state detection important for the experiments performed in Chapters 9-10.

The basic idea behind our state detection procedure using the $S_{1/2} \leftrightarrow D_{5/2}$ quadrupole transition is summarized in Fig. 8.1. Light near 1762 nm is used to selectively shelve the $|0\rangle$ state to the long lived (> 30s) $D_{5/2}$ manifold, with the $|1\rangle$ state being unaffected (Fig. 8.1 a), owing to the extremely narrow ($\approx$ mHz) linewidth of this transition. If shelved, the ion will not fluoresce, such that Doppler cooling light can be used to indicate which qubit state was populated before the shelving occurred (Fig. 8.1 b).

This chapter begins with a descriptions of how we calibrate our state detection via reading

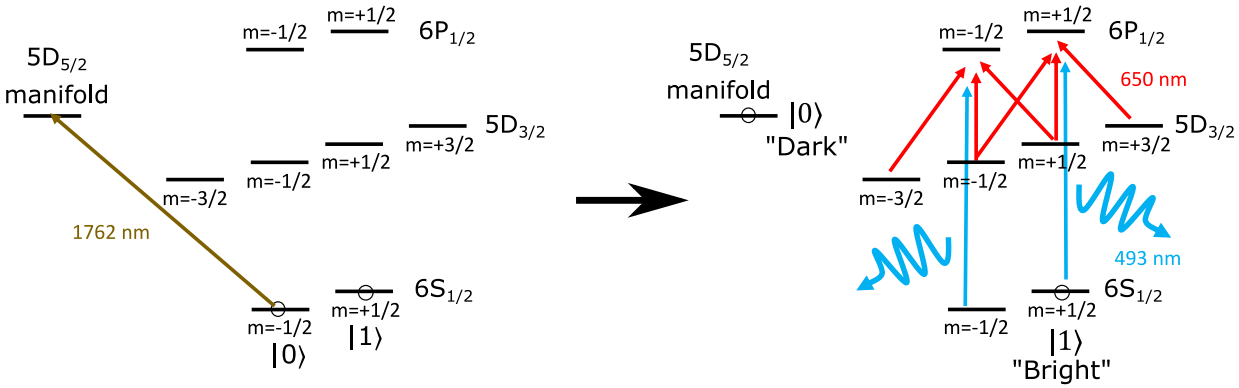

Figure 8.1: **State Detection via the Quadrupole Transition.** One of the ground qubit states is shelved to the $D_{5/2}$ manifold using light near 1762 nm. The shelved state will not emit 493-nm photons when illuminated with the 493 nm and 650 nm Doppler cooling beams, enabling high-fidelity deterministic state detection.

ion fluorescence on our PMT, discussed in Sec. 8.2, and of how we initially align the 1762-nm and 614-nm beams needed to shelve and remove (or "de-shelve") the ion to and from the $D_{5/2}$ manifold, discussed in Sec. 8.3. Spectroscopy data of the transitions used to shelve the ion are discussed in Sec. 8.4. The shelving itself, via a Rabi π-pulse, is discussed in Sec. 8.6.

In addition to being useful for state detection, we can also use this transition to make measurements of our optical pumping efficiency into a selected Zeeman qubit state, as well as make measurements of the temperature of the ion. We will briefly explore these topics in Sections 8.5 and 8.7 respectively and discuss their effects on the fidelity of state detection.

8.2 State Detection Histogramming

To verify that we have shelved the ion, we will perform state detection by applying our typical Doppler cooling 493-nm and 650-nm beams. If we have properly shelved the ion into the $D_{5/2}$ manifold, it will be unaffected by these beams and will not fluoresce, such that we will not detect any photons on our PMT (Fig. 8.1). We denote this state as "dark". Otherwise the state

will be “bright”.

Due to both counting statistics and the presence of background photons, we need to discriminate between how many photon clicks on our PMT, in a specified time window, indicate a bright state vs how many indicate a dark state. To determine this discriminator, the ion is first viewed on our camera, and we use an iris in this path to reduce background noise (see Chapter 3 for more details). We can then use a flipper mirror to direct this light to our state detection PMT. We measure the distribution[1] of photon counts corresponding to a bright state (blue in Fig. 8.2 (a)) by Doppler cooling the ion for the detection window and counting photon events on the PMT. In a similar manner, we determine the dark state distribution (orange in Fig. 8.2 (a)) by repeating this measurement after moving the ion out of the iris aperture by adjusting our trap electrode voltages. This simulates the ion being shelved into the $D_{5/2}$ manifold. Given the long > 30 s lifetime of this dark state, and the fact that our state detection here is on the order of a few milliseconds (1 ms in Fig. 8.2), this is an extremely good approximation of the number of photons expected to be detected when the ion is successfully shelved.

The vertical red line at a count value of 9 in Fig. 8.2 indicates the value used to discriminate between bright and dark states (for this particular calibration run). This value is chosen to minimize the state detection error, given by the total number of events (both bright and dark) on the “wrong” side of the discriminator divided by the total number of events, and shown in Fig. 8.2 (b). Error values vary slightly from experiment to experiment, depending on the amount of background noise in the lab (room lights on vs off, laser beam alignment to trap) and on the brightness of the ion, which varies slightly due to drifts in laser locking, or due to our chosen laser

[1] We expect the number of photons detected in this window to follow a Poissonian distribution based around the average number of photons expected.

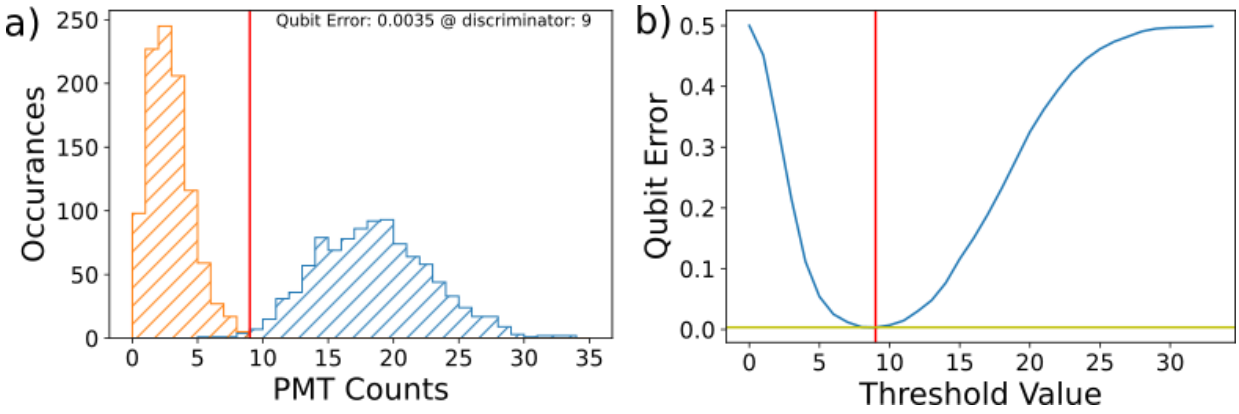

Figure 8.2: **Typical Bright State/Dark State Histograms.** **(a)** A bright state/dark state (blue/orange) histogram for our typical noise and Doppler cooling parameters and a 1 ms detection time. **(b)** State detection discrimination error as a function of discriminator for the data shown in (a). The red vertical line in both plots denotes the optimal discriminator value.

cooling parameters for a typical experiment. In most cases, state discrimination can be improved by longer PMT exposure times, at the cost of increased experimental run time. For the majority of our experiments, the state detection loop is by far the longest step (1-3 ms).

8.3 Initial Spatial Alignment and Frequency Tuning: Quantum Jumps

The alignment direction of our 1762-nm quadrupole addressing beam is described in Chapter 3. The initial process of alignment however, can be difficult, due to the fact that the 1762-nm beam is invisible, and because of the need to focus the beam along the axis of the trap, with the least amount of optical access. To achieve coarse spatial alignment to the ions, we use a visible guide beam that is spatially overlapped with the 1762-nm beam. For convenience and as discussed in Chapter 3, this guide beam is the 614-nm beam that will be used to de-shelve the ion from the $D_{5/2}$ manifold after state detection.

We initially collimate both beams through the trap, using the shadow of the trap in the 614-nm beam to center both beams along the trap axis. We then add in a focusing lens and repeat this

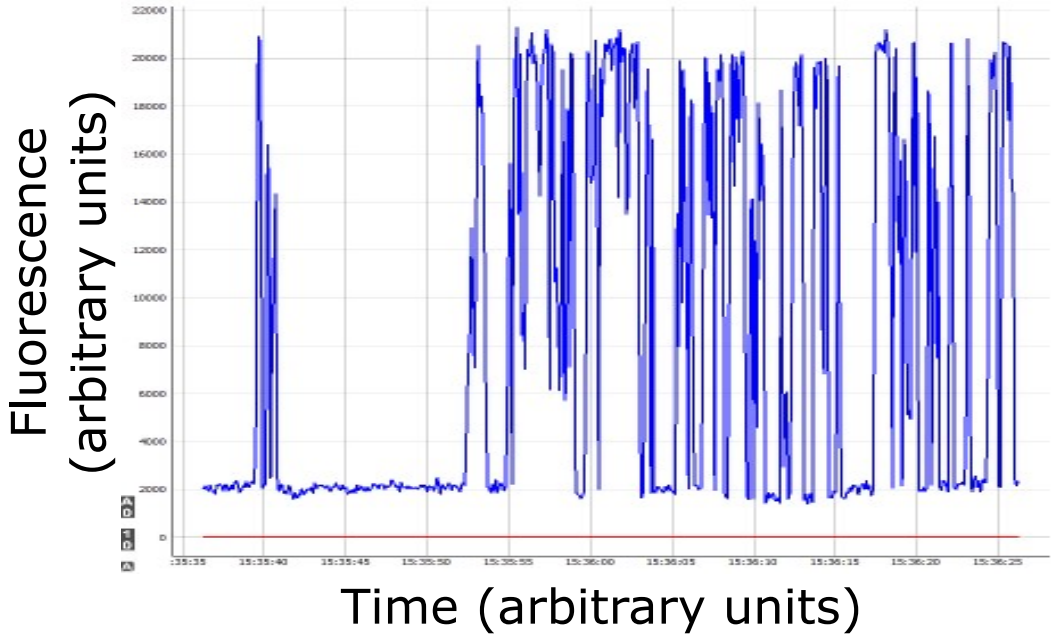

Figure 8.3: **Quantum Jumps.** Screenshot of live ion-fluorescence measurements (old control system). With the 1762-nm laser coarsely aligned to the ion and unlocked (but tuned somewhere near resonance), ion fluorescence is measured with a PMT. The ion periodically goes dark for some time, before going bright again. Improving alignment increases the frequency of the jumps between bright and dark (right side of figure).

procedure, aligning the 614-nm beam such that we get maximum transmission out of the other side of the vacuum chamber, while again using the shadow of the trap to verify we are between all four blades. This focusing lens is optimized for the 1762-nm beam focus and does not focus the 614-nm beam anywhere near the ion. We make this choice to maximize the Rabi frequency of the 1762-nm beam, as we have plenty of 614-nm power to spare if needed[2].

With this coarse alignment, it is possible to see interactions between the 1762-nm light and a trapped Ba+ ion[3]. With around 5 mW of 1762-nm light roughly aligned to the trap, and without the laser locked to our ULE cavity system (free running fast linewidth ≈100 kHz), we were able to observe "quantum jumps" [170], where the ion flourescence is suddenly quenched due to the ion being shelved into the $D_{5/2}$ manifold and out of the Doppler cooling cycle. Experimentally,

[2]We have up to about 1 mW available at the trap, though we typically use on the order of 100s of μW
[3]In fact it is possible to see this with collimated 1762-nm light

when viewing the ion on a camera and with our doppler cooling beams incident on the ion, we find that as we coarsely scan the 1762-nm laser frequency near where we expect resonance[4] to be [171,172], the ion will periodically disappear on the camera, going "dark" for a moment before going "bright" again on the camera. Both the frequency and the alignment of the 1762-nm beam can increase the frequency of this shuttering between bright and dark. We find that using this method we can get the laser within 10s of MHz of the center of all of the possible $S_{1/2} \leftrightarrow D_{5/2}$ quadrupole transitions. To coarsely align the 1762-nm beam to the ion spatially, we view these quantum jumps on our PMT, as shown in Fig. 8.3. Improved alignment of the beam increases the frequency of these jumps in fluorescence. Fig. 8.3 shows improved alignment moving from the left to the right, as the frequency of jumps increases dramatically.

In addition to coarsely aligning and tuning the frequency of the 1762-nm laser, we need to be confident in our 614-nm laser's ability to de-shelve the ion from the $D_{5/2}$ manifold. We can begin this (coarse) alignment by first inducing quantum jumps with the 1762-nm laser, followed by turning on and aligning the 614-nm light to completely quench these jumps, bringing the ion back to full brightness. Finer alignment is then performed by repeating the following sequence in an automated fashion:

1. Begin with the 614-nm laser off and the 1762-nm laser on.

2. Repeatedly perform bright/dark state detection, waiting for the ion to go dark.

3. When the ion goes dark, turn off the 1762-nm light and turn on a 614-nm pulse for a set time, power, and at a set frequency.

4. Measure and record if the ion is bright or dark.

[4] As viewed on our Bristol wavemeter discussed in Chapter 3

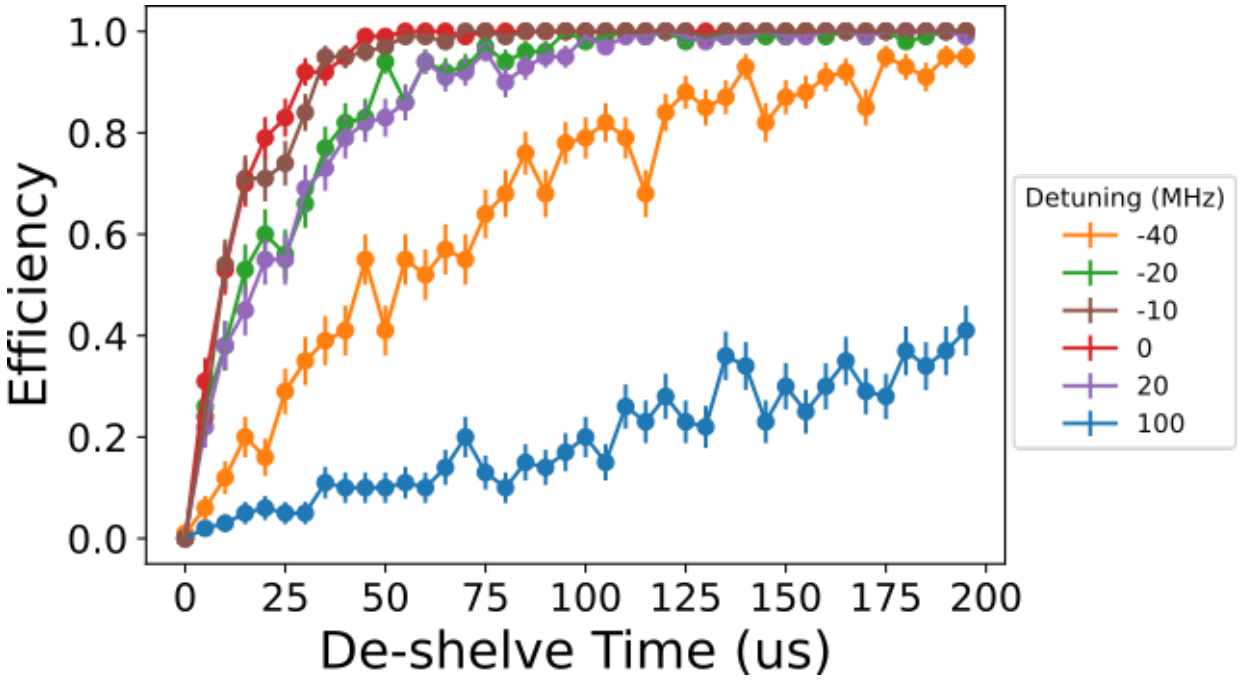

Figure 8.4: **614 Frequency Calibration.** The de-shelving efficiency of the 614-nm laser is used to tune the laser near resonance. Multiple scans at different frequencies are used to maximize the de-shelving efficiency. The presented scans are before optimization of optical alignment, with 100 runs per data point. Error bars are statistical.

5. Repeat 100s of times before scanning either the 614-nm pulse length or frequency.

The result of scanning the de-shelve time for various 614-nm lock frequencies is shown in Fig. 8.4. We use this procedure to tune the 614-nm laser system closer to ion resonance and to determine how long we need to pulse the beam to guarantee that the ion is de-shelved after an experimental run.

The 614-nm beam alignment may also be improved by repeating one of these experiments at a set frequency and de-shelve time whilst actively aligning the beams to increase the de-shelve efficiency. Once this efficiency approaches unity, we reduce the de-shelve time and repeat physically aligning the beam. After this procedure, we typically set the de-shelve time to be much longer (100 us - 1 ms) than is necessary (a few us when very well aligned) to allow for some drift

in 614-nm beam alignment[5]. This allows us to be extremely confident that between experimental runs, the ion is de-shelved.

8.4 Quadrupole Transition Spectroscopy

The procedure for performing spectroscopy on the 1762 nm $S_{1/2} \leftrightarrow D_{5/2}$ transition is as follows:

1. Prepare the ion into both of or one of the $S_{1/2}$ ground states using all polarizations of 650-nm light and, if preparing into a particular m-level of the $S_{1/2}$ manifold, 493-nm sigma light (5-50 μs).

2. Attempt to shelve the ion to the $D_{5/2}$ manifold using the 1762-nm laser for a chosen shelving time and frequency.

3. State Detect ($\approx 1-2$ ms depending on 493-nm and 650-nm laser power and frequencies).

4. Doppler cool the ion ($\approx 1-2$ ms). The de-shelving 614-nm laser is on for this step.

5. Repeat N times for each 1762-nm laser frequency step.

The corresponding laser pulse sequence is shown in Fig. 8.5. For spectroscopy, the 1762-nm pulse length is kept constant, and the frequency of the beam is changed at each step.

Fig 8.6 shows a result of one such spectroscopy scan, with the 1762-nm beam polarization set at $\approx 60^\circ$ to the plane of incidence between the B-field and 1762-nm beam path. This scan was performed with 20 kHz frequency steps and a pulse length of 13 μs for the 1762-nm light, with

[5]This beam is also sometimes misaligned as we improve the 1762 nm alignment using optics common to both beam paths.

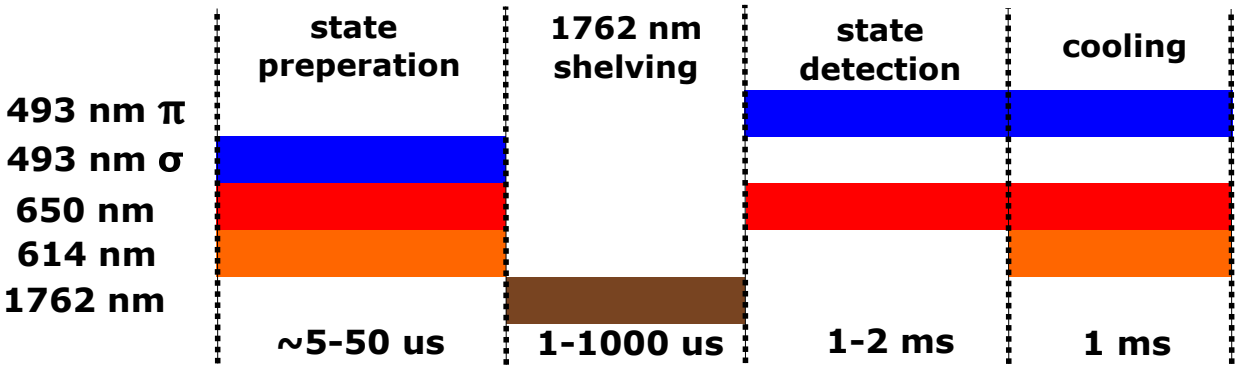

Figure 8.5: **Pulse sequence for addressing the 1762-nm quadrupole transitions.** When performing spectroscopy, the frequency of the 1762-nm beam is scanned, and the pulse length kept constant. For Rabi oscillations, the 1762-nm beam frequency is held constant and the pulse length is instead varied.

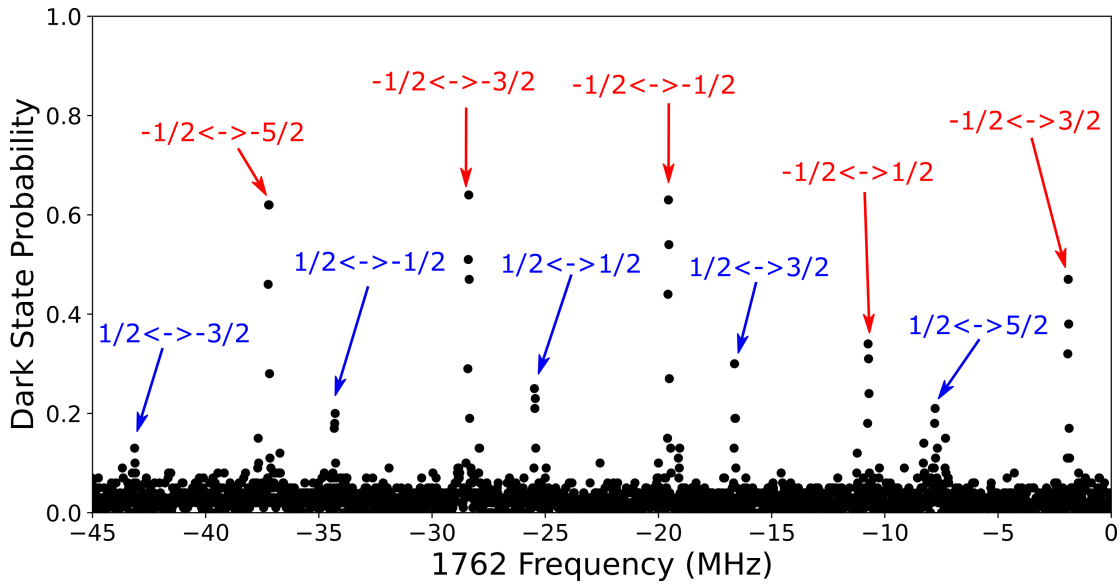

Figure 8.6: **Quadrupole Transition Spectroscopy Scan Before Optimization.** The 1762-nm laser frequency is scanned across the quadrupole transition. Scans are performed as a series of smaller 2 MHz AOM frequency steps, followed by a shift in laser lock frequency relative to the cavity by changing the frequency of the EOM used in locking, before the next AOM frequency scan. Transitions are labeled with the starting S-state Zeeman sub-level on the left and the resulting D-state Zeeman sub-level on the right. Labels are color coded by S-state Zeeman sub-level. Due to the polarization angle of the 1762-nm beam ($\approx 60°$) relative to the quantization axes, combined with random state preparation into the S-manifold, all 10 transitions are visible.

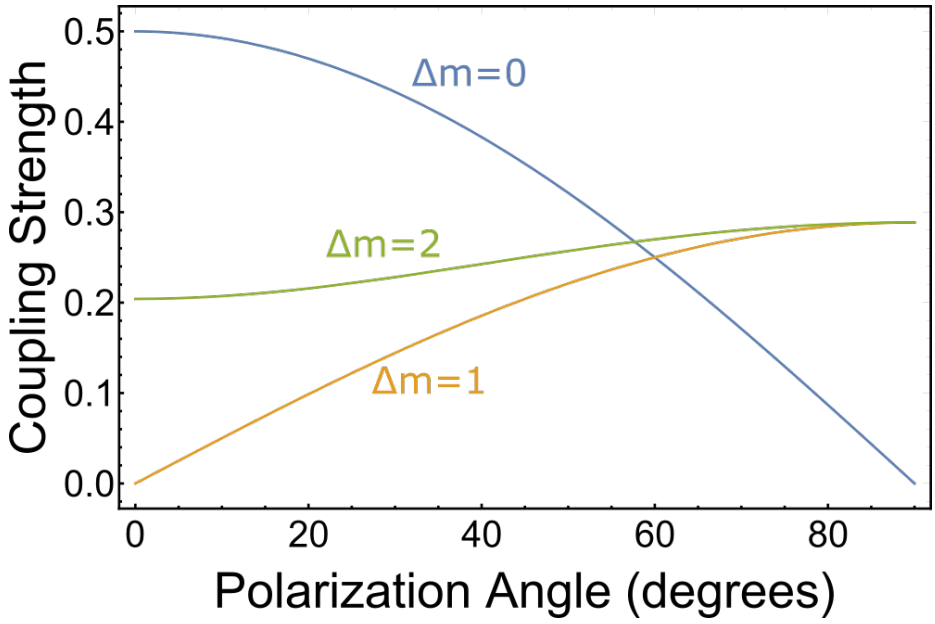

Figure 8.7: **Coupling Strength of Quadrupole Transitions as a Function of Beam Polarization.** Effect of beam polarization (relative to the plane of incidence with the quantization axis) on the relative Rabi frequencies of different transitions with the 1762 nm beam at an angle of 45° relative to the quantization axis. The theory used to produce these curves can be found in [102].

100 runs at each step, and without preparation into a particular ground state Zeeman sub-level (493-nm sigma beam OFF). Frequencies were recorded relative to an arbitrary zero point set near the highest frequency transition. All 10 possible quadrupole transitions are visible and labeled in this scan.

To maximize our shelving efficiency (and state detection fidelity) in our experiments, we use one of the $\Delta m = 0$ transitions, as these are least sensitive to any magnetic field noise on the ion [102]. We can increase our Rabi frequency to drive this transition by rotating the 1762-nm beam polarization to be roughly aligned parallel to the plane of incidence between this beam and the quantization axis defined by our applied magnetic field, as shown in Fig. 8.7. Fig. 8.8 shows a full spectroscopy scan across the quadrupole transitions after roughly optimizing this angle and including optical pumping into the $m = -1/2$ ground state before shelving (see Sec. 8.5). Here,

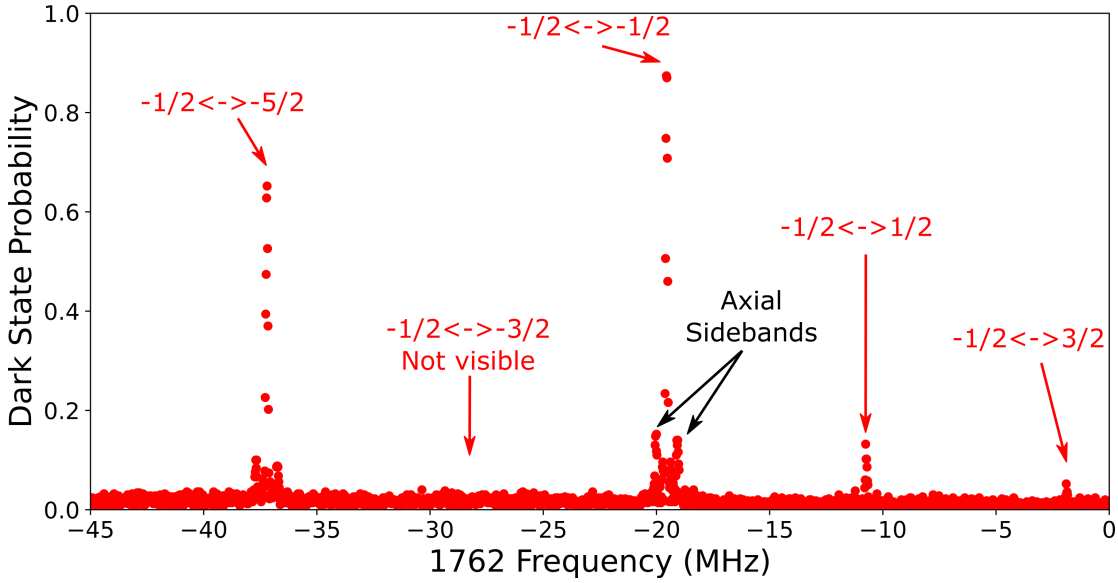

Figure 8.8: **Roughly Optimized Quadrupole Transition Spectroscopy.** After polarization and state-preparation optimization, the 1762-nm laser frequency is scanned across the quadrupole transitions. Only transitions involving the $\left|6S_{1/2}, m_j = -1/2\right\rangle$ ground state are readily visible, and the $\Delta m_j = 0$ transition strength is improved. Axial sidebands are visible for this transition.

we use 20 kHz frequency steps and set the 1762-nm pulse length to 8μs, and perform 500 runs at each step. With this configuration, only transitions involving the $m = -1/2$ ground state are easily visible, and the $\Delta m = 0$ transition Rabi frequency is increased. One of the $\Delta m = \pm 1$ transitions is still somewhat visible, indicative of some remaining polarization misalignment.

A zoom in on the $\left|6S_{1/2}, m_j = -1/2\right\rangle \leftrightarrow \left|5D_{5/2}, m_j = -1/2\right\rangle$ transition is shown in Fig. 8.9. This scan was performed with a frequency step size of 10 kHz, and with the 1762-nm pulse length set to just below the duration of a π-pulse. Both axial-motional sidebands are visible in this scan, located approximately 476 kHz from the central peak. We scan across this transition, including the motional sidebands, (almost) daily to track both the transition frequency and to provide a measure of the ion temperature, as will be discussed below. The drift in transition frequency, as measured by the relative laser frequency needed to drive the transition, is shown in Fig 8.10. A linear fit to the data suggests a drift in this frequency of ≈ 3.7 kHz/day.

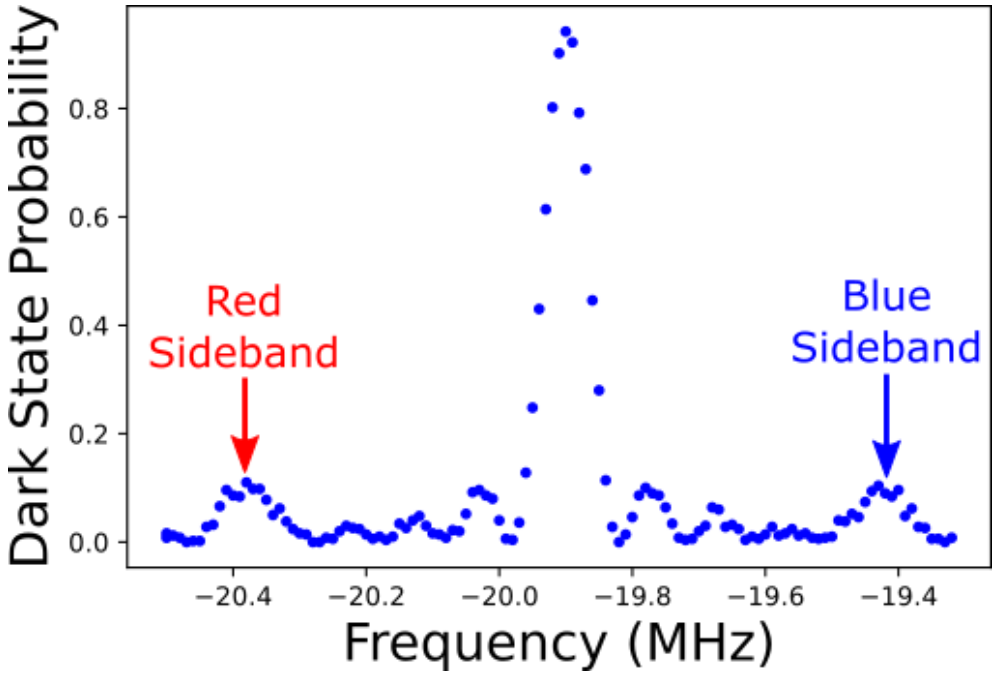

Figure 8.9: **Zoom in on $\Delta m_j = 0$ transition.** The 1762-nm laser is scanned across the $\left|6S_{1/2}, m_j = -1/2\right\rangle \leftrightarrow \left|5D_{5/2}, m_j = -1/2\right\rangle$ transition with a step size of 10 kHz. Axial motional sidebands are visible ≈ 476 kHz away from the carrier. Additional "peaks" near the power-broadened carrier are due to off resonant coherent excitation, visible with the strong drive.

Corresponding measurements of the ground state RF transition frequency (Chapter 9) suggest that this drift is not related to any slow changing magnetic field on the ion. Therefore this drift is believed to be caused either by a drift in resonance frequency of the 1762-nm laser's ULE locking cavity[6] or by a drift in the frequency source driving the EOM required to lock the laser (Chapter 3).

8.5 S-State Optical Pumping Efficiency

The remainder of this chapter will discuss using the $D_{5/2}$ quadrupole transition for state-selective shelving, ion-temperature measurements, and for the measurement of magnetic field noise present at the location of the ion. Each of these measurements will be limited by the ability

[6] According to the manufacturer, Stable Laser Systems, drifts of up to 10 kHz/day can be expected.

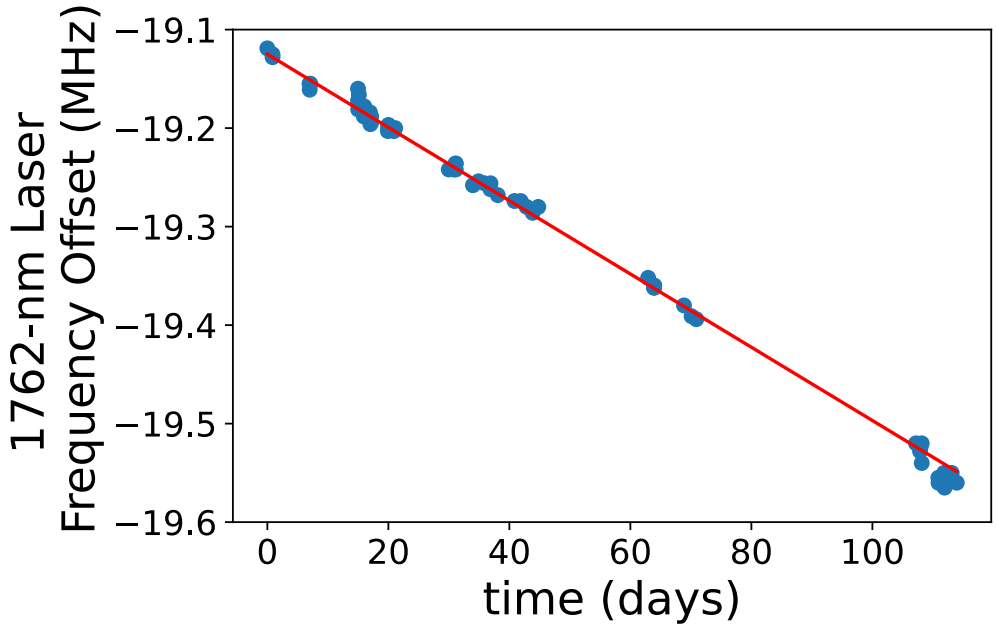

Figure 8.10: **Quadrupole Transition Frequency Drifts.** AOM frequency offset corresponding to resonance with the $\left|6S_{1/2}, m_j = -1/2\right\rangle \leftrightarrow \left|5D_{5/2}, m_j = -1/2\right\rangle$ transition, measured over time. Scatter in the data points is caused by only taking the highest data point in a spectroscopy scan, rather than fitting to each peak (to save computational time). The fitted line suggests a frequency drift of 3.7 kHz/day.

of our system to pump the ion into a particular Zeeman sublevel of the $S_{1/2}$ manifold. This ability depends on both the alignment of our σ-polarized 493-nm beam along the quantization axis defined by our magnetic field and on the purity of this beam's circular polarization. As discussed in Chapter 3, this beam shares its optical path with both σ-polarized 650-nm beams, and uses the same final quarter and half waveplates. Although these waveplates are roughly achromatic, they are optimized for the 650-nm beams, as these are critical for both efficient and high-fidelity photon production (Chapter 2). Therefore, by definition, these waveplates will not be in the optimal position for optical pumping into a particular Zeeman ground state[7].

To know what effect this has on the calibration of any of the following 1762-nm calibration measurements, we first need to measure this optical pumping efficiency. We perform a series

[7] though they should be pretty close

of consecutive spectroscopy measurements of both $\Delta m_j = 0$ quadrupole transitions under the same laboratory conditions, following a procedure similar to [173]. Figure 8.11 shows the result of such successive measurements for two different settings of the achromatic quarter waveplate in the σ-beam path. Here, we are careful to use the same power[8] for each measurement, such that each transition is driven with the same Rabi frequency. The length of the shelving pulse is also kept constant between both scans, set slightly below what is needed to drive a π-pulse. The populations, $p_{\pm 1/2}$, of the Zeeman sublevels, $\left|6S_{1/2}, m_j = \pm 1/2\right\rangle$ are then given by

$$p_{\pm 1/2} = \frac{A_{\pm}}{A_+ + A_-}, \tag{8.1}$$

where $A\pm$ represents the amplitude of the spectroscopy peak for the $\left|6S_{1/2}, m_j = \pm 1/2\right\rangle \leftrightarrow \left|5D_{5/2}, m_j = \pm 1/2\right\rangle$ transitions. Using equation 8.1, and the data shown in Figure 8.11, we calculate optical pumping efficiencies into $\left|6S_{1/2}, m_j = -1/2\right\rangle$ of 0.65 ± 0.02 and 0.96 ± 0.02 before and after optimizing the quarter waveplate angle. This sets a bound of 0.96 for the maximum population shelved by our 1762-nm laser in when using S-state pumping, but this is not necessarily the maximum shelving efficiency when considering state detection for the ion-photon entanglement experiments discussed in the next chapter, which uses the pulse sequence discussed in Sec. 2.3.4.

8.6 Rabi Flopping

With the 1762-nm laser tuned to resonance with the $\left|6S_{1/2}, m_j = -1/2\right\rangle \leftrightarrow \left|5D_{5/2}, m_j = -1/2\right\rangle$ transition, we can perform state-selective shelving by driving Rabi Oscillations. We drive these

[8] This is achieved by using the same AOM drive frequency to turn on the 1762 nm pulse - the frequency of the light is instead altered by changing the EOM frequency drive used to lock the laser discussed in Chapter 3.

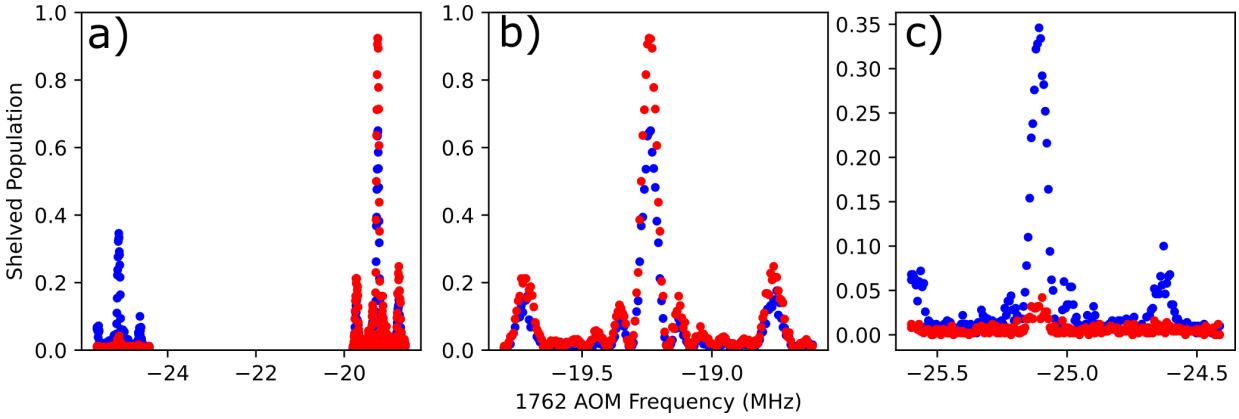

Figure 8.11: **S-State Optical Pumping Efficiency Scans.** Spectroscopy scans across both $\Delta m_j = 0$ quadrupole transitions. Blue(red) data correspond to data before(after) optimization of pumping efficiency via sigma beam quarter waveplate angle. a) Full scan. b) Zoom in on the $\left|6S_{1/2}, m_j = -1/2\right\rangle \leftrightarrow \left|5D_{5/2}, m_j = -1/2\right\rangle$ transition. c) Zoom in on the $\left|6S_{1/2}, m_j = +1/2\right\rangle \leftrightarrow \left|5D_{5/2}, m_j = +1/2\right\rangle$ transition.

oscillations in a similar fashion to the transition spectroscopy described above, but with the AOM frequency fixed and the shelve time varied (Fig. 8.5). Fig. 8.12 shows these oscillations on this transition, with optimal s-state preparation and with the 1762-nm laser polarization set to be parallel to the plane of incidence between it and the magnetic field present at the ion. For this scan, the 1762-nm laser power is set to 10 mW, and the beam alignment has been improved to maximize Rabi frequency via repeated Rabi scans followed by beam adjustment. We measure a Rabi frequency of 57.6 kHz, limited by the beam geometry discussed in Chapter 3. Nevertheless, the corresponding π-time of around 10 μs is fast enough to not greatly impact the speed of state detection, which takes on the order of a few milliseconds.

8.7 Ion Temperature Measurements

In addition to state selective shelving, we can use the $S_{1/2} \leftrightarrow D_{5/2}$ quadrupole transition to make measurements of the average temperature of the ion's motional modes. This temperature

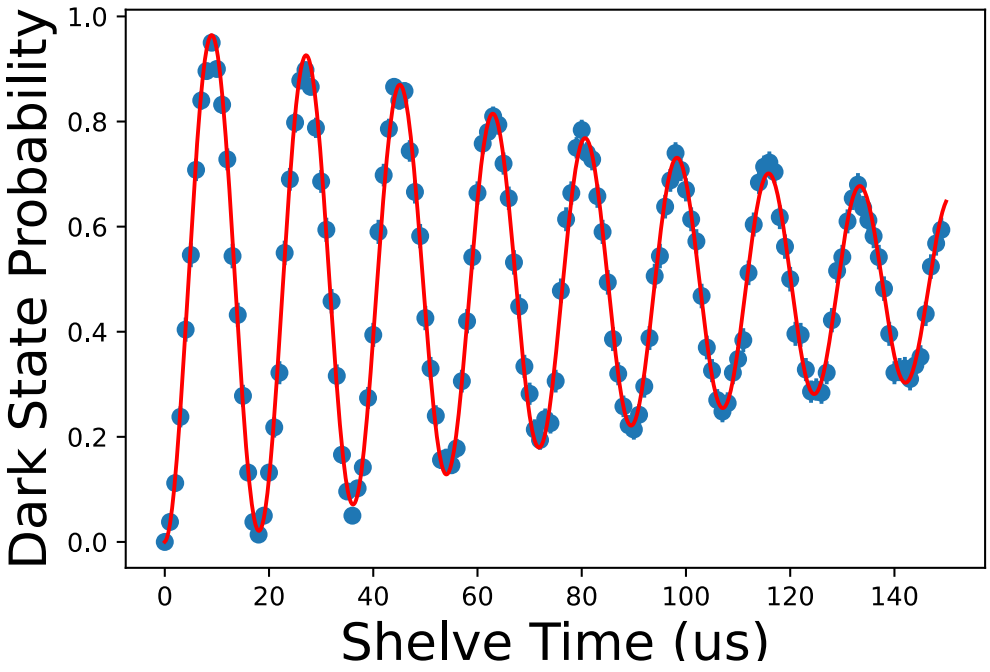

Figure 8.12: **Rabi Flopping on the 1762-nm Quadrupole Transition.** The 1762-nm laser frequency is set to be resonant with the $\left|6S_{1/2}, m_j = -1/2\right\rangle \leftrightarrow \left|5D_{5/2}, m_j = -1/2\right\rangle$ transition. The displayed fit using Eqn. 8.7 suggests a Rabi frequency of 57.57 ± 0.04 kHz and an average ion temperature of 53 ± 0.9 motional quanta in the axial mode.

also limits the number of coherent operations that can be performed with the 1762-nm laser. We measure this temperature via two different methods.

We first use the spectroscopic data from Fig 8.9 to measure the relative amplitudes of the motional sidebands with respect to the carrier. These amplitudes, for a given pulse duration, are determined solely by their Rabi frequencies. The Rabi frequency of a carrier transition, with the ion in motional level n, can be estimated as [67, 100]

$$\Omega_{n,n} \approx \Omega_0 \left(1 - \left(n + \frac{1}{2}\right)\eta^2 + \left(\frac{1}{4}n^2 + \frac{3}{4}n + \frac{1}{8}\right)\eta^4\right), \tag{8.2}$$

where η is the Lamb-Dicke parameter, defined in terms of the wave number of the incident light,

k, the ion mass, m, and the secular frequency, ω, as

$$\eta = k\sqrt{\frac{\hbar}{2m\omega}}. \tag{8.3}$$

The Rabi frequency of the blue sideband connecting motional state n to state n+1 can also be estimated as [67]

$$\Omega_{n,n+1} \approx \Omega_0 \eta \sqrt{n+1}\left(1 - \frac{1}{2}(n+1)\eta^2\right). \tag{8.4}$$

We can then write an expression for the ratio of the Rabi frequency of the blue sideband to the carrier to third order in η[9]

$$\frac{\Omega_{n,n+1}}{\Omega_{n,n}} \approx \eta\sqrt{n+1}\left(1 + n\eta^2/2\right). \tag{8.5}$$

In reality, the ion is not in a precise motional state, and its motion should be described as a thermal distribution of the possible motional levels. Nevertheless, as in [67], we can make an estimate of the average number of motional quanta, $\bar{n}$ by setting $n = \bar{n}$ in Eqn. 8.5. With the axial side bands seen at 476 kHz in Fig. 8.9, we calculate $\eta \approx 0.031$ using Eqn. 8.3. Also from this figure, we can read off the amplitudes of the carrier, A_C, and blue sideband, A_{BSB}, as 0.92 and 0.10, respectively. Their Rabi frequencies can then be estimated as

$$\Omega_{C,BSB} = arcsin\left(\sqrt{A_{C,BSB}/E}\right), \tag{8.6}$$

where E is the optical pumping efficiency of the 1762 beam, including imperfect state preparation, and $\Omega_C(\Omega_{BSB})$ is the Rabi frequency for the carrier (blue-sideband). Using $E = 0.96$, and

[9]Using the approximation $1/(1-x) \approx 1 + x$ where $x = 1 - (n + \frac{1}{2})\eta^2$.

Eqns. 8.6 and 8.5 we can calculate $\frac{\Omega_{BSB}}{\Omega_C} \approx 0.24$, which results in $\bar{n} \approx 55$. This corresponds to an axial ion temperature of $T \approx 1.3$ mK.

The Rabi oscillations shown in Fig. 8.12 decay in amplitude as a result of coupling to the ion's secular motion. This effect can itself be used to measure the temperature of the ion. With the ion in a thermal distribution of different n levels, the measured Rabi oscillation data is an incoherent sum of many oscillations at slightly different frequencies, weighted by the population in each particular n level. We can therefore use this data as a measure of ion temperature.

The overall shelved population as a function of the shelving pulse length can be written as [67]

$$P_{D_{5/2}} = \frac{1}{2}\left(1 - \sum_{n=1}^{\infty} p_n \cos(\Omega_{n,n} t)\right), \tag{8.7}$$

where the p_n terms represent the probability of the ion being in motional state n. Assuming a thermal distribution,

$$p_n = \frac{\bar{n}^n}{(\bar{n}+1)^{n+1}}. \tag{8.8}$$

By using equation 8.7, we can fit to the Rabi oscillation data shown in Fig. 8.12, after correcting for the imperfect S-state optical pumping efficiency described above. Using 1000 terms in the sum of Eqn. 8.7, and fitting for both the Rabi frequency and the average energy level for axial-motion of the ion, we measure $\bar{n} = 53 \pm 1$, corresponding to an ion temperature of 1.21 ± 0.03 mK, and in agreement with the coarse measurements made above using the amplitude of the motional sidebands.

The temperature of the ion, as measured via the methods discussed above can vary depending on the power and frequency settings of the 493-nm and 650-nm beams. The temperature demonstrated above was found by iteratively tuning the frequencies and powers of these beams to reduce

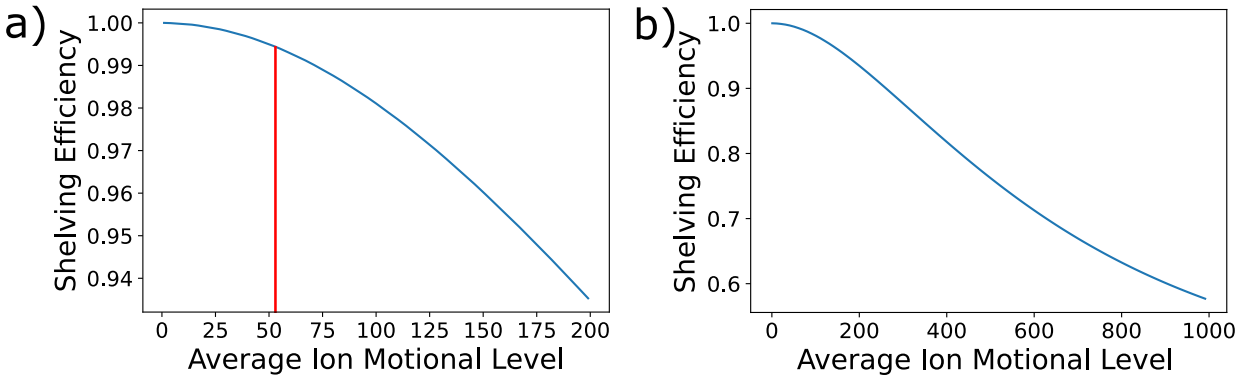

Figure 8.13: **Shelving Efficiency as a Function of Ion Temperature.** The maximum shelving efficiency achievable when limited solely by ion temperature, calculated using the first 5000 terms in Eq. 8.7, and assuming a thermal distribution of motional quanta around an average. a) Shelving efficiency for average ion motional quanta ranging from 0 to 200. The vertical red line corresponds to the minimum ion temperature measured in our lab given our Doppler cooling parameters. b) Efficiency for average motional quanta ranging from 0 to 1000.

this temperature, whilst still leaving the ion flourescence bright enough to make state detection measurements on the order of 1-2 ms. The lasers, being locked only via a wavemeter that experiences daily drifts in accuracy on the order of 10 MHz, experience some drift in frequency throughout the day. The ion-temperature is therefore measured using the Rabi oscillation method before any experimental runs to account for these drifts, which can quickly be corrected by small adjustments to the laser frequencies and powers.

The incoherence due to ion temperature also sets a theoretical limit on the fidelity of the shelving pulse, which is given by the amplitude of the first Rabi oscillation as described by equation 8.7, assuming perfect state preparation. Fig. 8.13 shows this shelving fidelity as a function of $\bar{n}$, calculated using 5000 terms for the sum in Eqn. 8.7. For $\bar{n} = 53$, we see that our shelving fidelity is limited to ≈ 0.994. A higher ion temperature of $\bar{n} = 100$ would limit this fidelity to ≈ 0.982.

Improvements could be made to our experimental setup to further reduce ion temperature. This could be achieved, for instance, via sideband cooling on the motional sidebands of the

$\Delta m_j = 2$ quadrupole transition [102], but would require a wider bandwidth 1762-nm AOM than we currently have available, which would additionally need to be setup in a double-pass configuration, costing us laser power. Another possible method is EIT-cooling [64, 172, 174], which could in theory be implemented with our current experimental setup. Finally, changing the 1762-nm beam direction to address the radial modes of the ion rather than the axial modes would, for the same ion temperature, result in a lower $\bar{n}$ and therefore increase the fidelity of the 1762-nm operations. Such a geometry is not possible in our setup however, with the relevant ion-chamber windows not properly coated for 1762-nm transmission in these directions (Chapter 3).

For now, these improvements have not been investigated, as a shelving error of $\approx 6\times10^{-3}$[10] is sufficient for the work presented in this thesis, with other errors expected to dominate ion-photon entanglement infidelities. Such improvements become important once other sources of infidelities are reduced, or if one wishes to perform qubit operations using the optical qubit. Using the $\Delta m_j = 0$ optical qubit, for instance, has the advantage of being less sensitive to magnetic fields than the Zeeman ground state-qubit. One can also imagine swapping ion-photon entanglement with the ground-state Zeeman qubit onto optical clock qubits for producing an atomic clock quantum sensor network.

[10] In Chapter 10, we operate at a slightly higher temperature, $\bar{n} \approx 80$.

Chapter 9: Ground State Zeeman Qubit in $^{138}Ba^{+}$

9.1 Introduction

Using the state detection described in Chapter 8, we have the ability to measure the effect of any manipulations we make on the S-State state Zeeman qubit, defined as $|0\rangle = \left|6S_{1/2}, m_j = -1/2\right\rangle$ and $|1\rangle = \left|6S_{1/2}, m_j = +1/2\right\rangle$. In this chapter, I will describe how we address this qubit and perform the operations crucial for the interrogation of ion-photon entanglement discussed in the following chapter. Additionally, I will demonstrate measurements of qubit decoherence and resonance frequency instability, due primarily to magnetic field noise, which can have a negative impact on the measured ion-photon entanglement fidelity measured in Chapter 10.

9.2 Addressing the Qubit - RF Antenna Design

One commonly used method to address qubits in trapped ions involves driving Raman transitions [27, 64, 104, 172], using a pair of optical beams (typically at 532 nm for Ba^{+}) with a relative detuning equal to the qubit splitting. One main advantage of the Raman method is that the same lasers, with different detunings, can also be used to address the motion of the ion, allowing for ion-ion entangling gates to be driven via the Molmer-Soresen interaction [27, 175]. As our lab has primarily been concerned with single ion/single photon experiments, and due to the fact

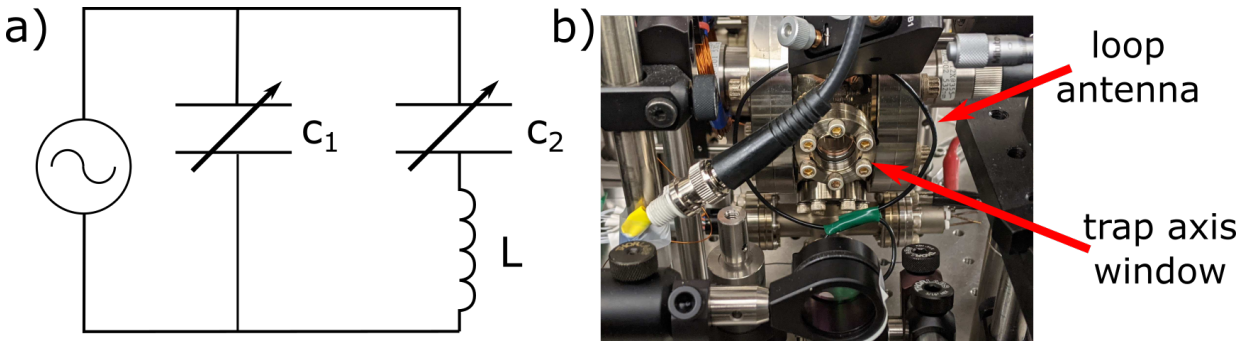

Figure 9.1: **RF Antenna Design.** **(a)** Circuit design for the antennas used to drive the radio-frequency ground state qubit in $^{138}Ba^{+}$. Two tunable capacitors (65-320 pF) allow for a resonant circuit that is impedance matched at the qubit's resonance frequency. Input couplers (20 dB), assist in tuning the circuit onto resonance via monitoring the reflection of a frequency sweep signal off of the circuit. These couplers are also used for monitoring the circuit during operations. **(b)** A loop antenna is placed $\approx$ 70mm away from the ion, oriented with the axis of the trap to drive qubit transitions. This is the antenna used for the ion-photon entanglement experiments described later in this thesis.

that there are other types of ion-ion gates we can potentially drive with other lasers in the lab (utilizing the quadrupole transition optical qubit [176–178]), we do not use this method. Instead, we opt to drive our Zeeman qubit directly with radio frequency (RF) radiation via a home-built RF antenna[1].

The RF antenna design Fig. 9.1 a. consists of a single loop of wire (18 gauge), connected in series with a capacitor, c_1 to form a resonant LC circuit. This capacitor is tunable to give us a better chance of matching the circuit frequency resonance with the ion. An additional tunable capacitor, c_2 is put in parallel with the LC circuit to allow for impedance matching to 50 Ω. The final antenna designs used tunable capacitors ranging from 65-320 pF.

Two different antennas at two separate positions were constructed to address the qubit. The first was placed just outside one of the horizontal viewports of the vacuum chamber, as shown in Fig. 9.1 b., with its center axis roughly oriented along the axis of the axis of the trap, and located

[1]This also has the benefit of being much cheaper then using a laser.

approximately 70 mm from the ion. The second antenna, in an attempt to provide a higher Rabi frequency, was placed just outside of the 0.6 NA photon collection window, approximately 20 mm from the ion, with its center axis perpendicular to this window. To optimize the amplitude of the field on the ion given the antenna geometry, wire loop diameters of ≈ 3 inches and ≈ 2 inches were used for the first and second antennas, respectively.

It turns out to be surprisingly difficult to construct an antenna-circuit combination resonant with the exact target frequency[2]. The addition of any parasitic capacitance on the order of 10s of pF can significantly lower the resonance of the circuit. Any unintentional mutual inductance with other components around the ion chamber can also change the circuit's resonance frequency. Therefore, the antenna circuits, in particular the gauge of the wire used in the loops as well as the number of total wire loops, were iteratively altered to properly operate near ion resonance.

Using the quadrupole spectroscopy scans shown in Chapter 8, we are able to precisely predict the required RF frequency. To precisely tune in the antenna resonance before attempting to interrogate the ion, frequency sweeps were applied (using a spectrum analyzer[3]) to the antenna circuits as a whole, and reflections off of the circuit as a function of frequency were measured on a spectrum analyzer via a 20 dB input pickoff[4]. The two tunable capacitors, c_1 and c_2 were then adjusted to minimize the reflections[5] off of the antenna at ion resonance.

The drive signal for the antenna is provided via the same frequency synthesizer[6] use to provide drive signals for our laser AOMs described in Chapter 3. The output of this synthesizer

[2] At least with the loop geometry used here.
[3] Rigol DSA815
[4] Minicircuits ZDC-20-3
[5] To protect control electronics from high power reflections of RF, the circuit should be re-tuned with the capacitors when moving the RF on the order of $\approx$100 kHz.
[6] Analog Devices AD9910 DDS

is sent through a 2 W amplifier [7], with the amplified signal sent to the antenna circuit. A TTL-controlled RF switch is used to pulse on and off the RF signal, and to ensure no undesired drive of the ion occurs. To protect equipment, a pair of 20 dB input pickoffs are used to monitor both the total input power and any reflections off of the antenna circuit.

9.3 Driving the Transition

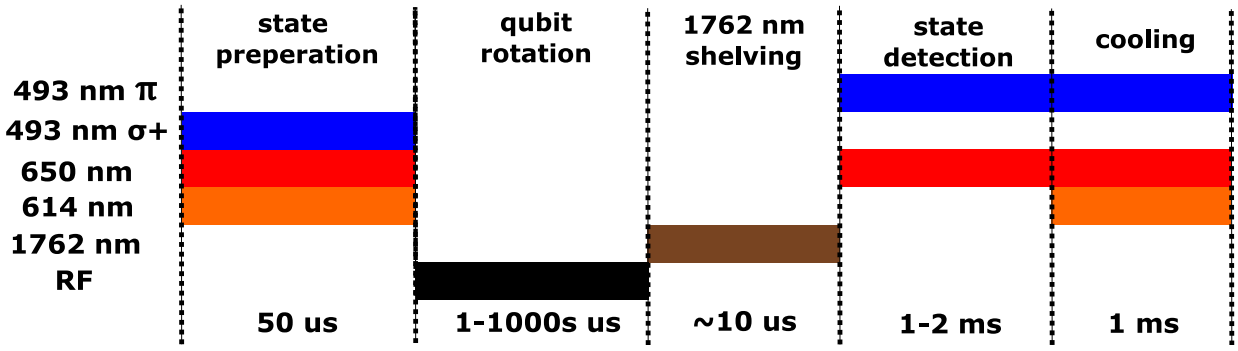

Figure 9.2: **Pulse Sequence for Addressing RF Qubit Transitions.** The ion is first prepared into $|0\rangle = \left|6S_{1/2}, m_j = -1/2\right\rangle$. Qubit rotations are then applied using an RF pulse of either constant time or frequency. Shelving with the 1762-nm laser allows for qubit state detection using 493-nm $\pi-$light and all polarizations of 650-nm light. A period of Doppler cooling is performed every cycle, including 614 nm light to remove any population shelved into the $D_{5/2}$ manifold.

To drive the RF qubit and measure the results of that drive, a pulse sequence similar to that used for addressing the quadrupole transition is performed. The ion is first prepared into $|0\rangle = \left|6S_{1/2}, m_j = -1/2\right\rangle$, using a 50 us pulse[8] of 493-nm σ light as well as all polarizations of 650-nm light. A pulse of RF is then applied to the ion, with constant length and frequency. State detection is then performed as described in Chapter 8, shelving the state $|0\rangle$ using a pulse of 1762-nm light. Finally 1-3 ms of state readout via ion fluorescence is performed and the result recorded, with a dark(bright) state indicating that the ion had been in $|0\rangle$ ($|1\rangle$) after after

[7] Mini-Circuits ZHL-1-2W-S+

[8] This pulse is much longer than what is necessary but allows for large drifts in 493-nm power.

the RF pulse. The ion is then Doppler cooled and de-shelved with 614 nm light for a short time before repeating the experiment. Depending on the experiment being performed, after a number of repetitions, either the RF pulse temporal length or frequency is changed, and the experiment is again repeated.

9.3.1 Finding the Resonance Frequency

Based on the spectroscopy of the quadrupole transition described in the previous chapter, we can make an estimate of the ground state qubit frequency splitting. Comparison of the frequencies required to drive the $\left|6S_{1/2}, m_j = -1/2\right\rangle \leftrightarrow \left|5D_{5/2}, m_j = -1/2\right\rangle$ and $\left|6S_{1/2}, m_j = +1/2\right\rangle \leftrightarrow \left|5D_{5/2}, m_j = -1/2\right\rangle$ transitions, for instance, represents a frequency splitting of ≈ 14.65 MHz. To perform direct spectroscopy of the ground state RF qubit, we set the antenna circuit described above to be resonant at this frequency estimate, and use the coil designed for use ≈ 70 mm away from the ion. Then, by performing the pulse sequence (Fig. 9.2 described above, with a constant RF pulse length of 100 μs, we can scan the RF frequency across a range of $\approx$ 100 kHz to find qubit resonance. An example of such a scan is shown in Fig. 9.3 a. With resonance found, tighter scans with smaller steps in frequency, such as the example shown in the bottom panel of Fig. 9.3, are taken multiple times a day to re-calibrate for observed drifts in RF resonance throughout the day. These drifts seem somewhat random, with resonance typically moving back and forth in a $\approx 1 - 2$ kHz window over the course of a day.

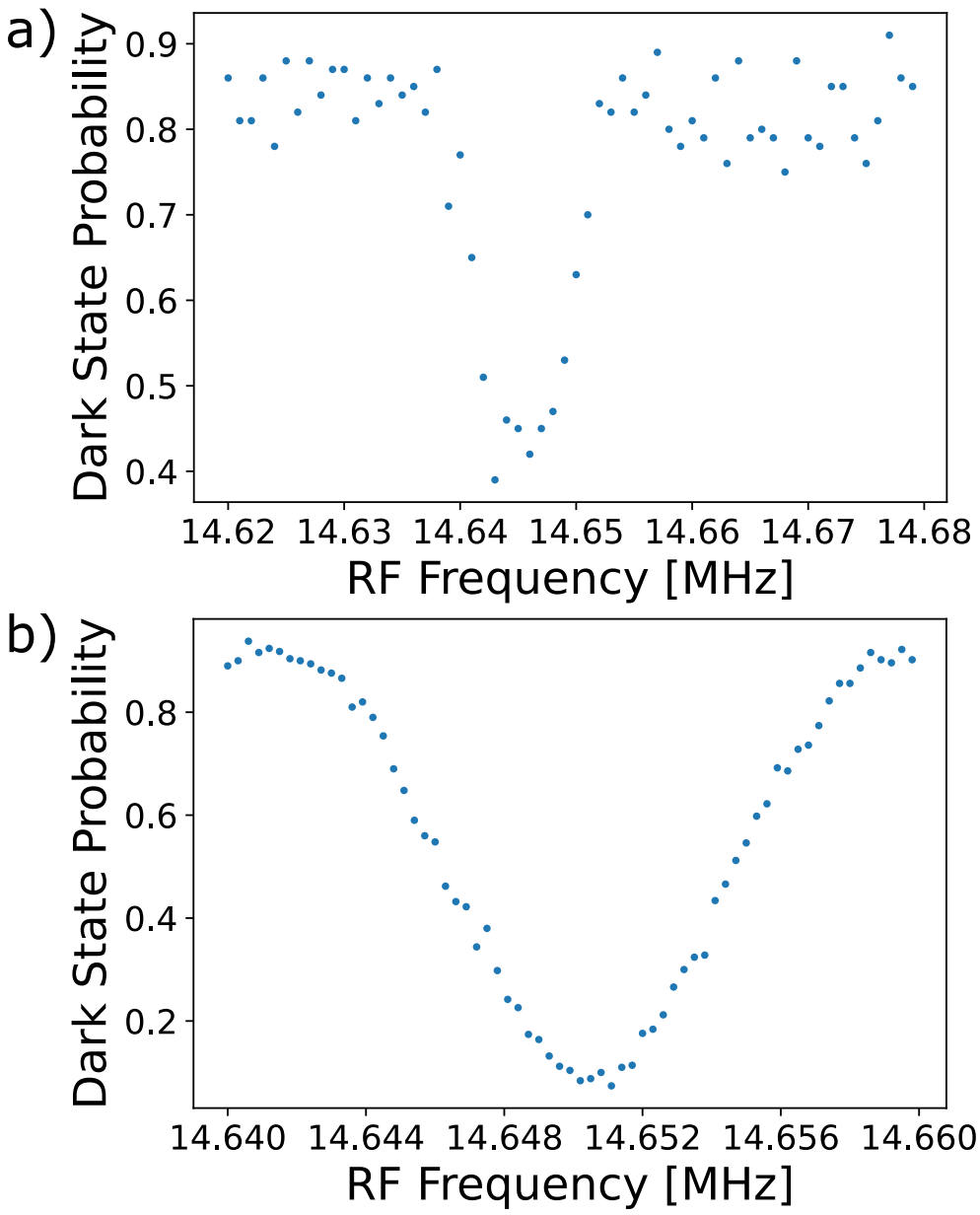

Figure 9.3: **Typical Spectroscopy Scans of the Ground State RF Qubit.** The two displayed scans were taken on different days, resulting in slightly different measurements of resonance. a) Example of a wider scan, taken for roughly finding the RF qubit resonance. b)Example of a tighter scan, used to find and monitor any changes in RF resonance throughout the day. Both scans use a RF pulse length of 100 μs (just below a π-time)

9.3.2 Rabi Flopping with Different Antenna Positions

With the resonance of the RF qubit located, we can perform rotations on the qubit. The same pulse sequence used for spectroscopy is used to perform rotations, except that the RF frequency is set to and kept at resonance, and the RF pulse length is what is now varied. Two examples of the resulting Rabi oscillation data are shown in Fig. 9.4, for the two different antenna positions and designs described in Section 9.2. Driving the first coil (Fig 9.4 a), aligned along the axis of the trap and placed ≈ 70 mm from the ion, results in a π-time of ≈ 120 μs. The second coil, placed ≈ 20 mm away from the ion and just outside of the photon collection window, can give π-times of down to ≈ 9 μs, as shown in Fig 9.4 b.

Unfortunately, although this second coil would be preferable to use, with its extremely fast π-time relative to things such as qubit decoherence (Section 9.4), the placement of our 0.6 NA photon collection lens just outside of this window greatly affects the coupling of RF to this antenna, with a measurable shift in the antenna circuit's resonance frequency and a large reduction in the intensity of RF seen by the ion. This, combined with a worry of the photon collection lens pushing the coil into the window (it is a very tight fit), has resulted in our lab deciding to use the first coil described, at the cost of Rabi frequency. Thankfully, in the entanglement experiment described in Chapter 10, RF rotations are only performed as part of a slow loop which also includes a much longer (3 ms) period of shelving and state detection, so the slower operations provided by this antenna do not serve as a major hindrance at this point.

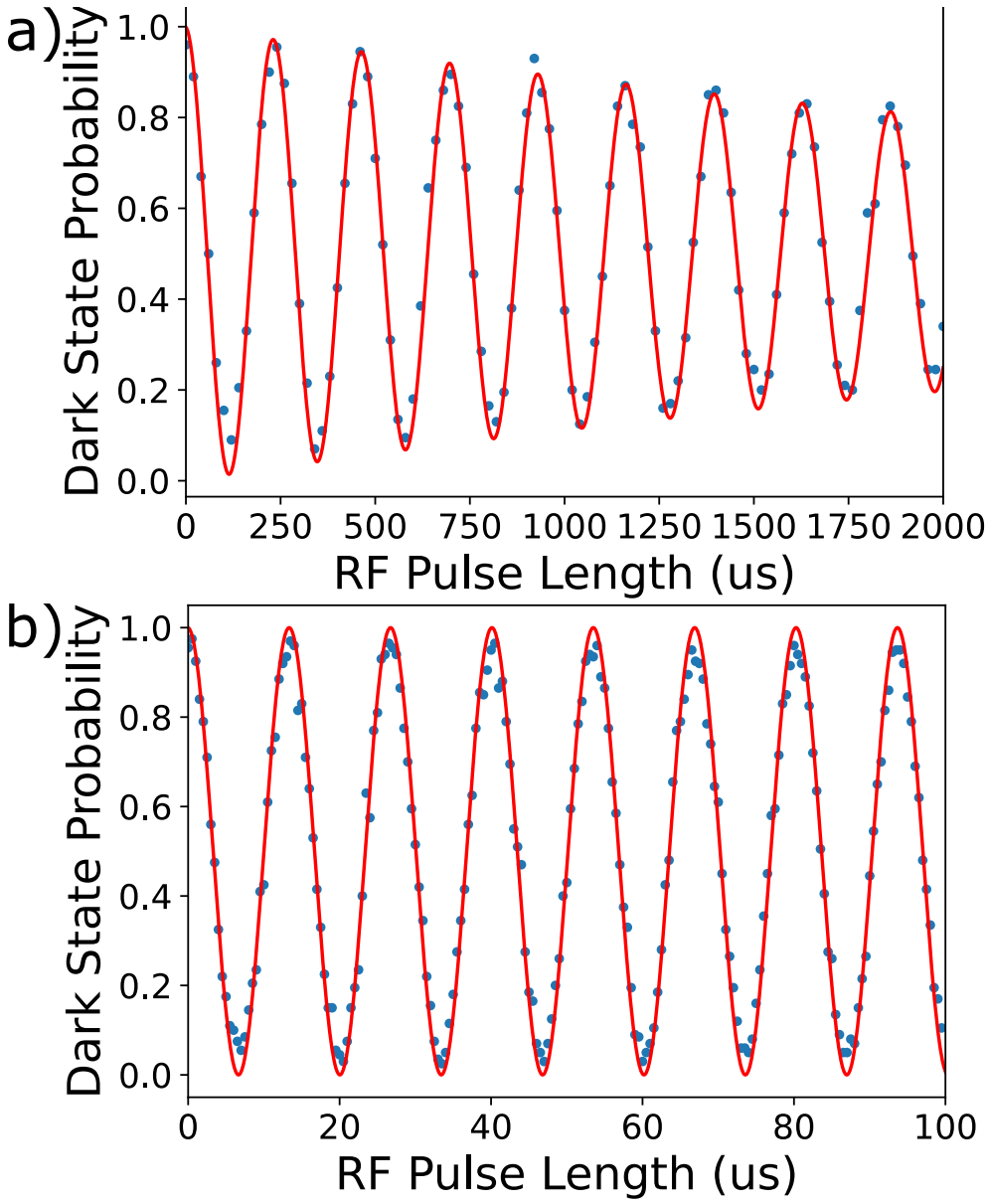

Figure 9.4: **Rabi Oscillations on the Ground State RF Qubit.** a) Rabi oscillations using the antenna placed approximately 70 mm away from the ion, resulting in a π-time of approximately 120 μs, or a Rabi frequency of $\approx$ 4.3 kHz. b) Rabi oscillations using the antenna placed approximately 20 mm away from the ion, resulting in a π-time of approximately 9 μs, or a Rabi frequency of $\approx$ 57 kHz. The red lines in both plots represent sinusoidal fits (with exponential decays in amplitude) to the data used to determine Rabi frequencies. Though a higher Rabi frequency is possible with the closer coil, the further coil is used for the entanglement experiments in the next chapter, as the presence of the photon collection lens reduces the effectiveness of the closer coil.

9.4 Coherence Time Measurements

One major concern of working with the first-order magnetic-field-sensitive Zeeman ground state qubits is that of dechoerence due to magnetic field noise at the ion's location. In this section, I present coherence measurements of our RF qubit. These measurements are required to predict the level of infidelity contributed by the dephasing induced by magnetic field noise present during the ion-photon entanglement experiments in Chapter 10. Additionally, measurements similar to those performed in this section can, with an increased RF drive amplitude, enable measurements of the frequency spectrum of the magnetic field noise [179], as well as enable the use of Ba^+ as a magnetic field sensor [62].

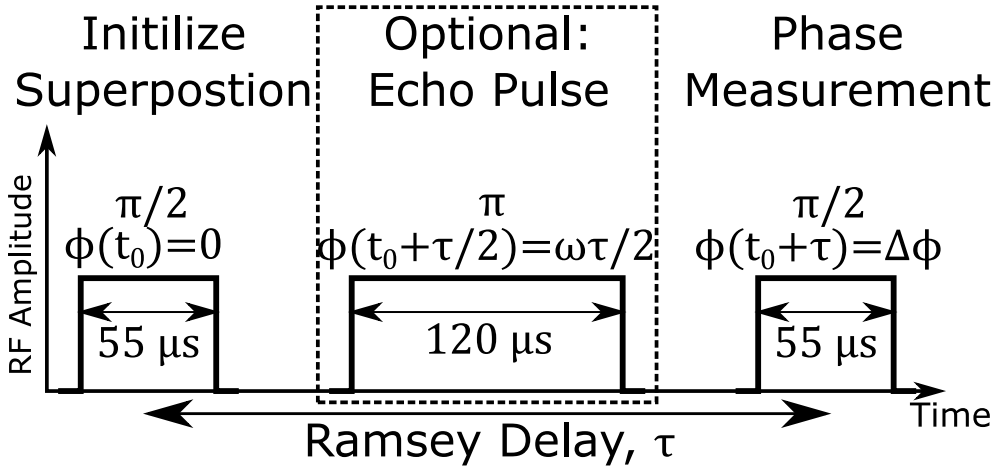

Figure 9.5: **RF Pulse Sequence for Coherence Measurements.** After state preparation into $|0\rangle$, the shown RF pulse sequence is applied before state detection. The RF qubit is initialized into an equal superposition state with a $\pi/2$ pulse of length 55 μs. After some controllable delay, τ, a second $\pi/2$ pulse with a control-able phase offset of $\Delta\phi$ is applied, effectively performing a measurement of the relative phase of the superposition. An additional 120 μs π echo pulse, in phase with the initial $\pi/2$ pulse can be applied for spin-echo measurements.

To perform coherence measurements a series of Ramsey [180] and spin-echo [181–183] measurements are performed. These measurements are performed using the pulse sequence of Fig. 9.2, with the qubit rotations instead performed as summarized in Fig. 9.5. In the first

type of experiment, after optically pumping the ion into $|0\rangle$, we prepare the qubit in an equal superposition state using a $\pi/2$ pulse of known phase. In a manner similar to [182], after a fixed delay time, a second $\pi/2$ pulse with a known phase difference to the initial pulse is applied to the qubit, and its state is measured. This phase difference is then scanned to produce one of the oscillations shown in Fig 9.6 a [9]. This is in contrast to the typical Ramsey-type experiment where the two $\pi/2$ RF pulses have fixed phases and the delay is instead varied. By taking multiple sets of data with different delay times ranging from 70-500 μs, the remaining curves shown in Fig 9.6 a are produced. The contrast of each of these oscillations are determined as the amplitude of sinusoidal fits to each data set.

The qubit coherence can be partially recovered using the spin-echo technique [181–183]. In the spin-echo measurement, the qubit is again prepared into an equal supepostion state with a $\pi/2$ pulse. Before the second $\pi/2$ pulse with varying phase however, a π echo pulse (which is in phase with the first $\pi/2$ pulse) is applied equidistant in time from both $\pi/2$ pulses. As with the first set of measurements, the phase of the second $\pi/2$ pulse is scanned to produce one of the oscillations shown in Fig 9.6 b. Multiple curves are produced with delay times between the two $\pi/2$ pulses ranging from 180 μs to 2.4 ms.

The resulting coherence time data is shown in Fig. 9.7, which displays the contrast in the Ramsey (blue, leftmost) and spin-echo (red, rightmost) oscillations as a function of delay between pulses. This contrast is corrected for the S-State shelving efficiency of 0.96 determined in Chapter 8. The coherence time resulting from each of these measurements is then determined as the time delay at which the contrast in the oscillations is reduced to $1/e \approx 0.37$. This gives coherence times of $t_2^* \approx 250$ μs for the qubit without an echo and $t_2 \approx 1.8$ ms when applying an

[9] Here, we are effectively performing a measurement of the relative phase of the superposition at this delay time

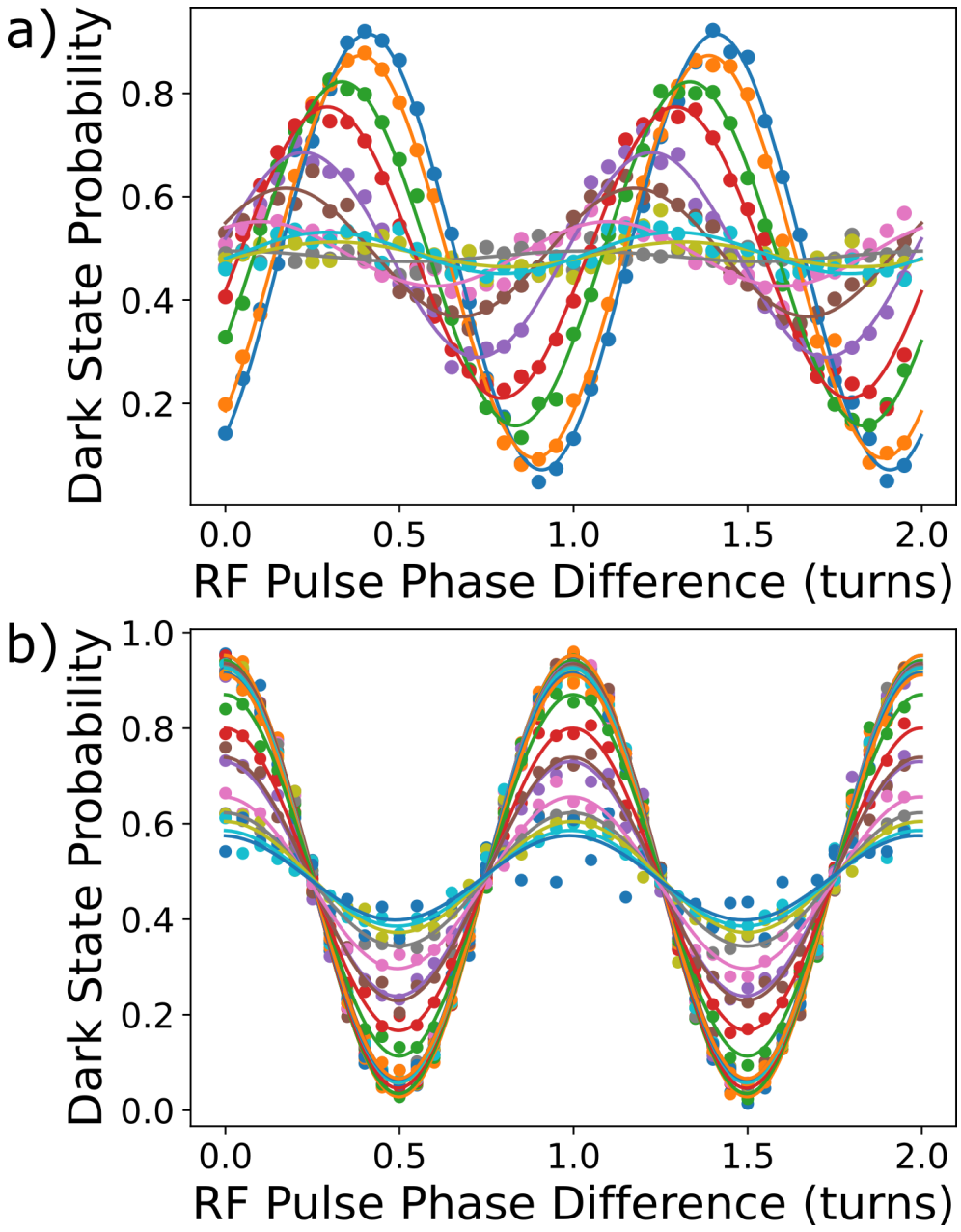

Figure 9.6: **Ground State Qubit Ramsey and Spin-Echo Measurements.** a) The result of 10 different Ramsey measurements, where the phase (in units of turns) between two successive $\pi/2$ pulses is scanned. Each data set corresponds to a different delay between the center of two pulses. Delays range from 70 μs to 500 μs. b) The result of 21 different spin-echo measurements, where the phase (in turns) between two $\pi/2$ pulses separated by a π echo pulse (centered between each $\pi/2$ pulse) is scanned. Each data set corresponds to a different delay between the center of the two $\pi/2$ pulses. Delays range from 180 μs to 2.4 ms. The sinusoidal fits for the individual data sets are used to extract the contrast values used for determining the coherence times of the qubit in each scenario.

echo pulse.

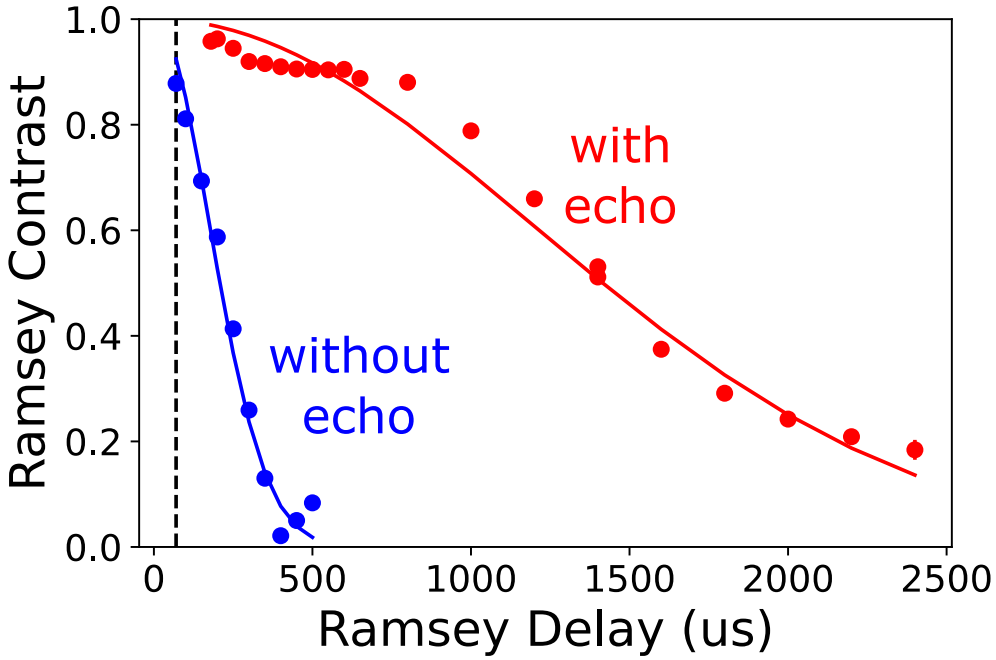

Figure 9.7: **Coherence Times of the RF Qubit.** Ramsey contrast values extracted from the sinusoidal fit amplitudes for the data shown in Fig. 9.6 for both the Ramsey phase scan (blue) and spin-echo scan (red) data sets. This data suggests coherence times of $t_2^* \approx 250\mu$s and $t_2 \approx 1.8$ ms, for the Ramsey- and echo-data respectively. The curves plotted with each data set are Gaussian decays with characteristic decay times set to each of these values, but are meant only to guide the eye. The dotted vertical line represents the fastest time after photon emission that our control system can perform ion-qubit operations in the ion-photon entanglement experiments demonstrated in Chapter 10.

This coherence time is a relevant concern for the ion-photon entanglement experiment described in Chapter 10. Due to experimental control system constraints, the soonest an RF pulse can be applied to the ion after photon production is around 70 μs (dotted line Fig. 9.7. This is represented by the vertical dotted line in Fig. 9.7. We see that including a spin-echo pulse as part of our state detection in the ion-photon experiment can help mitigate any dephasing/decoherence effects due to this delay.

9.5 Summary

As shown in this chapter, we are able to detect and manipulate the ground state Zeeman qubit in $^{138}Ba^{+}$. Although we are limited to relatively low Rabi rates when operating concurrently with single photon collection, the coherence time measurements shown demonstrate coherence times long enough for ion-photon entanglement measurements, at least when the network transmission time is low compared to the ≈ 1 ms coherence time we can achieve with a spin-echo pulse (1 ms corresponds to a one-way network length of ≈ 200 km). The main issue we have in the lab instead turns out to be slow drifts in the qubit resonance over time, evidenced by repeated scans similar to that shown in Fig. 9.3 b. Thankfully, if we measure resonance at the beginning of each experimental run, this drift is not fast enough to noticeably affect our ion-photon entanglement data discussed in the following chapter.

Chapter 10: Ion-Photon Entanglement at 780 nm

10.1 Introduction

The preservation of ion-photon entanglement after frequency conversion to 780 nm is a critical step towards connecting our trapped ion quantum node in both long-range and hybrid quantum networks. In this chapter, I present measurements of entanglement between a single Ba^+ ion and the photons we produce with it (Chapter 2), before and after frequency conversion. From these measurements, we determine bounds on the entanglement fidelity as well as the rate of entanglement generation for our current setup. This chapter is in some sense the culmination of the state detection work presented in Chapter 8, the qubit manipulation work presented in Chapter 9, and of course the frequency conversion work demonstrated in Chapters 4 and 5.

10.2 Experimental Details

The experimental layout is outlined in Fig. 10.1. It consists of four concatenated setups, connected via a series of single-mode optical-fibers (SMF). A $^{138}Ba^+$ ion produces 493-nm photons which are collected and coupled into a single-mode optical fiber using the 0.6 numerical-aperture (NA) lens system (Fig. 10.1(a)) discussed in Chapter 3. Photons coupled into the fiber are then either detected using a 493-nm polarization analyzer (Fig. 10.1(b)) or sent to the

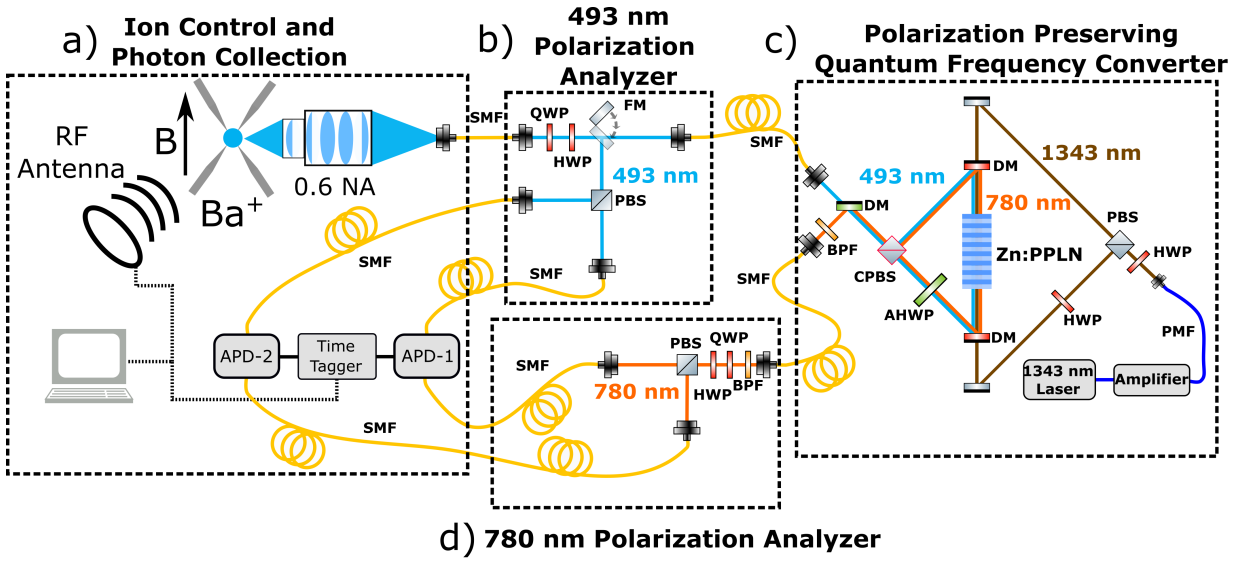

Figure 10.1: **Experimental Layout.** a) A $^{138}Ba^{+}$ ion produces 493-nm photons that are collected and coupled into a single mode fiber (SMF) by a 0.6 numerical aperture (NA) objective. The photon collection axis is orthogonal to the magnetic field at the ion. A radio-frequency (RF) antenna addresses the ion qubit based on photon measurements on avalanche photodiodes (APD-1 and APD-2). b) Photon polarization measurements at 493 nm are carried out via a polarization analyzer consisting of a quarter waveplate (QWP), half waveplate (HWP), and polarizing beamsplitter (PBS). A flipper mirror (FM) allows for the analyzer to be bypassed with the photons instead sent to the frequency conversion setup. c) Frequency conversion is performed using a waveguide written into Zn-doped periodically poled lithium niobate crystal (Zn:PPLN) at the center of two optical loops. Dichroic mirrors (DM) allow for combination and splitting of the multiple colors used. A custom-coated PBS (CPBS) and achromatic half waveplate (AHWP) operating at 493 nm and 780 nm enable these colors to share the same optical paths. A band-pass filter (BPF) is used to remove the majority of the noise photons produced by the 1343-nm pump light. d) A second polarization analyzer is used for 780-nm photonic qubit polarization measurements.

quantum frequency converter (Fig. 10.1(c)). If sent to the converter, the 493-nm photons are converted to 780-nm [92], coupled into another SMF and detected via a 780-nm polarization analyzer (Fig. 10.1(d)). For entanglement measurements, operations on the ion are performed using a radio-frequency field emitted from an antenna placed close to the ion (Chapter 9), and the measured ionic and photonic qubit states are used to determine bounds on the entanglement fidelity.

10.2.1 Ion-Photon Entanglement Generation and Photon Collection

To generate photons entangled with qubit states in $^{138}Ba^{+}$, we follow the sequence outlined in Fig. 10.2 and discussed in Chapter 2. We optically pump the ion into the $\left|5D_{3/2}, m_j = +3/2\right\rangle$ edge state using an 8 μs exposure of π-polarized 493-nm light along with π and σ^{+}-polarized 650-nm light (Fig. 10.2 a). At this step, we include a slight modification to the photon production scheme discussed in Chapter 2. A 1 μs exposure of π-polarized 650-nm light is then used to ensure any residual population left in $\left|5D_{3/2}, m_j = \pm 1/2\right\rangle$ is removed, thereby avoiding erroneous excitation in the next step (Fig. 10.2 b)[1]. A 200 ns pulse of σ^{-}-polarized 650-nm light then excites the ion to $\left|6P_{1/2}, m_j = +1/2\right\rangle$, from where the ion can spontaneously decay to $\left|6S_{1/2}, m_j = \pm 1/2\right\rangle$, producing a single 493-nm photon with a temporal probability distribution related to the lifetime of the $\left|6P_{1/2}, m_j = +1/2\right\rangle$ state. A 10 μs period is then included after the 650-nm excitation pulse to allow our control system to time-tag (Fig. 10.1 a) detected photons. We repeat this sequence in 500-attempt bursts, with each burst separated by 100 μs of Doppler cooling using all polarizations of 650-nm and 614-nm light and π-polarized 493-nm light. The 614 nm light is not

[1]Excitation from $\left|5D_{3/2}, m_j = +1/2\right\rangle$ would produce ion-photon entanglement with the photon polarization flipped, leading to infidelity.

shown in Fig. 10.2 for simplicity and is tuned to a frequency which allows pumping of population in the $5D_{5/2}$ state to the $6P_{3/2}$ state from where the ion can decay back into the $5D_{3/2}$ or $6P_{1/2}$ states.

Spontaneous emission of a 493-nm photon from the $\left|6^2P_{1/2}, m_j = +1/2\right\rangle$ state in the above sequence, combined with collection perpendicular to the quantization axis defined by a 5.23 Gauss magnetic field produced by two permanent magnets (Chapter 3), produces the polarization-based ion-photon entangled state described in Chapter 2 and given by Eqn. 2.6:

$$|\Psi_{IP}\rangle = \sqrt{\frac{1}{2}}\,|0\rangle\,|V\rangle + \sqrt{\frac{1}{2}}\,|1\rangle\,|H\rangle\,. \tag{10.1}$$

As discussed in Chapter 2, this entanglement relies on the orthogonality of σ^+-polarized and π-polarized photons when collection is perpendicular to the quantization axis. In free space, however, the large solid angle of our 0.6 NA photon collection would normally lead to significant and unavoidable polarization-based errors, as σ^+ and π-polarized photons are no longer orthogonal [31]. Thankfully, when coupling the collected light into a single-mode fiber, it has been shown that the non-orthogonal polarization components are canceled out at the expense of collection efficiency[2] [30], making Eq. 2.6 accurate for this experiment.

Also discussed in Chapter 2, the long temporal length of the 650-nm σ^- excitation pulse (200 ns), relative to the excited state lifetime of the $P_{1/2}$ manifold (≈ 10 ns), allows for multiple excitations of the ion in the event of decay back to the $D_{3/2}$ manifold ($\approx 25\%$ probability). Decay to, and subsequent excitation from, the $\left|5^2D_{3/2}, m_j = +1/2\right\rangle$ state to the $\left|6^2P_{1/2}, m_j = -1/2\right\rangle$ state, can lead to spontaneous emission of a 493-nm photon that produces the ion-photon entangled

[2] One still collects 80% of what you would expect otherwise.

state of Eq. 2.7 with the photon polarization states swapped. This state is orthogonal to the expected ion-photon entangled state, and will lead to a reduction in the measured entanglement fidelity [28, 31].

To reduce the effect of errors due to these multiple excitations, we implement a software gate on the detected photon signal, referenced to the start of the 650-nm σ^- excitation pulse[3]. We choose to only accept photon events occurring in a 40 ns window at the beginning of the photon's temporal profile, ignoring the $\approx 17\%$ of photon detection events which occur outside of this window. With the majority of photons produced via multiple excitations occurring towards the end of the photon's temporal profile (calculated via an optical Bloch equation model), this 40 ns software gate reduces the expected infidelity of the ion-photon entangled state due to multiple excitations from $\approx 9\%$ to $\approx 2\%$.

10.2.2 Quantum Frequency Converter

The entanglement-preserving quantum frequency converter used to convert the 493-nm photons emitted by the ion to 780-nm is discussed in detail in Sec. 4.3.3. A simplified schematic of this setup is shown in Fig. 10.1 c, where the 493-nm light is split at a custom-coated polarizing beamsplitter and each polarization is sent through opposite directions of the Zn-doped periodically poled lithium niobate crystal for conversion. The pump is also split by polarization and sent in opposite directions to enable conversion of each polarization with arbitrary control over the pump power sent in each direction of the loop. The pump-power dependent conversion efficiency (measured from the 493 nm input fiber to the 780 nm output fiber) of the converter as a function of pump power is shown in Fig. 4.10, for each polarization of input 493-nm light. We measure peak

[3] Recall the discussion in Chapter 2 that this can also be dealt with by using faster excitation pulses

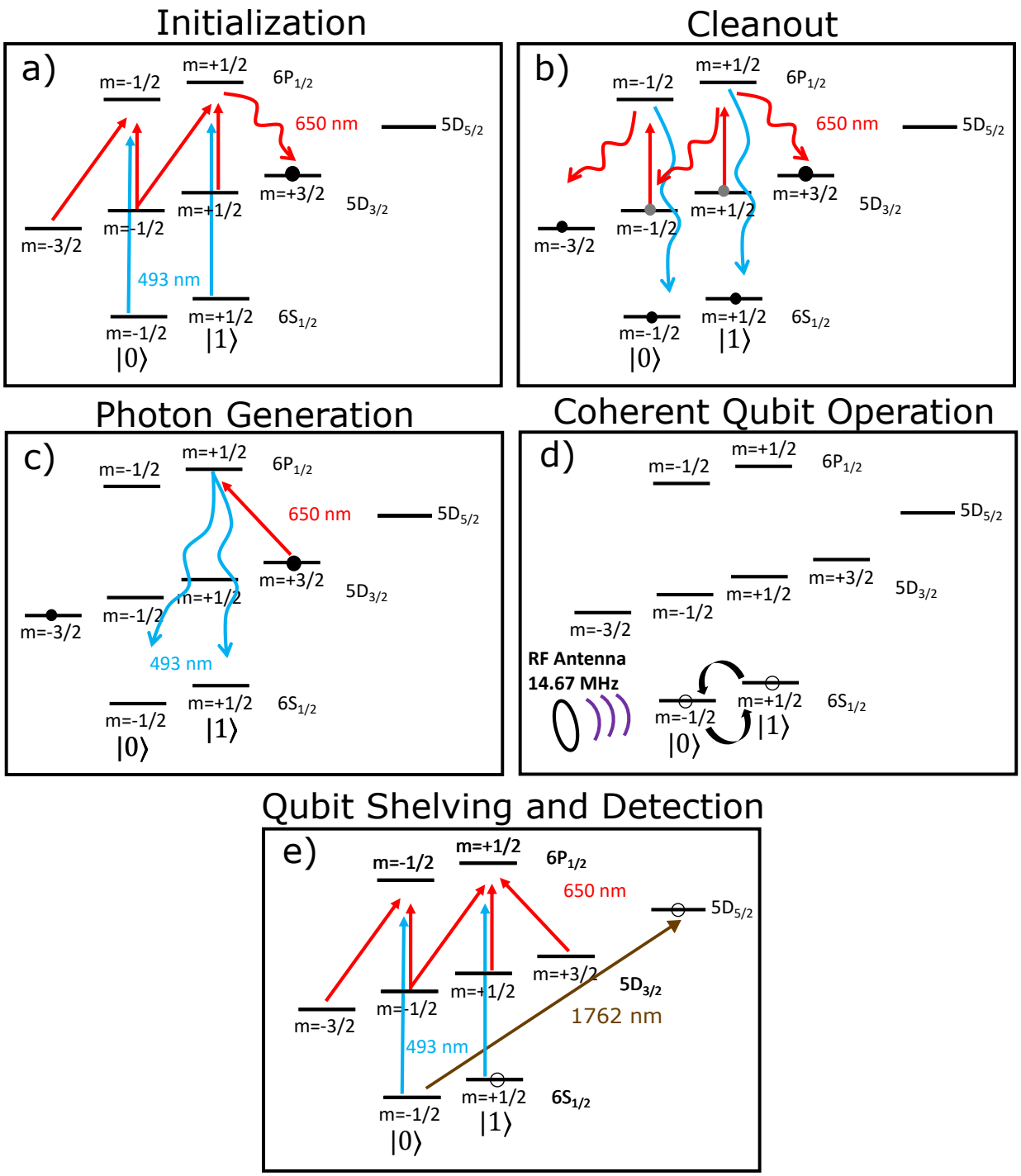

Figure 10.2: **Photon production and ion qubit control.** a) The ion is prepared into the $\left|5D_{3/2}, m_j = +1/2\right\rangle$ state. b) A clean out pulse is used to remove any remaining population in the $\left|5D_{3/2}, m_j = \pm 1/2\right\rangle$ states. c) The ion is excited to the $\left|6P_{1/2}, m_j = +1/2\right\rangle$ state, from which a photon entangled with the ion is emitted. d) If a photon is detected, coherent ion-qubit operations are driven by an RF antenna tuned to 14.67 MHz. e) Ion-qubit state detection is performed via optical shelving of the $|0\rangle$ state via the $\Delta m = 0$ quadrupole transition at 1762 nm.

conversion efficiencies of 37.9(9)% and 34.5(4)% for V and H polarizations, respectively. The pump powers in each direction are set to match the conversion efficiency for each polarization to the minimum of these two values, at 34.5%. At this conversion efficiency, we measure ≈ 200 counts/s noise on each of our single photon detectors, in addition to dark counts.

Using this conversion scheme, the converted 780-nm photon should retain the same entanglement with the ion as the 493-nm photon, given by Eq. 2.6, except with the polarization state of the photon swapped from H to V and vice-versa. This polarization swapping is due to the achromatic half waveplate (AHWP in Fig. 10.1 c) placed in the 493/780-nm loop through which each polarization travels once. If so desired, a second HWP placed just before the 780-nm fiber could be used to rotate the polarization back to the original state.

10.2.3 Qubit Measurement and Manipulation

Determination of the ion-photon entanglement fidelity requires the ability to perform coherent operations on both the trapped ion and photonic qubits, as well as make measurements on both qubits in different bases. We perform basis rotations and measurements on the photonic qubit at the polarization analyzers shown in Fig. 10.1, depending on the color of the photon. We perform operations on the ion by directly driving coherent qubit transitions using radio-frequency (RF) pulses tuned to qubit resonance as discussed in Chapter 9. Operations on the ion must be carefully timed relative to photon emission in order to ensure the proper phase of these gates.

10.2.3.1 Polarization Analyzers

The polarization analyzers shown in Figs. 10.1 b and d consist of both a quarter waveplate (QWP) and half waveplate (HWP), each mounted in a motorized rotation mount[4] with the rotation angles controlled by our FPGA control system. We use a flipper mirror (FM) on the 493 nm polarization analyzer (Fig. 10.1 b) to selectively route 493-nm photons to measurement or to the frequency converter and 780-nm analyzer. The waveplates allow us to transform any arbitrary photon polarization to a linear polarization, enabling us to undo any polarization rotations caused by birefringence present in the fiber(s) before each analyzer. Polarization-based photon measurements are then made by the polarizing beamsplitter cube and single photon detecting avalanche photodiodes[5] (APD), allowing simultaneous measurement of both orthogonal photon polarizations. This configuration allows for measurements in the horizontal-vertical ($\{H, V\}$) and diagonal-anti-diagonal ($\{D, A\}$) photonic qubit bases, sufficient for determination of upper and lower bounds on the ion-photon entanglement fidelity [68, 109] as will be shown in Sec. 10.3. The 780-nm analyzer also includes an additional 3 nm bandpass frequency filter[6] to reduce noise produced by the frequency converter.

10.2.3.2 Ion Control and Timing

The radio-frequency (RF) pulses used for ion qubit rotations are provided by the RF antenna shown in Fig. 10.1 a. The RF signal, produced by a direct digital synthesizer (DDS) connected to the experimental control system, is set on resonance with the ion qubit splitting at 14.67 MHz. We perform RF rotations at a fixed time delay relative to the recorded single photon detection

[4] Thorlabs: DDR25.
[5] PerkinElmer: SPCM-AQR-15-FC.
[6] Semrock LL01-780

time tags. Additionally, we use these time tags to actively program the DDS such that the phase of the applied RF is synchronous with the free evolution of the ion qubit, with a controllable offset dependent on the desired gate to be performed. Due to the timing delay required to program the phase and frequency of the DDS after photon detection ($\approx 70\mu$s), an additional spin-echo pulse is applied to the ion as a part of these operations to reduce ion-qubit dephasing effects due to local magnetic field noise [182, 183]. This spin-echo extends our qubit coherence time from $\approx$ 200 μs to $\approx$ 2 ms (see Sec. 9.4).

We perform state detection on the ion by optically shelving the $|0\rangle$ state to the $\left|D_{5/2}, m_j = -1/2\right\rangle$ state using the quadrupole transition at 1762 nm (Fig. 10.2 e), discussed in detail in Chapter 8. This is then followed by 3 ms of fluorescence detection on the ion using light at 493 nm and 650 nm. After state detection, we illuminate the ion with laser light at 614 nm to remove it from the $\left|D_{5/2}, m_j = -1/2\right\rangle$ state and allow the photon production sequence to recommence.

10.3 Results

We can determine a lower bound on the fidelity for our ion-photon entangled state at 493-nm by calculating [68]

$$\begin{aligned} F_{493} \geq \frac{1}{2}(&\rho_{H1,H1} + \rho_{V0,V0} - 2\sqrt{\rho_{H0,H0}\rho_{V1,V1}} \\ &+\tilde{\rho}_{H1,H1} + \tilde{\rho}_{V0,V0} - \tilde{\rho}_{H0,H0} - \tilde{\rho}_{V1,V1}). \end{aligned} \tag{10.2}$$

Here, the matrix elements $\rho_{\gamma b,\gamma b}$ (where γ is the photon polarization and b is the ion state) are given by $\mathrm{P}(\gamma)\mathrm{P}(b|\gamma)$, where $\mathrm{P}(\gamma)$ is the total probability of detecting a photon with

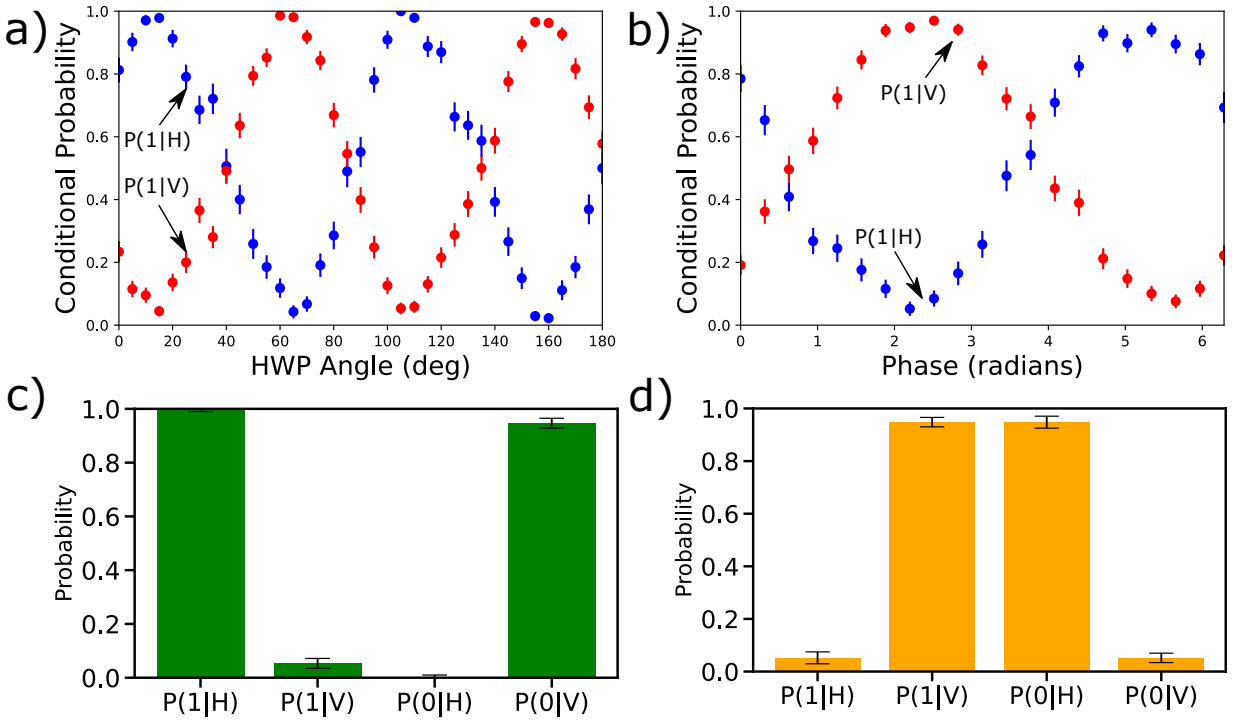

Figure 10.3: **Ion-photon correlations at 493 nm.** a) Calibration scans for the unrotated basis (z-basis) where the blue(red) data represents the probability of detecting the ion in state $|1\rangle$ given that the photon is detected in state $|H\rangle$ ($|V\rangle$) by APD-1(APD-2) for a given position of the HWP in Fig. 10.1 b. b) Calibration scans for rotated basis (x-basis), obtained by setting the HWP in Fig. 10.1 (b) to $40°$, and for a given phase of the $\pi/2$ pulse applied to the ion. c) Conditional measurement probabilities at the point of maximum correlations ($105°$) for the unrotated basis data in a). d) Conditional measurement probabilities at the point of maximum correlations ($7\pi/10$ radians) for the rotated basis data in b). All error bars are statistical, with 500 photon events for each data point.

polarization γ and $\mathrm{P}(b|\gamma)$ represents the conditional probability of measuring the ion in state b given a measurement of the photon's polarization as γ. The matrix elements $\tilde{\rho}_{\gamma b,\gamma b}$ are given with the same form but after a rotation by a polar angle of $\pi/2$ on the Bloch sphere of both the photon and ion qubits. In a similar manner, we can also calculate an upper bound on the fidelity as [109]

$$F_{493} \leq \frac{1}{2}\left(\sqrt{\rho_{H1,H1}} + \sqrt{\rho_{V0,V0}}\right)^2. \tag{10.3}$$

As described in Section 10.2.2, we measure the 780-nm ion-photon entanglement with the horizontal and vertical polarizations swapped compared with the 493-nm ion-photon entanglement, such that a lower bound is given by

$$\begin{aligned} F_{780} \geq \frac{1}{2}(&\rho_{H0,H0} + \rho_{V1,V1} - 2\sqrt{\rho_{H1,H1}\rho_{V0,V0}} \\ &+\tilde{\rho}_{H0,H0} + \tilde{\rho}_{V1,V1} - \tilde{\rho}_{H1,H1} - \tilde{\rho}_{V0,V0}), \end{aligned} \tag{10.4}$$

and the upper bound is given by

$$F_{780} \leq \frac{1}{2}\left(\sqrt{\rho_{H0,H0}} + \sqrt{\rho_{V1,V1}}\right)^2. \tag{10.5}$$

This choice is somewhat arbitrary in theory, as the half waveplate in either polarization analyzer (Fig. 10.1 b and d) can be used to swap $H \leftrightarrow V$.

10.3.1 Entanglement Fidelity Measurements

We first perform calibrations of the 493-nm photonic qubit measurement basis. This is performed by measuring the conditional probabilities, P($b|\gamma$), for varying rotation-angles of both the quarter and half waveplates in the 493-nm polarization analyzer (Fig. 10.1(b)). We optimize the quarter waveplate angle to provide the maximum ion-photon correlation visibility, |P(1|H)−P(1|V)|, when scanning the half waveplate angle. The 493-nm ion-photon correlations for this optimized quarter waveplate angle are shown in Fig. 10.3 (a) as a function of the half-waveplate angle. We record 500 detection events measured at each half-waveplate angle.

We then measure correlations between the ion and photonic qubit states following rotation of both qubits by $\pi/2$ on the Bloch sphere. With the quarter waveplate position optimized as described above, we apply a $\pi/2$ rotation to the photon polarization by setting the half waveplate to an angle of 40° (Fig. 10.3 a)). We rotate the ion measurement basis using a $\pi/2$ RF pulse with a set phase and a fixed delay time relative to the photon detection time tag. By scanning this phase, we scan the relative phase of rotation of the ion versus that of the qubit, again measuring correlations between the ion qubit state and the polarization of the photon. This results in the rotated-basis correlation fringes shown in Fig. 10.3 b, with 500 events measured at each phase of the applied RF.

At the point of maximum visibility in the unrotated basis, (105° in Fig. 10.3 a), we measure P($H|1$) = 1.00(1), P($V|0$) = 0.95(2), P($H|0$) = 0.00(1), and P($V|1$) = 0.05(2), as shown in Fig. 10.3 (c). Similarly, in the rotated basis (Fig. 10.3 b), we measure $\tilde{P}(H|0) = 0.95(2)$, $\tilde{P}(V|1) = 0.94(2)$, $\tilde{P}(H|1) = 0.05(2)$, and $\tilde{P}(V|0) = 0.06(2)$, at the point of maximum correlation ($7\pi/10$ radians). From these results, we use Eq. 10.2 and Eq. 10.3 to calculate bounds

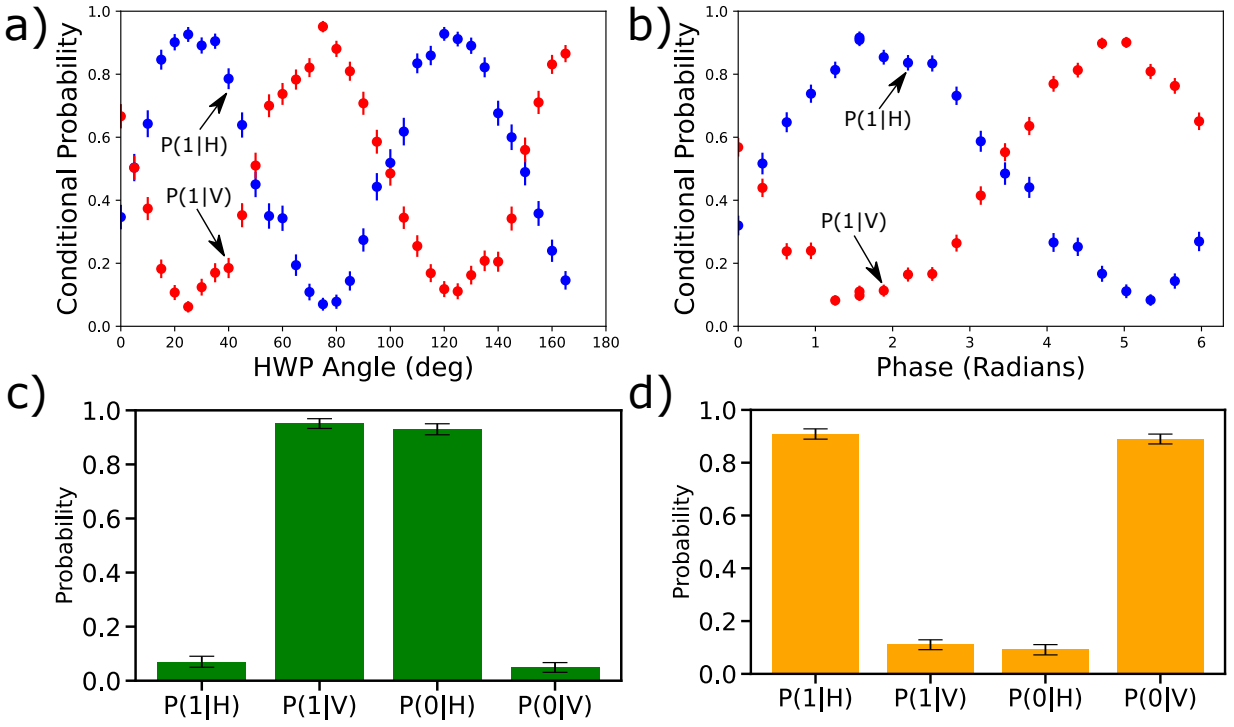

Figure 10.4: **Ion-photon correlations at 780 nm.** a) Calibration scans for the unrotated basis (z-basis) where the blue(red) data represents the probability of detecting the ion in state $|1\rangle$ given that the photon is detected in state $|H\rangle$ ($|V\rangle$) by APD-1(APD-2) for a given position of the HWP in Fig. 10.1 (b). b) Calibration scans for rotated basis (x-basis), obtained by setting the HWP in Fig. 10.1 (b) to 100°, and for a given phase of the $\pi/2$ pulse applied to the ion. c) Conditional measurement probabilities at the point of maximum correlation (75°) for the unrotated basis data in (a). d) Conditional measurement probabilities at the point of maximum correlation ($\pi/2$ radians) for the rotated basis data in (b). All error bars are statistical, with 500 photon events for each data point.

on the ion-photon entanglement at 493 nm, $0.93(2) \leq F_{493} \leq 0.96(2)$.

After measurement of ion-photon entanglement at 493 nm, we set the flipper mirror in Fig. 10.1 b to send the single photons into the quantum frequency conversion setup and 780 nm polarization analyzer. We use the same waveplate optimization procedure as described for the 493-nm data to optimize the 780-nm quarter waveplate position (Fig. 10.1 d), resulting in the optimized 780-nm ion-photon correlations shown in Fig. 10.4 a. By setting the half waveplate to 100° and using the same $\pi/2$ RF pulse procedure on the ion as described above, we measure correlations in the rotated basis, the results of which are shown in Fig. 10.4 b. The results in each basis are taken using 500 photon detection events for each data point.

For the 780-nm data, we measure, at the point of maximum correlation (75° in Fig. 10.4 (a)), $\mathrm{P}(H|0) = 0.93(2)$, $\mathrm{P}(V|1) = 0.95(2)$, $\mathrm{P}(H|1) = 0.07(2)$, and $\mathrm{P}(V|0) = 0.05(2)$ for the unrotated basis, shown in Fig. 10.4 (c). At the point of maximum visibility in the rotated basis ($\pi/2$ radians in Fig. 10.4 (b)), we measure $\tilde{P}(H|1) = 0.91(2)$, $\tilde{P}(V|0) = 0.89(2)$, $\tilde{P}(H|0) = 0.09(2)$, and $\tilde{P}(V|1) = 0.11(2)$, as represented by Fig. 10.4 (d). Using these values in Eq. 10.4 and Eq. 10.5, we find $0.84(2) \leq F_{780} \leq 0.94(2)$.

10.3.2 Sources of Infidelity

The measured lower bound of the entanglement fidelity for both photon wavelengths is well above the classical limit of $F > 0.5$. The fidelity is reduced from unity at both wavelengths by several experimental factors, summarized in Table 10.1. Common to both measurements are infidelities caused by imperfections in state detection[7] (1.5%), photon production[8] ($1.5 - 2\%$),

[7] Dominated by ion-temperature. Here, $n \approx 80$, see Chapter 8.
[8] Due to multiple excitations as discussed above.

and ion qubit rotations using the RF signal[9] (1%). The reduced fidelity at 780 nm, compared to that at 493 nm, can be attributed to the two following factors. First, a reduced signal-to-noise ratio (SNR) at 780-nm (SNR $\approx$ 10) compared to that at 493-nm (SNR $\approx$ 55) leading to infidelities in the entangled state of 6% and 1.2% respectively. Second, an increase in polarization rotation and measurement errors at 780 nm (causing $\approx 1-5\%$ infidelity) compared to the 493 nm measurement (causing $\approx 1-3\%$ infidelity). The infidelity caused by polarization rotation errors can be attributed to drifts in fiber birefringence over the course of the experiment(s) and from waveplate rotation errors causing non-optimal calibration of the photon polarization basis measurement. Improvements in detector efficiency ($\approx 58\%$ at 780 is used in this work with $> 90\%$ commercially available), along with narrower noise filtering of the DFG output can help to reduce errors by acting to increase the SNR. The improved signal rates combined with reduced noise rates will also result is shorter experimental run times leading to less drift in fiber birefringence over the experiment run-time and, therfore, higher measured ion-photon fidelity.

Error Source	Entanglement Infidelity 493 nm	Entanglement Infidelity 780 nm
State Detection	1.5	1.5
Photon Production	1.5-2.0	1.5-2.0
Polarization Rotation and Measurement	1-3	1-5
Signal-to-Noise Ratio	1.2	6
RF Gate Errors and Qubit Decoherence	1	1
Sum of Infidelities	6.2-8.7	11 - 15.5

Table 10.1: **Sources of Infidelity.** Summary of experimental imperfections and their contribution to the reduction in the measured fidelity at both 493 nm and 780 nm. Values are given in units of percent. The range of values given for certain values are a result of experimental uncertainties or are due to observed drifts throughout the experimental runtime.

[9] Due to drifts in resonance throughout the experiment.

10.3.3 Entanglement Rates

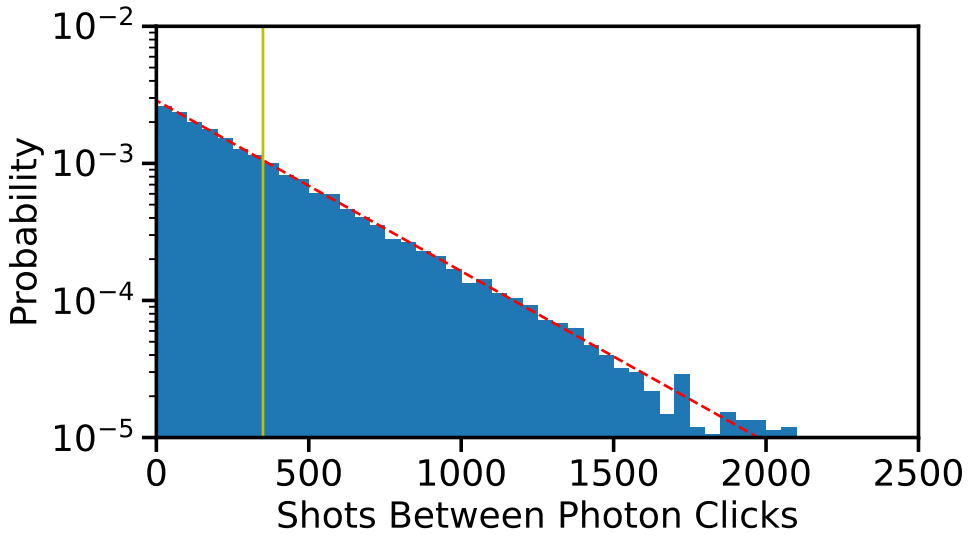

Figure 10.5: **493 nm Entanglement Rate.** Histograms of photon production attempts between successful detection at 493 nm, using 28500 total detection events. The exponential fit (red dashed line) suggests a mean (vertical line) of 350 attempts before a successful photon detection. This corresponds to a entangled photon production rate of 137 s^{-1} during the fast loop of the experiment.

In addition to the fidelity of the entanglement, we also make measurements of the generation rate of the observed ion-photon entanglement. By recording the number of experimental cycles between successive photon detection events during data collection, we produce the histograms shown in Fig. 10.5 and Fig. 10.6, for the 493 nm and 780 nm data, respectively. Exponential distribution fits to these data (dashed red lines) give an average of 350 photon production attempts between successful detection events at 493 nm (vertical line Fig. 10.5), with an average of 1068 attempts between successful detection events at 780 nm (vertical line Fig. 10.6). With an photon attempt repetition rate of $\approx 48\times10^3$ attempts/s this results in an average ion-photon entanglement generation rate of 143 events/s at 493 nm and 47 events/s at 780 nm. This entanglement rate at 780 nm is comparable with other trapped ion systems using a single stage of quantum frequency

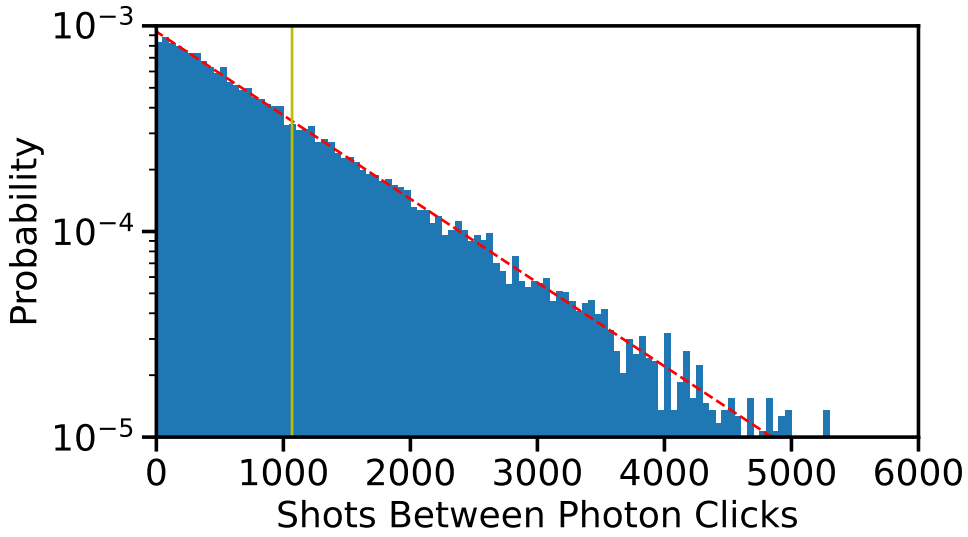

Figure 10.6: **780 nm Entanglement Rate.** Histograms of photon production attempts between successful detection at 780 nm, using 20700 total detection events. The exponential fit (red dashed line) suggests a mean (vertical line) of 1068 attempts before a successful photon detection. This corresponds to a entangled photon production rate of 45 s^{-1} during the fast loop of the experiment.

conversion [34].

These rates can be improved by reducing optical losses between each of the concatenated setups ($\approx 66\%$ transmission), increased photon detection efficiency ($> 90\%$ is possible at both 493 nm and 780 nm compared to the current values of $\approx 40\%$ and $\approx 58\%$), and better optimized fiber coupling using the 0.6 NA lens (currently $\approx 38\%$). Additionally, an increase in photon attempt rate would give the largest gains to entanglement rate. We are currently limited by a required 10 μs delay every loop to allow the control system to read-in photon time-tags and perform conditional logic to decide if a photon has been detected or not. This however, has been shown to be performed in well under a microsecond with customized hardware [30], which would immediately increase our photon production attempt rate by a factor of ≈ 2. A further increase in repetition rate could be achieved through use of a pulsed 493-nm laser, enabling faster state preparation and photon extraction in a manner similar to [30], which could provide repetition

rates approaching 1 MHz, or a factor of ≈ 20 improvement in entangled photon rate.

10.4 Conclusion

In summary, we have demonstrated the entanglement of 780-nm photons with a trapped $^{138}Ba^{+}$ ion, obtained through polarization-preserving quantum frequency conversion of the ion's native 493 nm emission. The ion-photon entanglement fidelity at 780 nm is bounded at $F \geq 0.84(2)$, well above the classical limit of $F \geq 0.5$, and may further be improved through increased filtering of noise produced in the quantum frequency process combined with a reduction in fiber-based polarization drifts. The demonstrated entanglement rate at 780 nm is comparable to similar trapped ion systems using quantum frequency conversion [34], but may be improved by up to a factor of ≈ 20 through improvements to our control system and experimental apparatus. Nevertheless, the demonstrated rates and fidelites can enable experimental investigations into hybrid quantum networks consisting of both trapped Ba^{+} ions and neutral Rb atoms as well as extending the networking range of Ba^{+} ions from a few meters to a few kilometers. This could enable direct entanglement between these two fundamentally different platforms [50], as well as allow investigations into improving trapped-ion-based quantum network using photon detection and storage techniques based on neutral atom systems [29].

Chapter 11: Using Nondestructive Photon Measurement and Storage to Improve Ion Network Entanglement Rates

Quantum networks using matter-qubit-based nodes [30, 66, 114, 184–188] typically rely on probabilistic entanglement heralding protocols, such as the protocol discussed in Chapter 2. For the case of trapped-ion nodes, the low photon collection efficiencies reported [28] lead to most entanglement attempts yielding a null result because no photon has been collected. This results in long dead times as null events from the Bell-state analyzer (BSA) measurements must be fed back to each node before reattempting entanglement. Increasing photon collection efficiency remains an on-going challenge with efforts ranging from the use of custom-designed cavities [189] and other in-vacuo optics [78, 79] to ex-vacu custom multi-element lenses [30, 31].

In this chapter, I describe a theoretical investigation into how integrating (neutral-atom-based) nondestructive single photon measurement (NDSPM) and photonic storage into a trapped ion-based network can increase ion-ion entanglement rates. The NDSPM acts as a flag for the presence of an ion-produced photon, allowing for the request of a new photon based on the result of the flag rather than the result of the BSA measurement. This reduces much of the dead time arising from photon loss and increases the photon request rate of each node. Photonic storage can then be placed at the inputs of the BSA to ensure synchronization at the BSA, allowing for more efficient use of photons produced by each node. Motivated by

the work presented in Chapters 5-7, we assume quantum frequency conversion (QFC) is used to make the optical frequency of ion-produced photons compatible with neutral-atom based-technologies and to produce telecom-wavelength photons suitable for long-distance networking. Using reasonable experimental parameters, we calculate relative entanglement rates at network distances of up to 50 km for Ba^+-based network nodes. We show analytically that such a network could increase two-node entanglement rates by over a factor of 100 as compared with an equivalent homogeneous network. This discussion is adapted from our previously published work [51] for use in this thesis.

11.1 Analytical Calculation of Entanglement Rates

We consider a symmetric two-node network (Fig. 11.1) where each node contains a trapped ion capable of emitting a single photon, in the form of a flying qubit, entangled with its internal states as in Chapters 2 and 10. Photons may be requested from each node at a maximum rate, r_{max}, with the nodes synchronized to produce photons at the same time via a shared clock signal. The ion-emitted photons are collected and coupled into at least one QFC setup to both reduce fiber loss and make their frequency compatible with NDSPM and photon storage devices. The QFC is then followed a network fiber of length L leading to a BSA.

In the following sections we will describe the entanglement generation rate between a pair of trapped ion nodes under three different configurations: First, in section 11.1.1, we describe entanglement rates for a standard homogeneous ion-based network but incorporate QFC to extend the network range. Next, in section 11.1.2, we describe entanglement rates when adding a neutral atom-based NDSPM to remove dead-time associated with waiting for a null-result to be returned

from the BSA measurement. Finally, in section 11.1.3 we describe the case where NDSPM and photonic storage are utilized to increase entanglement generation rates and improve the network efficiency.

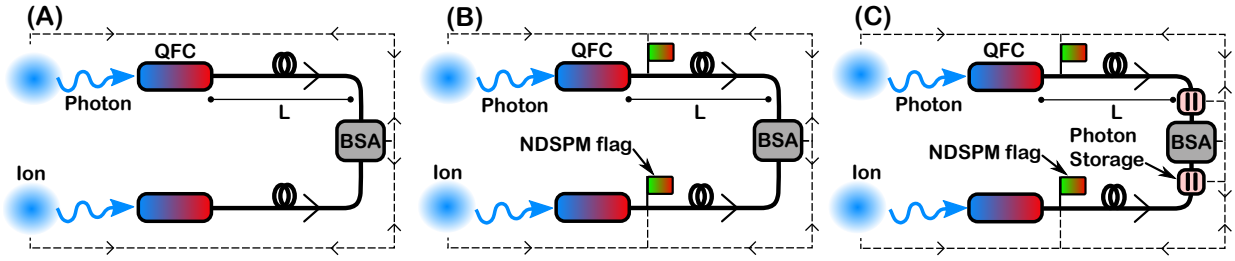

Figure 11.1: **Layout of the proposed two-node networks.** The nodes consist of trapped ions with QFC to provide optical frequency compatibility with NDSPM and photonic storage devices as well as create C-band photons for long distance transmission. (A) A standard homogeneous 2-node network as described in section 11.1.1. (B) and (C) show hybrid networks with a NDSPM flag placed directly after the conversion with additional photon storage devices are placed at the BSA in (C) as described in sections 11.1.2 and 11.1.3. Classical signal channels are indicated with black dashed lines with the fiber-based quantum channel indicated by the solid black lines. Extra QFC stages may be required before photonic storage and after NDSPM flags for C-band networks but are removed for clarity.

11.1.1 Entanglement Rate, $R_E(L)$, for Homogeneous Two-Node Networks

Using the entanglement swapping protocol discussed in Chapter 2, the length-dependent two-node entanglement generation rate, $R(L)$, of a standard homogeneous network (Fig. 11.1(A)) scales quadratically with detection probability (linearly for each node) as given by

$$R(L) = (1/2)r(L)P_B^2(L), \tag{11.1}$$

where $r(L)$ is the synchronized photon request rate of the nodes and $P_B(L)$ is the probability of a photon being emitted, collected, coupled into a fiber and detected at the BSA. The photon request rate, $r(L)$, is given by the slower of r_{max} or $(2t_n(L))^{-1}$, where $t_n(L)$ is the time taken for

a photon to travel the length of the network via the quantum channel and the time for information to be fed back to the node from the BSA via the classical channel. For most ion-based networks, the length of the network becomes the limiting factor after a few hundred meters.

For the network shown in Fig. 11.1(A), $P_B(L)$ is given by

$$P_B(L) = P_p P_Q^y P_f(L) P_d \tag{11.2}$$

where P_Q is the QFC efficiency, $P_f(L)$ is the probability of transmission along the network fiber, P_d is the BSA detector efficiency, P_p is the probability of a photon being emitted, collected and coupled into the network fiber and y is the total number of QFC steps used per network arm. We assume the nodes are synchronized via a clock signal. The probability of transmission along a fiber is modeled as an exponential loss as a function of the distance travelled along the fiber.

In practice, entanglement rates are greatly reduced by relatively low photon collection efficiencies (typically $\leq 10\%$ for trapped-ion systems [30]). This is because after each photon request event, network nodes experience a dead-time of $r(L)^{-1}$ waiting to receive the BSA measurement result to determine if entanglement was successful before proceeding to request another photon.

11.1.2 Entanglement Rate, $R'(L)$, with NDSPM

The traditional two-node network, described in Section 11.1.1 and shown in Fig. 11.1(A), may be capable of a large photon request rate, $r(L)$, but in the presence of low photon coupling into the network, many of these attempts are wasted due to a low value of P_p. Placing a NDSPM

device at both network nodes (Fig. 11.1(B)) which detects the presence of a travelling photon, without destroying the ion-photon entangled state, can serve as a herald to either allow the entanglement protocol to proceed or to trigger a node to request another photon.

When no photon is detected at the start of the network fiber, the NDSPM signal can be used to trigger a subsequent photon request at a time of t_{nd}, instead of $2t_n(L)$, where t_{nd} is the NDSPM response time. The response time of the NDSPM should not impede the entanglement protocol for a given network distance L, and so one requires $t_{nd} \ll 2t_n(L)$. In the example case analysis in Section 11.2 a NDSPM response time, t_{nd}, of 1 μs is used. Such rapid response is possible using a NDSPM scheme such as that proposed by Xia et al. [87] which uses an effective three-wave mixing scheme in a neutral rubidium atomic vapor contained within a hollow-core photonic crystal fiber to impart a detectable phase shift on a probe beam when a single photon is present. With this example, after measurement, photonic quantum state fidelities greater than 0.9 are expected, with detection efficiencies near 0.91 [87]. This fidelity is within the range where entanglement distillation could be used to purify the ion-ion entanglement produced in the network at the cost of entanglement rate [26]. Alternatively, higher fidelities can be achieved by lowering the NDSPM detection efficiency for this method. Note that other NDSPM implementations such as a neutral-atom coupled to an optical cavity [40] and non-destructive single photon triggers [190] may be used to similar effect, provided they satisfy $t_{nd} \ll 2t_n(L)$ whilst sufficiently preserving the fidelity of the ion-photon entangled state.

The addition of a NDSPM flag makes it possible to request photons at a modified maximum rate of $r'_{max} = 1/T$, where $T = r_{max}^{-1} + t_{nd}$, until a photon is successfully detected in the network fiber. The average photon request rate in this configuration, $r'(L)$, can be calculated using a weighted average between $2t_n(L)$ and T given by

$$r'(L) = \frac{1}{p[2t_n(L)] + (1-p)T}, \tag{11.3}$$

where the probability of a photon being detected, per-request by the NDSPM, is given by

$$p = P_p P_Q^n P_{nd}, \tag{11.4}$$

where P_{nd} is the NDSPM detection efficiency and n is the number of QFC steps used before the NDSPM. To match the number of QFC steps required for our system to interact with Rb, we consider a network with $n = 1$.

Although Eq. 11.3 represents the average request rate of a single node, there is no guarantee that both nodes will be attempting to produce a photon at the same time. One node can successfully send a photon into the network, and be awaiting a signal from the BSA, while the other node is still attempting to produce a photon. The only instance in which entanglement can occur is when both nodes simultaneously attempt to produce photons (for a symmetric network) which occurs with probability

$$\alpha(L) = \frac{\frac{1}{p}T}{\frac{1}{p}T + 2t_n(L)}. \tag{11.5}$$

This factor is equivalent to the ratio of the average time a node spends attempting to get a successful NDSPM, T/p, relative to the total time it takes on average to produce a photon and get a response from the BSA.

Analogous to Eq. 11.1, the entanglement rate is then given by

$$R'(L) = \alpha(L) r'(L) [P_{nd} \Gamma_{nd} P_B(L)]^2 / 2, \tag{11.6}$$

where Γ_{nd} represents the transmission of the NDSPM, allowing for the possibility of a photon being successfully detected, but not transmitted past the NDSPM device. Such a transmission loss is not fundamental to the NDSPM scheme proposed in [87], but has been observed [40]. Using experimental parameters presented in section 11.2, we show that this rate can exceed that given by Eq. 11.1.

11.1.3 Entanglement Rate, $R_E^*(L)$, with NDSPM and BSA Photonic Storage

The network with a NDSPM described in section 11.1.2 can only produce entanglement when both nodes simultaneously attempt to produce photons, with probability $\alpha(L)$. We can remove the requirement for simultaneous photon emission on a given experimental cycle by using photonic storage just before each input to the BSA to synchronize photon arrival times (Fig. 11.1(C)). A photon that successfully reaches the photonic storage at one BSA input is stored until the photonic storage for the other BSA input also contains a photon, whereupon both photons are released into the BSA. This release event can be triggered by control electronics at the location of the BSA using logic circuitry and classical information fed forward by each NDSPM in the event of a successful photon herald[1]. After the synchronized photon release from the storage elements, the result of the BSA measurement is fed back to the nodes so that they are again requested to produce photons.

This method will decrease the average attempt rate for each node, but with sufficient storage

[1]Note that information must also be sent backwards to each node to enable proper phase-tracking of the resulting ion-ion entangled state.

efficiency, will allow for more efficient use of photons produced by the nodes, and an increase in entanglement rate. In this section, we will determine the average amount of time it takes for both nodes to produce a successful NDSPM, which is a requisite before entanglement may be attempted. We can then use this time to determine the entanglement rate of a hybrid network incorporating both NDSPM and photonic storage. Again, the entanglement rate is compared with a homogeneous network's entanglement rate (Eq. 11.1), for the case of a barium ion and neutral rubidium-based hybrid network in section 11.2.

We begin by considering the number of photon-request attempts needed before node i receives a successful NDSPM flag. The probability this occurs on the xth photon request since the last command from the BSA is given by a Geometric Distribution

$$P_i(x) = (1-p)^{x-1}p, \tag{11.7}$$

where $i \in \{1, 2\}$.

The probability a node has successfully emitted a photon into the network after any of the first X repetitions is given by the cumulative distribution function,

$$\mathbb{P}_i(x \leq X) = 1 - (1-p)^X. \tag{11.8}$$

Assuming node 1 is successful, the two possible outcomes are that node 2 has either already produced a photon or that node 2 still needs to produce a photon. In the former case, the production of a photon from node 1 is the limiting factor, with both nodes successfully sending

a photon into the network by time XT. For the latter case, node 2 is the limiting factor and entanglement can only be attempted after waiting an additional $1/p$ repetitions on average. The average time for both nodes to successfully send a photon into the network is then $XT + T/p$ for this case. We can therefore calculate the average time between entanglement attempts as

$$T^*(L) = \sum_{X=1}^{\infty} P_1(X) \left[X\mathbb{P}_2(x \leq X) + \left(X + p^{-1}\right)\left(1 - \mathbb{P}_2(x \leq X)\right)\right] T + 2t_n(L), \quad (11.9)$$

where the additional term $2t_n(L)$ is the network round trip time described in Section 11.1.1. Inserting Eq. 11.8 into 11.9 and simplifying gives

$$T^*(L) = \frac{2p-3}{p(p-2)} T + 2t_n(L). \quad (11.10)$$

The inverse of $T^*(L)$ is then the node's effective repetition rate, $r^*(L)$. We can write the entanglement generation rate in a manner similar to Eq. 11.6 as

$$R^*(L) = r^*(L)[P_f(L)\Gamma_{nd} E_s P_Q^z P_d]^2/2, \quad (11.11)$$

where E_s is the efficiency of the photon storage just before the BSA and where z is the number of QFC steps used in each network arm after the NDSPM. (This is distinct from the total number of QFC steps, y, as defined in section 11.1.1). Depending upon the color for used for network transmission and color needed for photon storage, there might be multiple QFC steps after the NDSPM involved as discussed in Section 11.2.

Implicitly, we have thus far assumed infinite storage times. Any realistic storage will not be

able to store photons indefinitely. Assuming storage that decays exponentially in time with time constant τ, one can show that $R^*(L)$ is modified by the multiplicative factor (see Appendix A)

$$\beta(p, T, \tau) = \frac{p(1 + e^{T/\tau} - p)}{(2 - p)(e^{T/\tau} + p - 1)}. \tag{11.12}$$

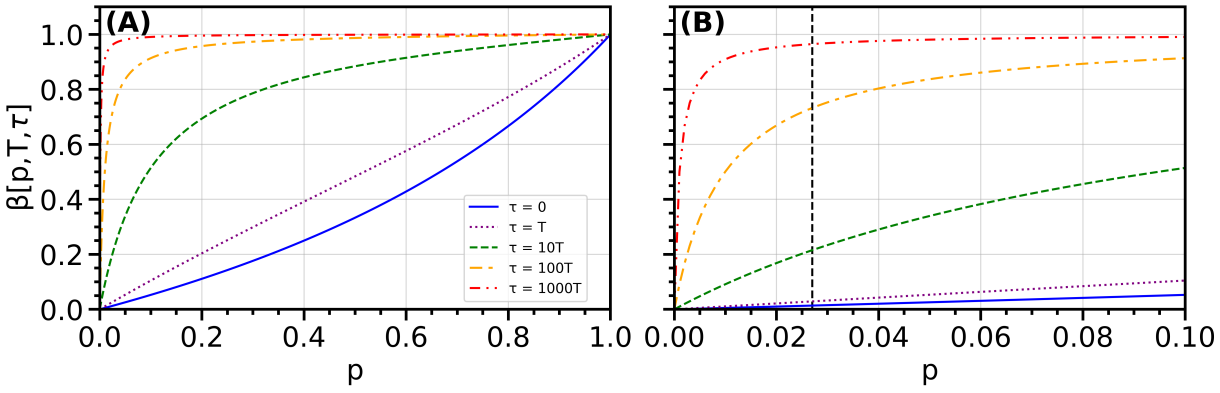

Figure 11.2: **Entanglement Rate Adjustment for Finite Storage Times**(a) Multiplicative factor, $\beta(p, T, \tau)$, required to adjust entanglement rates as a function of p for given ratios of storage time, τ, to experimental rep rate, T. b) Zoom-in of $0 < p < 0.1$, which is a typical operating range of current trapped ion systems. The dashed vertical line indicates the value of p used in Section 11.2.

Critically, this factor does not depend on the length of the network, and instead displays an exponential dependence on the ratio T/τ. This factor is plotted as a function of p for various ratios of T/τ in Fig. 11.2(a). As current trapped ion systems have $p < 0.1$, a zoom-in of the region $0 < p < 0.1$ is shown in Fig. 11.2(b). For typical ion systems, $\tau \gtrsim 1000T$ will ensure that finite storage reduces entanglement rates by $< 10\%$. For the remainder of this chapter, we will assume infinite storage, given the long storage times that have been demonstrated in neutral atomic media [84].

11.2 Case Study Using Barium Ions and Rubidium Atoms

To highlight the entanglement rate increase using the hybrid network tools described above, we present an example using network nodes comprised of single trapped Ba^+ ions. The ions are optically excited in a manner similar to Chapter 2 to emit a single 493-nm photon entangled with the ion's internal states. We use a maximum node photon request rate of $r_{max} = 2$ MHz as a realistic maximum for current ion trap experiments [30].

We set the probability of a photon being emitted, collected and coupled into the network fiber as $P_p = 0.06$ which assumes a 0.6 NA collection optic, 80% fiber coupling and an even Ba^+ isotope [28]. We use one QFC step ($y = 1$) for converting the 493 nm photon to 780 nm, making it compatible with neutral Rb NDSPM devices (efficiency $P_{nd} = 0.75$ corresponding to a fidelity of > 0.965 using the method in [87] and set $\Gamma_{nd} = 1$) and an additional QFC step ($y = 2$) to take the photon frequency to C-band. We note that a three-step distillation process as outlined in [26] is projected to increase a fidelity of > 0.965 to ≈ 0.9975 with an entanglement rate penalty of ≈ 8. An additional QFC step is required for the C-band network using photonic storage (Section 11.1.3) to take C-band back to 780 nm for compatibility with neutral-Rb storage devices (efficiency $E_s = 1$). Thus, $z = 0$ and $z = 2$ for the 780-nm and C-band based networks using storage, respectively. The QFC efficiencies are set at 60%[2]. We assume all network links comprise of optical fiber with a refractive index of 1.4 which is a good approximation for both near-IR and C-band networks. The fiber attenuation is set to 3 dB/km and 0.15 dB/km for the 780 nm and C-band network respectively. Table 11.1 gives the values used for entanglement rate calculations.

[2]We believe with better mode-matching optics and with custom optical coatings, this is achievable with our QFC systems.

Variable	Description	Value Used
r_{max}	maximum photon production rate	2 MHz
t_{nd}	NDSPM time	1μs
$t_n(L)$	network travel time	$1.4L/c$
P_p	per-shot photon collection efficiency	0.06
P_Q	QFC efficiency per stage	0.60
P_d	BSA detector efficiency	0.8
P_{nd}	NDSPM efficiency	0.75
E_s	Photon Storage Efficiency	1
Γ_{nd}	NDSPM transmission	1

Table 11.1: Values used in entanglement rate calculations.

In Figs. 11.3 and 11.4 we compare the entanglement generation rates for this example case in network configurations described in sections 11.1.1, 11.1.2 and 11.1.3 and operating at either 780 nm or in the C-band. The entanglement rates in Figs. 11.3 and 11.4 are determined using Eqs. 11.1, 11.6 and 11.11 (lines) and also using simulated data (data points in Fig. 11.3). See [51] for more details on the simulation.

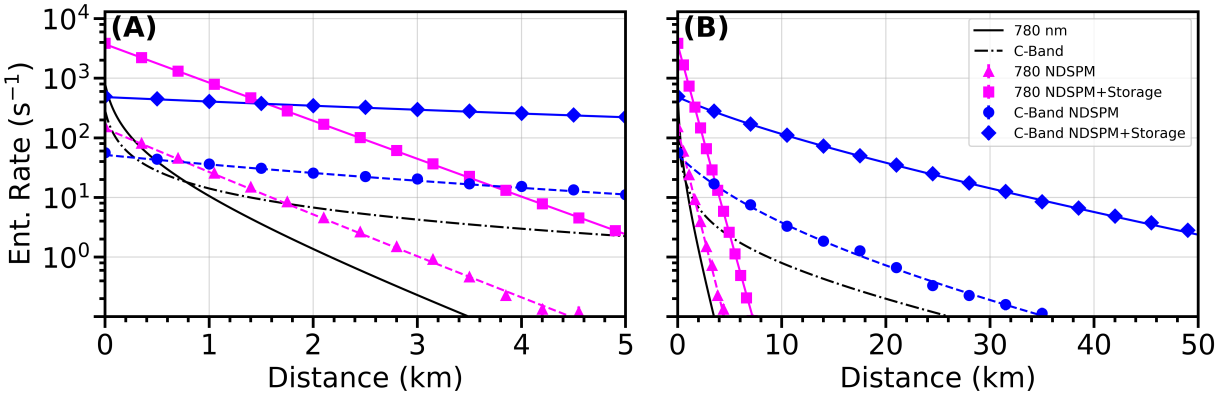

Figure 11.3: **Entanglement generation rates for various types of two node networks.** The entanglement generation rate of a two node network connected using 780 nm fiber links in a standard homogeneous network described in section 11.1.1 (black solid), using NDSPM as described in section 11.1.2 (magenta dashed and triangles) and using NDSPM and photon storage as described in section 11.1.3 (magenta solid and squares) as a function of network distance, L. Rates are also shown for a C-band-linked network in a standard homogeneous configuration (black dot-dashed), using NDSPM (blue dashed and circles) and using NDSPM and photon storage (blue solid and diamonds). (A) shows the rates over 5 km while (B) shows them over 50 km. The theory curves are determined from the analytical solutions given in this Chapter and the points are from simulated data [51] with statistical error bars smaller than the plot points.

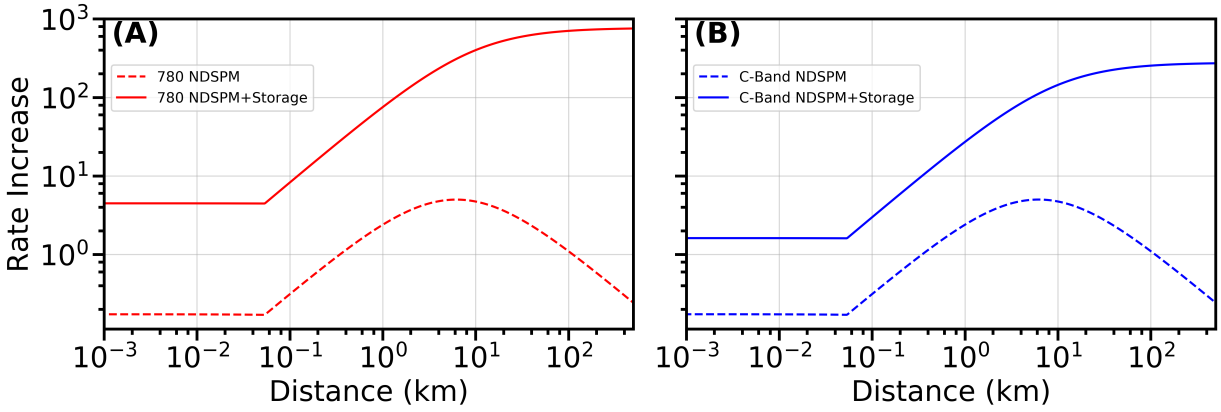

Figure 11.4: **Entanglement Rate Increases.** Increases are shown for networks with NDSPM (dashed) and NDSPM with storage (solid) over standard homogeneous networks using 780 nm photons, (A), and C-band photons, (B), as a function of distance, L. These are calculated from the ratios of the relevant curves in Fig. 11.3. In all cases the theory curves are determined from the analytical solutions given in this Chapter.

The black curves in Fig. 11.3 show the entanglement generation rates for basic two-node networks at 780 nm (black solid) and C-band (black dot-dashed) as described in section 11.1.1. The dashed curves show the rates for a network using NDSPM as described in section 11.1.2 using 780 nm photons (magenta and triangles) and C-band photons (blue and circles). When comparing hybrid networks using NDSPM (circles and triangles) to those using NDSPM and photonic storage (diamonds and squares), as described in sections 11.1.2 and 11.1.3 respectively, there is an increase in entanglement rates. For example, the 780 nm network with NDSPM outperforms a basic network using C-band photons up to $\approx$ 1.8 km. Then, by adding the photonic storage this distance can be increased to $\approx$5 km (magenta squares) in Fig. 11.3). Similarly, Fig. 11.3(A) shows that a C-band network using NDSPM outperforms the 780 nm network using NDSPM and photonic storage after $\approx$ 3.8 km.

The ratio of entanglement rate between a hybrid network using NDSPM (Eq. 11.6) and a homogeneous network (Eq. 11.1) shows a peak followed by a slow decline (dashed curves in

Fig. 11.4). This decline can be explained by Eqs. 11.3 and 11.5 where $2t_n(L)$ will dominate at large distances and, eventually, this method *underperforms* the homogeneous network rate $R(L)$. Comparing Eqs. 11.1 and 11.6, this occurs at lengths such that $P_{nd}^2 \frac{T}{2p^2} \lesssim t_n(L)$. The 780-nm network using photonic storage in addition to NDSPM (Eq. 11.11) for each node outperforms a standard 780-nm network at all distances for the values used in this work (solid curves in Fig. 11.4). At long distances $T^*(L) \approx r(L)^{-1}$, and for the 780-nm network, the rate ratio approaches an asymptotic limit given by $[\Gamma_{nd} E_s/(P_p P_Q)]^2 \approx 772$, the increase in success probability given a successful NDSPM. The C-band network with storage, having an additional stage of QFC versus the non-storage case, approaches and asymptotic limit of $[\Gamma_{nd} E_s/P_p]^2 \approx 278$. Note that in all cases, the "kink" in these curves represents the distance at which the standard network become limited in repetition rate by the network length.

The example cases in Figs. 11.3 and 11.4 use set values of the photon storage efficiency, $E_s = 1$, and NDSPM efficiency, $P_{nd} = 0.75$. Variations in these values will affect the network's entanglement rate increase over a homogeneous network. In Fig. 11.5 we show contour plots for both the 780 nm and C-band based networks as a function of E_s and P_{nd}. In both the 780 nm and C-band networks it can be seen that entanglement generation rates over an order of magnitude compared with a homogeneous network can be achieved with only modest values of E_s and P_{nd}. In fact, for the C-band network, factors of over 100 can be achieved after 10 km with E_s and P_{nd} values of ≈ 0.6.

We have described how integration of neutral-atom-based technologies into a trapped-ion based quantum network can overcome photon losses to yield significant increases in entanglement generation rates. We show this increase can be over a factor of 100 in both 780 nm and C-band based fiber network links. The use of hybrid technology in trapped-ion based quantum

networks is a promising method for establishing quantum networks with projected gains over their homogeneous counterparts in entanglement generation rates.

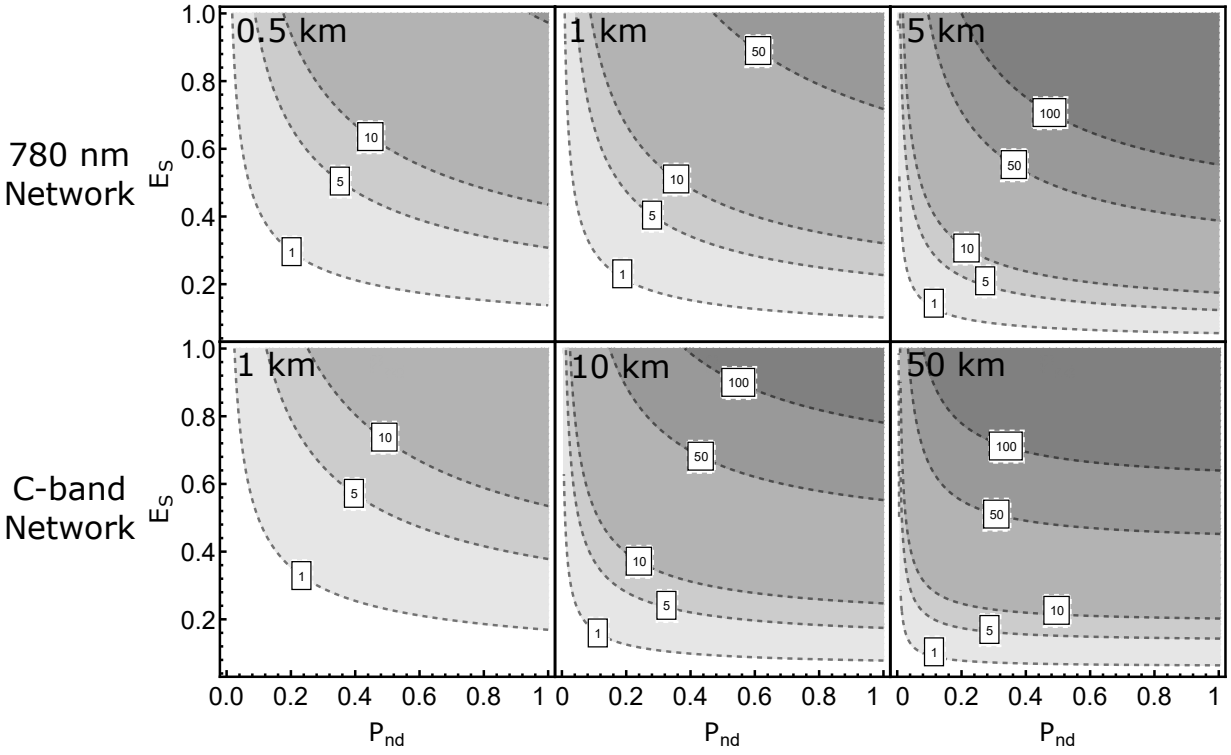

Figure 11.5: **Entanglement rate increase contours at both 780 nm and C-band as a function of E_s and P_{nd} for various distances.** All other variables are kept constant as given by Table 11.1 and as mentioned in Section 11.2.

Chapter 12: Outlook

In this thesis, I have presented our experimental apparatus that combines quantum frequency conversion with a trapped ion quantum communication node to enable both long-distance and hybrid quantum networking experiments. I have described projects where our group was among the first in the world[1] to demonstrate the conversion of single photons from a trapped ion, and to add in a second stage of frequency conversion to produce telecommunication wavelength photons for long distance quantum communication with trapped ions. This thesis also describes a series of experiments that demonstrate the feasibility of using quantum frequency conversion to connect our trapped ion node to disparate quantum systems, through the first ever demonstrated interactions of photons from a trapped ion with neutral atomic systems. This enables the integration of useful tools into a quantum network, as in the slow light experiment, as well as enabling direct entanglement between fundamentally different quantum systems, as shown in the two-photon interference experiment. Additionally, I have detailed our lab's development of both qubit manipulations and qubit state detection for our $^{138}Ba^{+}$ ion, and have presented an experiment where we demonstrate ion-photon entanglement before and after frequency conversion, using these techniques. Finally, I have demonstrated a "thought" experiment where we examine how combining this entanglement-preserving quantum frequency conversion with neutral-Rb based

[1] With the other two works being [33, 34].

technologies can potentially greatly improve entanglement rates in a hybrid quantum network. Looking forward, these results can be built upon in a variety of future experiments, which I will now briefly discuss from my point of view.

In terms of the quantum frequency conversion, it is very likely that conversion to the telecommunications O-band will enable much lower levels of noise, while still providing extremely low loss fiber transmission. In fact, our collaborators in the group of Edo Waks have recently constructed a quantum frequency converter meant to take our first stage 780-nm photons to the telecommunications O-band via an ARL-provided pump laser at 1989 nm. Preliminary measurements performed by graduate student Uday Saha seem to suggest that this converter has conversion efficiencies comparable to the 780 nm conversion presented in this thesis, with a drastic reduction in noise counts when comparted to the C-band converter.

Having demonstrated ion-photon entanglement at 780 nm, our lab is now particularly well positioned to serve as a node in a local-area quantum network. This can be done on two separate fronts: our lab hopes to generate ion-ion entanglement over a 780 nm network (and possibly over an O-band network) including our lab and the lab of Edo Waks, and there is also the obvious possibility of generating ion-neutral atom entanglement over the already existing fiber links between our lab and the lab of Steve Rolston and Trey Porto. Along the way, our lab will need to improve the repetition rate and polarization issues discussed in the ion-photon entanglement chapter. Higher repetition rates have been demonstrated by the Oxford trapped ion group using the same control system as we use, but require some custom-coding that we have not been able to implement yet. The polarization issues can likely be improved through active stabilization of these fibers. It is also likely that removal of many of the fiber butt-couplings that we currently use (put in place as we were developing the multiple components of our lab in parallel) will also

help reduce polarization drifts and increase photon rates.

Finally, the quadrupole transition work described in this thesis can be expanded to allow for the use of optical qubits in our lab. This will require improved cooling of our ions, probably via EIT-cooling [31, 172, 174], to further reduce ion temperatures and allow for high fidelity qubit operations. This would be, in my opinion, well worth the investment, as it will enable high-fidelity two-qubit gates (see [176]) using any of the many high power infrared lasers present in our lab (such as our QFC pump lasers at 1343 and 1590 nm). These two-qubit gates would enable even more interesting networking experiments involving both local and remote entanglement swapping.

Appendix A: Effect of Finite Storage Times on Networks Using Nondestructive Measurement and Storage

The entanglement rates given in Chapter 11 assume that the photons from each node can be stored indefinitely. Any realistic storage element will, however, have limits on the storage time. We will examine the effect of this finite storage time on entanglement rates.

When a photon from one of the nodes reaches the storage element, it is stored until the other node's photon is stored. Critically, this means that the relevant time scale is the difference between the arrival times of each of the photons to their respective storage devices. Because the network length is symmetric the relative arrival time is equivalent to the relative time between successful NDSPM of photons produced by each node. The travel time (and therefore the network length) has no effect on this time for the symmetric network considered. The probability that the second node successfully produces a photon M cycles after the first node successfully produces a photon is given by

$$
\begin{aligned}
P_{12}(M) &= \sum_{N=1}^{\infty} P_1(N) P_2(N+M) \\
&= \sum_{N=1}^{\infty} p^2 (1-p)^{2N+M-2} \\
&= \frac{p(1-p)^M}{2-p}.
\end{aligned} \tag{A.1}
$$

Similarly, the probability that the second node produces a photon M cycles before the first node successfully produces a photon is given by

$$
\begin{aligned}
P_{21}(M) &= \sum_{N=1}^{\infty} P_1(N) P_2(N-M) \theta(N-M) \\
&= \sum_{N=1}^{\infty} p^2 (1-p)^{2N-M-2} \theta(N-M) \\
&= \frac{(1-p)^M}{2-p}
\end{aligned} \tag{A.2}
$$

where $\theta(x)$ represents the left-side continuous Heaviside step function.

Using these values, we can calculate the weighted probability that the photons from both nodes are successfully stored. We consider single photon storage that decays exponentially over time, with decay constant τ. Both photons are then stored and successfully released with a probability, relative to the maximum storage probability of E_s, of

$$\beta(p,T,\tau) = \sum_{M=0}^{\infty}[P_{12}(M)+P_{21}(M)]e^{-MT/\tau} - P_{12}(0)$$
$$= \frac{p(1+e^{T/\tau}-p)}{(2-p)(e^{T/\tau}+p-1)}, \tag{A.3}$$

where T is the period as defined in Section 11.1.2. The $P_{12}(0)$ term is subtracted to keep from double counting for $M = 0$, where one should note $P_{12}(0) = P_{21}(0)$. The entanglement rate then is altered to

$$R^*(L) = \beta(p,T,\tau)r^*(L)[P_f(L)E_sP_Q^zP_d]^2/2. \tag{A.4}$$

Bibliography

[1] Martin Hilbert. Digital technology and social change: the digital transformation of society from a historical perspective. *Dialogues in Clinical Neuroscience*, 2022.

[2] David Kielpinski, Chris Monroe, and David J Wineland. Architecture for a large-scale ion-trap quantum computer. *Nature*, 417(6890):709–711, 2002.

[3] C. Monroe, R. Raussendorf, A. Ruthven, K. R. Brown, P. Maunz, L.-M. Duan, and J. Kim. Large-scale modular quantum-computer architecture with atomic memory and photonic interconnects. *Physical Review A*, 89:022317, Feb 2014.

[4] John Preskill. Quantum computing and the entanglement frontier. *arXiv preprint arXiv:1203.5813*, 2012.

[5] Han-Sen Zhong, Hui Wang, Yu-Hao Deng, Ming-Cheng Chen, Li-Chao Peng, Yi-Han Luo, Jian Qin, Dian Wu, Xing Ding, Yi Hu, et al. Quantum computational advantage using photons. *Science*, 370(6523):1460–1463, 2020.

[6] Peter W Shor. Algorithms for quantum computation: discrete logarithms and factoring. In *Proceedings 35th Annual Symposium on Foundations of Computer Science*, pages 124–134. Ieee, 1994.

[7] Guido Pagano, Aniruddha Bapat, Patrick Becker, Katherine S Collins, Arinjoy De, Paul W Hess, Harvey B Kaplan, Antonis Kyprianidis, Wen Lin Tan, Christopher Baldwin, et al. Quantum approximate optimization of the long-range ising model with a trapped-ion quantum simulator. *Proceedings of the National Academy of Sciences*, 117(41):25396–25401, 2020.

[8] Christian L Degen, Friedemann Reinhard, and Paola Cappellaro. Quantum sensing. *Reviews of Modern Physics*, 89(3):035002, 2017.

[9] Donghui Feng. Review of quantum navigation. In *IOP Conference Series: Earth and Environmental Science*, volume 237, page 032027. IOP Publishing, 2019.

[10] Peter Komar, Eric M Kessler, Michael Bishof, Liang Jiang, Anders S Sørensen, Jun Ye, and Mikhail D Lukin. A quantum network of clocks. *Nature Physics*, 10(8):582–587, 2014.

[11] Nicolas Gisin, Grégoire Ribordy, Wolfgang Tittel, and Hugo Zbinden. Quantum cryptography. *Reviews of Modern Physics*, 74(1):145, 2002.

[12] Stefano Pirandola, Ulrik L Andersen, Leonardo Banchi, Mario Berta, Darius Bunandar, Roger Colbeck, Dirk Englund, Tobias Gehring, Cosmo Lupo, Carlo Ottaviani, et al. Advances in quantum cryptography. *Advances in Optics and Photonics*, 12(4):1012–1236, 2020.

[13] H Jeff Kimble. The quantum internet. *Nature*, 453(7198):1023–1030, 2008.

[14] Rodney Van Meter. Quantum networking and internetworking. *IEEE Network*, 26(4):59–64, 2012.

[15] Rodney Van Meter, Ryosuke Satoh, Naphan Benchasattabuse, Takaaki Matsuo, Michal Hajdušek, Takahiko Satoh, Shota Nagayama, and Shigeya Suzuki. A quantum internet architecture. *arXiv preprint arXiv:2112.07092*, 2021.

[16] David Hucul, Ismail V Inlek, Grahame Vittorini, Clayton Crocker, Shantanu Debnath, Susan M Clark, and Christopher Monroe. Modular entanglement of atomic qubits using photons and phonons. *Nature Physics*, 11(1):37, 2015.

[17] Zheshen Zhang and Quntao Zhuang. Distributed quantum sensing. *Quantum Science and Technology*, 6(4):043001, 2021.

[18] Jonathan A Jones, Steven D Karlen, Joseph Fitzsimons, Arzhang Ardavan, Simon C Benjamin, G Andrew D Briggs, and John JL Morton. Magnetic field sensing beyond the standard quantum limit using 10-spin noon states. *Science*, 324(5931):1166–1168, 2009.

[19] Feihu Xu, Xiongfeng Ma, Qiang Zhang, Hoi-Kwong Lo, and Jian-Wei Pan. Secure quantum key distribution with realistic devices. *Reviews of Modern Physics*, 92(2):025002, 2020.

[20] Joseph F Fitzsimons. Private quantum computation: an introduction to blind quantum computing and related protocols. *npj Quantum Information*, 3(1):1–11, 2017.

[21] Stefanie Barz, Elham Kashefi, Anne Broadbent, Joseph F Fitzsimons, Anton Zeilinger, and Philip Walther. Demonstration of blind quantum computing. *Science*, 335(6066):303–308, 2012.

[22] Charles H Bennett, Gilles Brassard, Claude Crépeau, Richard Jozsa, Asher Peres, and William K Wootters. Teleporting an unknown quantum state via dual classical and einstein-podolsky-rosen channels. *Physical Review Letters*, 70(13):1895, 1993.

[23] Marek Zukowski, Anton Zeilinger, Michael A Horne, and Aarthur K Ekert. " event-ready-detectors" bell experiment via entanglement swapping. *Physical Review Letters*, 71(26), 1993.

[24] Uday Saha, James D Siverns, John Hannegan, Mihika Prabhu, Qudsia Quraishi, Dirk Englund, and Edo Waks. Routing single photons from a trapped ion using a photonic integrated circuit. *arXiv preprint arXiv:2203.08048*, 2022.

[25] Prajit Dhara, Norbert M Linke, Edo Waks, Saikat Guha, and Kaushik P Seshadreesan. Multiplexed quantum repeaters based on dual-species trapped-ion systems. *Physical Review A*, 105(2):022623, 2022.

[26] Ramil Nigmatullin, Christopher J Ballance, Niel De Beaudrap, and Simon C Benjamin. Minimally complex ion traps as modules for quantum communication and computing. *New Journal of Physics*, 18(10):103028, 2016.

[27] Ismail Volkan Inlek, Clayton Crocker, Martin Lichtman, Ksenia Sosnova, and Christopher Monroe. Multispecies trapped-ion node for quantum networking. *Physical Review Letters*, 118(25):250502, 2017.

[28] J. D. Siverns, X. Li, and Q. Quraishi. Ion–photon entanglement and quantum frequency conversion with trapped Ba^+ ions. *Applied Optics*, 56(3):B222–B230, Jan 2017.

[29] John Hannegan, Uday Saha, James D Siverns, Jake Cassell, Edo Waks, and Qudsia Quraishi. C-band single photons from a trapped ion via two-stage frequency conversion. *Applied Physics Letters*, 119(8):084001, 2021.

[30] LJ Stephenson, DP Nadlinger, BC Nichol, S An, P Drmota, TG Ballance, K Thirumalai, JF Goodwin, DM Lucas, and CJ Ballance. High-rate, high-fidelity entanglement of qubits across an elementary quantum network. *Physical Review Letters*, 124(11):110501, 2020.

[31] Clayton Crocker, Martin Lichtman, Ksenia Sosnova, Allison Carter, Sophia Scarano, and Christopher Monroe. High purity single photons entangled with an atomic qubit. *Optics Express*, 27(20):28143–28149, 2019.

[32] V Krutyanskiy, M Meraner, J Schupp, V Krcmarsky, H Hainzer, and BP Lanyon. Light-matter entanglement over 50 km of optical fibre. *npj Quantum Information*, 5(1):1–5, 2019.

[33] Thomas Walker, Koichiro Miyanishi, Rikizo Ikuta, Hiroki Takahashi, Samir Vartabi Kashanian, Yoshiaki Tsujimoto, Kazuhiro Hayasaka, Takashi Yamamoto, Nobuyuki Imoto, and Matthias Keller. Long-distance single photon transmission from a trapped ion via quantum frequency conversion. *Physical Review Letters*, 120:203601, May 2018.

[34] Matthias Bock, Pascal Eich, Stephan Kucera, Matthias Kreis, Andreas Lenhard, Christoph Becher, and Jürgen Eschner. High-fidelity entanglement between a trapped ion and a telecom photon via quantum frequency conversion. *Nature Communications*, 9(1):1–7, 2018.

[35] Dalia P Ornelas-Huerta, Alexander N Craddock, Elizabeth A Goldschmidt, Andrew J Hachtel, Yidan Wang, Przemyslaw Bienias, Alexey V Gorshkov, Steve L Rolston, and

James V Porto. On-demand indistinguishable single photons from an efficient and pure source based on a rydberg ensemble. *Optica*, 7(7):813–819, 2020.

[36] Andreas Reiserer and Gerhard Rempe. Cavity-based quantum networks with single atoms and optical photons. *Reviews of Modern Physics*, 87(4):1379, 2015.

[37] Bo Zhao, Markus Müller, Klemens Hammerer, and Peter Zoller. Efficient quantum repeater based on deterministic rydberg gates. *Physical Review A*, 81(5):052329, 2010.

[38] Simon Baur, Daniel Tiarks, Gerhard Rempe, and Stephan Dürr. Single-photon switch based on rydberg blockade. *Physical Review Letters*, 112(7):073901, 2014.

[39] Matthew D Eisaman, Axel André, F Massou, Michael Fleischhauer, Alexander S Zibrov, and Mikhail D Lukin. Electromagnetically induced transparency with tunable single-photon pulses. *Nature*, 438(7069):837–841, 2005.

[40] Andreas Reiserer, Stephan Ritter, and Gerhard Rempe. Nondestructive detection of an optical photon. *Science*, 342(6164):1349–1351, 2013.

[41] Anaïs Dréau, Anna Tchebotareva, Aboubakr El Mahdaoui, Cristian Bonato, and Ronald Hanson. Quantum frequency conversion of single photons from a nitrogen-vacancy center in diamond to telecommunication wavelengths. *Physical Review Applied*, 9(6):064031, 2018.

[42] Disheng Chen, Nikolay Zheludev, and Wei-bo Gao. Building blocks for quantum network based on group-iv split-vacancy centers in diamond. *Advanced Quantum Technologies*, 3(2):1900069, 2020.

[43] Qiong Chen, Wanli Yang, Mang Feng, and Jiangfeng Du. Entangling separate nitrogen-vacancy centers in a scalable fashion via coupling to microtoroidal resonators. *Physical Review A*, 83(5):054305, 2011.

[44] Filip Rozpedek, Raja Yehia, Kenneth Goodenough, Maximilian Ruf, Peter C Humphreys, Ronald Hanson, Stephanie Wehner, and David Elkouss. Near-term quantum-repeater experiments with nitrogen-vacancy centers: Overcoming the limitations of direct transmission. *Physical Review A*, 99(5):052330, 2019.

[45] Christoph Simon, Yann-Michel Niquet, Xavier Caillet, Joël Eymery, Jean-Philippe Poizat, and Jean-Michel Gérard. Quantum communication with quantum dot spins. *Physical Review B*, 75(8):081302, 2007.

[46] PM Intallura, MB Ward, OZ Karimov, ZL Yuan, P See, P Atkinson, DA Ritchie, and AJ Shields. Quantum communication using single photons from a semiconductor quantum dot emitting at a telecommunication wavelength. *Journal of Optics A: Pure and Applied Optics*, 11(5):054005, 2009.

[47] Harishankar Jayakumar, Ana Predojević, Thomas Kauten, Tobias Huber, Glenn S Solomon, and Gregor Weihs. Time-bin entangled photons from a quantum dot. *Nature Communications*, 5(1):1–5, 2014.

[48] Hyochul Kim, Ranojoy Bose, Thomas C Shen, Glenn S Solomon, and Edo Waks. A quantum logic gate between a solid-state quantum bit and a photon. *Nature Photonics*, 7(5):373–377, 2013.

[49] Nicolas Maring, Pau Farrera, Kutlu Kutluer, Margherita Mazzera, Georg Heinze, and Hugues de Riedmatten. Photonic quantum state transfer between a cold atomic gas and a crystal. *Nature*, 551(7681):485, 2017.

[50] A. N. Craddock, J. Hannegan, D. P. Ornelas-Huerta, J. D. Siverns, A. J. Hachtel, E. A. Goldschmidt, J. V. Porto, Q. Quraishi, and S. L. Rolston. Quantum interference between photons from an atomic ensemble and a remote atomic ion. *Physical Review Letters*, 123:213601, Nov 2019.

[51] John Hannegan, James D Siverns, Jake Cassell, and Qudsia Quraishi. Improving entanglement generation rates in trapped-ion quantum networks using nondestructive photon measurement and storage. *Physical Review A*, 103(5):052433, 2021.

[52] Shantanu Debnath, Norbert M Linke, Caroline Figgatt, Kevin A Landsman, Kevin Wright, and Christopher Monroe. Demonstration of a small programmable quantum computer with atomic qubits. *Nature*, 536(7614):63–66, 2016.

[53] Alexander Erhard, Joel J Wallman, Lukas Postler, Michael Meth, Roman Stricker, Esteban A Martinez, Philipp Schindler, Thomas Monz, Joseph Emerson, and Rainer Blatt. Characterizing large-scale quantum computers via cycle benchmarking. *Nature Communications*, 10(1):1–7, 2019.

[54] K. Wright, K. M. Beck, S. Debnath, J. M. Amini, Y. Nam, N. Grzesiak, J.-S. Chen, N. C. Pisenti, M. Chmielewski, C. Collins, K. M. Hudek, J. Mizrahi, J. D. Wong-Campos, S. Allen, J. Apisdorf, P. Solomon, M. Williams, A. M. Ducore, A. Blinov, S. M. Kreikemeier, V. Chaplin, M. Keesan, C. Monroe, and J. Kim. Benchmarking an 11-qubit quantum computer. *Nature Communications*, 10(1):1–6, 2019.

[55] JM Pino, JM Dreiling, C Figgatt, JP Gaebler, SA Moses, MS Allman, CH Baldwin, M Foss-Feig, D Hayes, K Mayer, C Ryan-Anderson, and B Neyenhuis. Demonstration of the trapped-ion quantum ccd computer architecture. *Nature*, 592(7853):209–213, 2021.

[56] Jacob Smith, Aaron Lee, Philip Richerme, Brian Neyenhuis, Paul W Hess, Philipp Hauke, Markus Heyl, David A Huse, and Christopher Monroe. Many-body localization in a quantum simulator with programmable random disorder. *Nature Physics*, 12(10):907–911, 2016.

[57] Jiehang Zhang, Guido Pagano, Paul W Hess, Antonis Kyprianidis, Patrick Becker, Harvey Kaplan, Alexey V Gorshkov, Z-X Gong, and Christopher Monroe. Observation of a many-body dynamical phase transition with a 53-qubit quantum simulator. *Nature*, 551(7682):601, 2017.

[58] Cornelius Hempel, Christine Maier, Jonathan Romero, Jarrod McClean, Thomas Monz, Heng Shen, Petar Jurcevic, Ben P Lanyon, Peter Love, Ryan Babbush, et al. Quantum

chemistry calculations on a trapped-ion quantum simulator. *Physical Review X*, 8(3):031022, 2018.

[59] P Jurcevic, H Shen, P Hauke, C Maier, T Brydges, C Hempel, BP Lanyon, Markus Heyl, R Blatt, and CF Roos. Direct observation of dynamical quantum phase transitions in an interacting many-body system. *Physical Review Letters*, 119(8):080501, 2017.

[60] Samuel M Brewer, J-S Chen, Aaron M Hankin, Ethan R Clements, Chin-wen Chou, David J Wineland, David B Hume, and David R Leibrandt. Al+ 27 quantum-logic clock with a systematic uncertainty below 10- 18. *Physical Review Letters*, 123(3):033201, 2019.

[61] BC Nichol, R Srinivas, DP Nadlinger, P Drmota, D Main, G Araneda, CJ Ballance, and DM Lucas. A quantum network of entangled optical atomic clocks. *arXiv preprint arXiv:2111.10336*, 2021.

[62] T Ruster, H Kaufmann, Marcelo Alejandro Luda, V Kaushal, Christian Tomás Schmiegelow, F Schmidt-Kaler, and UG Poschinger. Entanglement-based dc magnetometry with separated ions. *Physical Review X*, 7(3):031050, 2017.

[63] Laurent Stephenson. *Entanglement between nodes of a quantum network*. PhD thesis, University of Oxford, 2019.

[64] Clayton Crocker. *High Purity Single Photons Entangled with Barium Ions for Quantum Networking*. PhD thesis, University of Maryland, College Park, 2019.

[65] Allison Levin Carter. *Design and Construction of a Three-Node Quantum Network*. PhD thesis, University of Maryland, College Park, 2021.

[66] David L Moehring, Peter Maunz, Steve Olmschenk, Kelly C Younge, Dzmitry N Matsukevich, L-M Duan, and Christopher Monroe. Entanglement of single-atom quantum bits at a distance. *Nature*, 449(7158):68–71, 2007.

[67] Thomas W Noel. *Ion Photon Entanglement with Barium*. PhD thesis, University of Washington, 2014.

[68] Boris B Blinov, David L Moehring, L-M Duan, and Chris Monroe. Observation of entanglement between a single trapped atom and a single photon. *Nature*, 428(6979):153–157, 2004.

[69] David P DiVincenzo. The physical implementation of quantum computation. *Fortschritte der Physik: Progress of Physics*, 48(9-11):771–783, 2000.

[70] Pengfei Wang, Chun-Yang Luan, Mu Qiao, Mark Um, Junhua Zhang, Ye Wang, Xiao Yuan, Mile Gu, Jingning Zhang, and Kihwan Kim. Single ion qubit with estimated coherence time exceeding one hour. *Nature Communications*, 12(1):1–8, 2021.

[71] TP Harty, DTC Allcock, C J Ballance, L Guidoni, HA Janacek, NM Linke, DN Stacey, and DM Lucas. High-fidelity preparation, gates, memory, and readout of a trapped-ion quantum bit. *Physical Review Letters*, 113(22):220501, 2014.

[72] J. P. Gaebler, T. R. Tan, Y. Lin, Y. Wan, R. Bowler, A. C. Keith, S. Glancy, K. Coakley, E. Knill, D. Leibfried, and D. J. Wineland. High-fidelity universal gate set for $^{9}\mathrm{Be}^{+}$ ion qubits. *Physical Review Letters*, 117(6):060505, Aug 2016.

[73] CJ Ballance, TP Harty, NM Linke, MA Sepiol, and DM Lucas. High-fidelity quantum logic gates using trapped-ion hyperfine qubits. *Physical Review Letters*, 117(6):060504, 2016.

[74] Raghavendra Srinivas, SC Burd, HM Knaack, RT Sutherland, Alex Kwiatkowski, Scott Glancy, Emanuel Knill, DJ Wineland, Dietrich Leibfried, AC Wilson, DTC Allcock, and DH Slichter. High-fidelity laser-free universal control of two trapped ion qubits. *arXiv preprint arXiv:2102.12533*, 2021.

[75] Norbert M. Linke, Dmitri Maslov, Martin Roetteler, Shantanu Debnath, Caroline Figgatt, Kevin A. Landsman, Kenneth Wright, and Christopher Monroe. Experimental comparison of two quantum computing architectures. *Proceedings of the National Academy of Sciences*, 114(13):3305–3310, 2017.

[76] Prakash Murali, Dripto M Debroy, Kenneth R Brown, and Margaret Martonosi. Architecting noisy intermediate-scale trapped ion quantum computers. In *2020 ACM/IEEE 47th Annual International Symposium on Computer Architecture (ISCA)*, pages 529–542. IEEE, 2020.

[77] Chen-Kuan Chou. *Ion Photon Entanglement in a Parabolic Mirror Trap*. PhD thesis, University of Washington, 2017.

[78] Gabriel Araneda, Giovanni Cerchiari, Daniel B Higginbottom, Philip C Holz, Kirill Lakhmanskiy, Petr Obšil, Yves Colombe, and Rainer Blatt. The panopticon device: An integrated paul-trap–hemispherical mirror system for quantum optics. *Review of Scientific Instruments*, 91(11):113201, 2020.

[79] Gang Shu, Chen-Kuan Chou, Nathan Kurz, Matthew R Dietrich, and Boris B Blinov. Efficient fluorescence collection and ion imaging with the "tack" ion trap. *Journal of the Optical Society of America B*, 28(12):2865–2870, 2011.

[80] J. Schupp, V. Krcmarsky, V. Krutyanskiy, M. Meraner, T.E. Northup, and B.P. Lanyon. Interface between trapped-ion qubits and traveling photons with close-to-optimal efficiency. *PRX Quantum*, 2:020331, Jun 2021.

[81] Andy Eu-Jin Lim, Junfeng Song, Qing Fang, Chao Li, Xiaoguang Tu, Ning Duan, Kok Kiong Chen, Roger Poh-Cher Tern, and Tsung-Yang Liow. Review of silicon photonics foundry efforts. *IEEE Journal of Selected Topics in Quantum Electronics*, 20(4):405–416, 2013.

[82] YO Dudin and A Kuzmich. Strongly interacting rydberg excitations of a cold atomic gas. *Science*, 336(6083):887–889, 2012.

[83] J. Lampen, H. Nguyen, L. Li, P. R. Berman, and A. Kuzmich. Long-lived coherence between ground and rydberg levels in a magic-wavelength lattice. *Physical Review A*, 98:033411, Sep 2018.

[84] Irina Novikova, Ronald L Walsworth, and Yanhong Xiao. Electromagnetically induced transparency-based slow and stored light in warm atoms. *Laser & Photonics Reviews*, 6(3):333–353, 2012.

[85] Wui Seng Leong, Mingjie Xin, Chang Huang, Zilong Chen, and Shau-Yu Lan. Long light storage time in an optical fiber. *Physical Review Research*, 2:033320, Aug 2020.

[86] Dominik Niemietz, Pau Farrera, Stefan Langenfeld, and Gerhard Rempe. Nondestructive detection of photonic qubits. *Nature*, 591(7851):570–574, 2021.

[87] Keyu Xia, Mattias Johnsson, Peter L. Knight, and Jason Twamley. Cavity-free scheme for nondestructive detection of a single optical photon. *Physical Review Letters*, 116:023601, Jan 2016.

[88] Bastian Hacker, Stephan Welte, Gerhard Rempe, and Stephan Ritter. A photon–photon quantum gate based on a single atom in an optical resonator. *Nature*, 536(7615):193–196, 2016.

[89] T. M. Graham, Y. Song, J. Scott, C. Poole, L. Phuttitarn, K. Jooya, P. Eichler, X. Jiang, A. Marra, B. Grinkemeyer, M. Kwon, M. Ebert, J. Cherek, M. T. Lichtman, M. Gillette, J. Gilbert, D. Bowman, T. Ballance, C. Campbell, E. D. Dahl, O. Crawford, N. S. Blunt, B. Rogers, T. Noel, and M. Saffman. Multi-qubit entanglement and algorithms on a neutral-atom quantum computer. *Nature*, 604(7906):457–462, Apr 2022.

[90] Pascal Scholl, Michael Schuler, Hannah J Williams, Alexander A Eberharter, Daniel Barredo, Kai-Niklas Schymik, Vincent Lienhard, Louis-Paul Henry, Thomas C Lang, Thierry Lahaye, et al. Quantum simulation of 2d antiferromagnets with hundreds of rydberg atoms. *Nature*, 595(7866):233–238, 2021.

[91] Sepehr Ebadi, Tout T Wang, Harry Levine, Alexander Keesling, Giulia Semeghini, Ahmed Omran, Dolev Bluvstein, Rhine Samajdar, Hannes Pichler, Wen Wei Ho, et al. Quantum phases of matter on a 256-atom programmable quantum simulator. *Nature*, 595(7866):227–232, 2021.

[92] James D. Siverns, John Hannegan, and Qudsia Quraishi. Neutral-atom wavelength-compatible 780 nm single photons from a trapped ion via quantum frequency conversion. *Physical Review Applied*, 11:014044, Jan 2019.

[93] J. D. Siverns, J. Hannegan, and Q. Quraishi. Demonstration of slow light in rubidium vapor using single photons from a trapped ion. *Science Advances*, 5(10), 2019.

[94] Alexander Nicholas Craddock. *Rydberg Ensembles for Quantum Networking*. PhD thesis, University of Maryland, College Park, 2020.

[95] Dalia P Ornelas Huerta. *Experiments With Strongly Interacting Rydberg Atoms*. PhD thesis, University of Maryland, College Park, 2020.

[96] David J Griffiths. Introduction to electrodynamics, 2005.

[97] MG Raizen, JM Gilligan, James C Bergquist, Wayne M Itano, and David J Wineland. Ionic crystals in a linear paul trap. *Physical Review A*, 45(9):6493, 1992.

[98] Wenkai Fan, Li Du, Sihui Wang, and Huijun Zhou. Confining rigid balls by mimicking quadrupole ion trapping. *American Journal of Physics*, 85(11):821–829, 2017.

[99] David J Wineland, C Monroe, Wayne M Itano, Dietrich Leibfried, Brian E King, and Dawn M Meekhof. Experimental issues in coherent quantum-state manipulation of trapped atomic ions. *Journal of research of the National Institute of Standards and Technology*, 103(3):259, 1998.

[100] Dietrich Leibfried, Rainer Blatt, Christopher Monroe, and David Wineland. Quantum dynamics of single trapped ions. *Reviews of Modern Physics*, 75(1):281, 2003.

[101] Wolfgang Paul. Electromagnetic traps for charged and neutral particles. *Reviews of Modern Physics*, 62(3):531, 1990.

[102] Christian Roos. *Controlling the quantum state of trapped ions*. PhD thesis, University of Innsbruck, 2000.

[103] David Hucul, Justin E. Christensen, Eric R. Hudson, and Wesley C. Campbell. Spectroscopy of a synthetic trapped ion qubit. *Physical Review Letters*, 119:100501, Sep 2017.

[104] Ksenia Sosnova. *Mixed-species ion chains for quantum networks*. PhD thesis, University of Maryland, College Park, 2020.

[105] Günther Leschhorn, T Hasegawa, and T Schaetz. Efficient photo-ionization for barium ion trapping using a dipole-allowed resonant two-photon transition. *Applied Physics B*, 108(1):159–165, 2012.

[106] B Wang, JW Zhang, Chao Gao, and LJ Wang. Highly efficient and isotope selective photo-ionization of barium atoms using diode laser and led light. *Optics Express*, 19(17):16438–16447, 2011.

[107] Dirk Rei, Albrecht Lindner, Rainer Blatt, et al. Cooling of trapped multilevel ions: A numerical analysis. *Physical Review A*, 54(6):5133, 1996.

[108] Steve Olmschenk, Kelly C Younge, David L Moehring, Dzmitry N Matsukevich, Peter Maunz, and Christopher Monroe. Manipulation and detection of a trapped yb+ hyperfine qubit. *Physical Review A*, 76(5):052314, 2007.

[109] Carolyn Auchter, Chen-Kuan Chou, Thomas W Noel, and Boris B Blinov. Ion–photon entanglement and bell inequality violation with $^{138}Ba^{+}$. *Journal of the Optical Society of America B*, 31(7):1568–1572, 2014.

[110] Harald Weinfurter. Experimental bell-state analysis. *Europhysics Letters*, 25(8):559, 1994.

[111] YH Shih and Carroll O Alley. New type of einstein-podolsky-rosen-bohm experiment using pairs of light quanta produced by optical parametric down conversion. *Physical Review Letters*, 61(26):2921, 1988.

[112] Chong-Ki Hong, Zhe-Yu Ou, and Leonard Mandel. Measurement of subpicosecond time intervals between two photons by interference. *Physical Review Letters*, 59(18):2044, 1987.

[113] L.-M. Duan, M. D. Lukin, J. I. Cirac, and P. Zoller. Long-distance quantum communication with atomic ensembles and linear optics. *Nature*, 414:413, Nov 2001.

[114] Christoph Simon and William TM Irvine. Robust long-distance entanglement and a loophole-free bell test with ions and photons. *Physical Review Letters*, 91(11):110405, 2003.

[115] S Olmschenk, D Hayes, DN Matsukevich, P Maunz, DL Moehring, and C Monroe. Quantum logic between distant trapped ions. *International Journal of Quantum Information*, 8(01n02):337–394, 2010.

[116] Thomas Legero, Tatjana Wilk, Axel Kuhn, and Gerhard Rempe. Time-resolved two-photon quantum interference. *Applied Physics B*, 77(8):797–802, 2003.

[117] James D. Siverns and Qudsia Quraishi. Ion trap architectures and new directions. *Quantum Information Processing*, 16(12):314, Nov 2017.

[118] JD Siverns, LR Simkins, Seb Weidt, and WK Hensinger. On the application of radio frequency voltages to ion traps via helical resonators. *Applied Physics B*, 107(4):921–934, 2012.

[119] DJ Berkeland, JD Miller, James C Bergquist, Wayne M Itano, and David J Wineland. Minimization of ion micromotion in a paul trap. *Journal of Applied Physics*, 83(10):5025–5033, 1998.

[120] B Merkel, K Thirumalai, JE Tarlton, VM Schäfer, CJ Ballance, TP Harty, and DM Lucas. Magnetic field stabilization system for atomic physics experiments. *Review of Scientific Instruments*, 90(4):044702, 2019.

[121] Elizabeth A Donley, Thomas P Heavner, Filippo Levi, MO Tataw, and Steven R Jefferts. Double-pass acousto-optic modulator system. *Review of Scientific Instruments*, 76(6):063112, 2005.

[122] Eric D Black. An introduction to pound–drever–hall laser frequency stabilization. *American Journal of Physics*, 69(1):79–87, 2001.

[123] RWP Drever, John L Hall, FV Kowalski, J_ Hough, GM Ford, AJ Munley, and H Ward. Laser phase and frequency stabilization using an optical resonator. *Applied Physics B*, 31(2):97–105, 1983.

[124] James I Thorpe, K Numata, and J Livas. Laser frequency stabilization and control through offset sideband locking to optical cavities. *Optics Express*, 16(20):15980–15990, 2008.

[125] L Richter, H Mandelberg, M Kruger, and P McGrath. Linewidth determination from self-heterodyne measurements with subcoherence delay times. *IEEE Journal of Quantum Electronics*, 22(11):2070–2074, 1986.

[126] James McLoughlin. *Development and implementation of an Yb^+ ion trap experiment towards coherent manipulation and entanglement*. PhD thesis, University of Sussex, 2012.

[127] Tarun Dutta. *Precision measurement to study strongly correlated systems-from a single ion to phonons in an ion chain*. PhD thesis, National University of Singapore (Singapore), 2016.

[128] Jason Scott Pelc. *Frequency conversion of single photons: physics, devices, and applications*. PhD thesis, Standford University, 2012.

[129] Robert W Boyd. *Nonlinear optics*. Academic press, 2020.

[130] GA Magel, MM Fejer, and RL Byer. Quasi-phase-matched second-harmonic generation of blue light in periodically poled linbo3. *Applied Physics Letters*, 56(2):108–110, 1990.

[131] Martin M Fejer, GA Magel, Dieter H Jundt, and Robert L Byer. Quasi-phase-matched second harmonic generation: tuning and tolerances. *IEEE Journal of quantum electronics*, 28(11):2631–2654, 1992.

[132] Prem Kumar. Quantum frequency conversion. *Optics Letters*, 15(24):1476–1478, 1990.

[133] Jason S Pelc, Lijun Ma, CR Phillips, Qiang Zhang, C Langrock, O Slattery, Xiao Tang, and Martin M Fejer. Long-wavelength-pumped upconversion single-photon detector at 1550 nm: performance and noise analysis. *Optics Express*, 19(22):21445–21456, 2011.

[134] Paulina S Kuo, Jason S Pelc, Oliver Slattery, Yong-Su Kim, Martin M Fejer, and Xiao Tang. Reducing noise in single-photon-level frequency conversion. *Optics Letters*, 38(8):1310–1312, 2013.

[135] NV Surovtsev, VK Malinovskii, AM Pugachev, and AP Shebanin. The nature of low-frequency raman scattering in congruent melting crystals of lithium niobate. *Physics of the Solid State*, 45(3):534–541, 2003.

[136] RF Schaufele and MJ Weber. Raman scattering by lithium niobate. *Physical Review*, 152(2):705, 1966.

[137] Yu N Korkishko, VA Fedorov, TM Morozova, F Caccavale, F Gonella, and F Segato. Reverse proton exchange for buried waveguides in linbo 3. *Journal of the Optical Society of America A*, 15(7):1838–1842, 1998.

[138] William K Wootters and Wojciech H Zurek. The no-cloning theorem. *Physics Today*, 62(2):76–77, 2009.

[139] O Kashin, M Homann, V Matusevich, F Setzpfandt, T Pertsch, and R Kowarschik. Change of the refractive index in ppln waveguides due to the photorefractive effect. *Applied Physics B*, 104(3):547–551, 2011.

[140] Feng-Ming Yeh, Der-Chin Chen, Chuen-Lin Tien, and Shih-Chieri Lee. The off-axis parabolic mirror optical axis adjustment based on cyclic shearing interferometer. In *2015 Optoelectronics Global Conference (OGC)*, pages 1–4. IEEE, 2015.

[141] WJ Bates. A wavefront shearing interferometer. *Proceedings of the Physical Society (1926-1948)*, 59(6):940, 1947.

[142] Takashi Nomura, Kazuhide Kamiya, Hiroshi Miyashiro, Seiichi Okuda, Hatsuzo Tashiro, and Kazuo Yoshikawa. Shape measurements of mirror surfaces with a lateral-shearing interferometer during machine running. *Precision Engineering*, 22(4):185–189, 1998.

[143] Nicolas Maring, Dario Lago-Rivera, Andreas Lenhard, Georg Heinze, and Hugues de Riedmatten. Quantum frequency conversion of memory-compatible single photons from 606 nm to the telecom c-band. *Optica*, 5(5):507–513, 2018.

[144] Marlan O Scully and M Suhail Zubairy. *Quantum optics*. American Association of Physics Teachers, 1999.

[145] Rodney Loudon. *The quantum theory of light*. OUP Oxford, 2000.

[146] R Hanbury and RQ Twiss. A new type of interferometer for use in radio astronomy. *Phil. Mag.*, 45(7):663–682, 1954.

[147] Jun Ye, Steve Swartz, Peter Jungner, and John L Hall. Hyperfine structure and absolute frequency of the ^{87}Rb $5P_{3/2}$ state. *Optics Letters*, 21(16):1280–1282, 1996.

[148] G Muñoz-Matutano, D Barrera, CR Fernández-Pousa, R Chulia-Jordan, L Seravalli, G Trevisi, P Frigeri, S Sales, and J Martínez-Pastor. All-optical fiber hanbury brown & twiss interferometer to study 1300 nm single photon emission of a metamorphic inas quantum dot. *Scientific reports*, 6:27214, 2016.

[149] Rosa Brouri, Alexios Beveratos, Jean-Philippe Poizat, and Philippe Grangier. Photon antibunching in the fluorescence of individual color centers in diamond. *Optics Letters*, 25(17):1294–1296, Sep 2000.

[150] C. Becher, A. Kiraz, P. Michler, A. Imamoglu, W. V. Schoenfeld, P. M. Petroff, Lidong Zhang, and E. Hu. Nonclassical radiation from a single self-assembled inas quantum dot. *Physical Review B*, 63:121312, Mar 2001.

[151] K. J. Arnold, S. R. Chanu, R. Kaewuam, T. R. Tan, L. Yeo, Zhiqiang Zhang, M. S. Safronova, and M. D. Barrett. Measurements of the branching ratios for $6P_{1/2}$ decays in $^{138}\mathrm{Ba}^{+}$. *Physical Review A*, 100:032503, Sep 2019.

[152] Ryan M. Camacho, Michael V. Pack, and John C. Howell. Low-distortion slow light using two absorption resonances. *Physical Review A*, 73:063812, Jun 2006.

[153] Ryan M. Camacho, Michael V. Pack, John C. Howell, Aaron Schweinsberg, and Robert W. Boyd. Wide-bandwidth, tunable, multiple-pulse-width optical delays using slow light in cesium vapor. *Physics Review Letters*, 98:153601, Apr 2007.

[154] Jacob B Khurgin. Slow light in various media: a tutorial. *Advances in Optics and Photonics*, 2(3):287–318, 2010.

[155] Olga Kocharovskaya, Yuri Rostovtsev, and Marlan O Scully. Stopping light via hot atoms. *Physical Review Letters*, 86(4):628, 2001.

[156] Or Katz and Ofer Firstenberg. Light storage for one second in room-temperature alkali vapor. *Nature Communications*, 9(1):2074, 2018.

[157] N Akopian, L Wang, A Rastelli, OG Schmidt, and V Zwiller. Hybrid semiconductor-atomic interface: slowing down single photons from a quantum dot. *Nature Photon.*, 5(4):230, 2011.

[158] Nicolas Sangouard, Christoph Simon, Hugues De Riedmatten, and Nicolas Gisin. Quantum repeaters based on atomic ensembles and linear optics. *Reviews of Modern Physics*, 83(1):33, 2011.

[159] A. M. Dyckovsky and S. Olmschenk. Analysis of photon-mediated entanglement between distinguishable matter qubits. *Physical Review A*, 85:052322, May 2012.

[160] E Urban, Todd A Johnson, T Henage, L Isenhower, DD Yavuz, TG Walker, and M Saffman. Observation of rydberg blockade between two atoms. *Nature Physics*, 5(2):110–114, 2009.

[161] Hannes Gorniaczyk, Christoph Tresp, Johannes Schmidt, Helmut Fedder, and Sebastian Hofferberth. Single-photon transistor mediated by interstate rydberg interactions. *Physical Review Letters*, 113(5):053601, 2014.

[162] Thibault Peyronel, Ofer Firstenberg, Qi-Yu Liang, Sebastian Hofferberth, Alexey V Gorshkov, Thomas Pohl, Mikhail D Lukin, and Vladan Vuletić. Quantum nonlinear optics with single photons enabled by strongly interacting atoms. *Nature*, 488(7409):57–60, 2012.

[163] Y Stalgies, I Siemers, B Appasamy, T Altevogt, and PE Toschek. The spectrum of single-atom resonance fluorescence. *Europhysics Letters*, 35(4):259, 1996.

[164] Przemyslaw Bienias, James Douglas, Asaf Paris-Mandoki, Paraj Titum, Ivan Mirgorodskiy, Christoph Tresp, Emil Zeuthen, Michael J Gullans, Marco Manzoni, Sebastian Hofferberth, et al. Photon propagation through dissipative rydberg media at large input rates. *Physical Review Research*, 2(3):033049, 2020.

[165] Emil Zeuthen, Michael J Gullans, Mohammad F Maghrebi, and Alexey V Gorshkov. Correlated photon dynamics in dissipative rydberg media. *Physical Review Letters*, 119(4):043602, 2017.

[166] Markus Aspelmeyer, Thomas Jennewein, Martin Pfennigbauer, Walter R Leeb, and Anton Zeilinger. Long-distance quantum communication with entangled photons using satellites. *IEEE Journal of Selected Topics in Quantum Electronics*, 9(6):1541–1551, 2003.

[167] Alexey V Gorshkov, Axel André, Michael Fleischhauer, Anders S Sørensen, and Mikhail D Lukin. Universal approach to optimal photon storage in atomic media. *Physical Review Letters*, 98(12):123601, 2007.

[168] Moji Ghadimi, Valdis Blūms, Benjamin G Norton, Paul M Fisher, Steven C Connell, Jason M Amini, Curtis Volin, Harley Hayden, Chien-Shing Pai, David Kielpinski, et al. Scalable ion–photon quantum interface based on integrated diffractive mirrors. *npj Quantum Information*, 3(1):1–4, 2017.

[169] DN Matsukevich, Peter Maunz, David L Moehring, Steven Olmschenk, and Chris Monroe. Bell inequality violation with two remote atomic qubits. *Physical Review Letters*, 100(15):150404, 2008.

[170] Th Sauter, Werner Neuhauser, Rainer Blatt, and Peter E Toschek. Observation of quantum jumps. *Physical Review Letters*, 57(14):1696, 1986.

[171] A. Kramida, Yu. Ralchenko, J. Reader, and and NIST ASD Team. NIST Atomic Spectra Database (ver. 5.9), [Online]. Available: `https://physics.nist.gov/asd` [2016, January 31]. National Institute of Standards and Technology, Gaithersburg, MD., 2021.

[172] Ismail Volkan Inlek. *Multi-species trapped atomic ion modules for quantum networks*. PhD thesis, University of Maryland, College Park, 2016.

[173] Dahyun Yum, Debashis De Munshi, Tarun Dutta, and Manas Mukherjee. Optical barium ion qubit. *Journal of the Optical Society of America B*, 34(8):1632–1636, 2017.

[174] Regina Lechner, Christine Maier, Cornelius Hempel, Petar Jurcevic, Ben P Lanyon, Thomas Monz, Michael Brownnutt, Rainer Blatt, and Christian F Roos. Electromagnetically-induced-transparency ground-state cooling of long ion strings. *Physical Review A*, 93(5):053401, 2016.

[175] Anders Sørensen and Klaus Mølmer. Quantum computation with ions in thermal motion. *Physical Review Letters*, 82(9):1971, 1999.

[176] Brian C Sawyer and Kenton R Brown. Wavelength-insensitive, multispecies entangling gate for group-2 atomic ions. *Physical Review A*, 103(2):022427, 2021.

[177] Craig R Clark, Holly N Tinkey, Brian C Sawyer, Adam M Meier, Karl A Burkhardt, Christopher M Seck, Christopher M Shappert, Nicholas D Guise, Curtis E Volin, Spencer D Fallek, et al. High-fidelity bell-state preparation with ca+ 40 optical qubits. *Physical Review Letters*, 127(13):130505, 2021.

[178] CH Baldwin, BJ Bjork, M Foss-Feig, JP Gaebler, D Hayes, MG Kokish, C Langer, JA Sedlacek, D Stack, and G Vittorini. High-fidelity light-shift gate for clock-state qubits. *Physical Review A*, 103(1):012603, 2021.

[179] Wenzhe Wei, Peng Hao, Zhiyu Ma, Huixing Zhang, Liren Pang, Fangfei Wu, Ke Deng, Jie Zhang, and Zehuang Lu. Measurement and suppression of magnetic field noise of trapped ion qubit. *Journal of Physics B: Atomic, Molecular and Optical Physics*, 55(7):075001, 2022.

[180] Norman F Ramsey. A molecular beam resonance method with separated oscillating fields. *Physical Review*, 78(6):695, 1950.

[181] Erwin L Hahn. Spin echoes. *Physical Review*, 80(4):580, 1950.

[182] David J Szwer, Simon C Webster, Andrew M Steane, and David M Lucas. Keeping a single qubit alive by experimental dynamic decoupling. *Journal of Physics B: Atomic, Molecular and Optical Physics*, 44(2):025501, 2010.

[183] Thomas Ruster, Christian T Schmiegelow, Henning Kaufmann, Claudia Warschburger, Ferdinand Schmidt-Kaler, and Ulrich G Poschinger. A long-lived zeeman trapped-ion qubit. *Applied Physics B*, 122(10):1–7, 2016.

[184] Stephan Ritter, Christian Nölleke, Carolin Hahn, Andreas Reiserer, Andreas Neuzner, Manuel Uphoff, Martin Mücke, Eden Figueroa, Joerg Bochmann, and Gerhard Rempe. An elementary quantum network of single atoms in optical cavities. *Nature*, 484(7393):195, 2012.

[185] Matthias Lettner, Martin Mücke, Stefan l, Christoph Vo, Carolin Hahn, Simon Baur, Jörg Bochmann, Stephan Ritter, Stephan Dürr, and Gerhard Rempe. Remote entanglement between a single atom and a bose-einstein condensate. *Physical Review Letters*, 106(21):210503, 2011.

[186] B. Hensen, H. Bernien, A. E. Dréau, A. Reiserer, N. Kalb, M. S. Blok, J. Ruitenberg, R. F. L. Vermeulen, R. N. Schouten, C. Abellán, W. Amaya, V. Pruneri, M. W. Mitchell, M. Markham, D. J. Twitchen, D. Elkouss, S. Wehner, T. H. Taminiau, and R. Hanson. Loophole-free bell inequality violation using electron spins separated by 1.3 kilometres. *Nature*, 526(7575):682, Oct 2015.

[187] Robert Stockill, MJ Stanley, Lukas Huthmacher, E Clarke, M Hugues, AJ Miller, C Matthiesen, Claire Le Gall, and Mete Atatüre. Phase-tuned entangled state generation between distant spin qubits. *Physical Review Letters*, 119(1):010503, 2017.

[188] Peter C Humphreys, Norbert Kalb, Jaco PJ Morits, Raymond N Schouten, Raymond FL Vermeulen, Daniel J Twitchen, Matthew Markham, and Ronald Hanson. Deterministic delivery of remote entanglement on a quantum network. *Nature*, 558(7709):268–273, 2018.

[189] Hiroki Takahashi, Ezra Kassa, Costas Christoforou, and Matthias Keller. Strong coupling of a single ion to an optical cavity. *Physical Review Letters*, 124(1):013602, 2020.

[190] John C. Howell and John A. Yeazell. Nondestructive single-photon trigger. *Physical Review A*, 62:032311, Aug 2000.